Structural Investigation of Receptor Engagement and Monoclonal Antibodies Targeting *Plasmodium* Vaccine Antigens

A thesis presented by

Re'em Moskovitz

Lincoln College

to

The Scripps Research Institute, La Jolla, USA

and

The University of Oxford, Oxford, UK

Submitted in partial fulfillment of the requirements for the degree

Doctor of Philosophy in Biochemistry (OU/TSRI)

Under the supervision of

Prof. Ian A. Wilson

Prof. Matthew K. Higgins

April 2023

©2023 by Re’em Moskovitz
All rights reserved.

Acknowledgements

Through all the trials and tribulations that graduate school has thrown my way, my parents Liora and Ron and my sister Ma'ayan never stopped listening to my complaints and ramblings. I am forever grateful for their unconditional support. I'm very lucky to have had my friends there to help through the stressful times – Donna, Tam, Flora, Kate, and Juli, and everyone else, thank you.

I have a tremendous appreciation, and I am so thankful for the mentorship and supervision of Matthew Higgins. Thank you for taking me on as a student and closely mentoring me through my first structural biology project. Your scientific knowledge and passion discovery is admirable. I am also thankful to Edward Lowe for maintaining the crystallization facility and your expertise, to Simon Draper and Rob Moon for your collaboration and to Poy for the help across both Higgins and Wilson labs. I owe much of this to Snezana Vasiljević, Max Crispin, Nicole Zitzmann, and Raymond Dwek, who encouraged me to apply to this program and helped me fall in love with research.

Perhaps the most thanks are owed to Ian Wilson giving me the offer to join the Skaggs-Oxford program, helping through the many unexpected turns I've made through the past 6 years, and being a dedicated and attentive supervisor. Your scientific wisdom and willingness to leave no stone unturned is motivational. I am very privileged to have been the recipient of endless opportunities and your never-ending patience, writing advice, and academic rigor. I am thankful for your trust and support in coming up with new ideas. I am also thankful for the many members in the Wilson lab who have helped me throughout the way. First and foremost, I could not have done any of this without Gonzalo's expertise

and constant help. I would like to thank Robyn Stanfield, Xueyong Zhu, and Meng Yuan for dispensing invaluable advice about anything and everything X-ray crystallography. I would also like to thank Marc Elslinger for the technical support, Hank Tien for setting up an endless number of crystallization trials, and to Jeanne Matteson, Wenli Yu, and Beverly Ellis for the support in the lab. I am also thankful to all the beamline staff at SSRL, ALS, APS, and Diamond for their technical support.

I am fortunate to have had so much wisdom imparted my way from my committee, thank you Andrew Ward (chair), Dennis Burton, and Phil Dawson. I owe many thanks to Simon Newstead for my internal examiner, and for being my undergraduate tutor at Christ Church. I am also thankful to Bob Seder for being my external examiner and for your contributions to the field of malaria research, your work has been a source of inspiration throughout this thesis. I am also thankful for the collaboration from Fidel Zavala and Yevel Flores Garcia in John Hopkins University, your dedication to this project, rigorous and honest scientific discussion, and cooperation has not gone for granted. I would also like to thank Ding Zhang, Nathan Beutler, Thomas Rogers, Nelson Wu, Greg Martin, and Randall MacGill, Jessica (Woolf) Coppola, and Joseph Jardine for their collaboration and help with many parts of this thesis. I am incredibly grateful to the Skaggs family for the scholarship. Having the exceptional opportunity to complete my doctorate degree across two world-leading institutions in inspirational labs has exposed me to different paradigms of scientific thought, collaborations, and has been a formative experience. I am also grateful to PATH's Malaria Vaccine Initiative and The Bill & Melinda Gates Foundation for funding the malaria project, collaborative efforts, and resources.

Table of Contents

CHAPTER 1: Introduction *2*

1.1 Introduction *3*

1.2 The Plasmodium life cycle *6*

1.2.1 Liver-stage infection 8

1.2.2 Blood-stage invasion 9

1.2.3 Sexual reproduction and the mosquito host 10

1.3 Vaccination to target the liver stage *11*

1.3.1 The circumsporozoite protein is the main *Plasmodium* antigen for vaccination targeting the liver stage 12

1.3.2 Role of the circumsporozoite protein in Plasmodium infection of the human host 15

1.3.3 RTS,S: history and current standing 18

1.3.4 Correlates of antibody-mediated protection from RTS,S vaccination and natural infection against malaria 21

1.3.4.1 Effector functions: Fc receptor binding and phagocytic activity 22

1.3.4.2 Effector functions: complement activation 24

1.3.5 Monoclonal anti-PfCSP antibody-mediated protection from *P. falciparum* infection 26

1.3.5.1 Monoclonal antibodies binding to the major repeat domain 27

1.3.5.2 Monoclonal antibodies towards the C-terminal domain 28

1.3.5.3 Monoclonal antibodies to the minor repeat and junctional domain. 31

1.3.5.4 Monoclonal antibodies towards the N-terminal domain 32

1.3.6 Summary of our current knowledge of PfCSP as a vaccine candidate 32

1.4 Blood-Stage Vaccination *35*

1.4.1 DARC is an essential receptor for *Plasmodium vivax* invasion of reticulocytes 36

1.4.2 *Plasmodium vivax* DBP binds the DARC ectodomain on reticulocytes 38

1.4.3 The PvDBP-RII-DARC interaction 40

1.4.4 Natural immune response to PvDBP-RII 43

1.4.5 PvDBP-RII vaccination produces broadly inhibitory antibodies 45

1.4.6 Monoclonal antibodies towards PvDBP-RII target multiple epitopes 48

1.4.7 Summary of our current knowledge of PvDBP as a vaccine candidate and its interaction with DARC 51

1.5 Summary of thesis research *53*

1.6 References *58*

CHAPTER 2: Structural Insights on Novel Epitopes of the Plasmodium falciparum Circumsporozoite Protein N-Terminal Domain *70*

2.0 Abstract *71*

2.1 Introduction *72*

2.1.1 The N-terminal domain of CSP is important for parasite motility and invasion72

2.1.2 The PfCSP N-terminal domain is a target of monoclonal antibodies 73

2.2 Results *75*

2.2.1 Antibody Sources and Epitope Mapping 75

2.2.2 Determination of Antibody Epitopes by X-ray Crystallography 78

2.2.3 Structural Basis for 3F4 Binding to NtCSP 80

2.2.4 Structural Basis for 3A3 Binding to NtCSP 82

2.2.5 Germline Gene Usage of 3F4 and 3A3 82

2.2.6 Structural Basis for mNCSP6 Binding to NtCSP 84

2.2.7 Structural Basis for hmNCSP9 Binding to NtCSP 88

2.2.8 Structural Basis for mNCSP10 binding to NtCSP 90

2.2.9 Structural basis for mNCSP13 binding to NtCSP 93

2.2.10 Differential cross-strain binding potential of novel NtCSP targeting mAbs ... 94

2.2.11 *In Vivo* Protection of Murine mAbs in Mouse Liver Burden Model 98

2.2.12 Affinity maturation of 3A3 by Yeast Display 99

2.3 Discussion and future Work *103*

2.4 Materials and Methods *109*

2.4.1 Antibody Sequences and Cloning 109

2.4.2 Protein Expression and Purification 110

2.4.3 Bacterial Protein Expression (Performed by Gonzalo Gonzalez, Wilson lab) 110

2.4.4 Sequence and Structural Analysis 112

2.4.5 Epitope Mapping 112

2.4.6 Crystallization and Structure Determination 112

2.4.7 Affinity Determination of murine mAbs to NtCSP haplotypes (Performed by Nathan Beutler in collaboration with Dennis Burton, TSRI) 114

2.4.8 Affinity Maturation of 3A3 by yeast display (performed by Jessica Coppola in collaboration with Joseph Jardine, IAVI and Dennis Burton, TSRI) 115

2.4.9 Affinity Determination of 3A3 and affinity matured 3A3 variants (performed by Ding Zhang) 116

2.4.10 Mouse Protection Studies (performed in collaboration with Fidel Zavala, JHU) 116

2.5 Acknowledgements *117*

2.6 Declaration *117*

2.7 References *120*

CHAPTER 3: Structural Basis for High Avidity Binding of Monoclonal Antibodies from the MAL071 Trial to the αTSR domain *123*

3.0 Abstract *124*

3.1 Introduction *125*

3.1.1 Correlates of protection of antibodies targeting the CSP C-terminal domain . 125

3.1.2 Polymorphic epitopes of the CSP C-terminal domain 126

3.1.3 Monoclonal antibody binding to the CSP C-terminal domain 127

3.1.4 Aims 129

3.2 Results *130*

3.2.1 Determination of antibody epitopes by X-ray crystallography 130

3.2.2 Fab 369, 1525, and 1392 bind the polymorphic α-epitope of αTSR 132

3.2.2.1 Structural basis for Fab 367 binding to the αTSR domain 132

3.2.2.2 Structural basis for Fab 1525 binding to the αTSR domain 134

3.2.2.3 Structural basis for Fab 1392 binding to the αTSR domain 136

3.2.3 MAL071 mAbs target the α-epitope through conserved interactions 136

3.2.4 Fabs 369, 389, 1393, 1437, 1534, and 1550 bind the β-epitope of αTSR 139

3.2.4.1 Structural basis for Fab 369 binding to the αTSR domain 142

3.2.4.2 Structural basis for Fab 389 binding to the αTSR domain 144

3.2.4.3 Structural basis for Fab 1393 binding to the αTSR domain 146

3.2.4.4 Structural basis for Fab 1437 binding to the αTSR domain 148

3.2.4.5 Structural basis for Fab 1534 binding to the αTSR domain 150

3.2.4.6 Structural basis for Fab 1550 binding to the αTSR domain 152

3.2.5 mAb 1504 binds a novel epitope on the αTSR domain 154

3.2.6 Antibodies binding the β-epitope provide cross-strain binding to a panel of αTSR haplotypes 156

3.2.7 Antibodies binding the β-epitope share a small consensus epitope 158

3.2.8 Antibodies targeting the αTSR domain provide weak protection in mouse *in vivo* model 162

3.2.9 Antibodies binding conserved epitopes on αTSR have a higher avidity index 165

3.3 Discussion *168*

3.3.1 RTS,S vaccination elicits a broad range of mAbs targeting conserved αTSR epitopes 168

3.3.2 High affinity mAbs targeting αTSR do not confer sterile protection in mice . 169

3.3.3 CtCSP-mediated immunity reveals a missing link in our understanding of vaccine-mediated protective efficacy against malaria infection 170

3.4 Materials and Methods *174*

3.4.1 Sequences and Cloning 174

3.4.2 Sequence Analysis 174

3.4.3 Expression and purification of αTSR from *E. coli* (performed by Gonzalo Gonzales, Wilson lab) 174

3.4.4 Protein expression and purification in ExpiCHO cells 176

3.4.5 Crystallization and structural determination 177

3.4.6 Surface Plasmon Resonance (performed by Nathan Beutler, Burton Lab, TSRI) 180

3.4.7 Liver Burden Assay (performed by Yevel Flores Garcia, Zavala Lab, JHU) . 181

3.4.8 Antibody avidity enzyme-linked immunoassay 181

3.5 Acknowledgements *182*

3.6 Declaration *183*

3.7 References *188*

CHAPTER 4: Novel Immunogen Design Incorporating Protective CSP B-cell Epitopes into the αTSR Domain *192*

4.0 Abstract *193*

4.1 Introduction *194*

4.2 Results *197*

4.2.1 Immunogen design rationale *197*

4.2.2 Antibody binding to hybrid immunogens expressed on HEK cell surface 199

4.2.3 Nanoparticle expression and purification 201

4.2.4 Antigenicity of αTSR-based nanoparticles 202

4.2.5 Immunogenicity of αTSR-based nanoparticles 206

4.2.6 Hybrid-domain αTSR-based immunogens provide protection in mice 208

4.3 Discussion and future work *210*

4.4 Materials and methods *213*

4.4.1 Flow Cytometry 213

4.4.2 Nanoparticle design (by Nelson Wu, Schief lab) 213

4.4.3 Nanoparticle expression and purification in HEK239F cells 214

4.4.4 Negative stain electron microscopy (EM) (performed by Theresa Fassel, TSRI) 215

4.4.5 Antigenicity ELISA 215

4.4.6 Mouse immunization (performed by Yevel Flores-Garcia, Berenice Salgado-Jimenez, John Hopkins University) 216

4.4.7 Immunogenicity ELISA (performed by Yevel Flores-Garcia, Berenice Salgado-Jimenez, Zavala lab, John Hopkins University) 217

4.5 Acknowledgements *217*

4.6 Declaration *218*

CHAPTER 5: Structural Basis for Engagement of the DARC Ectodomain with the Minimal Binding Region of Plasmodium vivax DBP *223*

5.0 Abstract *224*

5.1 Introduction *225*

5.1.1 The *Plasmodium vivax* Duffy-binding protein (PvDBP) 225

5.1.2 Duffy-antigen receptor for chemokines (DARC) 226

5.1.3 PvDBP-RII binds the DARC extracellular domain 229

5.1.4 PvDBP-RII as a promising vaccine candidate 229

5.2 Results *232*

5.2.1 Purification of PvDBP-RII from *Escheria coli* inclusion bodies 232

5.2.2 Construct design for expression of PvDBP in mammalian cells 234

5.2.3 Purification and crystallization of PvDBP-RII in complex with DARC ectodomain and DB1 238

5.2.4 DARC binding is mediated by positively charged residues on subdomain 2 243

5.2.5 Binding epitope of inhibitory monoclonal antibody DB1 to PvDBP-RII 246

5.2.6 Molecular dynamics simulation of DARC ectodomain binding to PvDBP-RII 252

5.2.7 Isothermal titration calorimetry of PvDBP-RII binding to DARC ectodomain 254

5.2.8 Inhibition of merozoite invasion of erythrocytes by DARC ectodomain 254

5.2.9 Small-angle X-ray scattering of PvDBP-RII in complex with DARC ectodomain 257

5.2.11 Limited proteolysis of PvDBP ectodomain 261

5.2.12 $PvDBP_{Ecto}$ Binds $DARC_{Ecto}$ and Inhibitory Antibody DB10 in Solution 263

5.2.13 Purification of full-length DARC from mammalian cell culture 265

5.2.14 PvDBP Ectodomain Binds Full-Length DARC 268

5.3 Discussion and future Work 270

5.4 Materials and methods 274

5.4.1 Expression and purification of PvDBP-RII from *E. coli* inclusion bodies 274

5.4.2 PvDBP Construct Design and Structure Prediction 275

5.4.3 Transfection of HEK293F cells 275

5.4.4 Small-scale expression trials in HEK293F cells 276

5.4.5 Purification of full-length DARC from HEK293F cell expression 276

5.4.6 Transfection in Expi293F cells 277

5.4.7 Purification of Fab fragments from Expi293F cell expression 277

5.4.8 Purification of DARC ectodomain peptide from Expi293F cell expression ... 278

5.4.9 Purification of the PvDBP-RII-DARCEcto-DB1 triple complex from Expi293F cell expression 279

5.4.10 Large-scale expression and purification of PvDBP ectodomain from HEK293F cell expression 279

5.4.11 Structural determination of the PvDBP-RII-DB1-DARCEcto triple complex structure 280

5.4.12 Circular Dichroism 281

5.4.13 Limited Proteolysis 281

5.4.14 Pull-down of full-length DARC with PvDBP ectodomain 281

5.4.15 Western Blot 282

5.5 Declaration *282*

5.6 Acknowledgement *283*

5.6 References *285*

CHAPTER 6: Concluding Remarks *288*

6.1 Concluding remarks *289*

6.2 References *296*

APPENDIX 1: C.V. *300*

APPENDIX 2: Publications *302*

List of Figures

Figure 1.1. Global prevalence of Plasmodium falciparum and Plasmodium vivax malaria. *4*

Figure 1.2. The Plasmodium life cycle. *7*

Figure 1.3. Schematic of PfCSP protein domains and the leading malaria vaccine RTS,S. *14*

Figure 1.4. Structure of the C-terminal αTSR domain and antibody epitopes. *29*

Figure 1.5. Structure of DARC and PvDBP *37*

Figure 1.6. Structural Basis for Engagement of PvDBP-RII with DARC and Monoclonal Antibodies *42*

Figure 2.1. Antibody lineages and complementarity defining region sequences of murine and human mAbs that bind NtCSP. *76*

Figure 2.2. Epitope mapping of human and murine monoclonal antibody binding to NtCSP *77*

Figure 2.3. Buried surface area formed by antibody binding to NtCSP. *79*

Figure 2.4. Structural basis for 4F3 binding to NtCSP. *81*

Figure 2.5. Structural basis for 3A3 binding to NtCSP. *83*

Figure 2.6. Primary contacts mediating binding of 3F4 and 3A3 to NtCSP are germline encoded. *85*

Figure 2.7. Structural basis for mNCSP6 binding to NtCSP *86*

Figure 2.8. Structural basis for mNCSP9 binding to NtCSP. *89*

Figure 2.9. The binding of mNCSP9 to peptide 7 is stabilized by homotypic interactions in the crystal lattice. *91*

Figure 2.10. Structural basis for mNCSP10 binding to NtCSP. *92*

Figure 2.11. Structural basis for mNCSP13 binding to NtCSP. *95*

Figure 2.12. Binding of murine mAbs to a panel of NtCSP haplotypes. *97*

Figure 2.13. In vivo protection of mNCSP2-10 in mouse liver burden assay. *99*

Figure 2.14. Affinity maturation of 3A3 by yeast display. *101*

Figure 3.1. Structure of the C-terminal αTSR domain and antibody epitopes *128*

Figure 3.2. CDR sequences of MAL071 mAbs targeting the αTSR domain of CSP. *131*

Figure 3.3. Paratopes of α-epitope binding Fabs 367, 1525, and 1392. ..... *133*

Figure 3.4. Structural basis for binding of Fabs 367, 1525, and 1392 to αTSR. *135*

Figure 3.5. Conserved interactions mediating binding of Fab 367, 1525, and 1392 to the α-epitope. *137*

Figure 3.6. Paratopes of α-epitope binding Fabs 1512, 369, 389, and 1393. ..... *140*

Figure 3.7. Paratopes of α-epitope binding Fabs 1437, 1534, and 1550. ..... *141*

Figure 3.8. Structural basis for Fab 369 binding the αTSR domain of PfCSP. *143*

Figure 3.9. Structural basis for Fab 389 binding the αTSR domain of PfCSP. *145*

Figure 3.10. Structural basis for Fab 1393 binding the αTSR domain of PfCSP. *147*

Figure 3.11. Structural basis for Fab 1437 binding the αTSR domain of PfCSP. *149*

Figure 3.12. Structural basis for Fab 1534 binding the αTSR domain of PfCSP. 151

Figure 3.13. Structural basis for Fab 1550 binding the αTSR domain of PfCSP. 153

Figure 3.14. Fab 1504 binds a new epitope on αTSR. 155

Figure 3.15. Binding of MAL071 mAbs to a panel of CtCSP haplotypes. 157

Figure 3.16. Summary of buried surface area formed by MAL071 mAb binding to the β-epitope. 160

Figure 3.17. Defining a consensus β-epitope through interaction residues. 161

Figure 3.18. In vivo protection of MAL071 mAbs by mouse liver burden assay. 163

Figure 3.19. Combined in vivo protection of MAL071 mAbs by liver burden assay. ... 165

Figure 3.20. Binding to the conserved epitope on αTSR correlates with avidity. 166

Supplementary Figure 3.1. Individual B-factors of Fab 367 and Fab 1392 in complex with αTSR. 191

Figure 4.1. αTSR-based immunogen design. 198

Figure 4.2. Monoclonal antibody binding to αTSR variants expressed on HEK cell surface. 200

Figure 4.3. Expression and purification of nanoparticles in HEK293F cells 202

Figure 4.4. Negative-stain electron microscopy of purified nanoparticles 203

Figure 4.5 Antigenicity of modified αTSR nanoparticles to CtCSP binding mAbs 204

Figure 4.6 Antigenicity of modified αTSR nanoparticles to repeat and junctional epitope binding mAbs. 205

Figure 4.7. Immunogenicity of NP1-7 adjuvanted with AS01B in C57Bl/6 mice. 207

Figure 4.8. NP1-7 provide protection in C57Bl/6 mouse sporozoite challenge 209

Supplementary figure 4.1. Flow cytometry gating strategy. 222

Figure 5.1. PvDBP domain architecture and PvDBP-RII X-ray crystal structure. 227

Figure 5.2. Structural basis for engagement of PvDBP-RII with DARC and monoclonal antibodies. 228

Figure 5.3. Binding epitopes of monoclonal antibodies on PvDBP-RII. 231

Figure 5.4. Purification of PvDBP-RII after refolding of E. coli inclusion bodies. 233

Figure 5.5. Expression Construct Design for PvDBP Expression In Mammalian Cell Culture 235

Figure 5.6. Expression trial of PvDBP constructs in HEK293F cells. 237

Figure 5.7. Purification of DARC ectodomain, DB1 F(ab), and the PvDBP-RII-DARC-DB1 triple complex. 239

Figure 5.8. Comparison of PvDBP-RII-DARC X-ray crystal structures. 242

Figure 5.9. DARC ectodomain wraps around a protrusion in PvDBP-RII subdomain 2 244

Figure 5.10. DARC ectodomain binds PvDBP-RII through electrostatic interactions. 245

Figure 5.11. Structural basis for DB1 binding to PvDBP-RII. 247

Figure 5.12. DB1 binds a polymorphic hot-spot on PvDBP-RII Subdomain 2. 249

Figure 5.13. DB1 binds a different epitope to previously characterized mAbs. *250*

Figure 5.14. Binding site of human monoclonal antibody DB1. ..... *251*

Figure 5.15. Molecular dynamics simulations of Tyr30 and Tyr41 binding with and without sulphation. *253*

Figure 5.16. Isothermal titration calorimetry measurements of sulphated and unsulphated DARC ectodomain peptides binding to PvDBP-RII. *255*

Figure 5.17. Inhibition of transgenic P. knowlesi parasites expressing PvDBP by synthetic DARC ectodomain peptides. *256*

Figure 5.18. Small angle X-ray scattering of PvDBP-RII complexes. *258*

Figure 5.19. Purification of PvDBP ectodomain from HEK293F expression. *260*

Figure 5.20. Limited proteolysis of PvDBP ectodomain. *262*

Figure 5.21. PvDBP ectodomain forms a complex with DARC ectodomain. *264*

Figure 5.22. PvDBP ectodomain binds monoclonal antibody DB10. ..... *266*

Figure 5.23. Purification of DARC from mammalian cell culture. *268*

Figure 5.24. Pull-down of full length DARC with PvDBP ectodomain. *269*

List of Tables

Table 2.1. Crystallographic data collection and refinement……118

Table 2.2. Crystallographic data collection and refinement……119

Table 3.1. Crystallographic data collection and refinement……184

Table 3.2. Crystallographic data collection and refinement……185

Table 3.3. Crystallographic data collection and refinement……186

Table 3.4. Crystallographic data collection and refinement……187

Table 5.1. Crystallographic data collection and refinement……284

List of Abbreviations

αTSR	thrombospondin-like type 1 repeat
AI	avidity index
ALS	Advanced Light Source
ANOVA	analysis of variance
APS	Alternative Photon source
CD71	cluster of differentiation 71
cDNA	complementary deoxyribonucleic acid
CDR	complementarity defining regions
CHMI	controlled human malaria infection
CHS	cholesteryl hemisuccinate
CMC	critical micelle concentration
CSP	circumsporozoite protein
CtCSP	C-terminus of circumsporozoite protein
DARC	Duffy antigen receptor for chemokines
DBP	Duffy binding protein
DDM	N-dodecyl-β-maltoside
DMEM	Dulbecco's modified eagle medium
DNA	deoxyribonucleic acid
DTT	dithiothreitol
E. coli	*Escheria coli*
EBL	erythrocyte binding ligand

EBP	erythrocyte binding protein
EC50	half-maximal effective concentration
EDTA	ethylenediaminetetraacetic acid
ELISA	emzyme-linked immunosorbent assay
EM	electron microscopy
EU/ml	endotoxin units per mililiter
Fab	fragment antigen binding
FACS	fluorescent activated cell-sorting
Fc	fragment crystallizable
FcγR	Fc gamma receptor
G6PD	glucose-6-phosphate dehydrogenase
GAG	glycosaminoglycans
GFP	green fluorescent protein
GNL	Galanthus Nivalis Lectin
GPI	glycophosphatidylinositol
HA	haemagluttinin
HEPES	2-[4-(2-hydroxyethyl)piperazin-1-yl]ethanesulfonic acid
HIV	human immunodeficiency virus
HRP	horseradish peroxidase
IC50	half-maximal inhibitory concentration
IgG	Immunoglobulin G
IPTG	isopropyl β-D-1-thiogalactopyranoside

iRBC	infected red blooc cell
ITN	insecticide treated nets
Kd	dissociation constant
kDa	kilodalton
KLH	keyhole limpet heamocyanin
KSCN	potassium thiocyanate
mAb	monoclonal antibody
MFI	mean fluorescent intensity
MHC	major histocompatibility complex
mRNA	messenger RNA
MVA	modified vaccinia Ankara
MW	molecular weight
NiNTA	Nickel-nitrilotriacetic acid
NK cells	natural killer cells
NMR	nuclear magnetic resonance
NP	nanoparticle
NtCSP	N-terminus of circumsporozoite protein
OPA	opsonophagocytic activity
P. berghei	*Plasmodium berghei*
P. falciparum	*Plasmodium falciparum*
P. knowlesi	*Plasmodium knowlesi*
P. pastoris	*Pichia pastoris*

P. vivax	*Plasmodium vivax*
P. yoleii	*Plasmodium yoleii*
PBMC	peripheral blood mononuclear cells
PBS	phosphate buffered solution
PDB	protein data bank
PEG	polyethylene glycol
PFA	paraformaldehyde
PNG	Papua New Guinea
PNGase F	Peptide N-glycosidase F
PV	parasitophorous vacuole
RBC	red blood cell
RBP	reticulocyte binding protein
RMSD	root-mean-square deviation
RNA	ribonucleic acid
rsCSP	recombinant short circumsporozoite protein
RTM	room temperature
RU	response units
SARS-CoV-2	Severe acute respiratory syndrome coronavirus 2
SAXS	small-angle X-ray scattering
SDS-PAGE	sodium dodecyl sulfate–polyacrylamide gel electrophoresis
SEC	size exclusion chromatography
SHM	somatic hypermutation

SPR	surface plasmon resonance
SSRL	Stanford Synchrotron Radiation Lightsource
TBS	Tris buffered solution
TEV	tobacco etch virus
TfR1	Transferrin receptor 1 (CD71)
TM	transmembrane
TRIS	tris(hydroxymethyl)aminomethane
TSR	thrombospondin
TSRI	The Scripps Research Institute
UCSD	University of California, San Diego
WHO	World Health Organization
XDS	X-ray detector software

Abstract

Malaria remains a disease of great global healthcare burden, with over 600 thousand deaths annually. With an increase of multi-drug resistant malaria, achieving current mortality reduction targets hinges on the development of an efficacious malaria vaccine. Leading malaria vaccine RTS,S contains the major repeat epitope and C-terminal domain, but not the N-terminal domain of the *Plasmodium falciparum* circumsporozoite protein, which has been under investigated. Herein, the structural basis binding of six novel human and mouse antibodies with their N-terminal CSP peptide epitopes reveal the capacity for an antibody response towards multiple novel epitopes. The MAL071 RTS,S trial has provided renewed interest in antibodies targeting the C-terminal domain of CSP as correlates for protection. The structural basis for engagement of the C-terminal domain of CSP by ten monoclonal antibodies from the MAL071 trials demonstrates the broad antigenic landscape of this domain, including six new antibodies targeting the highly conserved β-epitope. The newfound immunological breadth of the β-epitope is then used to inform second-generation immunogen design combining key protective B-cell epitopes, successfully protecting mice from sporozoite challenge. *Plasmodium vivax* is responsible for most of the remaining malaria-associated mortality. Region II of the *P. vivax* Duffy-binding protein is a key antigen for a blood-stage vaccine. Here, the complete structural basis of PvDBP-RII engagement with the DARC ectodomain is revealed in complex with inhibitory human vaccination-induced monoclonal antibody DB1. This study significantly improves our understanding of receptor engagement by providing structural basis for previously described binding determinants and antibody-mediated inhibition of erythrocyte invasion by *P. vivax* merozoites.

CHAPTER 1:

Introduction

1.1 Introduction

Malaria has long been a disease of global healthcare burden with World Health Organization (WHO) estimates of over 200 million infections and 600,000 deaths annually (1). Despite considerable eradication efforts for over 50 years, historical trends of decline in malaria infections have slowed down and are not predicted to improve by 2030. In some countries, these trends have even been reversed, with an increase in malaria-associated mortality (1,2). Malaria prevention efforts also present a significant and increasing economic burden on affected countries (3). Altogether, the socio-economic impact of malaria on the global South, and specifically in Sub-Saharan Africa, presents one of the greatest challenges to development in the region. Complicated by multi-drug resistant malaria strains, low vaccine efficacy, and socioeconomic limitations, the fight against malaria demands innovation to achieve even the stated disease reduction targets.

Malaria is a vector-borne disease caused by infection with protozoan parasites of the *Plasmodium* genus, transmitted by mosquito bite from a female *Anopheles* species mosquito. Five *Plasmodium* species are known to routinely infect humans: *P. falciparum, P. vivax, P. malariae, P. ovale, and P. knowlesi.* Out of these, *P. falciparum* is the most virulent strain of malaria, endemic largely to sub-Saharan Africa, associated with 90% of total *Plasmodium* infections, and with over 1.4 billion people at risk globally **(Figure 1.1A)** (4,5). In comparison, *P. vivax* is associated with an order of magnitude fewer infections and deaths, but is endemic to large parts of South America, Asia, and Oceania, with over 2.5 billion people at risk **(Figure 1.1B)** (6). Together, *P. falciparum* and *P.*

vivax represent most of the global healthcare burden posed by malaria, but due to the virulent dominance of *P. falciparum,* it is responsible for over 90% of malaria-associated mortality worldwide and 95% in sub-Saharan Africa (7).

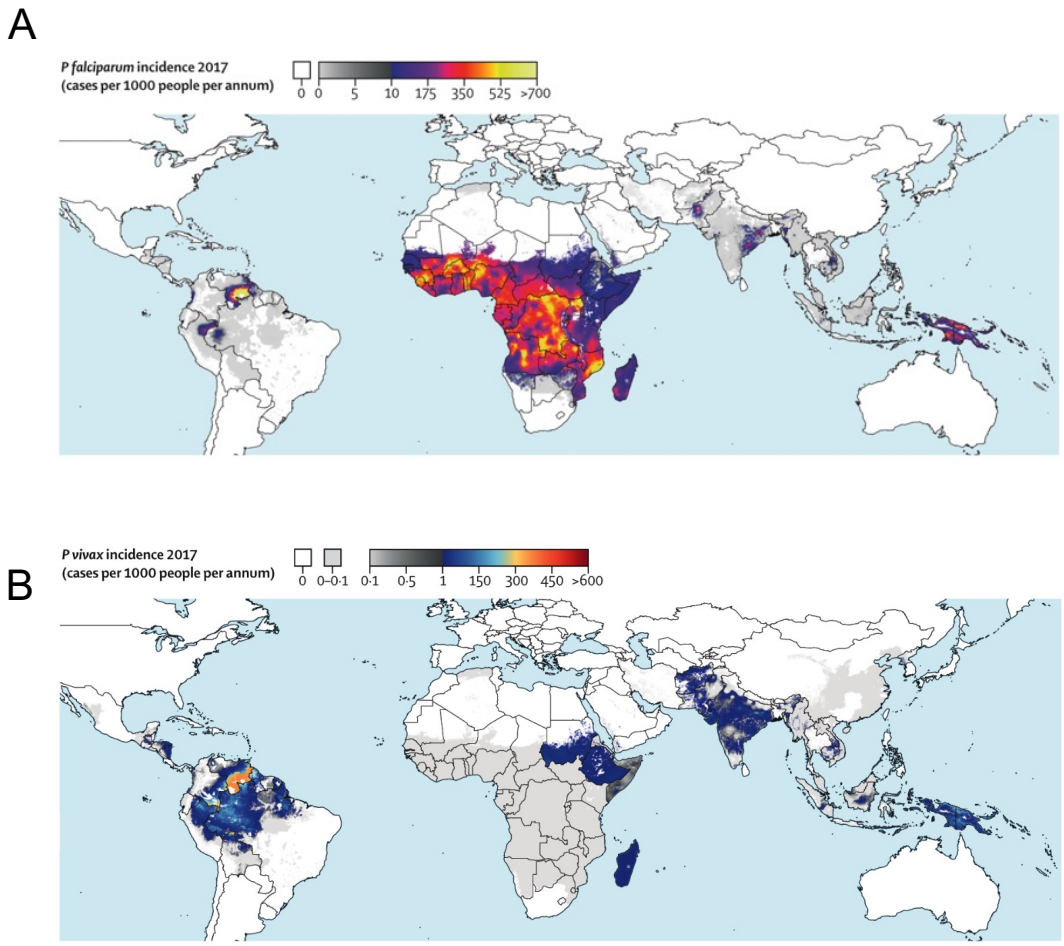


Figure 1.1. Global prevalence of *Plasmodium falciparum* and *Plasmodium vivax* malaria. Global incidences of *P. falciparum* and *P. vivax* malaria in 2017 are shown by cases per 1000 people per annum. *Plasmodium falciparum* is primarily localized to sub-Saharan Africa, Papua New Guinea, and Venezuela, and South-East Asia. *Plasmodium vivax* incidences are more prevalent in the equatorial regions of South America, India, Papua New Guinea, Madagascar, and Ethiopia. Maps are taken from Weiss *et al.* 2019 and Battle *et al*. 2019, The Lancet.

Reduction of malaria associated disease and mortality has taken a multi-pronged approach over the years. Early methods of containment and eradication include pesticide and environmental management, reducing transmission through decrease of *Anopheles* larvae and mosquito numbers. However, these approaches are limited in their potential for uniform widespread use and pose the risks of insecticide resistance and natural ecosystem and habitat destruction as secondary effects (8,9). Most success in malaria burden reduction has been achieved through the distribution and use of insecticide-treated nets (ITNs), estimated to be responsible for almost 70% of malaria cases averted from 2000 to 2015 (10). The protective efficacy of ITNs relies on their use, net distribution, longevity of active ingredients and physical integrity (11). Crucially, neither ITNs, pesticide use, nor environmental management are effective in preventing malaria disease following an infectious mosquito bite, where the responsibility falls on antimalarial drug treatment and vaccination.

Antimalarial drugs have been extensively used to treat and prevent infection; the first documented use of the antimalarial quinine dates to the 17th century, far predating the actual discovery of *Plasmodium* parasites (12). Quinine resistance in Brazil has been observed as early as the 1900s, and resistance to its synthetic relative chloroquine was observed in Thailand in the 1960s, raising concerns about the future of malaria control globally (13,14). Since then, new classes of antimalarials have been discovered and current antimalarial therapies include three compound classes: quinine derivatives, antifolate derivatives, and artemisinin derivatives, targeting multiple life-forms and processes of the *Plasmodium* parasite. However, each is subject to resistance

necessitating combination therapies for successful malaria control (15). The rise of multidrug resistant malaria strains has been increasing rapidly in the 2010s, endangering the efficacy of artemisinin combination therapies, which represent the first-line therapy of clinical malaria. Accordingly, there is strong emphasis on discovery of new antimalarial drug targets, and many new druggable targets and therapies are in the pipeline(16,17). Further complicating the successful administration of antimalarial therapies is their adverse side effects, most notably being potentially fatal hemolytic anemia in glucose-6-dehydrogenase deficiency (G6PD) patients(18). In some malaria-endemic areas, G6PD is estimated in 5% of the population, thereby producing risk with indiscriminate distribution of associated therapies(19). The rapid rise of drug resistance of *Plasmodium* species has too clarified that chemoprevention cannot be the only route of eradication; a safe, cost-effective, and efficacious malaria vaccine is needed now more than ever.

1.2 The *Plasmodium* life cycle

The *Plasmodium* parasite life cycle is a complicated series of events involving multiple cellular hosts in both the human and mosquito host, which has been covered in multiple reviews, and summarized in **Figure 1.2** (20–27). For the purposes of this thesis, the *Plasmodium* life cycle will be discussed broadly to contextualise the rationale and mechanism behind existing vaccination strategies, followed by in-depth discussion of individual targets which are the focus of this thesis.

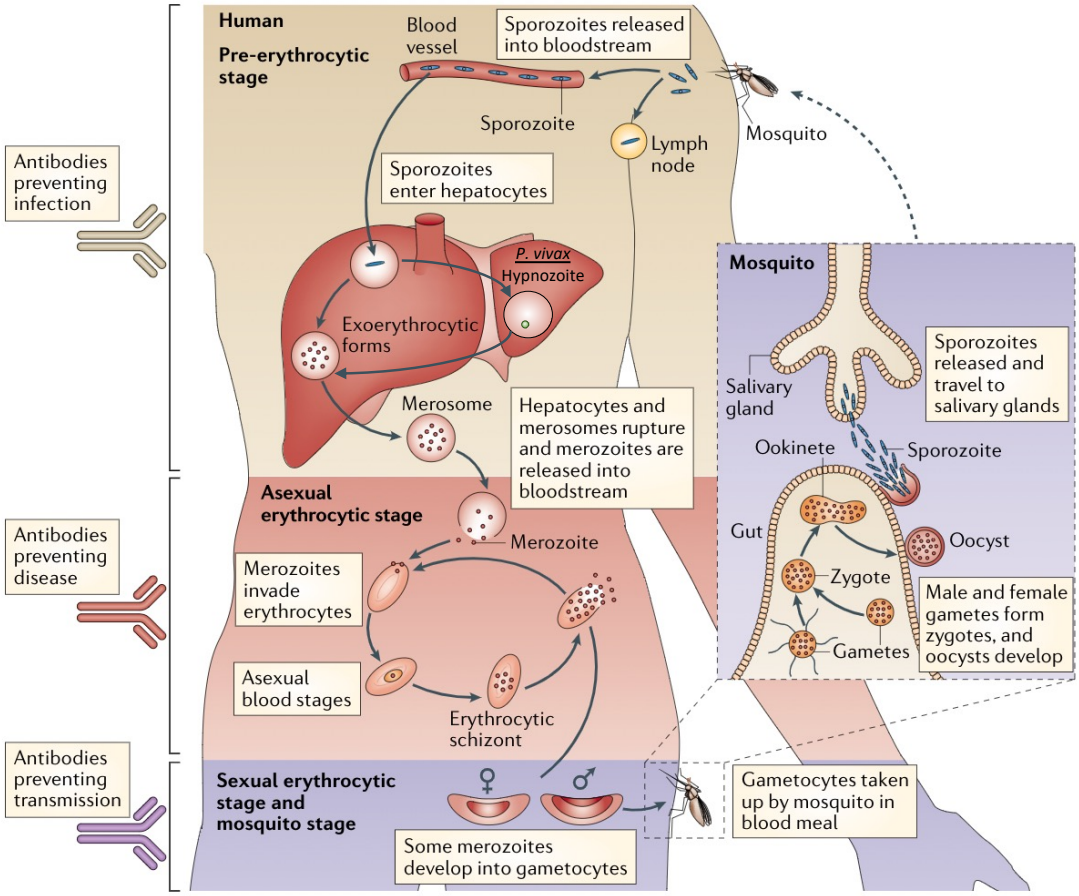


Figure 1.2. The *Plasmodium* life cycle. The life cycle of Plasmodium parasites involved multiple hosts and multiple cellular hosts within the mammalian host. Following inoculation into the dermis by infected mosquito bite, sporozoites migrate to the hepatic parenchyma and establish liver infection. The hypnozoite is a dormant form of *P. vivax*, capable of reactivation to produce relapse infection. Following exoerythrocytic asexual replication, merozoites enter the blood stream and invade erythrocytes (or CD71+ erythrocytes in the case of *P. vivax*). While asexual reproduction leads to cycles of erythrocyte rupture responsible in part for clinical malaria symptoms, gametocytogenesis produces gametocytes which can remain in circulation for over 6 months, to be taken up by an uninfected mosquito during a blood meal. Following gametocyte egress and zygote formation, ookinete migration to the salivary gland and oocyst maturation produce infection-competent sporozoites primed to invade the mammalian host. Figure is adapted from Julien & Wardemann, 2019, originally adapted from Sauerwein, Roestenberg, & Moorthy (2010).

1.2.1 Liver-stage infection (20–22)

The life cycle of *Plasmodium* parasites begins when an infected female anopheles mosquito takes a blood meal from a mammalian host, thereby depositing *Plasmodium* sporozoites into the host dermis. Sporozoites are the liver-infective form of the parasite, which migrate through gliding motility and cell-traversal to reach the liver. After first entering the bloodstream by traversing a dermal capillary, the sporozoites are transported to the hepatic capillary network, traversing across the endothelial barrier to enter the hepatic parenchyma. After traversal of multiple hepatocytes, a functional switch to an invasive phenotype occurs. This process involves complex coordination of parasite-host cell interactions mediated largely by the contents of micronemes and rhoptries, specialised invasive organelles secreted during and after invasion. After entering the host cell through membrane invagination and actin-myosin motor-powered cellular remodelling, the host membrane invagination encloses the parasite to form the parasitophorous vacuole (PV). In addition to protecting the parasite from immune recognition, the PV membrane is extensively modified so as to accommodate the energy requirements of the parasite in order to facilitate rapid exoerythrocytic asexual reproduction inside the hepatocyte.

During this stage, the parasitic load is amplified from one successfully invading sporozoite to tens of thousands of exoerythrocytic merozoites in just over two days for rodent infective *P. berghei* and 6.5 days for *P. falciparum.* Inside the PV-membrane, the parasite undergoes asexual reproduction involving schizogony, in a process of nuclear division without cell division. This is achieved by rapid DNA replication and branching

and growth of the parasite organelles. To support the extreme metabolic needs of schizogony, extensive membrane remodelling of the host membrane occurs that improves nutrient transport, lipid acquisition from hepatocytes, and *de novo* synthesis. Only shortly before release into the bloodstream, rapid invagination of the parasite plasma membrane produces individual infective exoerythrocytic merozoites in a process known as cytomere formation to form a mature schizont. Breakdown of the PV membrane is followed by detachment of the hepatocyte membrane. The merozoite-filled vesicle, known as the merosome, buds into the sinusoidal lumen. Eventual rupture of the merosome releases merozoites into the bloodstream and initiates blood-stage infection.

The hypnozoite is a unique dormant form of *P. vivax* that develops during hepatocyte infection and can cause relapse long after clearance of the primary infection (28). It is uncertain what causes some parasites to differentiate into hypnozoites. In one hypothesis, hypnozoites reactivate upon sensing the presence of an uninfected *Anopheles* mosquito host bite(29,30). Of concern, therapeutics known to target hyponozoites are those known to cause hemolytic anemia in G6PD deficient patients (31).

1.2.2 Blood-stage invasion (23–25)

Merozoites are the erythrocyte-infective form of the *Plasmodium* parasite released from a merosome following liver-stage infection or an already infected erythrocytic schizont. The initial contact between merozoite and erythrocyte constitutes a low affinity and reversible contact, which is followed by parasite reorientation to position the apical end of the merozoite towards the erythrocyte to form a so-called tight junction. In a complex

process involving the parasite actin-myosin motor, the tight junction migrates from apical to the posterior end of the merozoite. Much like sporozoite invasion of hepatocytes, this process involves secretion of invasion factors from micronemes and rhoptries, and a parasitophorous vacuole is formed to isolate the invading merozoite from the erythrocyte membrane.

The ring stage of intraerythrocytic development ensues following invasion and is characterized by the morphology seen by Giesma staining of infected red blood cells (iRBC). Apical organelle secretion following and the *Plasmodium* translocon of exported proteins contribute to stabilisation of the erythrocyte membrane cytoskeleton and establish new permeability pathways. One important feature of transition to the trophozoite stage is formation of knobs on the iRBC; *Plasmodium* protein accumulation at these loci mediates cytoadhesion to the endothelial lining of capillaries that is associated with severe malaria. Following daughter cell formation by schizogony (schizont stage), a coordinated series of signalling and degradative events breaks down the iRBC cytoskeleton and PV membrane in preparation for egress. Rupture of the iRBC then releases new merozoites to the bloodstream. The rupture of iRBCs upon egress contributes to hemolytic anemia, and this cyclical invasive stage results in periodic onset of fever and other classical clinical malaria symptoms.

1.2.3 Sexual reproduction and the mosquito host (26,27,32)

While most merozoites pursue intraerythrocytic asexual reproduction, a small portion differentiate into gametocytes for reinfection of the mosquito vector host and sexual

reproduction. Gametocytogenesis can be differentiated from asexual reproduction after the ring stage and take up to 9-12 days for development in the case of *P. falciparum*. During this time, iRBC membrane modification ensures gametocyte sequestration in peripheral hematopoietic tissue for development and the survival of gametocytes in circulation. Gametocytes remain surrounded by iRBC membrane and largely hidden from the immune system. Immune recognition of gametocytes in the mammalian host therefore requires recognition of surface antigens displayed on the erythrocyte membranes. When ingested during an anopheles mosquito bloodmeal, environmental changes provide activation signals for gametocyte egress and gametogenesis, followed by zygote formation, meiosis, and ookinete formation. Ookinetes are the mosquito-invasive form of the parasite. Ookinetes migrate out of the mosquito midgut lumen, where they develop into oocysts that will migrate to the mosquito salivary glands and produce mature sporozoites primed for the next round of infection.

1.3 Vaccination to target the liver stage

The rational for vaccination to target the liver-stage is simple: prevention of liver-stage infection precludes later stages of infection that result in clinical malaria disease and transmission to vector host mosquitos. Accordingly, liver-stage vaccination of *Plasmodium falciparum* has received significant attention, and the only currently WHO-recommended malaria vaccine, RTS,S, targets the main sporozoite antigen, the circumsporozoite protein (CSP) (33).

At the liver stage, malaria infection imposes the lowest antigenic load out of all stages of the malaria life cycle, providing a smaller antigenic load for neutralization. Due to the lesser exposure to sporozoite-stage antigens by the immune system, natural infection does not produce a humoral response that is sufficient for sterile immunity (34). However, it has been extensively demonstrated in mice, non-human primates, and humans that immunity can be acquired through immunization with inactivated sporozoites, with sporozoites under prophylaxis, or attenuated sporozoites(35,36). Sporozoite vaccination provides all possible antigens required for infection, and indeed sporozoite vaccination has achieved great success with up to 60-100% protection in malaria naïve adults(37,38). This efficacy is reduced in adults in endemic areas, potentially due to immunoregulation as result of lifelong natural infection (39). While showing favourable safety profiles in adults, sporozoite vaccinations have raised concerns due to side effects in children (40). Perhaps most critical to the success of sporozoite vaccination is the labour-intensive production of sufficient quantities of sporozoites for mass application. Although active research and industrial developments are addressing these concerns, many are addressed by subunit vaccination targeting specific antigens.

1.3.1 The circumsporozoite protein is the main *Plasmodium* antigen for vaccination targeting the liver stage

Recombinant protein and subunit vaccinations have revolutionized the world of healthcare by providing scalable platforms for production of immunogenic antigens (41). A successful recombinant vaccine requires the identification of protective antigens and their characterisation. Monoclonal antibodies isolated from mice following *P. berghei*

sporozoite immunization conferred protection against infection *in vivo*, validating that sporozoite vaccination conferred antibody-mediated protection(42). These mouse monoclonals are also observed to stain the same molecular weight bands as the key antigen labelled in metabolic pulse-chase experiments of sporozoites and uniformly coat the entire sporozoite surface, namely the circumsporozoite protein (CSP) (42,43). Following similar observations for *P. falciparum, P. vivax, and P. knowlesi*, monoclonals were used to identify the CSP sequence from an *E. coli* cDNA library isolated from the thoraces of *P. falciparum* infected mosquitos (44–46), providing the first basis for production of a recombinant malaria vaccine.

The circumsporozoite protein comprises of a secretion signal, an N-terminal domain, a central repeat region, and a C-terminal thrombospondin-like type-1 repeat (αTSR) domain followed by a glycosylphosphatidylinositol (GPI) membrane anchor(47) **(Figure 1.3A)**. The central repeat region contains amino acid repeats which vary in repeat length between species and vary in number of repeats between strains. While differing in sequence across *Plasmodium* strains, three sequence motifs are particularly well conserved; Region I (RI) immediately upstream of the central repeat region contains the conserved pentapeptide KLKQP, Region II+ in the CSP C-terminal domain contains a conserved cell adhesion motif (EWSXCXVTCG), whereas region III forms an amphipathic helix in the C-terminal domain(47). Although differing in sequence outside of these conserved regions, *Plasmodium* strains of different mammalian hosts retain this domain structure, implying conserved function of CSP proteins across *Plasmodium spp.* and conserved functions of the individual CSP domains (47–50). As such, *P. berghei* and

P. yoleii rodent malaria strains, and swapped-domain transgenic CSP parasites, have been extensively used as transgenic models to investigate the physiological roles of CSP

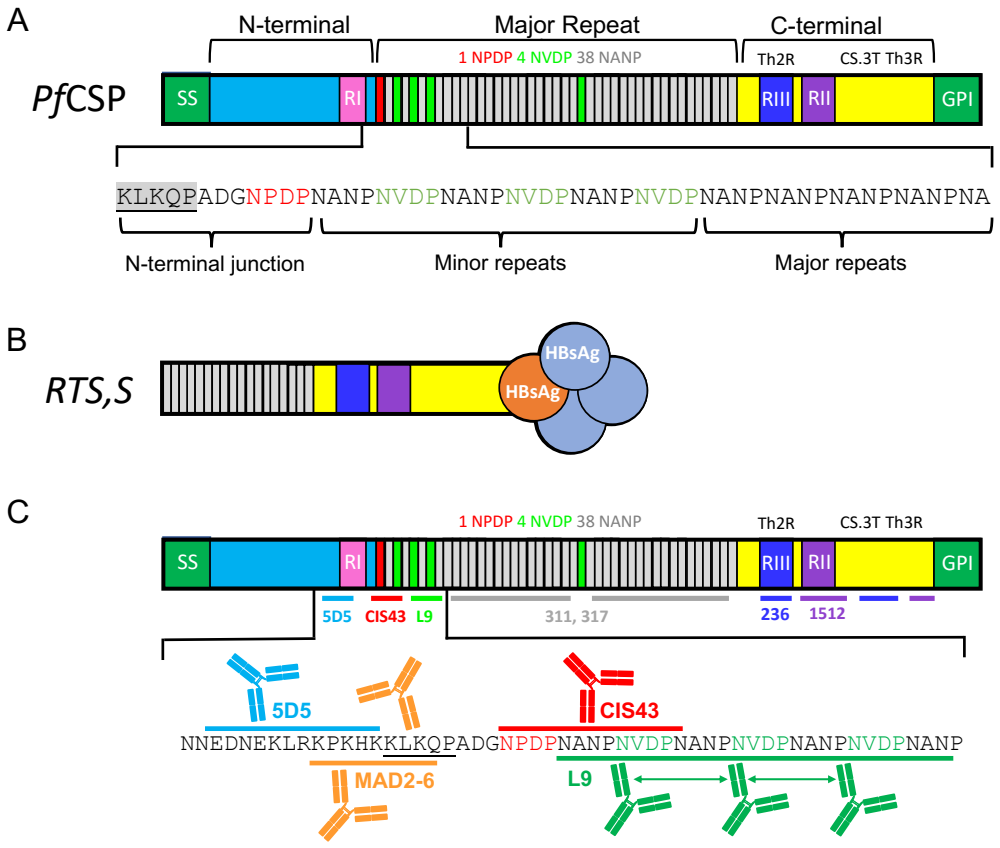


Figure 1.3. Schematic of PfCSP protein domains and the leading malaria vaccine RTS,S.

(A) The *Plasmodium falciparum* CSP protein is composed of an N-terminal signal sequence, an N-terminal domain, a central repeat region, and a C-terminal domain followed by a GPI anchor. The 3D7 strain contains one NPDP repeat, four NVDP repeats, and 38 NANP repeats. (B) The leading malaria vaccine candidate RTS,S is composed of 19 NANP repeats and the C-terminal domain of PfCSP fused onto the Hepatitis B surface antigen. (C) Schematic of CSP sequence annotated with key antibody epitopes. mAbs 311 and 317 (grey) bind major repeat NANP peptide sequences, mAb 236 (blue) binds the C-terminal α-epitope, while mAb 1512 (purple) binds the C-terminal β-epitope. In the N-terminal domain, mAb 5D5 (cyan) binds upstream of RI, and overlaps with MAD2-6 (orange). CIS43 (red) binds the junctional epitope, and L9 (green) binds the minor repeats, with homotypic Fab-Fab interactions indicated by green arrows.

through parasite development in the mosquito, infection of the mammalian host, and antibody- or vaccine-induced immunity to malaria infection**.**

1.3.2 Role of the circumsporozoite protein in Plasmodium infection of the human host

In the mammalian host, the CSP has been implicated in gliding motility and migratory processes with the detection of target liver cells resulting in the switch to invasive phenotype, often associated with N-terminal domain cleavage. Early studies using recombinant CSP constructs expressed in *E. coli* demonstrated binding of CSP to hepatocytes *in vitro* (51–55). Binding of CSP to hepatocytes membranes or HepG2 cells is inhibited by competition with heparin more potently than other glycosaminoglycans (GAGs), and strongly inhibited by heparinase treatment of HepG2 hepatocytes in culture. Using truncated recombinant CSP, it was shown that the CSP N-terminal domain is essential for both heparin and hepatocyte binding. In comparison, while some studies report increased binding of C-terminal deletion constructs to heparin(53), others report reduced binding of C-terminal deletion mutants to HepG2 cells, implying a more nuanced involvement of both domains in dictating tropism of CSP binding (52,54).

These analyses into hepatocyte binding have provided multiple molecular determinants of CSP-heparin binding within these domains. Deletion of the six terminal amino acid residues of the CSP N-term do not affect heparin binding yet prevent HepG2 cell binding (53). Mutation of lysine residues upstream of the conserved RI (KLKQP) sequence strongly decrease binding to negatively charged heparin polysaccharide chains, while

mutagenesis of the lysine residues in RI itself affect binding to a lesser extent (54). Additionally, CSP binding to HepG2 hepatocytes can be inhibited with soluble peptides mimicking Region I (55) and peptides corresponding to the conserved Region II of the CSP C-terminus (51,55). Altogether, these suggest that CSP-mediated sporozoite binding to liver cells involves electrostatic interactions with lysine residues in the CSP N-terminus. Additional factors effecting cell tropism and specificity of binding is provided by parts of both N- and C-terminus. These observations are in line with previously characterised heparin binding motifs comprising nearby positively charged residues, specifically lysine and arginine, and the conserved role of αTSR domains across many organisms in cell adhesion(55)**.**

Although key in recognition of hepatocytes, in large part through its interaction with heparin-containing GAGs, the N-terminus of CSP is proteolytically processed as the parasite transitions from motility to an invasive phenotype (43,56–58). Through pulse-chase labelling experiments of *P. berghei* sporozoites, it has been observed that two dominant bands are produced at 54 kDa and 44 kDa, both of which can be labelled extracellularly by iodination of sporozoites and probed with monoclonal antibody targeting *P. berghei* CSP (43). Further work has since elucidated the nature of this processing; by using polyclonal N- and C-terminal antisera to *P. berghei* CSP, it was shown that both bands can be labelled with C-terminal antisera while N-terminal antisera only labels the high molecular weight band (56). This processing was inhibited by E-64, a specific cysteine-protease inhibitor, suggesting cleavage of the CSP N-terminus on the sporozoite surface. Inhibition of CSP cleavage by E-64 prevents invasion of Hepa 1-6

hepatocytes by *P. berghei, P. yoleii, and P. falciparum,* but does not inhibit sporozoite internalization, implying that cell traversal and invasion are two distinct processes (56).

Highly sulfated proteoglycans, such as those found on hepatocyte surface, signal for the cleavage of CSP in the switch from parasite cell traversal and migration to invasion (57). The native site of CSP cleavage is the conserved region I; the cleavage of CSP is inhibited *in vitro* in RI-deletion transgenic *P. berghei*, which are greatly impaired in invasion of mice *in vivo* as assessed by parasite liver burden assay. Reciprocally, transgenic *P. berghei* parasites expressing cleaved CSP were more infective *in vitro* in multiple hepatocyte cell lines and were significantly more infective when injected intravenously in C57Bl/6 mice. *P. berghei* sporozoites expressing cleaved CSP were unable to establish liver-stage infection *in vivo* when injected into mice intra-dermally due to sporozoite inability to escape the injection site, further highlighting the importance of CSP cleavage for invasion (58).

In addition to revealing key prerequisites for sporozoite invasion, parasites lacking the CSP N-terminus demonstrate the potential for more complex behaviour and crosstalk between CSP domains; antisera against the C-terminus were able to inhibit hepatocyte invasion *in vitro* and liver stage invasion *in vivo* in parasites expressing PfCSP with a deletion of the N-terminus but not in wildtype sporozoites, suggesting increased C-terminal domain exposure upon CSP cleavage (58). Western blot analysis using antibodies isolated from immunisation with recombinant CSP constructs has aided in further characterising CSP conformation on sporozoites; mouse mAb 3A1 recognising

RI-upstream residues S69-E74 stains midgut sporozoites, while mAb 3B4 targeting RI-downstream residues K95-G100 stains both midgut and salivary gland sporozoites. However, live immunofluorescence analysis shows RI-targeting mAb 3B4 only stains 14% of sporozoites and αTSR-targeting 4B3 only 6% of sporozoites. These observations suggest both extensive cleavage of CSP at the salivary sporozoite stage and reduced exposure of downstream epitopes following cleavage (59). While some atomic force microscopy studies using CSP expressed in *P. pastoris* suggest a linear rod-like conformation, others interpret an alternative collapsed conformation (59,60). While it has become clear that CSP possessed structural and conformational characteristics beyond those of an extended disordered polypeptide, the exact mechanism of conformational changes or rearrangements throughout parasite development and invasion, and their ramifications to vaccine design, have yet to be explored.

1.3.3 RTS,S: history and current standing

The CSP-based subunit vaccine RTS,S/AS01 is the result of a long-term collaboration between GlaxoSmithKline and the PATH Malaria Vaccine Initiative. In the 1970s and 1980s, quickly after deciphering the domain structure of CSP, evidence was gathered to support the immunogenicity of peptides derived from the major repeat region of *P. falciparum* in mice, rabbits, and humans(61,62). In the late 1980s and early 1990s, further increase in anti-CSP titres through recombinant vaccination were achieved with fusion to the hepatitis B surface antigen (HBsAg)(63,64). Mouse immunization with repeat antigen provided *in vivo* protection from *P. berghei* in mice (65), and *P. falciparum* repeat-based vaccine was shown to provide limited efficacy in humans (66). Concurrent growing

appreciation of T-cell mediated immunity further propelled the field. Analysis of murine and human lymphoproliferative responses to *P. falciparum* peptides revealed key peptide epitopes in both the C- and N-termini of CSP (67–71). Out of these, a lymphocyte response to peptides corresponding to CSP C-terminus residues 361-380 and 370-390 correlated with protection from disease in a cohort of 28 Kenyan adults (P=0.003 and P=0.023, respectively) (70). To improve upon previous vaccines and combine the two approaches, RTS,S was designed to include 19 NANP repeats and the C-terminal peptide region (3D7 strain of *P.* falciparum) and fused to the hepatitis B surface antigen (72)**(Figure 1.3B)**. In October 2021, after over 25 years of assessment, the WHO approved RTS,S (adjuvanted with AS01) for use in areas of high malaria transmission(33).

RTS,S/AS01 administered in a 0-1-2 month (prime-boost-boost, 012M) has shown safety and efficacy in multiple clinical trials. In a phase IIa trial on malaria-naïve adults, RTS,S/AS01 showed 50% vaccine efficacy in a controlled human malaria challenge (CHMI)(73). In a phase IIb trial with Kenyan adults in a high malaria transmission area, vaccine efficacy against natural infection was 30% (74). Children native to malaria endemic areas encounter *Plasmodium* parasites before adulthood. As such, phase III trials focused on immunogenicity, safety, and efficacy in African children and infants testing the standard dose regime with a potential booster after 20th months (33,75). Over an average observation period of 38 months in 6–12-week-old infants and 48 months in 5-17-month-old children, efficiency of protection ranged from 18-36% for clinical malaria with an increased response seen in children compared to infants. Concerningly, in both

children and adults, antibody titres wane rapidly over 6 months after the final dose. In children and infants, antibody titers decay with a half-life of 45 days for the first 6 months (73,76–78).

Decrease in efficacy with pre-exposure to malaria echoes observations from sporozoite vaccination and suggests non-protective pre-exposure may contribute to reduction in vaccine efficacy. Efficacy reduction has also been attributed to strain mismatch in natural infection compared to the vaccine strain; 1-year cumulative efficacy in children is reduced from 50.3% to 33.4% when the infecting parasite strain is mismatched with the vaccine (79). Analysis of *P. falciparum* genetic diversity reveals only 5.2% of sequences match the 3D7 vaccine strain (80). Most recently, the MAL071 stage IIa trial included a delayed fractional dose regime in which the third dose is replaced with a fractional ($1/5^{th}$) dose at 7 months (Fx017M). This regime provided 86% protection from CHMI in malaria naïve adults compared to 64% under regular 012M dosing schedule (81). Even so, anti-CSP titres followed a pattern of decay after the third dose (77). The effects of dosing regimens, polymorphic epitopes, and rapidly decaying antibody titres on vaccine efficacy, have emphasized the need to investigate the vaccine-mediated response to the specific epitopes presented by RTS,S and their mechanisms of immunity to establish correlates of protection from *P. falciparum* infection.

1.3.4 Correlates of antibody-mediated protection from RTS,S vaccination and natural infection against malaria

The development of the RTS,S malaria vaccine focused on eliciting a high antibody titre to the major repeat (NANP) epitope of CSP, aided by the inclusion of the C-terminal (CtCSP) T-cell epitopes and HBsAg. The stage III trial analysis predicted a dose-response relationship between anti-circumsporozoite antibody titre (measured against repeat antigen) and efficacy against infection, where 121 EU/mL appeared to prevent 50% of infections. In line with antibody titre decay kinetics, observed efficacy starts at 74% and wanes to 28% (76). Whereas anti-NANP and anti-CtCSP titres correlate positively with each other and with protection in a standard dose regimen, combined analysis reveals that only increased anti-NANP titres and protection are independently associated in the phase III trial (82). As opposed to measuring antibody titres, antibody avidity index (AI) measures difference in binding upon introduction of chaotropic agents. While both anti-NANP and anti-CtCSP avidity index correlate with protection, only the latter is independently associated with protection, revealing differences between the dynamics of the antibody responses to the two different CSP domains on RTS,S (82). Anti-NANP titres fail to explain the improved efficacy of a delayed fractional dose regimen, as there was no significant difference in anti-NANP antibody titres between protected and unprotected vaccinees. Instead, antibody avidity on day of challenge is higher in delayed fractional dose than standard dose regimen for all antigens, and antibodies from the delayed standard dose regimen were overall higher in somatic hypermutation (81). Through *in vitro* stimulation of peripheral blood mononuclear cells (PBMCs) from the MAL071 trial, it was seen that CSP-responsive B-cells are more numerous in samples

from delayed fractional dose vaccinees (83). However, statistical significance was only reached with CtCSP-stimulated memory B-cells. Similarly, comparing subject by protection status, protection significantly correlated with IgG-secreting memory B-cells for all domains, and most significantly to CtCSP (83).

1.3.4.1 Effector functions: Fc receptor binding and phagocytic activity

Fc-mediated effector functions have provided further insight into antibody-mediated protection through different RTS,S vaccination regimens and natural infection. Binding of antibodies to Fc receptors is an increasingly recognised mechanism of protection from infection, mediating phagocytosis of opsonized pathogens by many classes of lymphocytes (84,85)**.** Through an *in vitro* assay testing for opsonophagocytic activity (OPA) using THP-1 monocyte cell line and antigen-coated fluorescent beads, standard dose regimen vaccinee protection inversely correlates with OPA and is mediated largely by anti-CtCSP antibodies(86). The delayed fractional dose regime showed significantly lower OPA than standard dose regimen, attributed by linear regression to OPA-promoting IgG1 antibodies in the standard dose regimen samples and negatively associated with IgG4 antibodies in delayed fractional dose samples (87). While this is a useful model to study OPA, THP-1 cells express high-affinity FcγRI that binds monomeric IgG, and neutrophils express lower affinity receptors FcγRIIa and FcγRIII that bind immune complexes, and it is neutrophils that are responsible for the majority of opsonization in whole blood (88). IgG from children vaccinated with RTS,S that are able to bind recombinant FcγRIIa and FcγRIIIa also produced a cytotoxic response in primary lymphocytes isolated from whole blood(89). In malaria-naïve adults vaccinated with

RTS,S under a standard dose regime, FcγRIIa and FcγRIIIa binding to IgG correlated with protection from CHMI (90).

Using a panel of serological measurements characterizing immunoglobulin and antigen specific effector functions, antibody avidity, and titres, combined with computational models which seek to identify minimal markers between the two vaccine arms of the MAL071 trial, four minimal markers were identified to differentiate between the two regimens, three of which are Fc-mediated effector functions (91). Dendritic cell phagocytosis mediated by CSP-specific antibodies and monocyte phagocytosis mediated by CtCSP-specific antibodies were higher in delayed fractional dose samples. Higher levels of CSP-specific NK cell-activating antibodies and higher $(NANP)_6$-specific IgA levels were higher in standard dose regimen samples. Both positive markers of the delayed fractional dose regimen moderately correlated with anti-CtCSP avidity, suggestion that avidity and Fc-effector functions may have coevolved (91). MAL068 is a stage II clinical trial comparing protection from CHMI following standard dose regime or one in which the first immunization is replaced with an adenovirus-based CSP vaccination (92). Using similar modelling approaches to highlight markers for protection, anti-$(NANP)_6$ binding to FcγRIII, anti-$(NANP)_6$ antibody-mediated NK cell chemokine secretion, and anti-$(NANP)_6$ antibody-mediated phagocytosis, all correlated with protection across vaccine arms (93,94).

The contradicting accounts regarding the importance of THP-1 monocyte binding assays and anti-CtCSP antibody role in OPA may arise due to differences in data interpretation

or inherently different antibody signatures of MAL068 and MAL071 vaccination protocols. Either cause provides further support for further investigation of the fine specificities of CSP and CtCSP antibodies, together with their role in Fc receptor binding, and highlight their importance as correlates of protection from *P. falciparum* infection.

1.3.4.2 Effector functions: complement activation

Complement activation has also been shown as a potential indicator for protection both in RTS,S vaccinees and in non-vaccinated children(95). The complement system is an evolutionarily ancient innate immune component, which operates through a proteolytic cascade to opsonise pathogens and has been summarised in multiple reviews(96,97). Briefly, the classical pathway of complement is initiated by C1q lectin productively binding to an antibody-opsonized pathogen to start a stepwise proteolytic cascade of complement factors. Cleavage of complement components produces opsonizing fragments (C3b, C4b, and C5b), which act in complex with downstream components as proteases. These bind receptors on macrophages to mediate phagocytosis of opsonized pathogens, and soluble fragments (C3a and C5a) act as soluble anaphylatoxins to promote a pro-inflammatory response. Terminal complement components C5-9 assembly and C9 polymerization forms the membrane attack complex (MAC), a lytic pore on the surface of the pathogen. Complement-mediated protection has received early attention in the context of transmission blocking vaccine antigen Pfs230(98). Although gametogenesis and gametocyte egress can occur more than 24 hours following a bloodmeal, human serum components in the mosquito bloodmeal remain sufficiently intact for complement-

mediated lysis, as seen by reduced transmission and MAC formation on gametocyte surface (99).

In the context of sporozoite invasion, both natural infection and vaccination have provided evidence anti-CSP antibody-mediated complement activation correlates with protection. In cohorts of adults from malaria endemic regions of Papua New Guinea (PNG) and Kenya, serum IgG was able to fix C1q, C2, C3, C4, and C5 to recombinant CSP produced in *P. pastoris*, as assessed by ELISA (100). In Kenyan adults, increased breadth of binding to the three key CSP domains was significantly and positively associated with C1q fixation (101). Similar observations are echoed in RTS,S vaccinated children, with individuals producing antibodies to both repeat and C-terminal epitopes showing higher C1q-fixation(102). High C1q-fixing antibodies are correlated with protection from clinical malaria in PNG children, and with protection from CHMI in malaria naïve adults following RTS,S vaccination (100,101). CSP-specific IgG from whole sporozoite immunization mediates serum-dependent sporozoite lysis, demonstrating that complement fixation can proceed to membrane attack complex lytic pore formation (103). The importance of multifunctional antibodies is reiterated by the authors who identified patient polyfunctionality score to significantly correlate with protection from CHMI in malaria-naïve adults (90). Similar observations are seen in the MAL071 trial with increased polyfunctionality correlating with protection across both arms of the trial(91).

Altogether painting a complex picture, increased research into antibody-mediated immune correlates of protection have produced a transition in focus from production of high titres of repeat targeting antibodies to production of higher quality antibodies with increased avidity and polyfunctionality. Investigation into monoclonal antibodies, their potency, and structural characterization of their binding to the immunogenic epitopes presented by natural *Plasmodium* infection, RTS,S vaccination, and sporozoite immunization, have been key in deciphering discriminants of antibody quality and functionality.

1.3.5 Monoclonal anti-PfCSP antibody-mediated protection from *P. falciparum* infection

Through the persistent and continued isolation of monoclonal antibodies, antibody characteristics key to mounting a successful immune response against malaria have emerged, elucidating the mechanisms behind avidity and protection. One key advance that has allowed extensive characterisation of monoclonal antibodies, polyclonal sera, and immunogenicity of vaccine designs against *P. falciparum,* without the need for labour intensive and costly CHMI, is the development of transgenic *P. berghei* parasites expressing full-length *P. falciparum* CSP (104). Luciferase-expressing transgenic parasites further improved this model system, enabling assessment of parasite liver burden through radiance measurements of mice abdomen following controlled *Plasmodium* infection (105). **Figure 1.3C** provides a schematic of key monoclonal antibody binding epitopes discussed below.

1.3.5.1 Monoclonal antibodies binding to the major repeat domain

As expected with the immunodominance of repeat targeting antibodies, most structural work has characterized binding of monoclonal antibodies to the major repeat domain of CSP. Certain antibody lineages, particularly V_H3-30 and V_H3-33, are often seen to dominate the immune response to NANP repeat antigens (106,107). X-ray crystal structures of NANP repeat peptides in complex with Fab fragments of protective antibodies from many lineages show binding to the NANP peptide proline through germline-encoded aromatic residues and stabilization of type-I β-turns and asparagine 3_{10} turns motifs in the repeat peptide (106–108). High resolution cryo-EM structures of many protective V_H3-30 and V_H3-33 Fabs in complex with long NANP repeat peptides show ordered long and short-range spiral and helical assemblies, mediated by homotypic interactions between adjacent Fabs, also utilizing germline-encoded residues (109–111). Such Fab fragments can bind to increased length NANP repeat antigens with over thousand-fold increased affinity (106,110). Germline-encoded homotypic interactions are further strengthened by somatic hypermutation to increase antigen affinity through avidity (112). Mutations to remove homotypic interactions without impacting core epitope binding greatly reduce *in vivo* protection via liver-burden assay, highlighting a unique role for such helical assemblies and homotypic interactions in protection (110).

Macromolecular spiral helical assemblies have been observed with monoclonals isolated from mice, immunization of transgenic mice with human antibody repertoire, RTS,S vaccination, and in *P. vivax* antibodies bound to *P. vivax* repeat peptides, suggesting that these are a common and representative feature of the B-cell response to *Plasmodium*

repeat antigens (110,111,113,114). While it is known that the repeat domain of *P. falciparum* is required for parasite development, its immunodominant nature has been suggested to distract the immune response from other potential protective epitopes (115). It has been observed in other pathogens that less immunogenic epitopes play key roles in protection (116). Recent work has supported this notion by demonstrating that while full-length CSP immunization predominantly leads to activation of B-cells targeted to the repeat domain (117), by using CSP constructs with shorter length repeat domains, a similar number of B-cells are activated by N-terminal, C-terminal, and repeat domains to produce a protective response (117).

1.3.5.2 Monoclonal antibodies towards the C-terminal domain

The C-terminus of CSP (CtCSP) is an αTSR (Thrombospondin-like type 1 repeat) domain, an evolutionarily ancient domain of eukaryotes found in many cell-surface receptors involved in adhesion (118). CtCSP contains three polymorphic T-cell epitopes, the Th2R, Th3R, and CS.T3 epitopes **(Figure 1.4A and 1.4B)**, that are known to increase antibody titres through T-helper cell stimulation (119,120). Accordingly, RTS,S-induced antibody titres to CtCSP are consistently higher than those to the repeat domain (81). Despite this, there has been little structural characterization of monoclonal antibody binding to CtCSP. The first structural characterization of monoclonal antibody binding to the αTSR domain was for murine mAb 1710 isolated from whole sporozoite immunization (121). The X-ray crystal structure of 1710 Fab in complex with αTSR shows binding to both polymorphic T-cell epitopes Th2R and Th3R, with 1710 HCDR3 inserting into the hydrophobic pocket formed between the Th2R α-helix and the Th3R

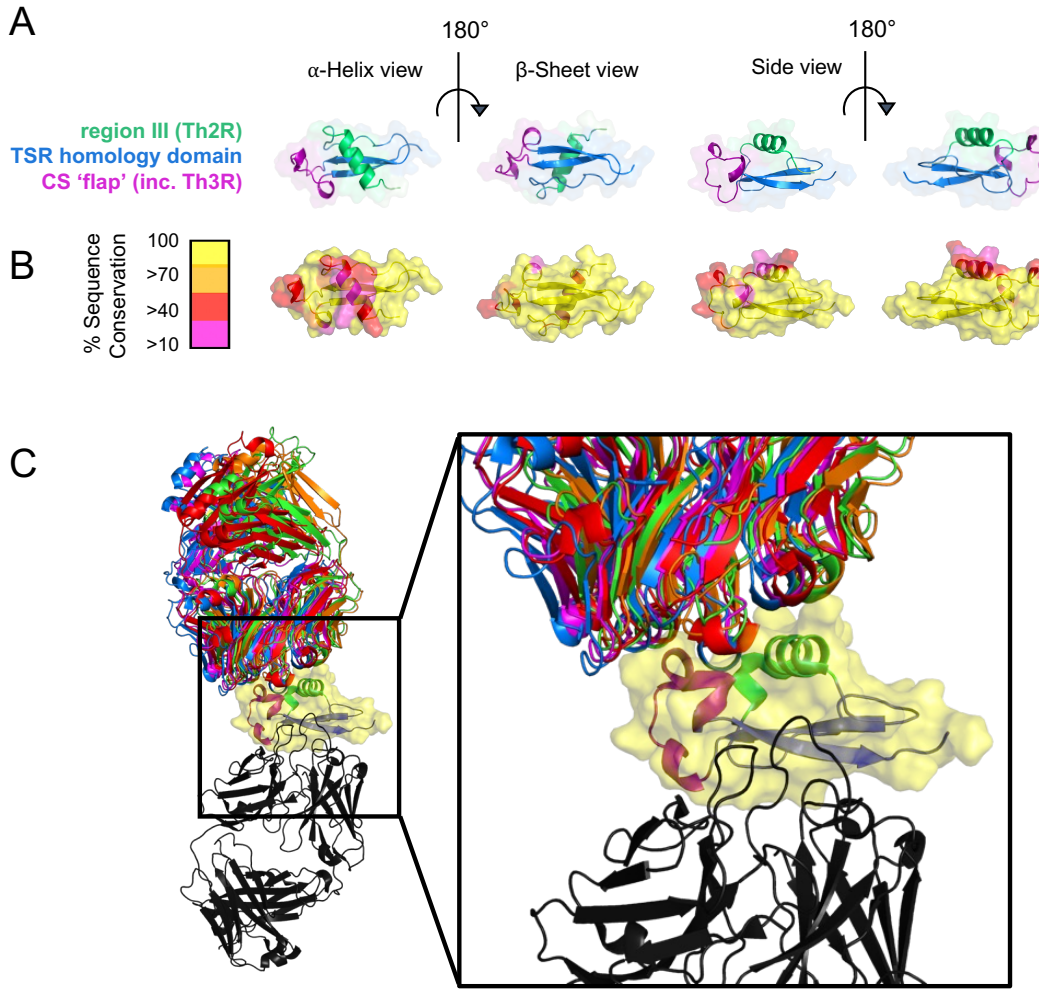


Figure 1.4. Structure of the C-terminal αTSR domain and antibody epitopes. (A) The structure of the αTSR epitope is composed of an amphipathic α-helix containing the Th2R T-cell epitope (green). The TSR homology region (blue) is composed of a pseudo-β-strand and the CS.T3 T-cell epitope, and two beta strands connected by the CS-flap (purple) which contains the Th3R T-cell epitope. (B) The surface of the αTSR domain is colored by sequence polymorphism across a panel of 15 haplotypes, showing a concentration of polymorphic residues across both Th2R and Th3R epitopes. (C) Structural alignment of antibodies binding to the αTSR domain defining the α-epitope (1710 in blue, 234 in orange, 236 in red, 352 in green, 1488 in magenta) and mAb 1512 (black) highlighting the conserved β-epitope. (1710 PDB: 6B0S, 234 PDB:7RXI, 236 PDB: 7RXJ, 1512 PDB:7RXP, 1488 PDB:7RXL, 352 PDB:7S0X).

CS-flap **(Figure 1.4C)**. However, mAb 1710 does not prevent sporozoite cell traversal *in vitro* or parasitaemia *in vivo* in mice and was declared non-protective (121). Epitope binning of CtCSP targeting mAb panel isolated from an individual immunized with whole sporozoites suggests the majority bind the same epitope as mAb1710 (122). Only a small percentage of sporozoites were stained by these mAbs in flow cytometry assays. This percentage increased significantly in the presence of repeat-binding mAbs, suggesting their effects may be potentiated by repeat mAbs and vice versa. These effects did not translate to protection in mice by liver burden assay; these monoclonals are not protective alone and do not appear to provide added protection when combined with repeat-binding monoclonals (122).

More recently, X-ray crystal structures from our lab of four mAbs from the MAL071 trial from the V_H3-21 (and closely related V_H3-48) lineage have revealed remarkably similar binding to the polymorphic epitope defined by mAb 1710, termed the α-epitope **(Figure 1.4C)** (123). Furthermore, X-ray crystal structure MAL071 V_H3-21 mAb1512 illustrated binding to the highly conserved opposite face of the domain, thereby defining a new β-epitope **(Figure 1.4C)**. In contrast to mAb 1710, α-epitope binding mAb 236 and β-epitope binding mAb 1512 both showed significant protection from *P. falciparum in vivo* by liver burden assay (123).

1.3.5.3 Monoclonal antibodies to the minor repeat and junctional domain.

In addition to overcoming the immunodominant and potentially immunomodulatory effects of the repeat domain, novel epitopes absent in RTS,S and previously uncharacterised within the context of CSP have been discovered, highlighting that the search for novel epitopes should not be discontinued. Two monoclonal antibodies have received particular attention: CIS43 targeting the junction domain immediately downstream of RI, and L9 targeting the minor repeat domain connecting the junctional epitope to the major repeats (124,125). These are both highly inhibitory by liver burden assay, and low dose of L9LS (Fc-modified for stability) is protective in CHMI in humans in a stage I trial (126). These, as well as other junctional epitope binding antibodies, show high cross reactivity to the major NANP repeat epitope (107,127). It has therefore been suggested that cross-reactive junctional and minor repeat binding antibodies originate as NANP-targeting antibodies and gain dual-specificity binding through affinity maturation and somatic hypermutation (107). This cross reactivity was later shown to not provide appreciable protection *in vivo* in mice by liver burden assay using transgenic *P. berghei* parasites expressing PbCSP with only the junctional, minor repeat, or major repeat domains of PfCSP (128). As such, these two epitopes provide protection independently of the major repeats. The recent cryo-EM structure of L9 Fab in complex with short recombinant CSP shows homotypic contacts reminiscent of, but differing from, those previously observed in major-repeat binding mAbs (129). While it is unclear whether the potency of these antibodies can be replicated by subunit vaccination independently of the major repeat domain, much second-generation vaccine design has focused on inclusion of these new epitopes.

1.3.5.4 Monoclonal antibodies towards the N-terminal domain

Due to its major role in migration and invasion, there has also been interest in the rare and elusive antibodies isolated that can target the N-terminus of CSP (130–133). Mouse monoclonal antibody 5D5 isolated following full-length CSP immunisation was mapped to bind residues E81-K95 directly upstream of RI and shown to both inhibit CSP processing *in vitro* and reduce parasite infectivity *in vivo* (131). These results were later disputed in a study in which 5D5 binding was shown to require antibody paratope glycosylation at Asn98 of the heavy chain for binding, and both antibodies failed to inhibit sporozoite traversal or stain salivary gland sporozoites (132). A recent monoclonal antibody that was isolated from human sporozoite vaccination, IgA MAD2-6 was also shown to bind the lysine-rich sequence upstream of RI (133). Uniquely, the MAD2-6 Fab crystal structure in complex with its target peptide KPKHKKLKQ revealed binding of two Fab fragments to overlapping KXKK motifs, and both registers were associated with *in vivo* inhibition of infection via liver burden assay, and failure of 5D5 to do the same(133). The effect of CSP cleavage on sporozoite invasion, its inhibition by N-terminus targeting antibodies, and RI-targeting antibodies provide multiple contradictions and conflicting observations, highlighting the necessity for further investigation.

1.3.6 Summary of our current knowledge of PfCSP as a vaccine candidate

RTS,S, the only WHO-approved vaccine against malaria was designed over 30 years ago. Since then, the wealth of structural, functional, and immunological characterization of

RTS,S efficacy and vaccinee derived sera have made apparent a key drawback and obstacle to be overcome; rapidly increasing antibody titres after immunization produce only short-lasting protection, made worse by strain mismatch. Meanwhile, the major repeat NANP epitope remains a source of potent and protective antibodies. Its relatively focussed immune response dominated by particular germline genes, structural and compositional simplicity, and immunodominance, have however raised the potential of it acting as an immunological decoy producing a low quality and short-lasting immune response, much like that seen through natural infection. Characterization of the antibody response to both HIV and SARS-CoV-2, have shown that antibodies may be more inhibitory *in vivo* than suggested by *in vitro* models (134,135), and new sites of vulnerability are still being identified on well-researched pathogens, even for influenza (136). While deemed by many as non-immunogenic, the CSP N-terminus is nevertheless the locus of almost all known functionality, playing key roles in adhesion, migration, and the functional switch to invasion. The C-terminal αTSR domain's-implied role in migration and adhesion also places it as a key target for inhibition. Yet, thorough characterization of antibodies to both of these domains have been underemphasized and underappreciated.

The recent discovery of highly potent antibodies targeting the minor repeat and junctional epitopes have shown that continued immunological survey for monoclonals targeting novel epitopes should continue. Indeed, a wave of second-generation vaccines is in development to address the limitations of RTS,S, putting to the test theories and new lessons learned through rigorous examination of the antibody-mediated immune response

to *RTS,S* as well as sporozoite vaccination. The culmination of extensive research to try to produce immune correlates of protection afforded by RTS,S vaccination has also produced an unexpected shift towards production of higher quality antibodies and the importance of Fc-mediated effector functions. The MAL071 trial has specifically shed light on the powerful role that high quality polyfunctional antibodies targeting the C-terminal domain may have in protection. However, the exact mechanisms of their action and the limitations of existing models in addressing these has not been probed with sufficient rigor and intention. I intend to address these in the Chapters following.

1.4 Blood-Stage Vaccination

Merozoites and sporozoites share a limited set of surface antigens providing potential for multi-stage protection from infection(137). However, the circumsporozoite protein is a pre-erythrocytic antigen, and with CSP-based vaccine failing to provide sterile protection, one option to achieve protection from infection may be a blood-stage vaccine component to provide added protection from *Plasmodium* infection and clinical malaria.

Blood-stage vaccination aims to elicit an immune response against antigens required for the attachment and invasion of blood cells by merozoites, thereby preventing the onset of blood-stage infection and reducing parasite burden and associated disease symptoms. Mouse experiments have shown sporozoite migration to the liver from the intradermal injection site can take up to 3 hours (138). In contrast, merosomes and erythrocytic schizonts rupture in close proximity to their infection targets. Attachment of *P. falciparum* merozoites is seen as soon as 3 seconds after schizont rupture, with successful invasion in as little as 38 seconds after rupture (139). The humoral response to merozoite antigen therefore requires rapid kinetics of inhibition to counteract the rapid kinetics of invasion. Furthermore, the cyclical infection of erythrocytes by merozoites produces a parasitic and antigenic load orders of magnitude higher than that encountered by liver-stage infection. Together with the continued selection pressure applied by both adaptive and innate serum factor, merozoites are poised for rapid antigenic drift and evolution away from host defences and present a myriad of immune evasion strategies(24,140).

Blood-stage vaccination is of unique interest in the case of *Plasmodium vivax* due to the elusive nature of the dormant hypnozoite. Following failure to inhibit liver-stage infection, hypnozoite reactivation can cause relapse infection months or years following primary infection (30). Therapies shown to kill hypnozoites are often those incompatible with patients with G6PD deficiencies, affecting up to 6% of the population in some highly malaria-endemic areas (19). Consequently, *P. vivax* produces a subset of individual in particular risk of untreatable chronic malaria. Recent analysis has estimated that *P. vivax* relapse due to hypnozoite reactivation constitutes 80% of infections in Papua New Guinea children (141). Previously thought to be benign in comparison to the more virulent *P. falciparum,* there have been multiple documentations of more severe clinical outcomes of *P. vivax* malaria in children (142,143). Together with the wide geographical net cast by the large endemic regions of Anopheles mosquitos facilitating *P. vivax* transmission, blood-stage vaccination targeting *P. vivax* stands the potential to decrease clinical malaria risk for billions of individuals.

1.4.1 DARC is an essential receptor for *Plasmodium vivax* invasion of reticulocytes

Whereas *Plasmodium falciparum* utilizes a panel of redundant attachment and invasion receptors, Duffy Antigen Receptor for Chemokines (DARC) has long been considered the only *P. vivax* receptor on erythrocytes through its interaction with *P. vivax* Duffy-binding protein (PvDBP). DARC, also known as the Duffy blood group (Fy antigen), is a homodimeric G-protein-coupled receptor with a short 60 amino acid extracellular domain **(Figure 1.5A)**. Known as a promiscuous receptor for chemokines, it has been suggested to regulate circulating inflammatory chemokine

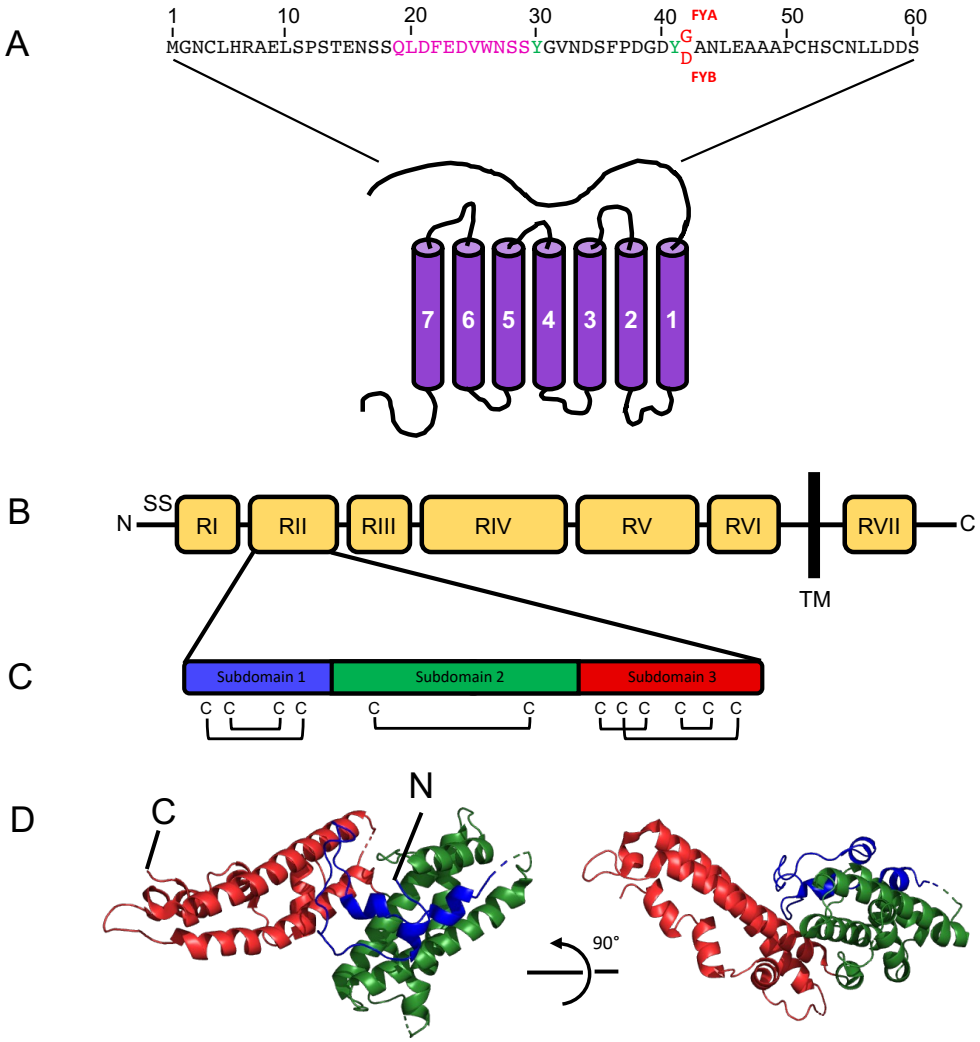


Figure 1.5. Structure of DARC and PvDBP. (A) DARC is a seven-pass transmembrane protein with a GPCR-like architecture, and a 60-amino acid N-terminal extracellular domain. DARC19-30 visible in the DARC-PvDBP-RII crystal structure are shown in pink, Tyr30 and Tyr41 targets of sulphation shown in green, and residue 42 responsible for the FY*A (G42) and FY*B (D42) allelic polymorphism shown in red. (B) Schematic of PvDBP domain organization as suggested by alignment with PkDBP and PfDBL protein structure (Adams et al. 1992). The N-terminal signal sequence is followed by RI-RVII correspond the region 1-6, followed by a transmembrane region, and the C-terminal region 7. (C) Schematic of the cysteine-rich RII domain of PvDBP showing subdomains and disulphide bong arrangement. Subdomain 1 in blue, subdomain 2 in green, and subdomain 3 in red. (D) The entire PvDBP-RII domain is shown from two different views. DBP: 4NUV.

levels by facilitating their trafficking and internalization (144). Two codominant allelic variants of DARC differ by a single nucleotide polymorphism producing an amino acid change in position 42 of the extracellular domain; FY*A producing the Fy^A antigen with glycine (G42) and FY*B producing Fy^B with aspartic acid (D42)(145). An additional allelic resulting from T-33C mutation in the Duffy promoter of FyB ($FY*B^{ES}$) producing the Duffy null allele Fy with no Duffy expression on erythrocytes (ES; Erythrocyte silent)(145).

It has long been observed that *P. vivax* malaria is largely excluded from sub-Saharan and West Africa, which remains the case to this day **(Figure 1.1B)** (6). This has been successfully attributed to the prevalence of Duffy negative individuals ($FY*B^{ES}$/ $FY*B^{ES}$) in this region, with DARC identified as a receptor for both *Plasmodium vivax* and *Plasmodium knowlesi* (146,147). Indeed, over 95% of individuals in West Africa are Duffy negative(148). Further variation is seen between the two functional FY alleles, with higher rates of *P. vivax* malaria seen in FY*B allele carriers compared to FY*A (149). Analysis of a two-nucleotide polymorphism at the 3′-flanking region suggests that FY*B is the ancestral allele, and it is probable that the FY*A allele and the $FY*B^{ES}$ allele increased in population frequency through strong positive selection from *P. vivax* in malaria endemic areas (150).

1.4.2 *Plasmodium vivax* DBP binds the DARC ectodomain on reticulocytes

The family of Duffy-binding proteins (DBPs) were identified as a single gene in *P. vivax* and *P. falciparum* and three genes in *P. knowlesi* sharing common sequence-based

architecture, consisting of seven regions **(Figure 1.5B)** (151). Region I-VI are extracellular, separated from the intracellular region VII by a transmembrane helix. Regions II and VI are cysteine-rich domains and contain a conserved cysteine positions in orthologous *Plasmodium* proteins. With the highest sequence homology, the cysteine-rich Region II of the Duffy-binding proteins from *P. vivax* and *P. knowlesi* share 70% sequence identity and conserved cysteine positions **(Figure 1.5C)**. Duffy binding proteins of *P. knowlesi* are localized to the microneme specialized secretory organelles, likely also the case for *Pv*DBP(152). By assessing the binding of COS-7 cells over-expressing individual DBP domains to Duffy positive erythrocytes, it was shown PvDBP Region II (153). The binding of PvDBP-RII and PkDBPα-RII to RBCs can be inhibited by recombinantly expressed DARC ectodomain peptide sulphated at positions Y30 and Y41, but not those with a Y41F mutation, suggesting an importance for DARC sulphation (154).

Epidemiological surveys in the Malagasy people of Madagascar have shown *P. vivax* infection in Duffy-negative individuals, seen in up to 27.8% of patient samples in some regions (155). Since then, there have been multiple accounts of *P. vivax* infection in Duffy-negative individuals, suggesting a potential alternative invasion pathway for *P. vivax* (156). Field isolate genome sequencing from Malagasy isolated reveal PvDBP gene duplications (157). Amplification of PvDBP genes correlates with increased PvDBP mRNA and decreased protection by protective antibodies, potentially due to increased PvDBP protein expression (140). Recently, an additional *P. vivax* erythrocyte binding protein (EBP2) has been characterized to bind young reticulocytes (158). Antisera raised

against PvDBP-RII and EBP2 failed to inhibit heterologous antigen binding to reticulocytes, suggesting they may act independently to facilitate invasion (158). While both PvDBP-RII and EBP2 show preference to Duffy-positive erythrocytes, EBP2 produced weak binding to Duffy-negative reticulocytes and may be key to their invasion. Nevertheless, PvDBP-RII shows significantly higher binding to reticulocytes compared to EBP2 when expressed on COS7 cell surface, and is likely still the main reticulocyte receptor for *P. vivax*(158). The potential of increased *P. vivax* burden in Africa and other largely Duffy-negative populations is an alarming prospect that emphasises the need for the development of an effective *P. vivax* control strategy.

1.4.3 The PvDBP-RII-DARC interaction

Investigation of the *Pv*DBP-DARC interaction and other interactions key to the *P. vivax* invasion process have been hampered due to the lack of long-term *in vitro* culture system(159). Whereas other *P. falciparum* merozoites establish infection in any circulating erythrocytes, *P. vivax* infection is restricted to reticulocytes expressing the transferrin receptor (TfR1/CD71^{+}), which interacts with *P. vivax* Reticulocyte Binding Protein 2b(160). Young reticulocytes comprise only 1-2% of total RBCs and rapidly develop into mature RBCs (normocytes), producing a barrier for the establishment of long-term *P. vivax* cultures *in vitro* (161). Although DARC expression remains consistent through the RBC maturation process, *Pv*DBP binds to reticulocytes with CD71^{HIGH}/RNA^{HIGH} staining phenotype significantly higher than other reticulocyte populations by flow cytometry, suggesting DARC domain remodelling or localization may change to produce the observed tropism(162). In absence of a long-term in vitro

culture system, *P. vivax* field isolates, *P. knowlesi* transgenic parasites, and cell-based assays, and structural characterization of recombinantly expressed proteins have been utilized to investigate *P. vivax* strain variants, the immune response to *P. vivax*, and the PvDBP-RII-DARC interaction.

The X-ray crystal structures of both *Pk*DBPα-RII and *Pv*DBP-RII at 3Å and 1.95Å respectively show an α-helical three-subdomain architecture stabilized by inter-subdomain disulphide bonds, with previously mapped residues required for DARC binding mapping onto subdomain 2 **(Figure 1.5D)** (163,164). The *Pv*DBP-RII crystal structure reveals subdomain 2 as a site of dimerization, which is proposed to facilitate DARC extracellular domain binding (164). In both structures, a positively charged pocket of key residues is seen removed from the dimerization and DARC binding site, which is hypothesized as the sulphotyrosine binding pocket. Through nuclear magnetic resonance experiments with labelled DARC ectodomain peptide, residues 14-43 of DARC produce the minimal binding region of DARC to *Pv*DBP-RII (165). Two separate crystal structures of PvDBP-RII (SalI strain) in complex with the DARC ectodomain peptides reveal PvDBP-RII:DARC ratios of 2:1 and 2:2, with DARC19-30 in an α-helical conformation binding both PvDBPRII monomers adjacent to the dimerization site in subdomain 2 **(Figure 1.6A)** (165). Supported by ITC affinity measurements, the authors propose a stepwise binding mechanism in which PvDBPRII dimerization upon binding of a single DARC ectodomain is followed by binding of a second DARC ectodomain.

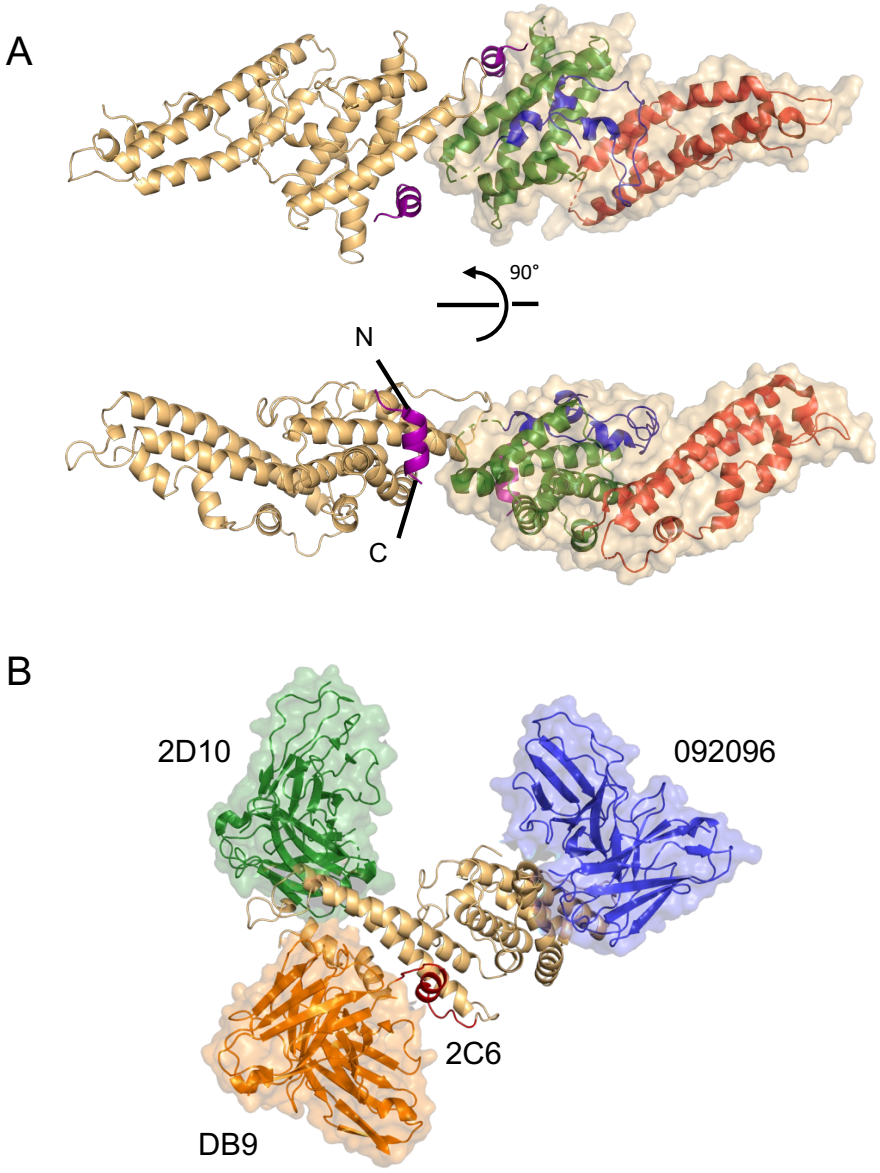


Figure 1.7. Structural Basis for Engagement of PvDBP-RII with DARC and Monoclonal Antibodies. (A) Crystal structure of PvDBP-RII in complex with DARC ectodomain peptide residues 19-30 (pink ribbon cartoon). One PvDBP-RII monomer is shown in light orange, whereas the other monomer is colored by subdomain (subdomain 1 in blue, subdomain 2 in green, subdomain 3 in red) with transparent yellow surface. PDB: 4NUV. (B) Alignment of available crystal structures of monoclonal antibodies binding to PvDBP-RII, showing the binding of 092096 (blue, PDB: 6OAO) to subdomain 2, while DB9 (orange, PDB:6R2S) and 2D10 (green, PDB: 5F3J) bind to opposite faces of subdomain 3. The binding epitope of 2C6 is additionally shown in red on the PvDBP-RII surface, overlapping with that of DB9.

Binding of recombinant PvDBP-RII to FY*B/FY*B erythrocytes is significantly higher than to FY*A/FY*A erythrocytes, in line with observed differential clinical incidences of *P. vivax* (166). Although the current understanding of the DARC-PvDBP-RII interaction provide a plausible mechanism for receptor engagement, the structural evidence regarding molecular mechanisms by which tyrosine sulfation and allelic polymorphisms affect infection remain a matter of hypothesis.

1.4.4 Natural immune response to PvDBP-RII

Following the identification of PvDBP-RII as the binding domain for DARC, much work has focused on documenting strain polymorphisms to understand the relationship between *P. vivax* strains and immune evasion. While showing a high sequence identity to *P. knowlesi* proteins, 20% of PvDBP-RII residues are highly polymorphic (167,168). Incidences of *P. vivax* infection in PNG patients increase in the first 5 years of life and decrease thereafter, suggesting that repeat infection mounts a significant and inhibitory immune response. This is accompanied with a decrease of multiple co-infection and selective enrichment of specific strains, suggestive of selection pressure on infecting strains (169). An increased T-cell response is seen with age to multiple peptide epitopes within the DARC binding site, and one mechanism of selection may act to enrich strains with reduced cross-reactive T-cell epitopes (170). Increased exposure with age further correlates with serum binding to PvDBP-RII and specific binding to multiple peptides representing major linear B-cell epitopes in the central binding motif of PvDBP-RII (171).

In a cohort of adults from Iran, a region of low but year-round transmission, sera inhibited binding of COS-7 cells expressing PvDBP-RII to erythrocytes even when expressing PvDBP-RII sequences heterologous to the infecting strain (172). The importance of acquiring strain transcending immunity is highlighted in a cohort of PNG children, where those with high levels of strain-transcending anti-PvDBP-RII antibody responses were significantly protected from *P. vivax* (173). This is reiterated by a study of sera samples from rural Amazonians, in which highest tercile of broadly inhibitory antibody responses significantly correlated with protection against clinical *P. vivax* compared to lower and middle terciles (174). Surprisingly, Amazonians heterozygous for a Duffy-positive allele (FY*A/FY*B^{ES} and FY*B/FY*B^{ES}) are significantly more likely to produce a persistent, strong, and broadly inhibitory response compared to homozygous or heterozygous double positive individuals (FY*A/FY*A, FY*A/FY*B, or FY*B/FY*B) (175).

In comparison to sera from individuals from endemic areas, sera from singly exposed individuals not reactive towards linear epitopes can still inhibit binding of erythrocytes to COS-7 cells expressing PvDBP-RII (176). However, many individuals did not seroconvert, as also observed in another study reporting 53% seroconversion rate following a single clinical *P. vivax* case, with rapidly decreasing antibody titres and reduced reactivity to heterologous strain PvDBP-RII (177). It is therefore likely that while a single exposure may produce sufficient short-term immunity directed at conformational epitopes, repeat exposure to natural infection may hold the key to targeting linear epitopes and the production long-lasting strain transcending immunity.

1.4.5 PvDBP-RII vaccination produces broadly inhibitory antibodies

The high polymorphism of PvDBP-RII and resulting implication for the production of a cross-reactive and protective response has been at the forefront of PvDBP-RII-based vaccine design. To explore whether low seroconversion rates in singly exposed individuals may be attributed to major histocompatibility complex (MHC) restrictions, multiple strains of mice were immunized with PvDBP-RII-IV based vaccines (176). Although not all mouse strains produced a strong response after a single dose immunization, repeat immunization produced strong response in all strains that suggest boost immunization may be relevant for a strong and long-lasting response (176). Rabbit immunizations with PvDBP-RII are also shown to inhibit binding of DARC ectodomain (Ig fusion construct) to recombinant PvDBP-RII (178). As suspected, inhibition of the DARC-PvDBP-RII interaction through the COS7-erythrocyte assay is significantly reduced when rabbit anti-PvDBP-RII sera is tested against heterologous strain PvDBP-RII sequences (179).

Following the validation of concerns raised by previous patient sera studies, multiple immunofocusing strategies have been tested to counteract the effects of sequence mismatch on PvDBP-RII immunogenicity and vaccine potential. Using sera from PNG patients, ten linear B-cell epitopes were identified to differentiate between samples with high or low inhibition of PvDBP-RII-DARC binding (180). With this knowledge, a PvDBP-RII mutant (DEKnull) was designed to remove dominant polymorphic B-cell epitope and shown to retain reactivity to human sera, suggesting naturally reactive epitopes are maintained by the DEKnull construct (181). Following the demonstration

that specific mixed-strain immunizations produce higher titres of cross-reactive antibodies than single-strain immunization, a follow-up study investigated the role of heterologous prime-boost protocols using the DEKnull synthetic variant (182,183). While SalI thrice immunized control mice showed comparable cross-inhibitory response as DEKnull thrice-immunized mice, DEKnull twice-primed mice boosted with heterologous strain PvDBPRII produced higher cross-reactive antibody titres (183). However, DEKnull-containing immunization protocols produced significantly lowered immunogenicity, lymphoproliferative stimulating capacity, and failed to produce significantly improve inhibition of the PvDBPRII-DARC interaction in the COS7-erythrocyte binding assay (183). The X-ray crystal structure of the DEKnull antigen at 2.1Å resolution revealed highly similar structure to wild-type PvDBP-RII, with overall root-mean-square (r.m.s.) difference of 0.4 Å (184). The DEKnulll protein retains binding to multiple inhibitory monoclonal antibodies, suggesting reduced titres of DEKnull immunizations may be attributed to reduction in antibodies produced against the polymorphic epitopes eliminated in DEKnull(184). A next-generation DEKnull-2 variant was designed to further remove polymorphic epitopes, displaying comparable immunogenicity and antisera cross reactivity compared to SalI strain, as well as inhibition of merozoite invasion in short-term *P. vivax* cultures (185)

In another effort to guide immune responses to key epitopes, three glycan masking variants of PvDBP-RII were produced to obstruct the proposed sulfotyrosine binding pocket, polymorphic residues, and surface loops but not the PvDBP-RII dimerization interface or DARC binding site (186). While demonstrating comparable immunogenicity

to wild-type PvDBP-RII, a glycosylated construct designed to occlude the proposed sulfotyrosine binding site had significantly reduced inhibition of the PvDBP-RII-erythrocyte interaction. The glycosylated variant designed to block polymorphic epitopes has measurably higher inhibitory activity, highlighting this strategy as promising for future vaccine design(186). Altogether, these studies further demonstrate the validity of PvDBP-RII as a candidate vaccine antigen and the potential of engineered constructs to produce a strain-transcending antibody response. Nevertheless, the common requirement for multiple immunizations to achieve a potent PvDBP-RII cross-neutralizing response reiterate previous observations from patient sera studies and recapitulate concerns regarding potential MHC restriction effects in other vaccine models.

Following demonstration of immunogenicity in non-human primates, two Phase I trials in *P. vivax* naïve individuals demonstrated safety and immunogenicity of PvDBP-RII-based vaccines (187–189). In the first study, 24 malaria naïve adults were divided into four groups immunized with an escalating dose of chimp adenovirus-based (ChAd63) PvDBP-RII (SalI strain), with two groups receiving booster immunization with a modified vaccinia Ankara virus-based (MVA) PvDBP-RII (SalI strain) vaccine(Payne et al. 2017). Whereas a single low dose ChAd63-PvDBP-RII vaccination failed to produce an antibody response, a single high dose ChAd63-PvDBP-RII vaccination produced antibody response stable for over 100 days, with boost regimen further increasing antibody titres. Recapitulating observations observed in mouse models, high-dose prime immunization (day 28) seroconversion rate was 60% and increased to 100% following boost immunization. While one singly immunized individual (25%) showed binding

inhibitory response to multiple heterologous *P. vivax* strains PvDBP-RII, all doubly immunized individuals showed strain-transcending, binding-inhibitory antibody responses (187). In a second study of 128 *P. vivax* naïve adults, recombinant PvDBP-RII vaccine was administered at three doses against control Hepatitis B vaccine (188). Following second dose immunization (day 56) and third immunization (day 84) seroconversion rate was 100%, with high antibody titres decreasing slightly but significantly by day 180. While all doses regimen produced anti-PvDBP-RII sera that inhibited PvDBP-RII-DARC binding by over 70% (day 84), highest inhibition was seen for the highest dose regimen. Immunized sera were able to inhibit heterologous strain PvDBP-RII binding to DARC. With all strains, inhibition was significantly decreased during the 6-month follow-up(188). Both studies confirm previous observations of repeat immunization requirement for widespread seroconversion and the production of an antibody response capable of inhibiting the PvDBP-RII-DARC binding. For the first time, these studies show human immunization with PvDBP-RII-based constructs elicit a strain-transcending and stable antibody responses.

1.4.6 Monoclonal antibodies towards PvDBP-RII target multiple epitopes

Concurrent to the exploration of PvDBP-RII-based vaccination and structural characterization of the PvDBP-RII-DARC interaction, investigation of the epitopes and inhibitory profiles of monoclonal antibodies have supplemented our understanding of natural or vaccine-mediated inhibition of PvDBP-RII-DARC binding. The binding epitopes of several monoclonal antibodies are shown in **Figure 1.6B**. In a panel of ten monoclonal antibodies isolated from PvDBP-RII mouse immunization, five antibodies

showed broad binding to five strains, four of which highly inhibitory in the COS7-erythrocyte binding assay (190). Unexpectedly, the X-ray crystal structure of broadly inhibitory mAb 2D10 scFv fragment in complex with PvDBP-RII at 4Å illustrated binding to subdomain 3 of PvDBP-RII (191). Through small angle X-ray scattering (SAXS), mutagenesis, and competition analysis, inhibitory mAb 2H2 was mapped to the same epitope as 2D10, and mAb 2C6 mapped to a distinct helical face of subdomain 3(191). Through phage display mutagenesis analysis, an additional inhibitory mAb 3C9 was mapped onto a further face of subdomain 3. Distant from any regions previously shown or proposed to be involved in the PvDBP-RII-DARC interaction, these mAbs provide evidence for novel binding interactions yet unaccounted for by the current PvDBP-RII-DARC binding model.

In another study, thirteen strain-transcending PvDBP-RII-binding monoclonal antibodies were isolated from Cambodian and Brazilian subjects with documented acute *P. vivax* incidences (192). Two mAbs (096092 and 053054) blocked binding of soluble DARC ectodomain with PvDBP-RII and competed with most other mAbs for PvDBP-RII binding, suggesting they bind the DARC19-30 binding site on subdomain 2. The X-ray crystal structures of mAb 053054 and 092096 scFv fragments in complex with PvDBP-RII at resolutions 2.9Å and 3.5Å illustrate binding of both scFv to an overlapping epitope on subdomain 2 comprised of both dimerization interface and DARC binding region (193). Both mAbs were tested against clinical *P. vivax* isolates and shown to inhibit merozoite invasion by 50%(192,193). By preventing the PvDBP-RII interaction through direct obstruction of both subdomain 2 dimerization interface and DARC binding site, it

is clear how mAbs 053054 and 092096 provide strain-transcending inhibition of *P. vivax* invasion of reticulocytes (193). Comparison of these two panels of monoclonals raises intrigue regarding the differential means of inhibition seen in mouse immunization versus natural human infection, with potential negative implications for the use of mouse models for the validation of PvDBP-RII vaccine constructs. Although clonally unrelated and isolated from multiple individuals, seven of thirteen characterized mAbs use the V_H1-24 antibody lineage, both posing potential concern of a restrictive response to the highly inhibitory dimerization epitope or providing a hopeful opportunity for germline-targeting immunogens.

Recently, a panel of ten monoclonal antibodies were isolated from ChAd63-PvDBP-RII and MVA-PvDBP-RII immunized subjects (194). Most mAbs showed differential inhibition of DARC ectodomain binding to PvDBP-RII, with DB2 and DB9 showing strain-transcendent inhibition. Due to recent advances in *P. knowlesi in vitro* culture, growth inhibition assays were conducted using transgenic *P. knowlesi* parasites in which PkDBPα was replaced with PvDBP (195). Inhibition rates in the transgenic model were highest for DB1, DB9, and DB10, with a significant correlation between on-rate and EC30 implying the opportunity for merozoite inhibition is time-limited. Furthermore, these results correlated with measurements from 12 field isolates, validating the transgenic parasite model. Although highly inhibitory in both parasite experiments, both DB1 and DB10 do not inhibit DARC ectodomain binding. The X-ray crystal structure of DB9 in complex with PvDBP-RII at 3.0Å resolution illustrates DB9 binding to subdomain 3, occupying a region with low sequence entropy similar to murine mAb 3C9.

Epitope mapping experiments place four other mAbs from the panel in the same epitope bin as DB9, suggesting they bind subdomain 3. Juxtaposing the DB9-PvDBP-RII complex onto the DARC-PvDBP-RII crystal structure, it is likely that DB9 inhibits binding to the DARC ectodomain and, therefore, merozoite invasion through steric clashes with the reticulocyte surface (194).

1.4.7 Summary of our current knowledge of PvDBP as a vaccine candidate and its interaction with DARC

While presenting unique challenges to its investigation, the biology of *P. vivax* presents PvDBP-RII as a highly promising candidate for a blood-stage vaccine. Through a plethora of studies, PvDBP-RII has been validated to produce strain-transcending antibodies in murine, rabbit, non-human primates, and human stage Ia trials. The recent wave of X-ray crystal structures describing novel inhibitory epitopes on the surface of PvDBP-RII improve our understanding of inhibitory mechanisms of merozoite invasion while posing new questions. The X-ray crystal structures of naturally acquired human mAbs 053054 and 092096 provide obvious basis for inhibition of merozoite invasion by direct inhibition of DARC binding. The X-ray crystal structure of human mAb DB9 and inhibitory murine mAbs 2C6 and 3C9 map to similar epitopes on subdomain 3, providing a novel mechanism for indirect inhibition by sterically preventing PvDBP-RII approach to the merozoite membrane. Inhibitory murine mAbs 2D10 and 2H2 have been found to bind the opposite face of subdomain 3. It is likely they achieve inhibition of the PvDBP-RII-DARC interactions unexplained by the interaction seen in the two available DARC-PvDBP-RII X-ray crystal structures. While NMR studies suggest involvement of residues

14-43 of the DARC ectodomain in PvDBP-RII binding, only residues 19-30 are seen in currently available X-ray crystal structures of the DARC-PvDBP-RII complex. This does not provide a basis for the molecular determinants of interaction of PvDBP-RII with sulfotyrosine at position 41 nor allelic variation at position 42, both of which have been shown to affect PvDBP-RII binding to DARC.

Further questions arise when considering the source of these antibodies. The majority of monoclonal antibodies isolated following both murine and human immunization with PvDBP-RII-based vaccines produce a dominant antibody response directed at subdomain 3. This is in stark difference to antibodies isolated from natural *P. vivax* infection in humans that bind subdomain 2. In both cases, multiple immunizations are required to produce a strong inhibitory immune response. Encouragingly, several antibodies of both murine and human source are cross-neutralizing and strain-transcending. Both MHC restrictions and differential antigen presentation by natural infection and vaccination may produce the difference in the observed response. In mice, it has been shown that multiple immunofocusing strategies can improve production of strain-transcending antibodies. Further investigation into the wider PvDBP-RII-DARC interaction and epitopes targeted by vaccine-induced monoclonal antibodies will improve our understanding of vaccine-mediated inhibition of *P. vivax* invasion in hopes of producing a rationally improved next-generation PvDBP-RII vaccine for clinical evaluation in humans. I intend to address these in these concerns in the Chapters following.

1.5 Summary of thesis research

The first X-ray crystal structure demonstrating the basis for antibody recognition of the major repeat epitope of PfCSP was published in 2017 in the Wilson lab(108). Since then, multiple novel protective epitopes on PfCSP (124,125,129), as well as common structural motifs used to bind previously known epitopes has been revealed through structural characterization of mAb binding to PfCSP (106,123). Under the supervision of Prof. Ian Wilson at The Scripps Research Institute, I sought to expand our understanding of the antigenic landscape presented by the under-investigated N-terminal and C-terminal domains of CSP. Through our collaboration with Ding Zhang (Lerner lab/Wilson lab), we obtained a panel of antibody sequences from a human antibody phage display library, out of which four mAbs bound the CSP N-terminus. The X-ray crystal structure of Fab 3F4 and Fab 3A3 bound to their N-terminal CSP peptide epitopes identified a new epitope on the CSP N-terminus bound by 3A3 and demonstrates the ability of two human mAbs to bind the CSP N-terminus through germline encoded residues. From our collaborators Nathan Beutler (Burton lab, TSRI) and Thomas Rogers (TSRI/UCSD), we obtained seven monoclonal antibodies, in this case isolated from mouse immunization with an N-terminal CSP immunogen, that also mapped to the CSP N-terminus. The X-ray crystal structure of mNCSP6 reveals its binding to the RI cleavage site, with a distinct epitope to other mAbs shown to bind this region. The X-ray crystal structure of Fab mNCSP13 to its N-terminal CSP epitope reveals another new epitope on the CSP N-terminus, also bound by mAbs mNCSP2, 14, and 27. The differential ability of mAbs targeting this new conserved epitope to bind across a panel of CSP N-terminus haplotypes raises the question of whether the CSP N-terminus possesses secondary structural characteristics.

Two mAbs which were not susceptible to polymorphisms and bound across CSP N-terminus haplotypes are mAbs mNCSP9 and mNCSP10. The X-ray crystal structures of these mAbs in complex with their NtCSP peptide epitope reveal that they bind an overlapping epitope to 3A3 by similarly engaging PfCSP Tyr63 and Trp62 in an α-helical turn. mNCSP2, 6, 9, and 10 were all shown to provide protection by mouse liver burden assay, contradicting to previous claims that mAbs targeting the N-terminus are not protective. The protection granted by mNCSP9 and 10 prompted us to collaborate with Jessica (Woolf) Coppola (Burton lab, TSRI) and Joseph Jardine (IAVI) to affinity mature 3A3 by yeast display. Through limited mutagenesis, limited to a single amino acid in each CDR, they were able to produce affinity variants of 3A3 with sub-nanomolar affinity to the N-terminal peptide target of which 3A3. Therefore, we have been able to show that the human antibody repertoire has the capacity to produce high affinity antibodies targeting new and conserved N-terminal CSP epitopes which are the target of protective mouse antibodies.

Through our collaboration with PATH's Malaria Vaccine Initiative, we obtained a panel of 15 structurally uncharacterized mAb sequences from the MAL071 trial (81) mapped to the C-terminal domain of CSP. The X-ray crystal structure of Fabs 367, 1392, and 1392 build upon the previous observations made in our lab that mAbs binding the polymorphic α-epitope utilize a similar set of binding interactions to bind the polymorphic α-epitope (123). Our collaborator Nathan Beutler (Burton lab) further showed that these mAbs fail to provide strain transcending binding to a panel of CSP C-terminus haplotypes. In contrast, the X-ray crystal structures of Fabs 369, 389, 1393, 1437, 1534, and 1550,

demonstrate the ability of a range of antibodies to bind the conserved β-epitope using multiple germline lineages which utilize shorter CDRH3s than mAb 1512, and therefore may be more clinically relevant for RTS,S-mediated protection. The mAb 1504 crystal structure identifies yet another conserved epitope, corresponding to the highly conserved cell adhesion motif RII+(47). In addition to binding across multiple CSP C-terminus haplotypes, mAbs binding conserved epitope have a higher avidity index than mAbs binding polymorphic epitopes. An increased avidity index towards CtCSP and binding across multiple haplotypes have both been separately identified as correlates of protection. Here, we provide the first potential direct link between the two.

Inspired by the newfound breadth of antibodies targeting conserved epitopes CSP, I proposed a second-generation vaccine design which seeks to eliminate the response to polymorphic epitopes on the C-terminus of CSP by replacing the polymorphic CS-flap with established highly protective B-cell epitopes of CSP, including major repeats, minor repeats, and junctional peptides. Through our collaboration with Nelson Wu (Schief lab, TSRI), we expressed a panel of hybrid-domain C-terminal haplotypes on the surface of lumazine synthase 60-mer nanoparticles and assessed their immunogenicity with the help of our collaborators Yevel Flores Garcia and Fidel Zavala (John Hopkins University). All nanoparticle designs incorporating CSP repeat and junctional epitopes into the αTSR domain provided comparable protection to RTS,S, providing a proof of concept for this immunogen design.

Under the supervision of Prof. Matthew Higgins at the University of Oxford, I was able to characterize the binding of the *Plasmodium vivax* blood-stage invasion ligand, the Duffy binding protein to the ectodomain of its erythrocyte receptor DARC. By expressing both DARC ectodomain and PvDBP-RII in mammalian cells, I was able to crystallize PvDBP-RII in complex with the DARC ectodomain revealing in molecular detail the binding site for the sulphated tyrosine 41 and the basis for increased binding to allelic polymorphism of residue 42 of the DARC ectodomain. Through the work of our colleagues Tossapol Pholcharee and Bora Guloglu (Higgins lab) and collaborators Sophia DonVito, Franziska Mohring, and Rob Moon (London School of Hygiene and Tropical Medicine), we were able to demonstrate the relative importance of Tyr41 sulphation over that of Tyr30 in DARC ectodomain binding and merozoite invasion (196).

The crystal structure of PvDBP-RII in complex with DARC also included the inhibitory monoclonal antibody DB1, isolated from a PvDBP-RII-based stage I clinical trial (187), provided to us by our collaborator Simon Draper (University of Oxford). DB1 binds at the putative dimerization interface of subdomain 2 of PvDBP-RII, separate from the DARC binding site, to a the highly polymorphic DEK epitope (184). Without inhibiting DARC binding, the obvious mechanism for DB1 inhibition would be inhibition of dimerization. However, our colleague Tossapol Pholcharee's SAXS experiments showed that even at high concentrations, PvDBP-RII expressed from mammalian sources does not dimerize in solution, putting into question the dimerization mechanism (196). Therefore, we also began to characterize the full-length PvDBP ectodomain, providing the basis for continued investigation of the PvDBP-DARC interaction. Altogether, the

work provided in this thesis provides an expansion of our understanding of the immunological landscape presented by two *Plasmodium* vaccine antigens, PfCSP and PvDBP-RII, that can be used to inform next-generation vaccine design, as well as characterize parasite invasion processes and effector functions mediating immunity.

1.6 References

1. WHO. *World malaria report 2022*. *WHO* https://www.who.int/teams/global-malaria-programme/reports/world-malaria-report-2022 (2022).
2. Bill & Melinda Gates Foundation. *2022 Goalkeepers Report*. (2022).
3. Andrade, M. v. *et al.* The economic burden of malaria: a systematic review. *Malar J* **21**, 283 (2022).
4. Gething, P. W. *et al.* A new world malaria map: *Plasmodium falciparum* endemicity in 2010. *Malar J* **10**, 378 (2011).
5. Weiss, D. J. *et al.* Mapping the global prevalence, incidence, and mortality of *Plasmodium falciparum*, 2000–17: a spatial and temporal modelling study. *The Lancet* **394**, 322–331 (2019).
6. Battle, K. E. *et al.* Mapping the global endemicity and clinical burden of *Plasmodium vivax*, 2000–17: a spatial and temporal modelling study. *The Lancet* **394**, 332–343 (2019).
7. Guerra, C. A. *et al.* The Limits and Intensity of *Plasmodium falciparum* Transmission: Implications for Malaria Control and Elimination Worldwide. *PLoS Med* **5**, e38 (2008).
8. Walker, K. & Lynch, M. Contributions of Anopheles larval control to malaria suppression in tropical Africa: review of achievements and potential. *Med Vet Entomol* **21**, 2–21 (2007).
9. Alout, H., Roche, B., Dabiré, R. K. & Cohuet, A. Consequences of insecticide resistance on malaria transmission. *PLoS Pathog* **13**, e1006499 (2017).
10. Bhatt, S. *et al.* The effect of malaria control on *Plasmodium falciparum* in Africa between 2000 and 2015. *Nature 2015 526:7572* **526**, 207–211 (2015).
11. Lindsay, S. W., Thomas, M. B. & Kleinschmidt, I. Threats to the effectiveness of insecticide-treated bednets for malaria control: thinking beyond insecticide resistance. *Lancet Glob Health* **9**, 1325–1331 (2021).
12. Achan, J. *et al.* Quinine, an old anti-malarial drug in a modern world: Role in the treatment of malaria. *Malar J* **10**, 144 (2011).
13. Powell, R. D., Brewer, G. J., Alving, A. S. & Millar, J. W. Studies on a strain of chloroquine-resistant *Plasmodium falciparum* from Thailand. *Bull World Health Organ* **30**, 29–44 (1964).
14. da Silva, A. F. C. & Benchimol, J. L. Malaria and Quinine Resistance: A Medical and Scientific Issue between Brazil and Germany (1907–19). *Med Hist* **58**, 1–26 (2014).
15. Menard, D. & Dondorp, A. Antimalarial Drug Resistance: A Threat to Malaria Elimination. *Cold Spring Harb Perspect Med* **7**, a025619 (2017).
16. Belete, T. M. Recent Progress in the Development of New Antimalarial Drugs with Novel Targets. *Drug Des Devel Ther* **14**, 3889 (2020).
17. Sinha, S., Sarma, P., Sehgal, R. & Medhi, B. Development in assay methods for in vitro antimalarial drug efficacy testing: A systematic review. *Front Pharmacol* **8**, 754 (2017).
18. Braga, C. B. E. *et al.* Side Effects of Chloroquine and Primaquine and Symptom Reduction in Malaria Endemic Area (Mâncio Lima, Acre, Brazil). *Interdiscip Perspect Infect Dis* **2015**, (2015).

19. Nascimento, J. R. *et al.* Prevalence of glucose 6-phosphate dehydrogenase deficiency in highly malaria-endemic municipalities in the Brazilian Amazon: A region-wide screening study. *The Lancet Regional Health Americas* **12**, 100273 (2022).
20. Sinnis, P. & Coppi, A. A long and winding road: The *Plasmodium* sporozoite's journey in the mammalian host. *Parasitol Int* **56**, 171–178 (2007).
21. Prudêncio, M., Rodriguez, A. & Mota, M. M. The silent path to thousands of merozoites: the *Plasmodium* liver stage. *Nat Rev Microbiol* **4**, 849–856 (2006).
22. Vaughan, A. M. & Kappe, S. H. I. Malaria Parasite Liver Infection and Exoerythrocytic Biology. *Cold Spring Harb Perspect Med* **7**, a025486 (2017).
23. Warncke, J. D. & Beck, H.-P. Host Cytoskeleton Remodeling throughout the Blood Stages of *Plasmodium falciparum*. *Microbiol Mol Biol Rev* **83**, (2019).
24. Wright, G. J. & Rayner, J. C. *Plasmodium falciparum* Erythrocyte Invasion: Combining Function with Immune Evasion. *PLoS Pathog* **10**, e1003943 (2014).
25. Cowman, A. F. & Crabb, B. S. Invasion of Red Blood Cells by Malaria Parasites. *Cell* **124**, 755–766 (2006).
26. Aly, A. S. I., Vaughan, A. M. & Kappe, S. H. I. Malaria Parasite Development in the Mosquito and Infection of the Mammalian Host. *Annu Rev Microbiol* **63**, 221 (2009).
27. Liu, Z., Miao, J. & Cui, L. Gametocytogenesis in malaria parasite: commitment, development and regulation. *Future Microbiol* **6**, 1369 (2011).
28. Wells, T. N. C., Burrows, J. N. & Baird, J. K. Targeting the hypnozoite reservoir of *Plasmodium vivax*: the hidden obstacle to malaria elimination. *Trends Parasitol* **26**, 145–151 (2010).
29. Huldén, L., Huldén, L. & Heliövaara, K. Natural relapses in vivax malaria induced by Anopheles mosquitoes. *Malar J* **7**, 1–11 (2008).
30. Hulden, L. & Hulden, L. Activation of the hypnozoite: A part of *Plasmodium vivax* life cycle and survival. *Malar J* **10**, 90 (2011).
31. Campo, B., Vandal, O., Wesche, D. L. & Burrows, J. N. Killing the hypnozoite – drug discovery approaches to prevent relapse in *Plasmodium vivax*. *Pathog Glob Health* **109**, 1022 (2015).
32. Neveu, G. & Lavazec, C. Erythrocyte Membrane Makeover by *Plasmodium falciparum* Gametocytes. *Front Microbiol* **10**, 2652 (2019).
33. Nadeem, A. Y., Shehzad, A., Islam, S. U., Al-Suhaimi, E. A. & Lee, Y. S. Mosquirix^{TM} RTS, S/AS01 Vaccine Development, Immunogenicity, and Efficacy. *Vaccines (Basel)* **10**, 1033–1039 (2022).
34. Hoffman, S. L. *et al.* Naturally Acquired Antibodies to Sporozoites Do Not Prevent Malaria: Vaccine Development Implications. *Science* **237**, 639–642 (1987).
35. Doll, K. L. & Harty, J. T. Correlates of protective immunity following whole sporozoite vaccination against malaria. *Immunol Res* **59**, 166–176 (2014).
36. Goh, Y. S., McGuire, D. & Rénia, L. Vaccination with sporozoites: Models and correlates of protection. *Front Immunol* **10**, 1227 (2019).
37. Seder, R. A. *et al.* Protection against malaria by intravenous immunization with a nonreplicating sporozoite vaccine. *Science* **341**, 1359–1365 (2013).

38. Mordmüller, B. *et al.* A PfSPZ vaccine immunization regimen equally protective against homologous and heterologous controlled human malaria infection. *npj Vaccines* **7**, 100 (2022).
39. Sirima, S. B. *et al.* A randomized controlled trial showing safety and efficacy of a whole sporozoite vaccine against endemic malaria. *Sci Transl Med* **14**, eabj3776 (2022).
40. Oneko, M. *et al.* Safety, immunogenicity and efficacy of PfSPZ Vaccine against malaria in infants in western Kenya: a double-blind, randomized, placebo-controlled phase 2 trial. *Nature Medicine 2021 27:9* **27**, 1636–1645 (2021).
41. Nascimento, I. P. & Leite, L. C. C. Recombinant vaccines and the development of new vaccine strategies. *Brazilian Journal of Medical and Biological Research* **45**, 1102–1111 (2012).
42. Yoshida, N., Nussenzweig, R. S., Potocnjak, P., Nussenzweig, V. & Aikawa, M. Hybridoma Produces Protective Antibodies Directed Against the Sporozoite Stage of Malaria Parasite. *Science* **207**, 71–73 (1980).
43. Yoshida, N., Potocnjak, P., Nussenzweig, V. & Nussenzweig, R. S. Biosynthesis of Pb44, the protective antigen of sporozoites of *Plasmodium berghei*. *J Exp Med* **154**, 1236 (1981).
44. Zavala, F., Cochrane, A. H., Nardin, E. H., Nussenzweig, R. S. & Nussenzweig, V. Circumsporozoite proteins of malaria parasites contain a single immunodominant region with two or more identical epitopes. *J Exp Med* **157**, 1947–1957 (1983).
45. Enea, V. *et al.* DNA Cloning of *Plasmodium falciparum* Circumsporozoite Gene: Amino Acid Sequence of Repetitive Epitope. *Science* **225**, 628–630 (1984).
46. Nardin, E. H. *et al.* Circumsporozoite proteins of human malaria parasites *Plasmodium falciparum* and *Plasmodium vivax*. *J Exp Med* **156**, 30 (1982).
47. Dame, J. B. *et al.* Structure of the Gene Encoding the Immunodominant Surface Antigen on the Sporozoite of the Human Malaria Parasite *Plasmodium falciparum*. *Science* **225**, 587–593 (1984).
48. Arnot, D. E. *et al.* Circumsporozoite Protein of *Plasmodium vivax*: Gene Cloning and Characterization of the Immunodominant Epitope. *Science (1979)* **230**, 815–818 (1985).
49. Eichinger, D. J., Arnot, D. E., Tam, J. P., Nussenzweig V. & Enea, V. Circumsporozoite protein of *Plasmodium berghei*: gene cloning and identification of the immunodominant epitopes. *Mol Cell Biol* **6**, 3965–3972 (1986).
50. Lal, A. A. *et al.* Structure of the gene encoding the circumsporozoite protein of *Plasmodium yoelii*. A rodent model for examining antimalarial sporozoite vaccines. *J Biol Chem* **262**, 2937–2940 (1987).
51. Cerami, C. *et al.* The basolateral domain of the hepatocyte plasma membrane bears receptors for the circumsporozoite protein of *Plasmodium falciparum* sporozoites. *Cell* **70**, 1021–1033 (1992).
52. Frevert, U. *et al.* Malaria circumsporozoite protein binds to heparan sulfate proteoglycans associated with the surface membrane of hepatocytes. *J Exp Med* **177**, 1287 (1993).
53. Rathore, D., Sacci, J. B., De La Vega, P. & McCutchan, T. F. Binding and Invasion of Liver Cells by *Plasmodium falciparum* Sporozoites: Essential Involvement of

the Amino Terminus of Circumsporozoite Protein. *J Biol Chem* **277**, 7092–7098 (2002).
54. Zhao, J., Bhanot, P., Hu, J. & Wang, Q. A Comprehensive Analysis of *Plasmodium* Circumsporozoite Protein Binding to Hepatocytes. *PLoS One* **11**, e0161607 (2016).
55. Ying, P. *et al.* The malaria circumsporozoite protein: Interaction of the conserved regions I and II-plus with heparin-like oligosaccharides in heparan sulfate. *Exp Parasitol* **85**, 168–182 (1997).
56. Coppi, A., Pinzon-Ortiz, C., Hutter, C. & Sinnis, P. The *Plasmodium* circumsporozoite protein is proteolytically processed during cell invasion. *J Exp Med* **201**, 27–33 (2005).
57. Coppi, A. *et al.* Heparan Sulfate Proteoglycans Provide a Signal to *Plasmodium* Sporozoites to Stop Migrating and Productively Invade Host Cells. *Cell Host Microbe* **2**, 316–327 (2007).
58. Coppi, A. *et al.* The malaria circumsporozoite protein has two functional domains, each with distinct roles as sporozoites journey from mosquito to mammalian host. *J Exp Med* **208**, 341–356 (2011).
59. Herrera, R. *et al.* Reversible Conformational Change in the *Plasmodium falciparum* Circumsporozoite Protein Masks Its Adhesion Domains. *Infect Immun* **83**, 3771 (2015).
60. Plassmeyer, M. L. *et al.* Structure of the *Plasmodium falciparum* Circumsporozoite Protein, a Leading Malaria Vaccine Candidate. *J Biol Chem* **284**, 26951–26963 (2009).
61. Ballou, W. R. *et al.* Immunogenicity of Synthetic Peptides from Circumsporozoite Protein of *Plasmodium falciparum*. *Science* **228**, 996–999 (1985).
62. Herrington, D. A. *et al.* Safety and immunogenicity in man of a synthetic peptide malaria vaccine against *Plasmodium falciparum* sporozoites. *Nature* **328**, 257–259 (1987).
63. Vreden, S. G. S., Verhave, J. P., Oettinger, T., Sauerwein, R. W. & Meuwissen, J. H. E. T. Phase I Clinical Trial of a Recombinant Malaria Vaccine Consisting of the Circumsporozoite Repeat Region of *Plasmodium Falciparum* Coupled to Hepatitis B Surface Antigen. *Am J Trop Med Hyg* **45**, 533–538 (1991).
64. Rutgers, T. *et al.* Hepatitis B Surface Antigen as Carrier Matrix for the Repetitive Epitope of the Circumsporozoite Protein of Plasmodium Falciparum. *Bio/Technology* **6**, 1065–1070 (1988).
65. Zavala, F. *et al.* Synthetic peptide vaccine confers protection against murine malaria. *J Exp Med* **166**, 1596 (1987).
66. Brown, A. E. *et al.* Safety, immunogenicity and limited efficacy study of a recombinant *Plasmodium falciparum* circumsporozoite vaccine in Thai soldiers. *Vaccine* **12**, 102–108 (1994).
67. Blum-Tirouvanziam, U. *et al.* Localization of HLA-A2.1-restricted T cell epitopes in the circumsporozoite protein of *Plasmodium falciparum*. *J Immunol* **154**, 3922–3931 (1995).
68. Sinigaglia, F. *et al.* A malaria T-cell epitope recognized in association with most mouse and human MHC class II molecules. *Nature* **336**, 778–780 (1988).

69. Aidoo, M. *et al.* Identification of conserved antigenic components for a cytotoxic T lymphocyte-inducing vaccine against malaria. *The Lancet* **345**, 1003–1007 (1995).
70. Hoffman, S. L. *et al.* Human lymphocyte proliferative response to a sporozoite T cell epitope correlates with resistance to *falciparum* malaria. *J Immunol* **142**, 1299–1303 (1989).
71. Romero, P. *et al.* Cloned cytotoxic T cells recognize an epitope in the circumsporozoite protein and protect against malaria. *Nature* **341**, 323–326 (1989).
72. Gordon, D. M. *et al.* Safety, Immunogenicity, and Efficacy of a Recombinantly Produced *Plasmodium falciparum* Circumsporozoite Protein-Hepatitis B Surface Antigen Subunit Vaccine. *J Infect Dis* **171**, 1576–1585 (1995).
73. Kester, K. E. *et al.* Randomized, Double-Blind, Phase 2a Trial of *Falciparum* Malaria Vaccines RTS,S/AS01B and RTS,S/AS02A in Malaria-Naive Adults: Safety, Efficacy, and Immunologic Associates of Protection. *J Infect Dis* **200**, 337–346 (2009).
74. Polhemus, M. E. *et al.* Evaluation of RTS,S/AS02A and RTS,S/AS01B in Adults in a High Malaria Transmission Area. *PLoS One* **4**, e6465 (2009).
75. RTSS Clinical Trials Partnership. Efficacy and safety of RTS,S/AS01 malaria vaccine with or without a booster dose in infants and children in Africa: final results of a phase 3, individually randomised, controlled trial. *The Lancet* **386**, 31–45 (2015).
76. White, M. T. *et al.* Immunogenicity of the RTS,S/AS01 malaria vaccine and implications for duration of vaccine efficacy: secondary analysis of data from a phase 3 randomised controlled trial. *Lancet Infect Dis* **15**, 1450–1458 (2015).
77. Moon, J. E. *et al.* A Phase IIa Controlled Human Malaria Infection and Immunogenicity Study of RTS,S/AS01 E and RTS,S/AS01 B Delayed Fractional Dose Regimens in Malaria-Naive Adults. *J Infect Dis* **222**, 1691 (2020).
78. Mugo, R. M. *et al.* Seven-year kinetics of RTS, S/AS01-induced anti-CSP antibodies in young Kenyan children. *Malar J* **20**, 452 (2021).
79. Neafsey, D. E. *et al.* Genetic Diversity and Protective Efficacy of the RTS,S/AS01 Malaria Vaccine. *N Engl J Med* **373**, 2025–2037 (2015).
80. Pringle, J. C. *et al.* RTS,S/AS01 malaria vaccine mismatch observed among *Plasmodium falciparum* isolates from southern and central Africa and globally. *Sci Rep* **8**, 6622 (2018).
81. Regules, J. A. *et al.* Fractional Third and Fourth Dose of RTS,S/AS01 Malaria Candidate Vaccine: A Phase 2a Controlled Human Malaria Parasite Infection and Immunogenicity Study. *J Infect Dis* **214**, 762–771 (2016).
82. Dobaño, C. *et al.* Concentration and avidity of antibodies to different circumsporozoite epitopes correlate with RTS,S/AS01E malaria vaccine efficacy. *Nat Commun* **10**, 2174 (2019).
83. Pallikkuth, S. *et al.* A delayed fractionated dose RTS,S AS01 vaccine regimen mediates protection via improved T follicular helper and B cell responses. *elife* **9**, e51889 (2020).
84. Wines, B. D. *et al.* Dimeric FcγR Ectodomains as Probes of the Fc Receptor Function of Anti-Influenza Virus IgG. *The Journal of Immunology* **197**, 1507–1516 (2016).

85. Vanderven, H. A. & Kent, S. J. The protective potential of Fc-mediated antibody functions against influenza virus and other viral pathogens. *Immunol Cell Biol* **98**, 253–263 (2020).
86. Chaudhury, S. *et al.* The biological function of antibodies induced by the RTS,S/AS01 malaria vaccine candidate is determined by their fine specificity. *Malar J* **15**, 301 (2016).
87. Chaudhury, S. *et al.* Delayed fractional dose regimen of the RTS,S/AS01 malaria vaccine candidate enhances an IgG4 response that inhibits serum opsonophagocytosis. *Sci Rep* **7**, 7998 (2017).
88. Feng, G. *et al.* Mechanisms and targets of Fcγ-receptor mediated immunity to malaria sporozoites. *Nat Commun* **12**, 1742 (2021).
89. Feng, G. *et al.* Induction, decay, and determinants of functional antibodies following vaccination with the RTS,S malaria vaccine in young children. *BMC Med* **20**, 289 (2022).
90. Kurtovic, L. *et al.* Multifunctional Antibodies Are Induced by the RTS,S Malaria Vaccine and Associated With Protection in a Phase 1/2a Trial. *J Infect Dis* **224**, 1138 (2021).
91. Das, J. *et al.* Delayed fractional dosing with RTS,S/AS01 improves humoral immunity to malaria via a balance of polyfunctional NANP6- and Pf16-specific antibodies. *Med* **2**, 1269-1286.e9 (2021).
92. Ockenhouse, C. F. *et al.* Ad35.CS.01 - RTS,S/AS01 Heterologous Prime Boost Vaccine Efficacy against Sporozoite Challenge in Healthy Malaria-Naïve Adults. *PLoS One* **10**, e0131571 (2015).
93. Suscovich, T. J. *et al.* Mapping functional humoral correlates of protection against malaria challenge following RTS,S/AS01 vaccination. *Sci Transl Med* **12**, 4757 (2020).
94. Young, W. C. *et al.* Comprehensive Data Integration Approach to Assess Immune Responses and Correlates of RTS,S/AS01-Mediated Protection From Malaria Infection in Controlled Human Malaria Infection Trials. *Front Big Data* **4**, e672460 (2021).
95. Kurtovic, L. *et al.* Complement in malaria immunity and vaccines. *Immunol Rev* **293**, 38–56 (2020).
96. Dunkelberger, J. R. & Song, W. C. Complement and its role in innate and adaptive immune responses. *Cell Res* **20**, 34–50 (2009).
97. Vandendriessche, S., Cambier, S., Proost, P. & Marques, P. E. Complement Receptors and Their Role in Leukocyte Recruitment and Phagocytosis. *Front Cell Dev Biol* **9**, 624025 (2021).
98. Healer, J. *et al.* Complement-mediated lysis of *Plasmodium falciparum* gametes by malaria-immune human sera is associated with antibodies to the gamete surface antigen Pfs230. *Infect Immun* **65**, 3023 (1997).
99. Coelho, C. H. *et al.* A human monoclonal antibody blocks malaria transmission and defines a highly conserved neutralizing epitope on gametes. *Nat Commun* **12**, 1750 (2021).
100. Kurtovic, L. *et al.* Human antibodies activate complement against *Plasmodium falciparum* sporozoites, and are associated with protection against malaria in children. *BMC Med* **16**, 61 (2018).

101. Kurtovic, L., Drew, D. R., Dent, A. E., Kazura, J. W. & Beeson, J. G. Antibody Targets and Properties for Complement-Fixation Against the Circumsporozoite Protein in Malaria Immunity. *Front Immunol* **12**, 775659 (2021).
102. Kurtovic, L. *et al.* Induction and decay of functional complement-fixing antibodies by the RTS,S malaria vaccine in children, and a negative impact of malaria exposure. *BMC Med* **17**, 45 (2019).
103. Behet, M. C. *et al.* The Complement System Contributes to Functional Antibody-Mediated Responses Induced by Immunization with *Plasmodium falciparum* Malaria Sporozoites. *Infect Immun* **86**, e00920-17 (2018).
104. Persson, C. *et al.* Cutting Edge: A New Tool to Evaluate Human Pre-Erythrocytic Malaria Vaccines: Rodent Parasites Bearing a Hybrid *Plasmodium falciparum* Circumsporozoite Protein. *J Immunol* **169**, 6681–6685 (2002).
105. Flores-Garcia, Y. *et al.* Optimization of an in vivo model to study immunity to *Plasmodium falciparum* pre-erythrocytic stages. *Malar J* **18**, 426 (2019).
106. Pholcharee, T. *et al.* Structural and biophysical correlation of anti-NANP antibodies with in vivo protection against *P. falciparum*. *Nat Commun* **12**, 1063 (2021).
107. Tan, J. *et al.* A public antibody lineage that potently inhibits malaria infection through dual binding to the circumsporozoite protein. *Nat Med* **24**, 401–407 (2018).
108. Oyen, D. *et al.* Structural basis for antibody recognition of the NANP repeats in *Plasmodium falciparum* circumsporozoite protein. *Proc Natl Acad Sci* **114**, E10438–E10445 (2017).
109. Oyen, D. *et al.* Cryo-EM structure of *P. falciparum* circumsporozoite protein with a vaccine-elicited antibody is stabilized by somatically mutated inter-Fab contacts. *Sci Adv* **4**, 8529 (2018).
110. Martin, G. M. *et al.* Affinity-matured homotypic interactions induce spectrum of PfCSP-antibody structures that influence protection from malaria infection. *bioRxiv* 2022.09.20.508747 (2022) doi:10.1101/2022.09.20.508747.
111. Kucharska, I. *et al.* High-density binding to *Plasmodium falciparum* circumsporozoite protein repeats by inhibitory antibody elicited in mouse with human immunoglobulin repertoire. *PLoS Pathog* **18**, e1010999 (2022).
112. Imkeller, K. *et al.* Antihomotypic affinity maturation improves human B cell responses against a repetitive epitope. *Science* **360**, 1358–1362 (2018).
113. Kucharska, I. *et al.* Structural basis of *Plasmodium vivax* inhibition by antibodies binding to the circumsporozoite protein repeats. *eLife* **11**, e72908 (2022).
114. Fisher, C. R. *et al.* T-dependent B cell responses to *Plasmodium* induce antibodies that form a high-avidity multivalent complex with the circumsporozoite protein. *PLoS Pathog* **13**, e1006469 (2017).
115. Chatterjee, D. & Cockburn, I. A. The challenges of a circumsporozoite protein-based malaria vaccine. *Expert Rev Vaccines* **20**, 113–125 (2021).
116. Burton, D. R. A new lease on life for an HIV-neutralizing antibody class and vaccine target. *Proc Natl Acad Sci U S A* **118**, e2026390118 (2021).
117. Chatterjee, D. *et al.* Avid binding by B cells to the *Plasmodium* circumsporozoite protein repeat suppresses responses to protective subdominant epitopes. *Cell Rep* **35**, 108996 (2021).

118. Adams, J. & Tucker, R. The Thrombospondin Type 1 Repeat (TSR) Superfamily: Diverse Proteins With Related Roles in Neuronal Development. **218**, 280–299 (2000).
119. White, M. T. *et al.* The Relationship between RTS,S Vaccine-Induced Antibodies, CD4+ T Cell Responses and Protection against *Plasmodium falciparum* Infection. *PLoS One* **8**, e61395 (2013).
120. Noe, A. R. *et al.* Bridging Computational Vaccinology and Vaccine Development Through Systematic Identification, Characterization, and Downselection of Conserved and Variable Circumsporozoite Protein CD4 T Cell Epitopes From Diverse *Plasmodium falciparum* Strains. *Front Immunol* **12**, (2021).
121. Scally, S. W. *et al.* Rare PfCSP C-terminal antibodies induced by live sporozoite vaccination are ineffective against malaria infection. *J Exp Med* **215**, 63 (2018).
122. Wang, L. T. *et al.* Protective effects of combining monoclonal antibodies and vaccines against the *Plasmodium falciparum* circumsporozoite protein. *PLoS Pathog* **17**, e1010133 (2021).
123. Beutler, N. *et al.* A novel CSP C-terminal epitope targeted by an antibody with protective activity against *Plasmodium falciparum*. *PLoS Pathog* **18**, e1010409 (2022).
124. Kisalu, N. K. *et al.* A human monoclonal antibody prevents malaria infection and defines a new site of vulnerability on *Plasmodium falciparum* circumsporozoite protein. *Nat Med* **24**, 408 (2018).
125. Wang, L. T. *et al.* A potent anti-malarial human monoclonal antibody targets circumsporozoite protein minor repeats and neutralizes sporozoites in the liver. *Immunity* **53**, 733 (2020).
126. Wu, R. L. *et al.* Low-Dose Subcutaneous or Intravenous Monoclonal Antibody to Prevent Malaria. *N Engl J Med* **387**, 397–407 (2022).
127. Oyen, D. *et al.* Structure and mechanism of monoclonal antibody binding to the junctional epitope of *Plasmodium falciparum* circumsporozoite protein. *PLoS Pathog* **16**, e1008373 (2020).
128. Flores-Garcia, Y. *et al.* The P. falciparum CSP repeat region contains three distinct epitopes required for protection by antibodies in vivo. *PLoS Pathog* **17**, e1010042 (2021).
129. Martin, G. M. *et al.* Structural basis of epitope selectivity and potent protection from malaria by PfCSP antibody L9. *bioRxiv* (2022) doi:10.1101/2022.10.07.511358.
130. Rathore, D. *et al.* An Immunologically Cryptic Epitope of *Plasmodium falciparum* Circumsporozoite Protein Facilitates Liver Cell Recognition and Induces Protective Antibodies That Block Liver Cell Invasion. *J Biol Chem* **280**, 20524–20529 (2005).
131. Espinosa, D. A. *et al.* Proteolytic Cleavage of the *Plasmodium falciparum* Circumsporozoite Protein Is a Target of Protective Antibodies. *J Infect Dis* **212**, 1111–1119 (2015).
132. Thai, E. *et al.* A high-affinity antibody against the CSP N-terminal domain lacks *Plasmodium falciparum* inhibitory activity. *J Exp Med* **217**, e20200061 (2020).
133. Tan, J. *et al.* Functional human IgA targets a conserved site on malaria sporozoites. *Sci Transl Med* **13**, eabg2344 (2021).

134. Pegu, A. *et al.* Neutralizing antibodies to HIV-1 envelope protect more effectively in vivo than those to the CD4 receptor. *Sci Transl Med* **6**, 243ra88 (2014).
135. Zhou, P. *et al.* Broadly neutralizing anti-S2 antibodies protect against all three human betacoronaviruses that cause severe disease. *bioRxiv* e479488 (2022) doi:10.1101/2022.03.04.479488.
136. Bangaru, S. *et al.* A Site of Vulnerability on the Influenza Virus Hemagglutinin Head Domain Trimer Interface. *Cell* **177**, 1136-1152.e18 (2019).
137. Nahrendorf, W., Scholzen, A., Sauerwein, R. W. & Langhorne, J. Cross-stage immunity for malaria vaccine development. *Vaccine* **33**, 7513–7517 (2015).
138. Yamauchi Lucy M., L. M., Coppi, A., Snounou, G. & Sinnis, P. *Plasmodium* sporozoites trickle out of the injection site. *Cell Microbiol* **9**, 1215–1222 (2007).
139. Gilson, P. R. & Crabb, B. S. Morphology and kinetics of the three distinct phases of red blood cell invasion by *Plasmodium falciparum* merozoites. *Int J Parasitol* **39**, 91–96 (2009).
140. Popovici, J. *et al.* Amplification of Duffy binding protein-encoding gene allows *Plasmodium vivax* to evade host anti-DBP humoral immunity. *Nat Commun* **11**, a953 (2020).
141. Robinson, L. J. *et al.* Strategies for Understanding and Reducing the *Plasmodium vivax* and *Plasmodium ovale* Hypnozoite Reservoir in Papua New Guinean Children: A Randomised Placebo-Controlled Trial and Mathematical Model. *PLoS Med* **12**, e1001891 (2015).
142. Kumar, R., Agarwal, D. & Kumar, P. Severe *Plasmodium vivax* Malaria in Children: An emerging threat. *J Pediat Sci* **6**, (2014).
143. Naha, K., Dasari, S. & Prabhu, M. Spectrum of complications associated with *Plasmodium vivax* infection in a tertiary hospital in South–Western India. *Asian Pac J Trop Med* **5**, 79–82 (2012).
144. Tournamille, C. *et al.* Structure–function analysis of the extracellular domains of the Duffy antigen/receptor for chemokines: characterization of antibody and chemokine binding sites. *Br J Haematol* **122**, 1014–1023 (2003).
145. Langhi, D. M. & Bordin, J. O. Duffy blood group and malaria. Hematology **11**, 389–398 (2006).
146. Miller, L. H., Mason, S. J., Dvorak, J. A., McGinniss, M. H. & Rothman, I. K. Erythrocyte Receptors for (*Plasmodium Knowlesi*) Malaria: Duffy Blood Group Determinants. *Science* **189**, 561–563 (1975).
147. Miller, L. H., Mason, S. J., Clyde, D. F. & McGinniss, M. H. The Resistance Factor to *Plasmodium vivax* in Blacks. *N Engl J Med* **295**, 302–304 (1976).
148. Howes, R. E. *et al.* The global distribution of the Duffy blood group. *Nat Commun* **2**, a1265 (2011).
149. Cavasini, C. E. *et al.* Duffy blood group gene polymorphisms among malaria *vivax* patients in four areas of the Brazilian Amazon region. *Malar J* **6**, a167 (2007).
150. Li, J., Iwamoto, S., Sugimoto, N., Okuda, H. & Kajii, E. Dinucleotide repeat in the 3' flanking region provides a clue to the molecular evolution of the Duffy gene. *Hum Genet* **99**, 573–577 (1997).
151. Adams, J. H. *et al.* A family of erythrocyte binding proteins of malaria parasites. *Proc Natl Acad Sci* **89**, 7085–7089 (1992).

152. Adams, J. H. *et al.* The duffy receptor family of *Plasmodium knowlesi* is located within the micronemes of invasive malaria merozoites. *Cell* **63**, 141–153 (1990).
153. Chitnis, C. E. & Miller, L. H. Identification of the erythrocyte binding domains of *Plasmodium vivax* and *Plasmodium knowlesi* proteins involved in erythrocyte invasion. *J Exp Med* **180**, 497–506 (1994).
154. Choe, H. *et al.* Sulphated tyrosines mediate association of chemokines and *Plasmodium vivax* Duffy binding protein with the Duffy antigen/receptor for chemokines (DARC). *Mol Microbiol* **55**, 1413–1422 (2005).
155. Ménard, D. *et al. Plasmodium vivax* clinical malaria is commonly observed in Duffy-negative Malagasy people. *Proc Natl Acad Sci* **107**, 5967–5971 (2010).
156. Golassa, L., Amenga-Etego, L., Lo, E. & Amambua-Ngwa, A. The biology of unconventional invasion of Duffy-negative reticulocytes by *Plasmodium vivax* and its implication in malaria epidemiology and public health. *Malar J* **19**, 299 (2020).
157. Menard, D. *et al.* Whole Genome Sequencing of Field Isolates Reveals a Common Duplication of the Duffy Binding Protein Gene in Malagasy *Plasmodium vivax* Strains. *PLoS Negl Trop Dis* **7**, e2489 (2013).
158. Ntumngia, F. B. *et al.* A novel erythrocyte binding protein of *Plasmodium vivax* suggests an alternate invasion pathway into duffy-positive reticulocytes. *mBio* **7**, 1261–1277 (2016).
159. Thomson-Luque, R. & Bautista, J. M. Home Sweet Home: *Plasmodium vivax*-Infected Reticulocytes—The Younger the Better? *Front Cell Infect Microbiol* **11**, e675156 (2021).
160. Gruszczyk, J. *et al.* Transferrin receptor 1 is a reticulocyte-specific receptor for *Plasmodium vivax*. *Science* **359**, 48–55 (2018).
161. Bermúdez, M., Moreno-Pérez, D. A., Arévalo-Pinzón, G., Curtidor, H. & Patarroyo, M. A. *Plasmodium vivax in vitro* continuous culture: The spoke in the wheel. *Malar J* **17**, 301 (2018).
162. Ovchynnikova, E. *et al.* DARC extracellular domain remodeling in maturating reticulocytes explains *Plasmodium vivax* tropism. *Blood* **130**, 1441–1444 (2017).
163. Singh, S. K., Hora, R., Belrhali, H., Chitnis, C. E. & Sharma, A. Structural basis for Duffy recognition by the malaria parasite Duffy-binding-like domain. *Nature* **439**, 741–744 (2005).
164. Batchelor, J. D., Zahm, J. A. & Tolia, N. H. Dimerization of *Plasmodium vivax* DBP is induced upon receptor binding and drives recognition of DARC. *Nat Struct Mol Biol* **18**, 908–914 (2011).
165. Batchelor, J. D. *et al.* Red Blood Cell Invasion by *Plasmodium vivax*: Structural Basis for DBP Engagement of DARC. *PLoS Pathog* **10**, e1003869 (2014).
166. King, C. L. *et al.* Fya/Fyb antigen polymorphism in human erythrocyte duffy antigen affects susceptibility to *Plasmodium vivax* malaria. *Proc Natl Acad Sci* **108**, 20113–20118 (2011).
167. Ampudia, E., Patarroyo, M. A., Patarroyo, M. E. & Murillo, L. A. Genetic polymorphism of the Duffy receptor binding domain of *Plasmodium vivax* in Colombian wild isolates. *Mol Biochem Parasitol* **78**, 269–272 (1996).
168. Tsuboi,', T. *et al.* Natural variation within the principal adhesion domain of the Plasmodium vivax duffy binding protein. *Infect Immun* **62**, 5581–5586 (1994).

169. Cole-Tobian, J. L. *et al.* Age-Acquired Immunity to a *Plasmodium vivax* Invasion Ligand, the Duffy Binding Protein. *J Infect Dis* **186**, 531–539 (2002).
170. Xainli, J. *et al.* Age-Dependent Cellular Immune Responses to *Plasmodium vivax* Duffy Binding Protein in Humans. *J Immunol* **169**, 3200–3207 (2002).
171. Xainli, J. *et al.* Epitope-Specific Humoral Immunity to *Plasmodium vivax* Duffy Binding Protein. *Infect Immun* **71**, 2515 (2003).
172. Valizadeh, V., Zakeri, S., Mehrizi, A. A., Mirkazemi, S. & Djadid, N. D. Natural acquired inhibitory antibodies to *Plasmodium vivax* Duffy binding protein (PvDBP-II) equally block erythrocyte binding of homologous and heterologous expressed PvDBP-II on the surface of COS-7 cells. *Med Microbiol Immunol* **205**, 85–95 (2016).
173. King, C. L. *et al.* Naturally acquired Duffy-binding protein-specific binding inhibitory antibodies confer protection from blood-stage *Plasmodium vivax* infection. *Proc Natl Acad Sci* **105**, 8363–8368 (2008).
174. Nicolete, V. C., Frischmann, S., Barbosa, S., King, C. L. & Ferreira, M. U. Naturally Acquired Binding-Inhibitory Antibodies to *Plasmodium vivax* Duffy Binding Protein and Clinical Immunity to Malaria in Rural Amazonians. *J Infect Dis* **214**, 1539–1546 (2016).
175. Souza-Silva, F. A. *et al.* Duffy Antigen Receptor for Chemokine (DARC) Polymorphisms and Its Involvement in Acquisition of Inhibitory Anti-Duffy Binding Protein II (DBPII) Immunity. *PLoS One* **9**, e93782 (2014).
176. Michon, P., Fraser, T. & Adams, J. H. Naturally acquired and vaccine-elicited antibodies block erythrocyte cytoadherence of the *Plasmodium vivax* Duffy binding protein. *Infect Immun* **68**, 3164–3171 (2000).
177. Ceravolo, I. P. *et al.* Naturally acquired inhibitory antibodies to *Plasmodium vivax* Duffy binding protein are short-lived and allele-specific following a single malaria infection. *Clin Exp Immunol* **156**, 502–510 (2009).
178. Grimberg, B. T. *et al. Plasmodium vivax* Invasion of Human Erythrocytes Inhibited by Antibodies Directed against the Duffy Binding Protein. *PLoS Med* **4**, 1940–1948 (2007).
179. VanBuskirk, K. M. *et al.* Antigenic drift in the ligand domain of *Plasmodium vivax* duffy binding protein confers resistance to inhibitory antibodies. *J Infect Dis* **190**, 1556–1562 (2004).
180. Chootong, P. *et al.* Mapping Epitopes of the *Plasmodium vivax* Duffy Binding Protein with Naturally Acquired Inhibitory Antibodies. *Infect Immun* **78**, 1095 (2010).
181. Ntumngia, F. B. & Adams, J. H. Design and immunogenicity of a novel synthetic antigen based on the ligand domain of the *Plasmodium vivax* Duffy binding protein. *Clin Vaccine Immunol* **19**, 30–36 (2012).
182. Ntumngia, F. B. *et al.* Immunogenicity of single versus mixed allele vaccines of *Plasmodium vivax* Duffy binding protein region II. *Vaccine* **31**, 4382–4388 (2013).
183. Ntumngia, F. B. *et al.* Immunogenicity of a synthetic vaccine based on *Plasmodium vivax* Duffy binding protein region II. *Clin Vaccine Immunol* **21**, 1215–1223 (2014).
184. Chen, E., Salinas, N. D., Ntumngia, F. B., Adams, J. H. & Tolia, N. H. Structural Analysis of the Synthetic Duffy Binding Protein (DBP) Antigen DEKnull Relevant

for *Plasmodium vivax* Malaria Vaccine Design. *PLoS Negl Trop Dis* **9**, e0003644 (2015).
185. Ntumngia, F. B. *et al.* An engineered vaccine of the *Plasmodium vivax* Duffy binding protein enhances induction of broadly neutralizing antibodies. *Sci Rep 2017* **7**, 13779 (2017).
186. Sampath, S. *et al.* Glycan Masking of *Plasmodium vivax* Duffy Binding Protein for Probing Protein Binding Function and Vaccine Development. *PLoS Pathog* **9**, e1003420 (2013).
187. Payne, R. O. *et al.* Human vaccination against *Plasmodium vivax* Duffy-binding protein induces strain-transcending antibodies. *JCI Insight* **2**, e93683 (2017).
188. Singh, K. *et al.* Malaria vaccine candidate based on Duffy-binding protein elicits strain transcending functional antibodies in a Phase I trial. *NPJ Vaccines* **3**, 48 (2018).
189. Moreno, A. *et al.* Preclinical assessment of the receptor-binding domain of *Plasmodium vivax* Duffy-binding protein as a vaccine candidate in rhesus macaques. *Vaccine* **26**, 4338–4344 (2008).
190. Ntumngia, F. B. *et al.* Conserved and variant epitopes of *Plasmodium vivax* duffy binding protein as targets of inhibitory monoclonal antibodies. *Infect Immun* **80**, 1203–1208 (2012).
191. Chen, E. *et al.* Broadly neutralizing epitopes in the *Plasmodium vivax* vaccine candidate Duffy Binding Protein. *Proc Natl Acad Sci* **113**, 6277–6282 (2016).
192. Carias, L. L. *et al.* Identification and Characterization of Functional Human Monoclonal Antibodies to *Plasmodium vivax* Duffy-Binding Protein. *J Immunol* **202**, 2648–2660 (2019).
193. Urusova, D. *et al.* Structural basis for neutralization of *Plasmodium vivax* by naturally acquired human antibodies that target DBP. *Nat Microbiol* **4**, 1486–1496 (2019).
194. Rawlinson, T. A. *et al.* Structural basis for inhibition of *Plasmodium vivax* invasion by a broadly neutralizing vaccine-induced human antibody. *Nat Microbiol* **4**, 1497–1507 (2019).
195. Mohring, F. *et al.* Rapid and iterative genome editing in the malaria parasite *Plasmodium knowlesi* provides new tools for *P. vivax* research. *eLife* **8**, e45829 (2019).
196. Moskovitz, R. & Pholcharee, T., *et al*. Structural basis for DARC binding in reticulocyte invasion by Plasmodium vivax. *Nat Comms **14***, 3637 (2023).

CHAPTER 2:

Structural Insights on Novel Epitopes of the Plasmodium falciparum Circumsporozoite Protein N-Terminal Domain

2.0 Abstract

The N-terminal domain of the *Plasmodium falciparum* circumsporozoite protein is the locus of most known functionalities required for migration and invasion in the mammalian host. However, due to its perceived lack of immunogenicity, only a few monoclonal antibodies have been characterized to bind the domain, and it has been excluded from most immunogen designs. Using monoclonal antibodies 3A3 and 3F4 isolated from a human antibody phage display library, we reveal the structural basis for binding of to the lysine rich region of the CSP N-terminus by 3F4, and binding to a new epitope by 3A3, using germline encoded residues. From a panel of monoclonal antibodies isolated from mouse immunization we show the structural mechanism of binding of four monoclonal antibodies to the CSP N-terminus, mNCSP6 targeting the lysine-rich sequence targeted by 3F4, mNCSP9 and 10 binding the new epitope bound by 3A3, and mNCSP13 binding a second new epitope. mNCSP2, 6, 9 and 10 show significant protection in the mouse liver burden assay. Using a yeast display library, 3A3 was affinity matured to achieve sub-nanomolar binding, demonstrating that the human antibody repertoire has the capacity to produce high affinity monoclonal antibodies targeting conserved and protective epitopes on the CSP N-terminal domain.

2.1 Introduction

2.1.1 The N-terminal domain of CSP is important for parasite motility and invasion

The circumsporozoite protein of *Plasmodium falciparum* is the main antigen target for a vaccine targeting the liver-stage of the malaria infection (1,2). Efforts to characterise the specific domain function of CSP have revealed the N-terminal domain of CSP (NtCSP) as the site of most currently known CSP functionalities relevant to mammalian infection (3–8). Mutagenesis studies have shown a series of lysine residues of NtCSP are key in heparin binding (3,4). While the first six amino acids of NtCSP do not affect recombinant NtCSP binding to heparin, they are required for binding of NtCSP to HepG2 hepatocytes *in vitro* (4), providing additional molecular determinants for parasite tropism. Antibodies raised against NtCSP bind midgut sporozoites but not salivary gland sporozoites, suggesting that the circumsporozoite protein on the parasite surface undergoes conformational changes that mask NtCSP(9). Furthermore, the highly conserved KLKQP sequence at the junction between NtCSP and the central repeat domain, known as Region I (RI), is the site of CSP cleavage (10), which is observed in the switch between a migratory and invasive phenotype(5,11). This cleavage is triggered by heparan sulphate proteoglycans on hepatocyte surface and is inhibited by a specific inhibitor of cysteine protease E-64 (5). Parasites expressing cleaved CSP can establish infection following intravascular injection but fail to leave the injection site if injected intradermally, thereby implicating NtCSP in the migration process from the dermis injection site to the liver following a mosquito bite (8).

2.1.2 The PfCSP N-terminal domain is a target of monoclonal antibodies

Due to the proteolytic shedding of NtCSP and its perceived low immunogenicity, it has been excluded from most CSP-based vaccine designs including leading vaccine candidate RTS,S, in favour of the highly immunogenic major repeat epitope(12,13). However, recent work investigating the murine naïve B-cell response to CSP has shown that the immunodominance of the major repeat domain decreases activation of CtCSP and NtCSP specific B-cells (14). The authors further demonstrate that immunization with reduced valency CSP produce robust protection while inducing antibodies against subdominant epitopes. Previous mouse immunization studies with NtCSP peptide produced antisera inhibitory in hepatocyte invasion assay, with robust antibody response mapped to the lysine-rich region upstream of RI (15).

Contradictory observations regarding the protective nature of this epitope have risen by the structural characterization of murine monoclonal antibody 5D5(16,17). Initial characterization of 5D5 has shown it capable of inhibiting CSP cleavage in metabolic pulse chase experiments, as well as providing protection from an *in vivo* mouse sporozoite challenge (16). In the X-ray crystal structure of 5D5 bound to its peptide epitope, the antibody was shown to bind the $_{81}$EDNEKLRKPKHK$_{92}$ lysine-rich peptide upstream of RI using charge complementarity relying on glycosylation of antibody heavy chain residue Asn98 (17). In this study, however, 5D5 failed to inhibit sporozoite traversal and did not provide protection from *in vivo* intravenous sporozoite challenge in mice. The human monoclonal IgA antibody MAD2-6, isolated from whole sporozoite

immunization, was also mapped onto the lysine-rich region upstream of RI (18). The X-ray crystal structure of MAD2-6 with its target peptide unexpectedly revealed two Fab fragments bound on opposite sides of a single $_{89}$KPKHKKLKQ$_{97}$ peptide. Passive transfer of MAD2-6 IgA provides significant protection in mice, while 5D5 fails to do the same.

Previous structural characterizations of monoclonal antibodies from sporozoite immunization have revealed the highly protective minor repeat and junctional epitopes downstream of RI, reasserting that CSP possessed protective epitopes outside of the major repeat region (19–21). The X-ray crystal structures of MAD2-6 and 5D5 have revealed two different mechanisms of engaging an overlapping N-terminal epitope. However, it is unclear whether other epitopes presented by NtCSP can be successfully engaged by either murine or human monoclonal antibodies to provide protection. Here, the structural basis of NtCSP binding by six human and mouse monoclonal antibodies is elucidated and demonstrates two novel epitopes on NtCSP. Drawing from a malaria-naïve human antibody phage display library, it is shown that this human antibody repertoire possesses sequences that bind several epitopes on NtCSP through germline-encoded residues, and that murine antibodies targeting these epitopes provide protective efficacy in mice.

2.2 Results

2.2.1 Antibody Sources and Epitope Mapping

To investigate the scope of epitopes presented by NtCSP, monoclonal antibodies were obtained from two different sources. To probe the capacity of the human antibody repertoire to produce monoclonal antibodies which bind CSP, our collaborator Ding Zhang in the Lerner Lab isolated a panel of human antibody sequences from a human antibody phage display library, which was assumed to be malaria-naïve (22,23). Eleven heavy-light chain pairs were found to bind recombinant short CSP (rsCSP). Four monoclonal antibodies were successfully expressed as Fab fragments and bound NtCSP**.** To determine whether the murine antibody repertoire is capable of high-affinity antibodies targeting NtCSP, our collaborators in the Burton lab (TSRI) immunized mice with NtCSP residues Tyr26-Gly100 (NF54, 3D7 isolate) fused to keyhole limpet haemocyanin (KLH). Seven mAbs targeting NtCSP were isolated by Nathan Beutler (Thomas Rogers UCSD/TSRI and Dennis Burton TSRI). The sequences of the human and mouse mAb CDRs and lineages are shown in Kabat numbering in **Figure 2.1.**

To map the specific NtCSP epitope bound by both murine and human mAbs, a panel of fourteen overlapping peptides spanning NtCSP Tyr26-Asn105 were synthesized. Antibody binding to the panel of peptides was assessed by bio-layer interferometry, and the results tabulated according to the peptides with highest binding **(Figure 2.2)**. Human monoclonal 3F4 and murine mNCSP6 bound peptides in the lysine-rich region upstream of RI corresponding to CSP residues Glu81-Gly100 and Leu86-Asn105, respectively. While these two antibodies bound to the region containing epitopes of previously

characterized 5D5 and MAD2-6, the remainder of antibodies bound novel NtCSP epitopes. 3H2 bound CSP Asp41-Glu60, 3H11 bound Leu51-Arg70, and 3A3 binding Tyr56-Asn75. Surprisingly, the murine antibodies mNCSP9 and mNCSP10 bound in the same region. The remaining murine mAbs bound to the N-terminal residues Tyr26-Thr45, thereby identifying a second novel epitope.

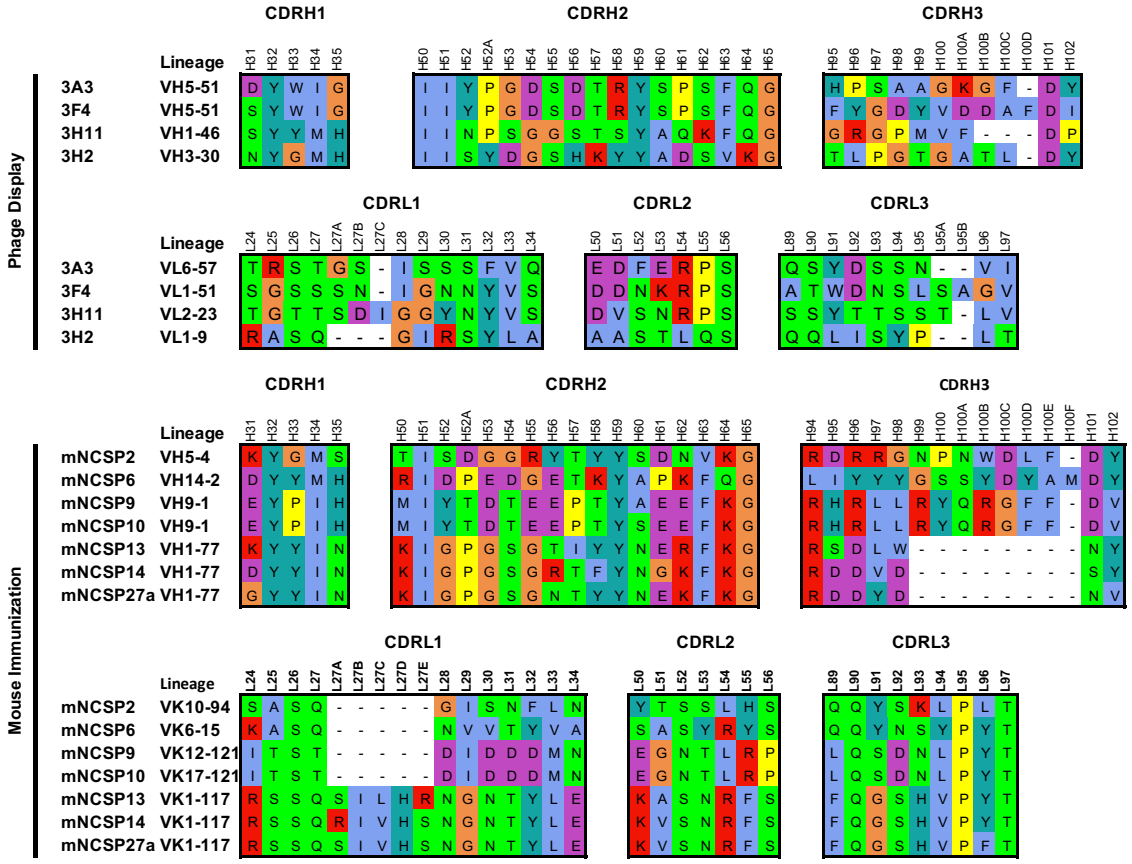


Figure 2.1. Antibody lineages and complementarity defining region sequences of murine and human mAbs that bind NtCSP. Antibody VH and VL lineages are shown alongside CDR sequences as determined and aligned by AbYsis in clustal X default coloring. Hydrophobic (blue), positively charged (red), negatively charged (magenta) polar (green), aromatic (cyan), glycine (orange), proline (yellow), and cysteine (pink), white (unconserved, gaps).

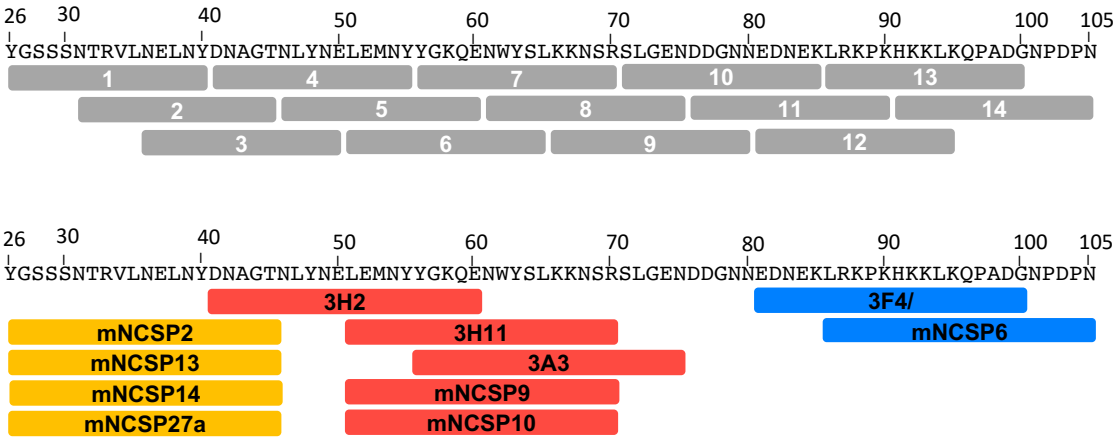


Figure 2.2. Epitope mapping of human and murine monoclonal antibody binding to NtCSP.

(A) Peptide panel designed for mapping the epitopes of monoclonal antibodies shown to bind NtCSP. The amino acid sequence of NtCSP residues 26-105 is shown, with overlapping 15-amino acid peptides numbered 1-14 in grey. (B) Epitope mapping results of NtCSP binding antibodies. mAb 4F3 binds to peptides 12-13 and mNCSP6 binds peptides 13-14 in the lysine-rich region upstream of RI (blue). mAb 3H2 binds peptides 4-5, 3A3 binds peptides 7-8, and 3H11, mNCSP9, and mNCSP10 bind peptides 6-7, defining a new epitope at center of NtCSP (red). mAbs mNCSP2, mNCSP13, mNCSP14, and mNCSP27 bind peptides 1-2, defining a second new epitope (yellow).

2.2.2 Determination of Antibody Epitopes by X-ray Crystallography

The termination of antibody epitopes by X-ray crystallography has become a valuable tool in vaccinology. Through mapping specific interactions required for binding across multiple antibodies, common binding determinants can be identified. The fine specificity of epitopes targeted by antibodies can then be used to guide future vaccine design and inform potential mechanism of action of said antibodies as therapeutics. Following standard lab protocols, the direct expression of antibodies as Fabs allows for rapid purification without the need for overnight enzymatic cleavage. Fabs were first purified by protein G affinity chromatography and further purified through size exclusion chromatography. Fractions corresponding to monomeric Fab peaks were pooled and concentrated for crystallization screens and set up with 5-fold molar excess of peptide. Due to the relatively well-ordered nature of Fab immunoglobulin domains as well as introducing mutations to the light chain (24) to further facilitate crystallization, crystals grew in many crystallization conditions. Datasets collected from crystals that diffracted to high resolution were then phased using molecular replacement with separate search models of Fab variable and constant domains. To avoid over-interpretation of the data, Fabs were manually refined, and missing electron density used to build the bound peptide backbone into the structure. In all cases detailed below, the resolution of the data produced clear electron density to show the side-chains of residues involved in all mentioned specific interactions. Altogether, the X-ray crystal structures of 3F4, 3A3, mNCSP6, mNCSP9, mNCSP10, and mNCSP13 were determined in complex with their respective peptide epitopes **(Crystallography data tables 2.1 and 2.2)** and a summary of the epitopes is provided in **Figure 2.3.**

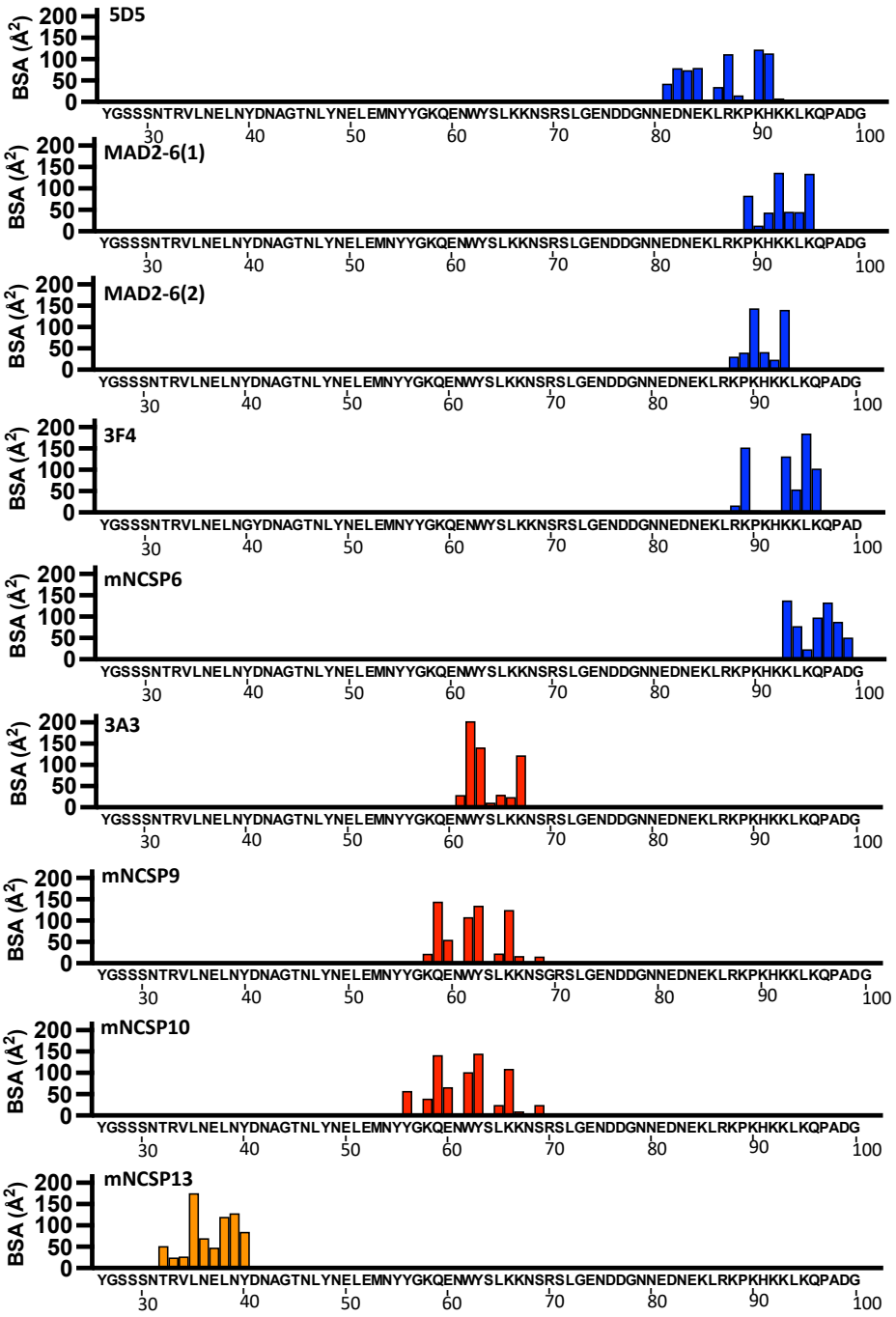


Figure 2.3. Buried surface area formed by antibody binding to NtCSP. Buried surface area formed by binding of 5D5, MAD2-6 Fab1 and Fab2, 3F4, and mNCSP6 to peptides corresponding to RI and the lysine-rich sequence upstream (blue), buried surface area of peptide 7 binding to 3A3, mNCSP9, and mNCSP10 (red), and buried surface area of peptide 1 binding to mNCSP13 (yellow).

2.2.3 Structural Basis for 3F4 Binding to NtCSP

To determine the binding mode and fine specificity of the epitope of 4F3, the X-ray crystal structure of 3F4 Fab in the presence of peptide corresponding to CSP Glu84-Gln96 was determined at 2.37Å resolution. The asymmetric unit cell contained a single Fab with strong electron density for a bound peptide corresponding to CSP Arg87-Gln96. The peptide binds along the groove formed at the heavy-light chain interface, making extensive contacts for a total buried surface area of 600Å^2 **(Figure 2.4A)**. The majority of interactions are contributed by heavy chain residues, which are responsible for over 75% of the buried surface area (464Å^2 out of 600Å^2). A network of interactions formed between peptide Lys88 and CDRH3 Tyr99 anchors the N-terminal region of the peptide **(Figure 2.4B)**; the Lys88 side chain amine participates in a salt-bridge network with the CDRL2 Glu50 and CDRH3 Asp100A and Asp100B carboxyls, while the backbone carbonyl group of Asp100A forms a further hydrogen bond with the Lys88 side chain amine. The nearby CDRH3 Tyr99 interacts with the Lys88 nonpolar aliphatic moiety through its aromatic ring, and coordinates Lys88 backbone carbonyl through its side-chain hydroxyl group. The backbone carbonyl of Lys92 interacts with the CDRH3 Tyr99 backbone amide, while its side chain amine forms a salt bridge with CDRH3 Asp100A. As a result of this network of interactions, the bound peptide wraps around CDRH3 Tyr99, stabilizing a type-I β-turn between Pro89 and Lys92, and contributes to a total 130Å^2 BSA by CDRH3 Tyr99 alone. Anchoring the C-terminal portion of the visible peptide electron density, Lys95 forms salt bridges with CDRH2 Asp54 and Asp56, and the nearby CDRH2 Arg58 coordinates the backbone carbonyl group of Leu94 **(Figure 2.4C)**.

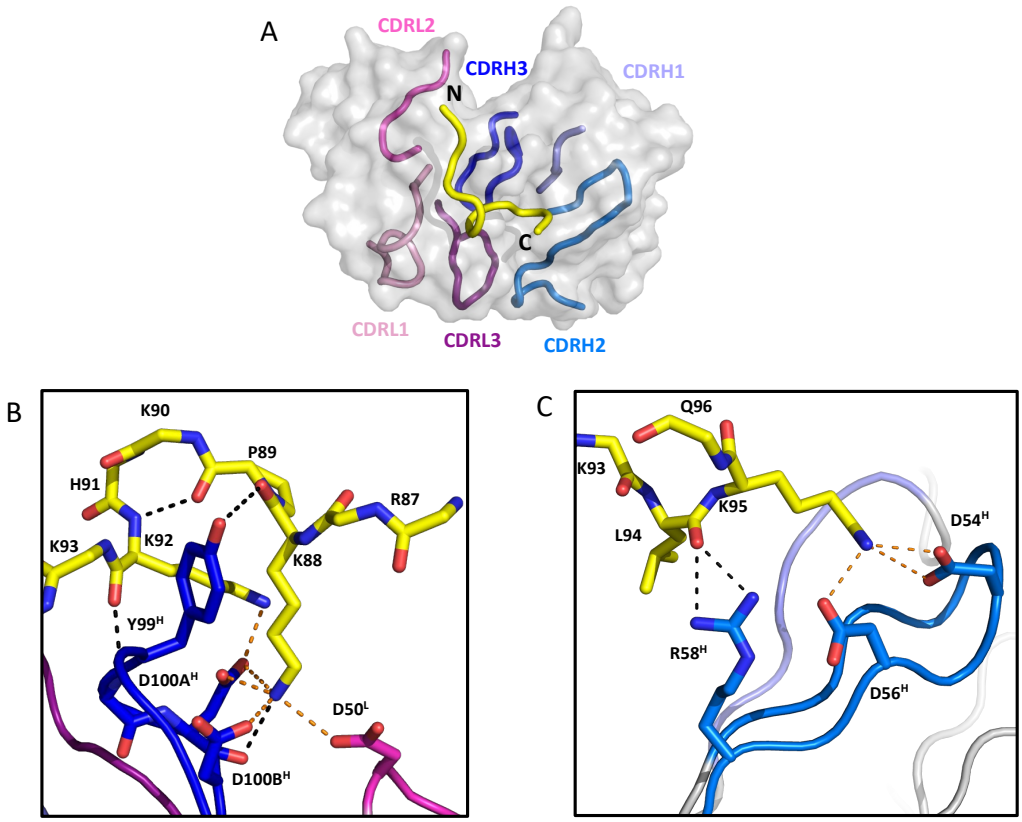


Figure 2.4. Structural basis for 4F3 binding to NtCSP. (A) The NtCSP peptide bound to 3F4 interacts along the interface formed between the heavy and light chains (yellow tube). The surface of 3F4 Fab is shown from a birds-eye view in gray. CDRs are shown in cartoon tube representation in light blue (CDRH1), marine (CDRH2), and dark blue (CDRH3), pink (CDRL1), magenta (CDRL2), and dark purple (CDRH3). (B) Detailed view of the interactions stabilizing Lys88 and peptide binding around CDRH3 Tyr99. (C) Detailed view of Lys95 binding to CDRH2 to anchor the C-terminal region of the bound peptide. The backbone of the bound peptide is shown as yellow sticks colored by atom, backbone of 3F4 is shown in cartoon tube representation, relevant backbone and side chains are shown as sticks. CDRs are colored as in (A), framework residues are in grey. Dashed lines represent hydrogen bonding (black) and salt bridge (orange) interactions.

2.2.4 Structural Basis for 3A3 Binding to NtCSP

To determine the binding epitope of 3A3 to its target N-terminal peptide, the X-ray crystal structure of 3A3 Fab in the presence of peptide 7 was determined at 1.95Å resolution. The asymmetric unit cell contains a single copy of 3A3 Fab with strong electron density for peptide residues corresponding to CSP Asn61-Lys67. The peptide can be seen to bind perpendicular to the groove formed by the heavy-light chain interface, forming a total buried surface area of 520Å^2 **(Figure 2.5A)**. At its N-terminus, peptide residues Asn61-Leu65 form a single helical turn placing Trp62 and Tyr63 in an aromatic pocket formed by both framework and CDR residues from both heavy (Trp 30, Trp33) and light (Tyr 91) chains **(Figure 2.5B).** The backbone carbonyl residues of CDRL3 Asp92 and Ser94 interact with the polar side chains of Tyr63 and Trp62, respectively, further stabilizing their binding in this region, and positioning CDRL3 Tyr91 to form a pi-pi stacking interaction with Tyr63. At the C-terminus of the peptide, Lys67 interacts with CDRH2 Asp54 and Asp56, within distance for Tyr52 to interact with the lysine aliphatic moiety **(Figure 2.5C).**

2.2.5 Germline Gene Usage of 3F4 and 3A3

The X-ray crystal structures of 3A3 and 3F4 demonstrate the potential for malaria-naïve human antibody sequences to interact with multiple NtCSP epitopes. Interestingly, both 3F4 and 3A3 anchor Lys95 and Lys67, respectively, through a network of salt-bridges formed by VH5-51 residues. By virtue of their different light chain lineages, they achieve structural and functional plasticity to bind different NtCSP epitopes. The isolation of these antibodies from a malaria-naïve human antibody library implies that they have not

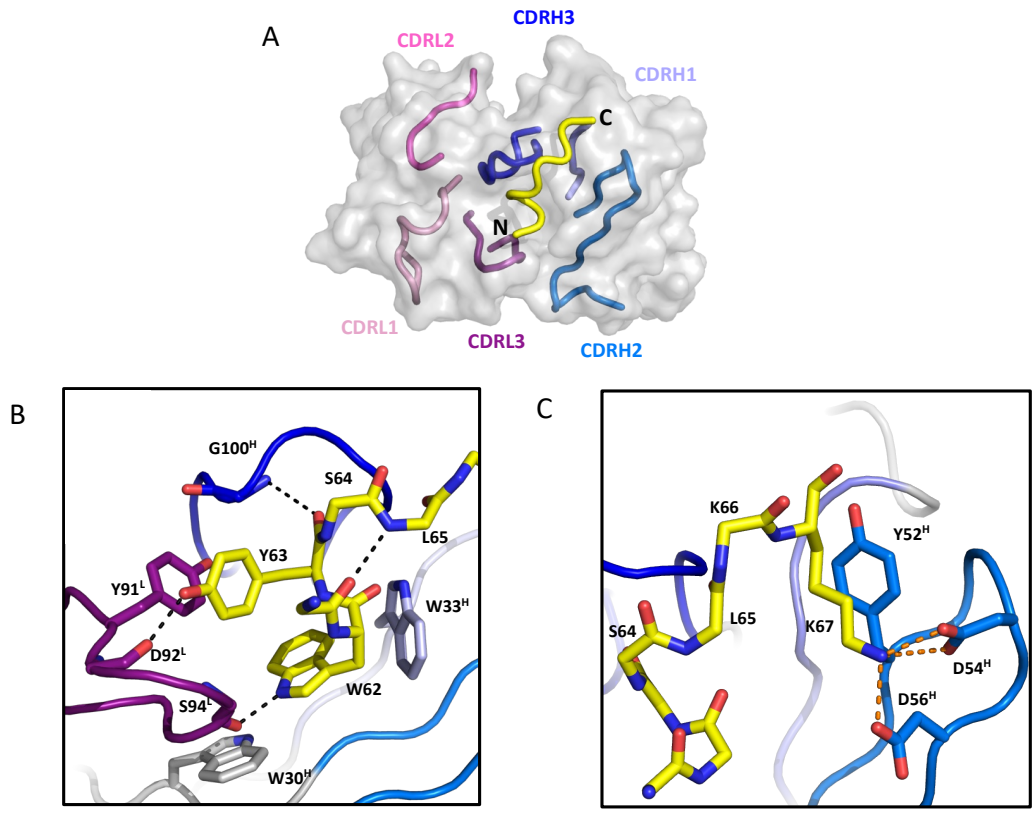


Figure 2.5. Structural basis for 3A3 binding to NtCSP. (A) NtCSP Peptide binds to 3A3 perpendicular to the interface between the light and heavy chain (yellow tube). The surface of 3A3 Fab is shown from a birds-eye view in gray. CDRs are shown in cartoon tube representation in light blue (CDRH1), marine (CDRH2), and dark blue (CDRH3), pink (CDRL1), magenta (CDRL2), and dark purple (CDRH3). (B) Detailed view of interactions formed by Trp62 and Lys63 binding at the N-terminus of the peptide epitope. (C) Detailed view of the salt bridge formed by Lys67 anchoring the C-terminus of the bound peptide to CDRH2. The backbone of the bound peptide is shown as yellow sticks colored by atom, backbone of 3A3 is shown in cartoon tube representation, relevant backbone and side chains are shown as sticks. CDRs are colored as in (A), framework residues are in grey. Dashed lines represent hydrogen bonding (black) and salt bridge (orange) interactions.

undergone affinity maturation directed at *Plasmodium* antigens. Even so, they are not precluded from having undergone somatic hypermutation directed at other antigens. **Figures 2.6** show the sequence alignment of 3F4 and 3A3 with their predicted germline sequences, the BSA formed upon peptide binding, and the involvement of specific polar interactions. Some V-J genes could not be determined by IgBlast. Nevertheless, in the regions for which a germline sequence was available the sequence alignments indicate that SHM do not co-localize to residues identified to mediate binding in the X-ray crystal structures. This would suggest these antibodies have not undergone SHM directed towards these epitopes. The somatic hypermutation of distant residues may still affect CDR conformation and positioning of relevant residues. However, these alignments demonstrate that contacts required for 3F4 and 3A3 binding are produced by germline-encoded residues.

2.2.6 Structural Basis for mNCSP6 Binding to NtCSP

To determine the binding mode of mNCSP6 to its N-terminal CSP epitope, the X-ray crystal structure of humanized mNCSP6 Fab with peptide 13 was solved at a resolution of 2.1Å. A single Fab is present in the asymmetric unit, with clear electron density for eight amino acids of peptide 13 corresponding to mature CSP residues Lys93-Gly100. The peptide can be seen binding perpendicular to the groove formed by the heavy and light chain interface, forming a total buried surface area of 543 $Å^2$**(Figure 2.7A).**

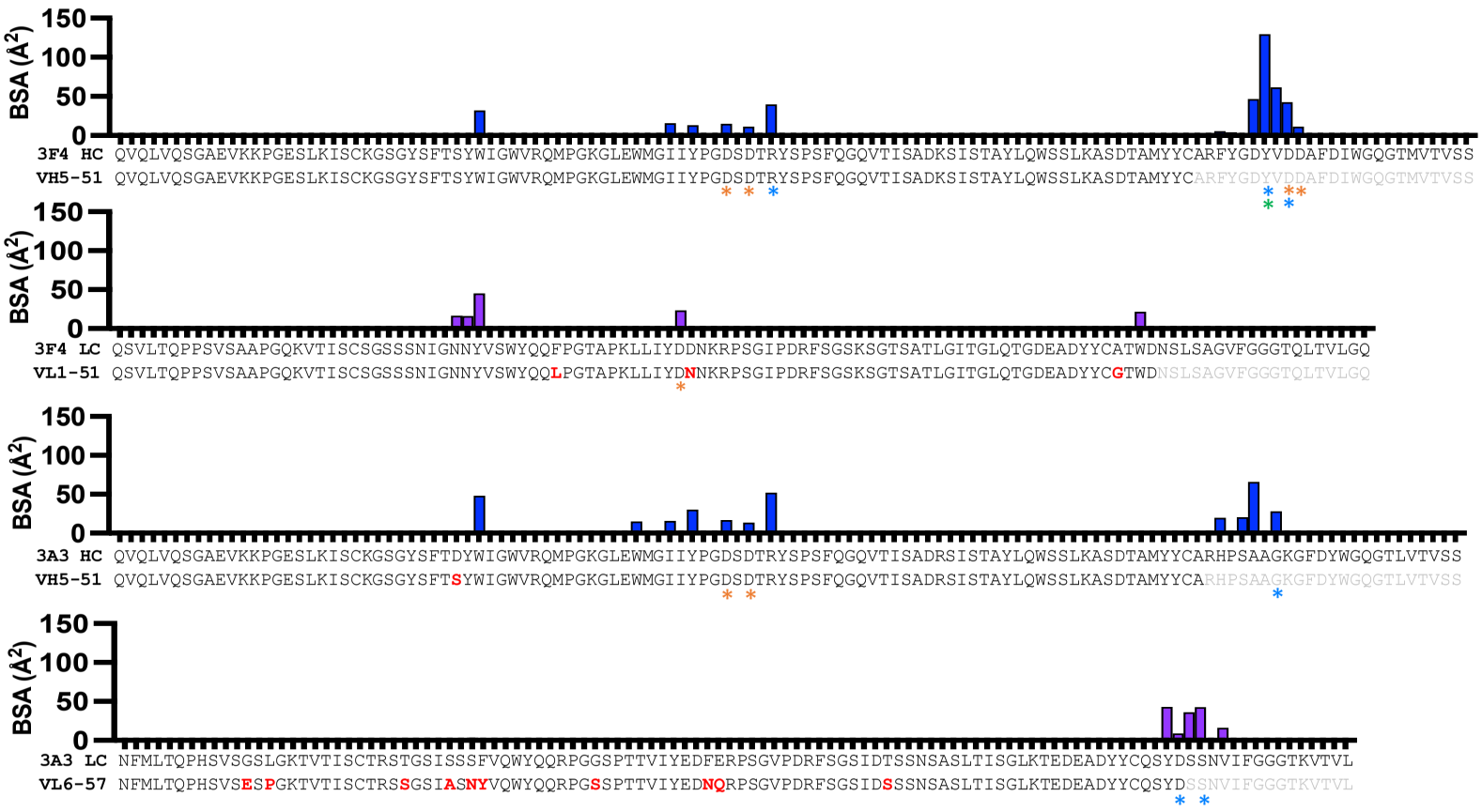


Figure 2.6. Primary contacts mediating binding of 3F4 and 3A3 to NtCSP are germline encoded. Sequences of 3F4 heavy and light chains are shown with a bar chart of buried surface area formed by the peptide interface. Original germline residues that differ from 3F4 sequence are shown underneath in red. Antibody residues binding the NtCSP peptide using backbone interactions in blue asterisks, residues binding peptide via side chain hydrogen bonding in green asterisk, residues binding via side-chain salt bridge in orange asterisks. V-J genes which could not be determined by IgBlast are in gray.

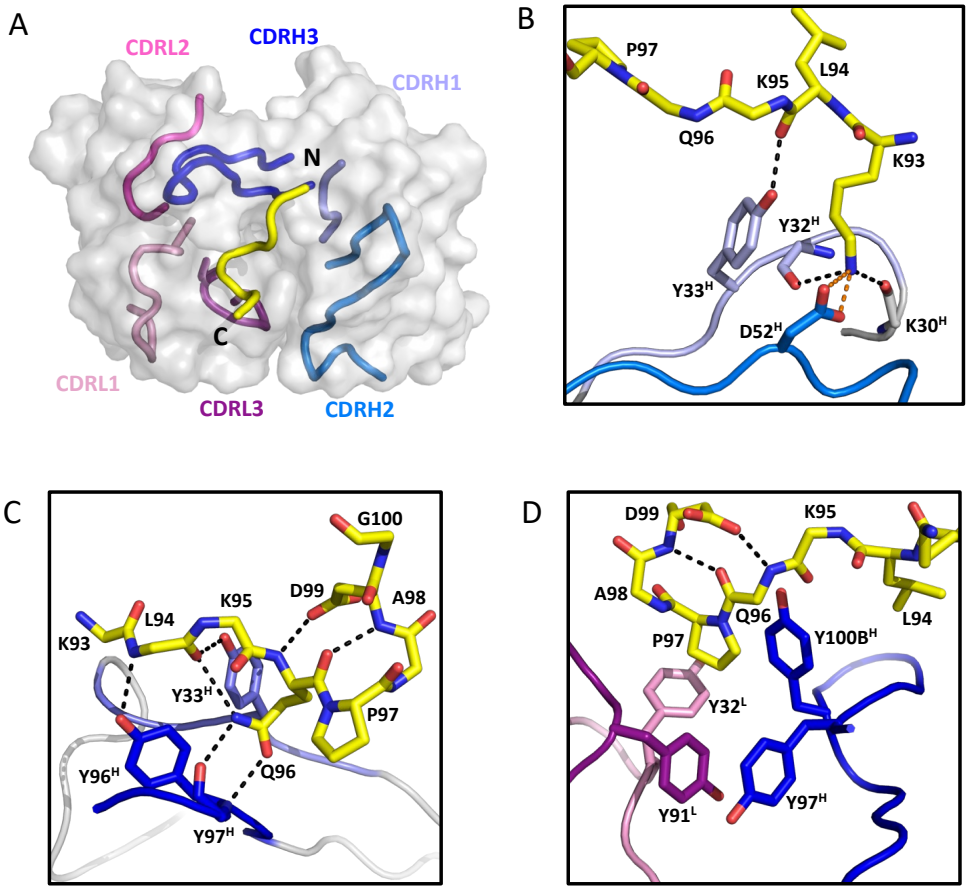


Figure 2.7. Structural basis for mNCSP6 binding to NtCSP. (A) Peptide 13 binds to mNCSP6 oriented perpendicular to the groove formed by the heavy and light chains (yellow tube). The surface of mNCSP6 Fab is shown from a birds-eye view in gray. CDRs are shown in cartoon tube representation in light blue (CDRH1), marine (CDRH2), and dark blue (CDRH3), pink (CDRL1), magenta (CDRL2), and dark purple (CDRH3). (B) Detailed view of interactions stabilizing Lys93. (C) Interactions stabilizing the conformation of bound peptide 13. (D) Peptide Pro72 binding a hydrophobic pocket. The backbone of the bound peptide is shown as yellow sticks colored by atom, backbone of mNCSP6 is shown in cartoon tube representation, relevant backbone and side chains are shown as sticks. CDRs are colored as in (A), framework residues are in grey. Dashed lines represent hydrogen bonding (black) and salt bridge (orange) interactions.

The bound peptide chiefly interacts with the heavy chain, which is responsible for 67% of the buried surface area (363Å^2), forming several networks of specific interactions which contribute to binding. At the N-terminus of the visible peptide electron density, Lys93 is anchored via a salt-bridge with CDRH2 Asp52, and further stabilized by hydrogen-bonding to the backbone carbonyls of nearby heavy chain framework residues Lys30 and CDRH1 Tyr32 **(Figure 2.7B)** (n.b. Kabat numbering for the antibodies are used throughout). The peptide is further stabilized by several backbone interactions; CDRH1 Tyr33 and CDRH3 Y96 hydroxyl groups form hydrogen-bonding interactions with backbone carbonyl groups of K95 and L94, respectively, and peptide Gln96 doubly interacts with CDRH3 Tyr96 backbone carbonyl and amide **(Figure 2.7C).** The C-terminal portion of the peptide is stabilized through multiple intra-peptide secondary structure motifs, with a pseudo 3_{10} turn between Asn96 and Leu94, a type-I β-turn between Gln96 and Asp99, and a further hydrogen bond formed between Asp99 carboxyl and Gln96 backbone amide **(Figure 2.7C and 2.7D).** Reminiscent of previous modes of engagement seen by major repeat peptide antigen, the peptide Pro97 is buried in a hydrophobic pocket formed by CDRH3 Tyr97 and Tyr100B, CDRL1 Tyr32, and CDRL3 Tyr91 **(Figure 2.7D)**.

2.2.7 Structural Basis for hmNCSP9 Binding to NtCSP

Next, the X-ray crystal structure of mNCSP9 humanized Fab in complex with its NtCSP peptide epitope was solved at a resolution of 2.3Å. The asymmetric unit cell contains two Fabs, both bound to peptide 7 with a clear peptide electron density corresponding to CSP residues Tyr56-Ser69. The peptide binds perpendicular to the groove formed by the heavy and light chain and assumes an α-helical conformation from residues Lys58-Ser69, for total buried surface area of 587Å^2 **(Figure 2.8A).** Due to the occupation of the peptide backbone by its α-helical conformation, the binding of mNCSP9 to its peptide antigen relies on specific side-chain interactions at each helical turn. The majority of these interactions are with the mNCSP9 heavy chain, contributing to 80% of the total buried surface area (461 Å^2). In the first helical turn, the Gln59 side-chain amide forms hydrogen bonds with heavy-chain framework Thr30 backbone carbonyl and CDRH2 Thr52A hydroxyl group that is also within interaction distance of the Gln59 side-chain carbonyl group **(Figure 2.8B)**. This network is stabilized by CDRH2 Asp53 coordination of Glu59 backbone amide. One helical turn further down the peptide α-helix, Trp62 indole amide forms hydrogen bonds with backbone carbonyl groups of both CDRH3 Leu98 and Arg102, while Tyr63 hydroxyl is coordinated by CDRH3 His95 and CDRH2 His35 **(Figure 2.8C)**. The last helical turn of the bound peptide is stabilized by formation of salt-bridges between Lys66 and CDRL1 Asp32, and CDRL2 Asp50, and further hydrogen bonding to CDRL3 Ser91 backbone carbonyl **(Figure 2.8D)**.

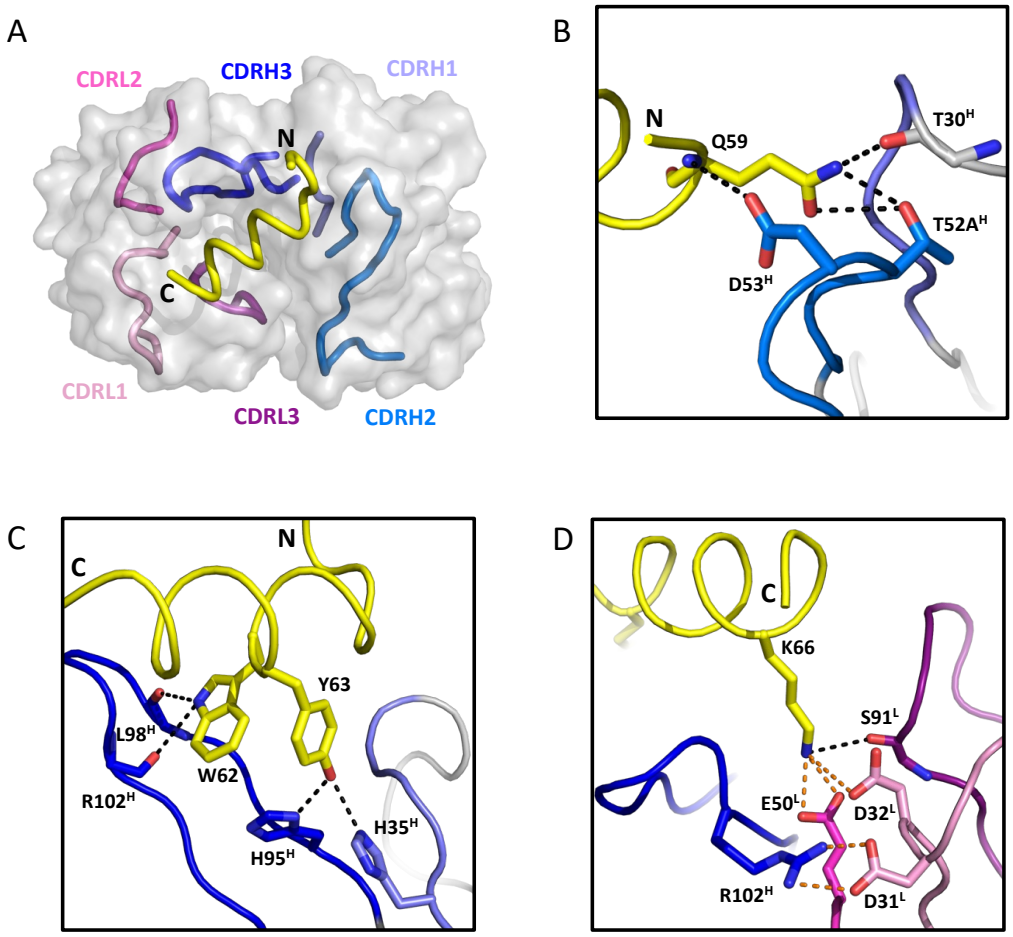


Figure 2.8. Structural basis for mNCSP9 binding to NtCSP. (A) Peptide 7 bind mNCSP9 as an α-helix perpendicular to the groove formed by the heavy and light chain (yellow tube). The surface of mNCSP9 Fab is shown from a birds-eye view in gray. CDRs are shown in cartoon tube representation in light blue (CDRH1), marine (CDRH2), and dark blue (CDRH3), pink (CDRL1), magenta (CDRL2), and dark purple (CDRH3). (B) Gln59 is stabilized by heavy chain residues in network of hydrogen bonds. (C) Trp62 and Tyr63 are coordinated by backbone and side chain residues from CDRH1 and CDRH3. (D) The last helical turn of peptide 7 is stabilized by a salt bridge network of Lys66 with CDRH1 and CDRH2 acidic residues. The backbone of mNCSP9 and bound peptide are shown as yellow cartoon tube, relevant backbone and side chains are shown as sticks and colored by atom. CDRs are colored as in (A), framework residues are in grey. Dashed lines represent hydrogen bonding (black) and salt bridge (orange) interactions.

In addition to canonical antibody-antigen interactions, adjacent mNCSP9 Fabs bound to peptide 7 in the crystal packing are seen to interact through both bound peptide and heavy chain variable domains **(Figure 2.9A)**. In the bound peptide, the Tyr56 hydroxyl group of one complex forms a hydrogen bonding network with the Lys58 backbone carbonyl and Trp62 backbone amide of the second complex in the ASU, forming a total buried surface area of 193Å^2**(Figure 2.9B)**. The heavy chain variable domain framework Thr30 of both heavy chains interact, while only one heavy chain framework Thr28 hydroxyl group interacts with CDRH2 Asp53 backbone carbonyl of the neighboring complex, with a total buried surface area of 168Å^2**(Figure 2.9C)**.

2.2.8 Structural Basis for mNCSP10 binding to NtCSP

The X-ray crystal structure of mNCSP10 was also determined in the presence of peptide 7 and solved at a resolution of 1.7Å. The asymmetric unit contains a single Fab, a clear electron density for peptide residues corresponding to CSP Tyr56-Ser69, and four Calcium ions. The peptide binds perpendicular to the groove formed by the heavy and light chain interface and assumes a α-helical conformation from residues Lys58-Ser69, for a total buried surface area of 664Å^2 **(Figure 2.10A)**. Due to the similarity in antibody sequences of mNCSP9 and mNCSP10, it is unsurprising that engage their CSP epitope in much the same way. Firstly, Gln59 is coordinated in a hydrogen bonding network with heavy-chain framework Thr30 and CDRH2 Thr52A, with CDRH2 Asp53 further hydrogen bonding to the Gln59 backbone amide **(Figure 2.10B)**. In the following helical turn, Trp62 hydrogen bonds with CDRH3 Ser98 backbone carbonyl, and Tyr63 hydroxyl group forms hydrogen bonds with both CDRH3 His95 and His35. In the last helical turn,

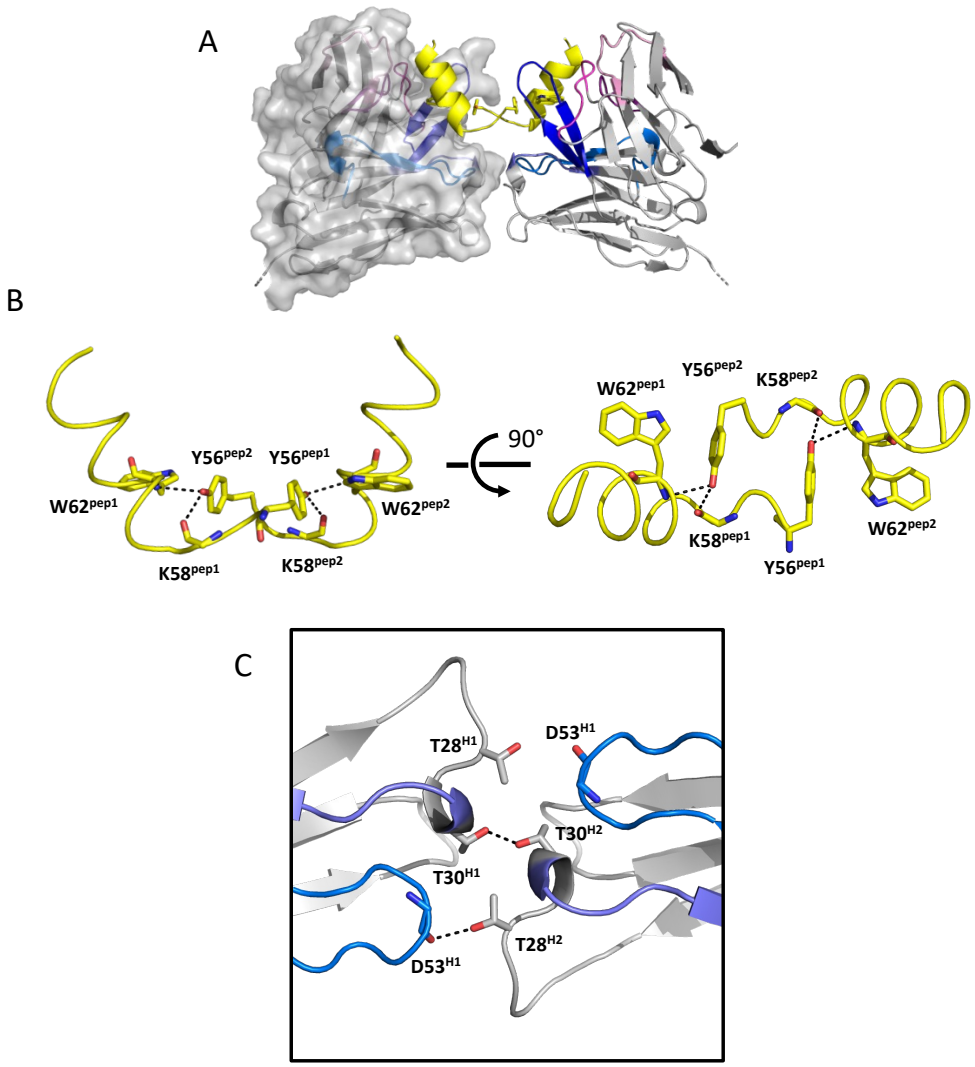


Figure 2.9. The binding of mNCSP9 to peptide 7 is stabilized by homotypic interactions in the crystal lattice. (A) Two interacting mNCSP9 VH and VL domain pairs are shown in cartoon ribbon representation, one monomer shown in transparent grey surface representation. Bound peptide is shown as a cartoon ribbon. (B) Two peptides bound to adjacent interacting mNCSP9 Fab fragments in the crystal lattice interact through a hydrogen bonding network between Tyr56 of one peptide with Lys58 and Trp62 of the other. Bound peptide is shown as yellow cartoon tube, and relevant side chains as sticks colored by element. (C) VH domains of interacting Fabs form a nearly symmetrical network of hydrogen bonds. CDRs are shown in cartoon representation in light blue (CDRH1), marine (CDRH2), and dark blue (CDRH3), pink (CDRL1), magenta (CDRL2), and dark purple (CDRH3), and grey (framework). Black dashed lines represent hydrogen bonds.

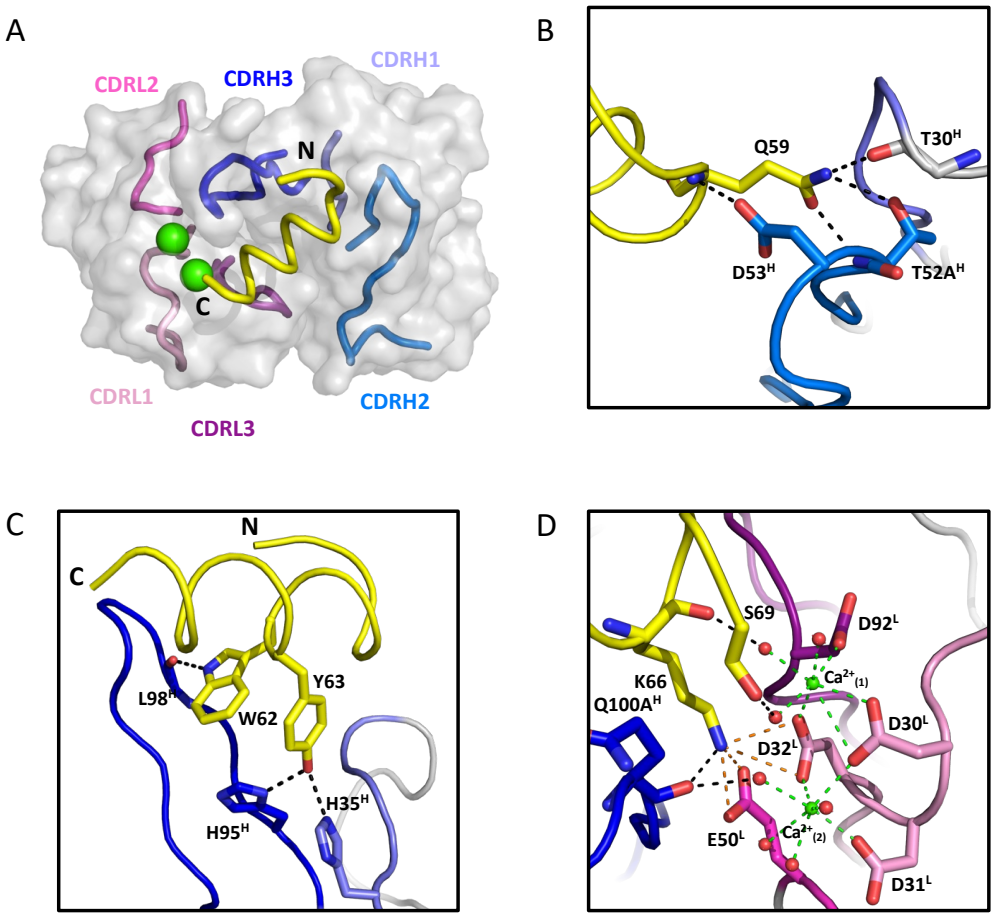


Figure 2.10. Structural basis for mNCSP10 binding to NtCSP. (A) Peptide 7 bind mNCSP10 as an α-helix perpendicular to the groove formed by the heavy and light chain (yellow tube). (B) The surface of mNCSP10 Fab is shown from a birds-eye view in gray. CDRs are shown in cartoon tube representation in light blue (CDRH1), marine (CDRH2), and dark blue (CDRH3), pink (CDRL1), magenta (CDRL2), and dark purple (CDRH3). (B) Gln59 is stabilized by a heavy chain residues in a bonding network. (C) Trp62 and Tyr63 are coordinated by backbone and side chain residues from CDRH1 and CDRH3. (D) The salt bridge interaction anchoring Lys66 is extended by binding of two calcium ions Ca^{2+}(1) and Ca^{2+}(2) (green spheres) and coordinated water molecules (red spheres). mNCSP10 and bound peptide is shown as yellow cartoon tube, relevant backbone and side chains are shown as sticks colored by element. CDRs are colored as in (A), framework residues are in grey. Dashed lines represent hydrogen bonding (black), salt bridge (orange) interactions, and metal ion coordination (green).

Lys66 forms salt bridge interactions with CDRL1 Asp32 and CDRL2 Glu50 much like in the mNCSP9 crystal structure **(Figure 2.10C)**.

Differences between the two structures arise due to the calcium ions bound in the mNCSP10 structure **(Figure 2.10D)**. The calcium likely comes from the 0.2 M calcium chloride used in the crystallization (see Materials and Methods). The first calcium ion $Ca^{2+}_{(1)}$ is doubly coordinated by CDRL1 Asp30, singly coordinated by both CDRL1 Asp32 and CDRL3 Asp92, and further coordinated by three water molecules for a total coordination number of seven. The second calcium ion is singly coordinated by the side chains of CDRL1 Asp31 and Asp32, and CDRL2 Glu50, and binds a further four water molecules for a total coordination number of seven. Through their coordination of structured water molecules, these calcium ions extend the binding surface presented by mNCSP10 to produce novel hydrogen bonding interactions with the Lys66 backbone carbonyl group and Ser69 side-chain hydroxyl. Instead of interacting with a bound calcium ion, CDRL1 Asp31 forms a salt bridge CDRH3 Arg102 in the mNCSP9 structure **(Figure 2.9D)**. The different conformation of CDRH3, potentially due to the liberation of Arg102, positions the backbone carbonyl of Gln100A to form a hydrogen bond with Lys66 side-chain amine and a structured water molecule coordinated by $Ca^{2+}_{(2)}$ **(Figure 2.10D)**.

2.2.9 Structural basis for mNCSP13 binding to NtCSP

Lastly, the X-ray crystal structure of humanized mNCSP13 Fab in the presence of peptide 1 was solved at resolution of 1.85Å. The asymmetric unit cell contains a single copy of

Fab with clear electron density for peptide corresponding to CSP residues Thr32-Tyr40. The peptide to binds in the groove formed at the heavy-light chain interface for a total buried surface area of 708Å^2 that is evenly contributed by the heavy and light chain (335Å^2 and 374Å^2, respectively) **(Figure 2.11A)**. The N-terminal portion of the visible peptide is primarily engaged by interactions with its backbone; light-chain framework Tyr49 hydroxyl group and CDRH2 Lys50 coordinate the backbone carbonyl groups of Arg33 and Val34, respectively, while CDRH3 Ser99 backbone carbonyl is positioned to interact with both Leu35 and Asn36 backbone amides **(Figure 2.11B)**. The latter portion of the visible peptide is stabilized through side-chain interactions. Seen from a different view, CDRL2 Lys50 forms a salt bridge with Glu37, and also interacts with CDRL1 Tyr32 side-chain hydroxyl **(Figure 2.11C)**. The C-terminal anchor of the bound peptide is Asn39, which is bound by a network of hydrogen bonding interactions with CDRH1 Asn35, CDRH2 Lys50, and CDRH3 Ser98 backbone carbonyl **(Figure 2.11D)**. Peptide binding additionally positions Asn36 to form both a pseudo 3_{10} turn through its side chain binding to the Leu38 backbone amide, and a type-1 β-turn with Asn39, likely contributing to peptide stability **(Figure 2.11C and 2.11D)**

2.2.10 Differential cross-strain binding potential of novel NtCSP targeting mAbs

The N-terminal domain of CSP is highly conserved across different strains of *Plasmodium falciparum*. Nevertheless, multiple haplotypes have been observed(25–28); several isolates contain a 19-amino acid insertion following Asn80, polymorphisms in residues Asp82-Arg87, and polymorphisms immediately after the conserved KLKQP sequence of RI. To assess whether murine antibodies binding to novel NtCSP epitopes

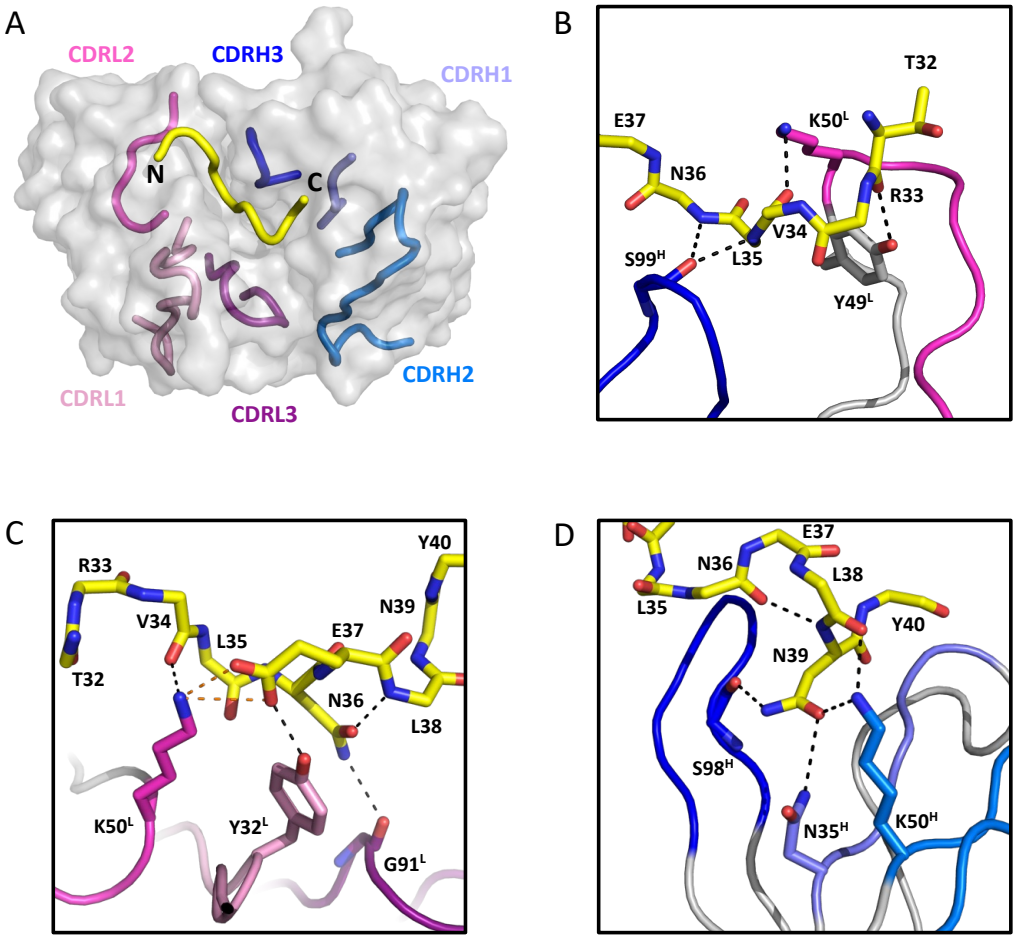
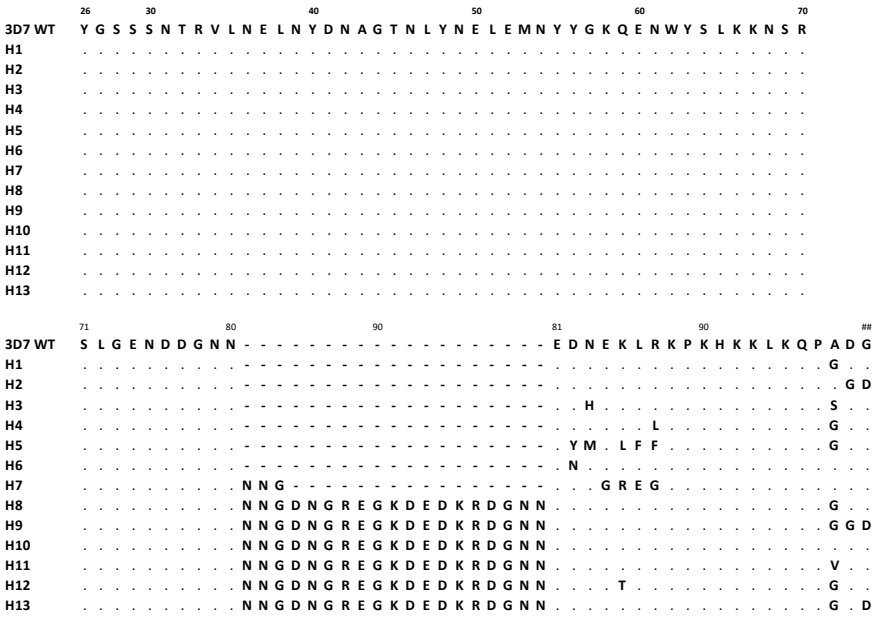


Figure 2.11. Structural basis for mNCSP13 binding to NtCSP. (A) The bound peptide lays along the groove formed by the mNCSP13 heavy and light chain interface (yellow tube). The surface of mNCSP13 Fab is shown from a birds-eye view in gray. CDRs are shown in cartoon tube representation in light blue (CDRH1), marine (CDRH2), and dark blue (CDRH3), pink (CDRL1), magenta (CDRL2), and dark purple (CDRH3). (B) The C-terminal of bound peptide is anchored through stabilization of the peptide backbone. (C) Detail view of interactions of light chain residues stabilizing bound peptide backbone and select side chains stabilizing an Asn3-10 pseudo-turn. (D) Asn39 participates in a network of hydrogen bonds stabilizing peptide binding and a type-1 β-turn. The backbone of the bound peptide is shown as yellow sticks colored by element, backbone of mNCSP13 is shown in cartoon tube representation, relevant backbone and side chains are shown as sticks. CDRs are colored as in (A), framework residues are in grey. Dashed lines represent hydrogen bonding (black) and salt bridge (orange) interactions.

can provide cross-strain neutralization, our collaborators in the Burton Lab (TSRI) determined the binding affinity of mNCSP mAbs to a panel of fourteen NtCSP sequence variants expressed in mammalian cells **(Figure 2.12A)** by surface plasmon resonance (SPR) **(Figure 2.12B)**. All mAbs tested bound reference strain 3D7 (WT), but no mAbs bound H5. Unsurprisingly, 5D5 bound WT and all strains with amino-acid insertions after Asn80 but did not bind haplotypes with sequence polymorphisms in the Asn82-Asn87 region overlapping with its characterized epitope. As expected from the lack of polymorphisms in its mapped epitope, mNCSP27 bound all tested haplotypes (except H5). The remaining mAbs, however, did not bind as expected by simple comparison of their binding epitopes with haplotype sequences. Whereas the peptide sequence bound by mNCSP6 in its X-ray crystal structure is identical in 3D7, H6, H7, and H10, mNCSP binding was only detected to 3D7 and H10. Likewise, the epitope mapped for mNCSP2, mNCSP14, and delineated in the X-ray crystal structure of mNCSP13, contains no polymorphism across all haplotypes tested, yet each bound a reduced set of haplotypes. The epitope bound by mNCSP9 and mNCSP10 is identical in all haplotypes tested, but binding was not detected to H11.

The lack of binding for H6 and H7 by mNCSP6 may be due to the nearby upstream polymorphisms. This would imply successful binding depends on interactions or conformational isomerism not observed in its crystal structure, and its minimal functional epitope may span further than the Leu86-Gly100 peptide used in crystallization. In the case of mNCSP2, mNCSP13, and mNCSP14, the observed loss of binding by polymorphisms in distant regions of the NtCSP sequence suggests that NtCSP may

A



B

KD(M)	mNCSP2	mNCSP13	mNCSP14	mNCSP27	mNCSP9	mNCSP10	mNCSP6	5D5	NEG
H1	BT	BT	1.5E-07	1.4E-07	2.3E-08	2.3E-08	BT	2.8E-09	BT
H2	BT	BT	BT	2.9E-08	1.9E-08	8.5E-09	BT	3.0E-07	BT
H3	BT	BT	BT	1.3E-08	8.1E-08	2.2E-07	BT	BT	BT
H4	BT	BT	BT	1.9E-08	2.4E-08	2.7E-08	BT	BT	BT
H5	BT	BT	BT	BT	BT	BT	BT	BT	BT
H6	BT	BT	2.2E-07	1.4E-08	2.8E-08	1.9E-08	BT	BT	BT
H7	BT	BT	2.0E-09	2.4E-08	2.2E-07	4.5E-08	BT	BT	BT
H8	BT	BT	8.6E-08	1.2E-07	6.1E-08	6.8E-08	BT	3.7E-08	BT
H9	BT	1.1E-07	4.31E-09	6.0E-09	6.0E-08	2.3E-08	BT	3.1E-08	BT
H10	BT	BT	1.2E-08	7.6E-09	2.9E-08	9.3E-08	1.2E-09	2.4E-07	BT
H11	BT	BT	7.5E-07	2.0E-07	BT	BT	BT	1.5E-07	BT
H12	BT	BT	2.87E-09	1.3E-07	5.2E-08	1.1E-07	BT	2.8E-08	BT
H13	BT	1.1E-09	1.0E-07	1.3E-08	5.9E-09	3.2E-08	BT	1.9E-07	BT
WT	1.3E-07	1.8E-07	1.7E-07	1.4E-08	2.2E-08	7.8E-08	1.5E-09	2.4E-07	BT

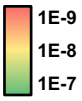
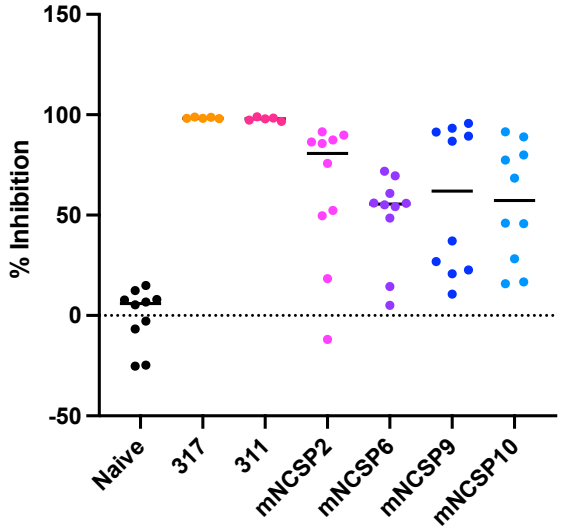


Figure 2.12. Binding of murine mAbs to a panel of NtCSP haplotypes. (A) NtCSP haplotype sequences used to determine the potential of murine antibodies that bind NtCSP epitopes to produce cross-strain binding. Dashed likes represent gaps/missing residues. Periods represent conservation relative to 3D7 reference strain. (B) SPR affinity measurement of mAbs to the panel of NtCSP haplotypes, using 5D5 as a positive control and anti-ZIKV mAb as negative control. Kd measurements are colored to show highest affinity (red) and lowest affinity (green) for each antibody across the different haplotypes tested. BT=below threshold.

possess secondary structure characteristics affecting epitope availability. The effect of sequence polymorphisms may alter yet undiscerned secondary structural features that can alter epitope presentation, thereby producing the unexplained binding differences. The novel epitope characterized for both mNCSP9 and mNCSP10 was least impacted compared to the novel epitope targeted by mNCSP2, 13, 14, and 27, or the previously characterized RI region bound by mNCSP6. This central NtCSP epitope is less susceptible for masking in the SPR assay caused by potential secondary structure characteristics or unwanted non-specific interactions and retains the potential to provide strain-transcending parasite opsonization.

2.2.11 *In Vivo* Protection of Murine mAbs in Mouse Liver Burden Model

Next, mNCSP2-10 were tested for *in vivo* protection from sporozoite challenge in mice by our collaborators **(Figure 2.13)** (Burton Lab (TSRI) and Zavala Lab (JHU)). Mice were injected with 300ug murine IgG_{2b} 16 hours prior to intravenous challenge with transgenic *P. berghei-P. falciparum* CSP sporozoites expressing luciferase, and parasite liver burden measured as bioluminescence after 42 hours. Known protective major NPNA repeat targeting antibodies 311 and 317 were used as positive control, displaying consistent and significant reduction of over 90% ($p=0.0007$). Compared to mAbs 311 and 317, the reduction in parasite liver burden of mNCSP2-10 has higher animal-to-animal variability ranging from no protection to that nearly equal to mAbs 311 and 317. Notwithstanding, mAbs mNCSP2-10 all produced a statistically significant decrease in parasite liver burden ($P<0.001$) in the range of 50-80%.



Mann-Whitney	mNCSP2	mNCSP6	mNCSP9	mNCSP10	317	311
P-Value	0.0007	0.0005	<0.0001	<0.0001	0.0007	0.0007
Exact or Approx.	exact	exact	exact	exact	exact	exact
P Value Summary	***	***	****	****	***	***

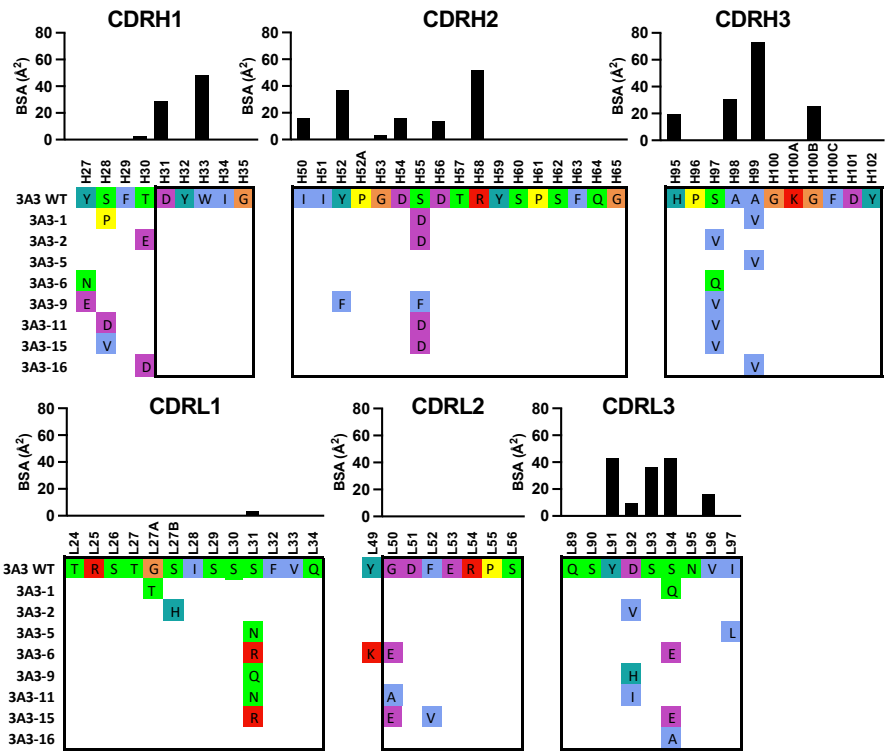
Figure 2.13. *In vivo* protection of mNCSP2-10 in mouse liver burden assay. Parasite liver burden was measured by bioluminescence of *P. berghei* sporozoites expressing luciferase-conjugated *P. falciparum* CSP 42 hours following passive transfer of 300 ug of murine IgG2b in C57BI/6 mice. Percent inhibition represent the percent reduction of parasite liver burden compared to that of naïve control infected mice. A two-sided Mann-Whitney test was used to determine statistical significance.

2.2.12 Affinity maturation of 3A3 by Yeast Display

Due to their lack of CSP-specific affinity maturation, the binding affinity of 3A3 isolated from phage display library is in the micromolar range. Because of its weak binding, it is unlikely to be protective regardless of epitope. The structural similarities of epitope binding between 3A3, mNCSP9, and mNCSP10, raise the potential that, with improved binding, 3A3 might also demonstrate protective efficacy in mice. We therefore selected

3A3 for affinity maturation against peptide 7 by yeast display (affinity maturation was performed by Jessica (Woolf) Coppola, in collaboration with Joseph Jardine, IAVI and Dennis Burton, TSRI), and SPR binding evaluated by Ding Zhang, Wilson Lab). After rounds of both single-chain and combinatorial positive and negative selection rounds, heavy-light chain pairings were sequenced. Eight chosen sequences, together with wildtype 3A3 and buried surface area formed by the peptide 7 epitope are shown in **Figure 2.14A**. Several mutational clusters are apparent by sequence alignment, indicative of convergence in stabilization of the peptide epitope. Except for 3A3-5, all sequences contain a novel acidic residue, expected to stabilize the multiple lysine residues in the target epitope. For example, four sequences contain a CDRH2 S55D mutation adjacent to Asp54 and Asp56 which form salt-bridge interactions with Lys67 in the 3A3 X-ray crystal structure. Similarly, acidic residues localized to CDRH1 are in proximity to Lys66 or Lys67. The CDRH3 of 3A3 contributes to binding through its stabilization of both Trp62 and Tyr63. The clustering of valine mutations in this region may improve binding by altering CDRH3 conformation to increase shape complementarity and buried surface area, or decrease interaction distance to Trp62 and Lys63. To assess the improvement in binding of these sequences over wildtype 3A3, IgG binding to peptide 7 was characterized by SPR **(Figure 2.14B)**. Wildtype 3A3 bound immobilized peptide 7 with Kd of 1.49×10^{-7} M, and all affinity matured sequences bound peptide 7 with Kd ranges of 10^{-9} to 10^{-11} M. This 2-4 log increase of binding affinity is primarily due to a change in K_{off} rates, which decreased from 1.76×10^{-1} M to 10^{-4} to 10^{-6} for 3A3 variants.

A



B

	ka1 (1/Ms)	kd1 (1/s)	ka2 (1/RUs)	kd2 (1/s)	Chi² (RU²)	kD1
3A3	$1.19x10^{6}$	$1.76x10^{-1}$	$4.56x10^{-5}$	$3.64x10^{-6}$	0.607	**$1.49\ x10^{-7}$**
3A3-1	$1.99x10^{5}$	$3.32x10^{-5}$	$3.22x10^{-2}$	$4.93x10^{-1}$	5.85	**$1.67\ x10^{-10}$**
3A3-2	$2.25x10^{5}$	$4.7x10^{-4}$	$1.14x10^{-1}$	1.12	8.72	**$2.09\ x10^{-09}$**
3A3-5	$2.00x10^{5}$	$1.05x10^{-4}$	$5.62x10^{-1}$	10.6	3.72	**$5.26\ x10^{-10}$**
3A3-6	$1.16x10^{5}$	$3.83x10^{-6}$	$1.26x10^{-2}$	$2.30x10^{-1}$	5.938	**$3.30\ x10^{-11}$**
3A3-9	$2.31x10^{5}$	$5.09x10^{-4}$	$9.37x10^{-1}$	8.56	9.01	**$2.20\ x10^{-09}$**
3A3-11	$1.92x10^{5}$	$4.92x10^{-4}$	$1.59x10^{-2}$	$3.39x10^{-1}$	6.33	**$2.56\ x10^{-9}$**
3A3-15	$1.59x10^{5}$	$3.88x10^{-5}$	$1.20x10^{-2}$	$1.73x10^{-1}$	8.20	**$2.44\ x10^{-10}$**
3A3-16	$2.75x10^{5}$	$5.01x10^{-4}$	1.49	29.4	4.81	**$1.82\ x10^{-09}$**

Figure 2.14. Affinity maturation of 3A3 by yeast display. (A) 3A3 CDR and relevant nearby sequences aligned to eight paired heavy and light chain sequences produced by yeast display affinity maturation. Amino acids are shown in clustal X default coloring; Hydrophobic (blue), positively charged (red), negatively charged (magenta) polar (green), aromatic (cyan), glycine (orange), proline (yellow), and cysteine (pink). (B) Binding affinities of 3A3 and affinity matured variants to peptide 7 by surface plasmon resonance (shown to 3 significant figures).

Initial mutagenesis libraries chosen by our collaborators were informed by the already existing 3A3 structure. It is therefore logical for the 3A3 structure to offer a likely structural basis for the increased affinity produced by these selected mutations. Through limited mutagenesis of a single amino acids in each CDR, the germline interactions producing weak binding affinity of 3A3 to its target peptide were improved by up to four orders of magnitude. These results suggest that the human antibody repertoire contains potential for production of high-affinity antibodies to novel NtCSP epitopes with limited somatic hypermutation.

2.3 Discussion and future Work

The monoclonal antibody response to the N-terminal domain of CSP has been under investigated relative to the highly immunogenic major repeat epitope. Even though its specific function is not understood, the wealth of serological and structural studies regarding its immunogenicity have elaborated on the various binding mechanisms leading to protection by major repeat targeting antibodies. The opposite is the case for NtCSP; it is the site of most known CSP functionalities in the mammalian host. Even so, only limited effort has been put towards characterizing its full potential as a vaccine target. Isolation and characterization of monoclonal antibodies from sporozoite immunization have revealed the highly protective L9 (21) and CIS43 (19) targeting the minor repeat and junctional epitope, respectively, reinforcing the notion that more protective epitopes may yet be uncharacterized on the circumsporozoite protein. The immunogenicity of the major repeat epitope has been shown to suppress expansion of B-cells targeting subdominant epitope in mouse immunization studies (14). We have therefore looked to other sources of antibodies to provide an extensive characterization of antibodies targeting the NtCSP epitope to define new potential sites of vulnerability.

The X-ray crystal structures described herein provide multiple novel epitopes as well as different modes of interaction of previously described epitope regions. Through comparison of these epitopes with previous studies assessing NtCSP functional determinants, we can propose mechanisms of inhibition to guide future experimental design. The buried surface area formed by different antibody binding to specific NtCSP residues is shown in **Figure 2.3**. The lysine-rich sequence upstream of RI has been shown

key in heparin binding (3), while RI is the site of CSP cleavage(11). The non-protective murine 5D5 does not directly obstruct the CSP cleavage site, while protective MAD2-6 directly binds RI, potentially contributing to protection through direct competition with the yet undiscovered protease responsible for CSP cleavage. Mutagenesis analysis of NtCSP has shown that, while Lys85, Lys88, Lys90, and Lys92 almost entirely abrogate the interaction of NtCSP with heparin, mutagenesis of Lys67, Lys93, and Lys95 have little effect in comparison (3). The crystal structure of human 3F4 illustrates it binds to NtCSP most similarly to MAD2-6, interacting with Pro89, and engaging Lys88, Lys93 and Lys95. Meanwhile, mNCSP6 binds the RI conserved KLKQP cleavage sequence further downstream and interacts specifically with Lys93. Our results therefore suggest that 3F4 could directly inhibit heparin binding, while mNCSP6 is only likely to do so to a minimal extent. Both 3F4 and mNCSP6 directly bind to residues of the Region I (KLKQP) cleavage sequence and may affect CSP processing.

In contrast to the differences in epitopes targeted by RI-binding antibodies, the NtCSP epitope bound by mNCSP9 and mNCSP10 is identical in sequence. Differences in binding arise due to the homotypic interactions seen in the mNCSP9 crystal packing and calcium ions in the mNCSP10 structure. The absence of calcium ions from the mNCSP9 structure and the absence of homotypic interactions from the mNCSP10 structure would suggest that neither are necessary for binding. Through binding an epitope that overlaps with 3A3, they too engage the bound peptide through a similar series of interactions: stabilization of Trp62 and Lys63, and engaging a nearby downstream lysine via multiple

aspartate side chains. The novel epitope targeted by mNCSP13 has no human mAb counterpart to date and is distinct from any previously characterized epitopes on NtCSP.

The structural characterization of human 3F4 and 3A3 binding to their NtCSP epitopes through germline-encoded residues supports the potential of the naïve human B-cell repertoire to produce an antibody response to CSP N-terminal epitopes. Moreover, three of the mAbs identified by phage display bind a region of interest distinct from that characterized to bind MAD2-6 and 5D5 (Leu51-Arg70). Through mouse immunization with NtCSP, we further identified two mAbs binding this new epitope, as well as several mAbs binding a distinct epitope not bound by any human mAbs (CSP Tyr26-Thr45). The scope of this work does not exhaust the possibility that human antibodies can bind this novel epitope, which may be a result of the limited scope of this study. Yet, any differential preference for antibody epitopes between the human and mouse repertoire may caution the use of mice models for study of NtCSP-targeting antibody-mediated immunity and should be investigated further.

Both new epitopes targeted by the antibodies characterized are well conserved amongst *P. falciparum* strains, with potential for binding CSP from multiple strains of *P. falciparum*. It is therefore surprising that binding to the epitope of mNCSP2, 13, and 14 at the N-terminus of NtCSP is abrogated by polymorphisms downstream. The differential ability of mNCSP2, 13, and 14 to bind their conserved epitope supports the presence of secondary structural characteristics within NtCSP. Additionally, their differential binding to our panel of haplotypes implicates the polymorphic residues causing loss of binding to

be involved in said secondary structure. In both mNCSP9 and mNCSP10 structures the bound peptide is stabilized as an α-helix, and in the 3A3 structure a single helical turn is stabilized in the region of Trp62 and Tyr63 binding. This propensity for the stabilization of the peptide as a helix supports the hypothesis that the N-terminal domain possessed secondary structural tendencies. Although NtCSP is abundant in aromatic, acidic, and basic residues which can facilitate secondary and tertiary structure, no intra- or inter-domain interaction of CSP have been determined to date.

The susceptibility to distant polymorphisms of the epitope shared by mNCSP2, 13, 14 and 27 is not shared by mNCSP9 and mNCSP10, targeting the same epitope as 3A3. The common structural features seen in both murine and human mAbs binding this epitope would suggest 3A3 could also provide strain-transcending protective efficacy. While our ongoing work seeks to assess the protective efficacy of improved 3A3 variants, future studies should seek to underpin the specific mechanism by which targeting this epitope provides protection. Several recent studies have highlighted the role of complement in protection from malaria (29–32). Antibodies raised to all CSP domains have been shown to fix complement C1q (29), a correlate of protection in children from malaria endemic regions(32). The lack of sequence diversity in this region implies either a lack of selection pressure or its participation in conserved interactions. Indeed, both new epitopes detailed in this study have been shown to bind negative complement regulator C4b-binding protein (33), increasing sporozoite resistance to complement-mediated lysis. One potential mechanism of action for antibodies targeting these epitopes is through

competition with C4b-binding protein, re-sensitizing sporozoites to complement-mediated lysis.

The propensity of the epitope shared by 3A3, mNCSP9, and mNCSP10 to bind in an α-helical conformation can be used to inform future immunogen design. Stabilization of peptide epitopes as loops grafted onto other proteins has been used to decrease conformational promiscuity, resulting in higher antibody titers in mice immunizations (34). The helical propensity of this epitope provides a unique opportunity for immunogen design, which has now been shown capable of eliciting an antibody response in both mice and humans. Immunogens that stabilize this epitope in a structured helix can ensure surface exposure of Trp62 and Tyr63, and relevant residues at each adjacent helical turn. Computational analysis of $CD4^+$ epitopes of CSP has produced a cluster of $CD4^+$ epitopes overlapping the 3A3 epitope (35). The conjunction of CSP $CD4^+$ epitopes has been shown to help overcome major histocompatibility restrictions in providing a humoral response to major repeat peptides (36). Regardless of potential for producing a protective antibody response to the epitope itself, the lymphoproliferative boosting potential of this T-cell epitope cluster in conjunction with known protective CSP B-cell epitopes should be investigated.

The use of mice and transgenic *P. berghei-P.falciparum* CSP parasites for *in vivo* protection studies has propelled the malaria vaccinology effort forward by providing a cost-effective model to assess antibody protective efficacy. However, sporozoite challenge through intravenous injection may be circumventing any potential protective

mechanisms provided by NtCSP targeting antibodies. Sporozoites expressing CSP with cleaved N-terminal domain fail to leave the site of intradermal injection, whereas they successfully establish infection by intravenous challenge (8). Cytotoxic anti-circumsporozoite antibodies have been shown to target sporozoites in the host skin (37), and sporozoites inoculated into the skin of mice previously immunized with irradiated sporozoite-immunized mice exhibit reduced motility (38). Opsonization of the N-terminal domain, which is key in parasite migration, may therefore offer protection by reducing parasite motility and increasing the exposure time of parasites to other antibodies or various cytotoxic serum factors. Previously, our ability to explore these potential mechanisms of protection was limited by the lack of characterized antibodies with binding to NtCSP. This study thus provides a substantial expansion of the molecular toolkit and new opportunities, which can now be used to illuminate the full potential of antibody-mediated NtCSP-based protection.

2.4 Materials and Methods

2.4.1 Antibody Sequences and Cloning

Sequences and DNA constructs of murine antibodies were provided by Nathan Beutler, Tom Rogers, and Dennis Burton at Scripps Research. Murine monoclonal antibodies were isolated following mouse immunization with N-terminal domain of the *P. falciparum* circumsporozoite protein (NF54 strain, isolate 3D7, residues Tyr26-Gly100) fused to keyhole limpet haemocyanin (KLH). Humanized murine antibody sequences were produced by insertion of variable heavy chain domain into AbVec-hIgG1 vector with murine Ser113 preceding human Ala114, and insertion of variable light chain domain into AbVec-IgKC vector with residue murine Lys107 preceding human Arg108 (Kabat numbering). For Fab production, stop codon mutations were introduced into heavy-chain constructs C-terminal to EPKSC sequence at the end of the C_H1 domain. To assist with crystallization of humanized murine Fabs, light-chain residues Thr197-THQGLSSP-Val205 were mutagenized to Thr197-QGTTS-Val203 by overlapping primer mutagenesis (24). Sequences of antibodies from naïve phage display library were isolated in collaboration Ding Zhang, Lerner/Wilson Laboratories, Scripps Research following previously described methods (22,23). Coding sequences for phage display antibodies were optimized for human expression and inserted into pCMV3 vector N-terminal to the IgK secretion signal peptide. For expression of Fab, sequences were inserted into pCMV3 vector with stop codon following the C_H1 EPKSC sequence.

2.4.2 Protein Expression and Purification

Fabs of monoclonal antibodies were expressed in ExpiCHO mammalian cells. Recombinant DNA of light and heavy chains were purified separately and co-transfected using Expifectamine transfection reagent following the manufacturer's protocol. Cells were cultured at 37°C, shaking at 125rpm, 8% CO_2 for 18-24 hours and then transferred to 32°C, 125rpm and 8% CO_2 for further 10-12 days. Transfection enhancer was added on day 1, and transfection feed medium added on days 1 and 5. Cell culture supernatants were harvested by centrifugation at 4,000-6,000 xg and filtered through 0.22 μm or 0.45 μm filter. Soluble Fabs were purified by protein G affinity chromatography; filtered supernatants were loaded onto HiTrap™ protein G 5ml column (Cytiva), washed with 5 column volumes PBS, eluted with 0.1M glycine pH 2.8 solution, and neutralized with 1M Tris pH8.0 solution. Relevant elution fractions were pooled and concentrated before further purification by size-exclusion chromatography on a HiLoad™ Superdex200 16/600 column or HiLoad™ Superdex75 16/600 column equilibrated with TBS pH 8.0.

2.4.3 Bacterial Protein Expression (Performed by Gonzalo Gonzalez, Wilson lab)

Coding sequence of CSP N-terminal domain Tyr26-Gly100 (mature protein) were inserted into pET32 vector with a N-terminal 6xHis-SUMO tag and a C-terminal Avi-tag. BL21(DE3) competent cells transformed with SUMO-NtCSP were grown in LB broth supplemented with Kanamycin at 30°C and induced with 1mM IPTG for overnight expression at 22°C. Bacterial pellets were harvested by centrifugation at 6000xg for 8 minutes and lysed on ice with a microfluidizer in PBS containing 0.5M NaCl, ROCHE

protease inhibitor, and benzonase. Lysed cell supernatant was clarified by centrifugation at 26000xg for 30mins 4°C and filtered through a 0.2 μM filter. SUMO-NtCSP was purified by nickle affinity chromatography (Roche cOmplete His-Tag Purification Resin). Briefly, following binding resin was washed with 20 mM TRIS pH8, 1 M NaCl, 5 mM Imidazole, washed again with 20mM TRIS pH 8, 200 mM NaCl, 5mM Imidazole, eluted with 200 mM imidazole, and dialyzed overnight at 4C in 20mM TRIS pH 8, 100 mM NaCl, 2mM DTT, and SUMO protease. For AviTag biotinylation, the sample was re-purified by nickel affinity purification and relevant elution fractions dialyzed against 50mM TRIS pH8, 200mM KCl. BirA was added to 40 uM NtCSP and 10 mM ATP, 10 mM magnesium acetate, and 50 μM D-biotin at room temperature for 1 hour. Lastly, sample was diluted ten-fold with 10mM sodium phosphate pH 7.2, loaded onto HiTrap Heparin HP column and eluted with sodium chloride gradient using 10mM sodium phosphate pH 7.2 supplemented with 2M sodium chloride.

Recombinant short CSP (rsCSP) contains the NF54 isolate 3D7 CSP sequence Tyr26-Ser383 with a truncated repeat domain of 3 NVDP and 19 NANP repeats, an N-terminal 6xHis tag and a C-terminal 6xHis and AviTag. As described in (39,40), rsCSP in pET28a vector was used to transform *E. coli* SHUFFLE competent cells (New England Biolabs), and a single colony was used to start an overnight culture, which were used to inoculate larger culture the following day. Once at OD 0.6-0.8, bacterial cultures were induced with 0.5 mM IPTG shaking at 16°C overnight. The following day, cultures were harvested by centrifugation, lysed by microfluidization, clarified by centrifugation and filtration, and incubated overnight with Ni Roche cOmplete resin (Roche). Sample was eluted with 75

mM TRIS pH 9, 200 mM imidazole into tubes containing NaCl for final concentration of 0.5 M. Biotinylation was performed as described above. Sample aliquots of both NtCSP and rsCSP were frozen and stored at -80°C.

2.4.4 Sequence and Structural Analysis

Antibody lineages and germline sequences were determined using IgBlast (NCBI). Sequence alignment of CDRs and relevant mutants was produced by AbYsis. Buried surface area analysis was performed using the PDBePISA server of EMBL-EBL. Structure figures were generated by Mac PyMOL (Schrödinger). Graphical data were plotted using GraphPad Prism.

2.4.5 Epitope Mapping

Peptide panel comprised of 14 overlapping peptides corresponding to CSP Tyr26-Gly100 (strain NF54, 3D7 isolate) were synthesized with an N-terminal Biotin-PEG2-GGGSGGG linker (Innopep). Binding was measured by bio-layer interferometry using streptavidin (SA) biosensors and Octet BLI (Sartorius). Peptides were diluted to 10ug/ml, and antibodies were diluted to 1uM. Biotinylated NtCSP was used as positive control.

2.4.6 Crystallization and Structure Determination

All Fabs were expressed as detailed above and prepared at 10 mg/ml in the presence of 5-fold equimolar excess of peptide for crystallization screening on our high-throughput robotic Rigaku CrystalMation system at TSRI by sitting-drop vapor diffusion. Peptide sequences, crystallization conditions which produced the best diffracting crystals, and

cryoprotectant are summarized below. X-ray diffraction data were collected at synchrotron beamlines APS 23ID-B (3F4 and 3A3) and APS 23 ID-D (mNCSP6, mNCSP9, mNCSP10, and mNCSP13). Crystals were briefly screened and diffraction data from crystals with diffraction maxima extending beyond 4Å were collected. Datasets encompassing an entire 360° crystal rotation were collected by capturing 0.2° rotations every 1 second. Diffraction data were processed using HKL2000(41). Structures were then determined using molecular replacement in Phaser(42) using search models of variable region produced by AbPred(43) and appropriate search model for constant region of either kappa or lambda Fabs. Structures were refined in REFMAC5(44) and PHENIX(45), manually built and refined in Coot(46), and validated using MolProbity(47).

Fab 3F4

Peptide: Ac-EKLRKPKHKKLKQ-NH_2

Chaperone: Equimolar C-terminal 6xHis-tagged protein G domain III

Crystallization condition: 20% PEG 3350, 0.2 M potassium nitrate, pH 6.5

Cryoprotectant: none.

Fab 3A3

Peptide: Biotin-PEG2-GGGSGGGYGKQENWYSLKKNSR-NH_2

Chaperone: Equimolar C-terminal 6xHis-tagged protein G domain III

Crystallization condition: 20% PEG 4000, 10% isopropanol, 0.1 M HEPES pH 7.5

Cryoprotectant: none.

Fab humanized mNCSP6

Peptide: Ac-LRKPKHKKLKQPADG-NH_2

Crystallization condition: 25% glycerol, 1.5 M ammonium sulfate

Cryoprotectant: none.

Fab humanized mNCSP9

Peptide: Ac-YGKQENWYSLKKNSR-NH_2

Crystallization condition: 20% PEG 6000, 0.1M citric acid pH 5.0

Cryoprotectant: 30% glycerol

Fab humanized mNCSP10

Peptide: Ac-YGKQENWYSLKKNSR-NH_2

Crystallization condition: 20% PEG 3350, 0.2 M calcium chloride pH 5.1

Cryoprotectant: 30% ethylene glycol

Fab humanized mNCSP13

Peptide: Ac-YGSSSNTRVLNELNY-NH_2

Crystallization condition: 20% PEG 3350, 0.2 M sodium citrate pH 8.2

Cryoprotectant: 30% ethylene glycol

2.4.7 Affinity Determination of murine mAbs to NtCSP haplotypes (Performed by Nathan Beutler in collaboration with Dennis Burton, TSRI)

Affinity experiments were performed on a Biacore 8k at 25°C. All experiments were carried out with a flow rate of 30 µL/min in a mobile phase of HBS-EP+ [0.01 M HEPES (pH 7.4), 0.15 M NaCl, 3 mM EDTA, 0.0005% (v/v) Surfactant P20]. A series S protein-G sensor chip was used. Each mAb was injected over the chip followed by a wait period to normalize captured response units (RU). A concentration series of NtCSP peptides was injected across the antibody and control surface for 2 min, followed by 2000–5000 second

dissociation phase. Regeneration of the surface in between injections of NtCSP peptides was achieved with a single, 120 s injection of 10 mM, pH 1.7 glycine. Kinetic analysis of each reference subtracted injection series was performed using the BIAEvaluation software (Cytiva). All sensorgram series were fit to a 1:1 (Langmuir) binding model of interaction.

2.4.8 Affinity Maturation of 3A3 by yeast display (performed by Jessica Coppola in collaboration with Joseph Jardine, IAVI and Dennis Burton, TSRI)

Heavy chain (HC) and light chain (LC) libraries were synthesized containing one mutation per CDR loop from the starting sequence, for up to three mutations per chain. The libraries contained all amino acid changes except those that introduced a cysteine, methionine or a motif that could produce a biochemical liability, such as putative N-linked glycosylation sites. The HC and LC libraries were initially paired with the unmodified LC and HC, respectively, so that all mutations in these first-round libraries are localized in a single chain. Both libraries, consisting of 2-6 million unique antibody clones, were cloned via homologous recombination into yeast and displayed on the surface as molecular Fab. These single chain diversity libraries were screened with three positive sorts against peptide 7 (NWYSLKKNSR) with decreasing antigen concentration each sort to increase selective pressure. These positive sorts were interspersed by one negative sort with biotinylated HEK membrane to reduce non-specific binders. After four rounds of selection, DNA from the HC and the LC libraries was harvested from the enriched population of improved variants and used to construct a combinatorial H/L library with mutations in both chains. This library was again displayed on the surface of yeast and underwent four more rounds of selection using the same positive and negative sort strategy. At the completion of the H/L

combinatorial screening campaign, the matured clones were sequenced and analyzed for preferred mutations. Eight antibodies were chosen to be reformatted as human IgG for further characterization.

2.4.9 Affinity Determination of 3A3 and affinity matured 3A3 variants (performed by Ding Zhang)

SPR experiment was done in Biacore S200 model, Series S SA chips were used. PBS with 0.05% P20 was used as running buffer. Peptide 7 with biotin tag was immobilized on one flow cell with target RU ~120, paring with a reference flow cell. Antibody with series of 7 dilutions (200 nM, 100 nM, 50 nM, 25 nM, 10 nM, 5 nM, 1 nM) were used as analyte for kinetics measurement, zero concentration included as base signal. Experiment was set as multi-cycle kinetics, with regeneration between each cycle. pH 2.7 glycine buffer was used as regeneration buffer. Analyte contact time and dissociate time set as 120/600s, 3 cycles of 30 seconds regeneration. A blank buffer control was included in each dilution. Data collected with all sample setup in one single experiment. Final sensogram presented with signal from ligand flow cell subtracted by reference flow cell. Kinetics parameters were calculated by fitting with bivalent analyte model (1:2 binding ratio).

2.4.10 Mouse Protection Studies (performed in collaboration with Fidel Zavala, JHU)

Mice were injected intravenously with 300 μg/mouse of monoclonal antibodies (human IgG1). Sixteen hours later, mice were challenged with $2x10^3$ chimeric sporozoites injected IV. Forty-two hours after challenge, mice were injected with 100 μl of D-

Luciferin (30 mg/mL), anesthetized with isoflurane and imaged with the IVIS spectrum to measure the bioluminescence expressed by the chimeric parasites. Results were provided as Total Flux (photons/sec) and percent liver burden reduction was calculated as 100*(1-(VALUE/meanNaïve)). For pairwise analysis of significance, each mAb was compared to the naïve control by the Mann-Whitney two-tailed test.

2.5 Acknowledgements

I would like to thank Ding Zhang, Nathan Beutler, and Thomas Rogers for providing us with the monoclonal antibody sequences. I would also like to thank Nate and Ding for performing the SPR experiments. I am very thankful to Fidel Zavala and Yevel Flores Garcia for their collaboration. I would like to thank Jessica (Woolf) Coppola and Joseph Jardine for their help with the affinity maturation. I would lastly like to thank Hank Tien for setting up all the crystallization screens.

2.6 Declaration

Nathan Beutler (Burton lab) isolated the antibody sequences for mNCSP mAbs, and Ding Zhang (Lerner lab/Wilson lab) isolated the antibody sequences for phage display mAbs. Jessica Coppola (Burton lab) performed the 3A3 affinity maturation. Yevel Flores Garcia (Zavala lab, John Hopkins University) performed liver burden assay. Nathan Beutler and Ding Zhang performed SPR experiments.

Table 2.1. Crystallographic data collection and refinement

Data collection	**Fab 3F4**	**Fab 3A3**	**Fab hmNCSP6**
Beamline	APS 23ID-B	APS 23ID-B	APS 23ID-D
Wavelength	1.03317	1.03317	1.0332
Space group	P 4_1 2_1 2	P 2_1 2_1 2_1	P 3_1 2 1
Cell dimensions			
a, *b*, *c* (Å)	63.36, 63.36, 280.95	62.77, 64.82, 142.38	117.66, 117.66, 95.07
α, β, γ (°)	90, 90, 90	90, 90, 90	90, 90, 120
Resolution (Å)	47.05-2.37 (2.46-2.37)	47.93-1.95 (2.02-1.95)	44.91-2.1 (2.18-2.10)
R_{merge}	0.133 (0.570)	0.137 (1.02)	0.150 (1.29)
R_{meas}	0.152 (0.887)	0.143 (1.12)	0.159 (1.39)
R_{pim}	0.055 (0.457)	0.041 (0.443)	0.054 (0.515)
Total Reflections	306,401 (1688)	477,051 (21985)	373,724 (30130)
Unique Reflections	22,208 (814)	42,729 (3898)	44,521 (4273)
$CC_{1/2}$	0.995 (0.503)	0.998 (0.45)	0.997 (0.659)
I / sI	11.1 (1.1)	12.72 (1.57)	10.41 (1.58)
Completeness (%)	91.00 (34.33)	98.9 (91.6)	97.2 (94.0)
Redundancy	13.8 (2.1)	11.2 (5.6)	8.4 (7.1)
Refinement			
Resolution (Å)	47.05-2.37 (2.45-2.37)	47.93 -1.95 (2.021 -1.95)	44.91-2.1 (2.18 -2.1)
No. reflections	22,189 (814)	42,617 (3893)	43,389 (4118)
Reflections in R_{free}	1107 (39)	2052 (191)	2115 (192)
R_{work} / R_{free}	0.201/0.244	0.212/0.243	0.225/0.253
No. atoms	3888	3563	3726
Protein	3789	3339	3437
Ligand/ion	0	35	0
Water	99	189	289
B-values (Å^2)			
Average B-factors	54	46	40
Protein	54	46	40
Ligand/ion	0	43	0
Water	48	42	44
Wilson B-value	50	32	33
R.m.s. deviations			
Bond lengths (Å)	0.002	0.007	0.002
Bond angles (°)	0.55	0.87	0.64
Ramachandran Plots(%)			
Favoured	96.57	95.14	97.71
Allowed	3.23	4.63	1.83
Outliers	0.2	0.23	0.46
Clashscore	2.8	6.45	2.66

Numbers in parentheses refer to the highest resolution shell.

$R_{merge} = \Sigma_{hkl} \Sigma_i | I_{hkl,i} - \langle I_{hkl} \rangle | / \Sigma_{hkl} \Sigma_i I_{hkl,i}$ and $R_{meas} = \Sigma_{hkl} (n/(n-1))^{1/2} \Sigma_i | I_{hkl,i} - \langle I_{hkl} \rangle | / \Sigma_{hkl} \Sigma_i I_{hkl,I}$ and $R_{pim} = \Sigma_{hkl} (1/(n-1))^{1/2} \Sigma_i | I_{hkl,i} - \langle I_{hkl} \rangle | / \Sigma_{hkl} \Sigma_i I_{hkl,i}$, where $I_{hkl,i}$ is the scaled intensity of the ith measurement of reflection h, k, l, $\langle I_{hkl} \rangle$ is the average intensity for that reflection, and n is the redundancy.

$CC_{1/2}$ = Pearson correlation coefficient between two random half datasets.

$R_{work} = \Sigma_{hkl} | F_o - F_c | / \Sigma_{hkl} | F_o |$ x 100, where F_o and F_c are the observed and calculated structure factors, respectively.

R_{free} was calculated as for R_{work}, but on a test set comprising 5% of the data excluded from refinement.

Table 2.2. Crystallography data collection and refinement

Data collection	**Fab hmNCSP9**	**Fab hmNCSP10**	**Fab hmNCSP13**
Beamline	APS 23ID-D	APS 23ID-D	APS 23ID-D
Wavelength	1.0332	1.0332	1.0332
Space group	P 3_1 1 2	$P2_1$ 2_1 2_1	P 2_1 2_1 2_1
Cell dimensions			
a, *b*, *c* (Å)	72.94, 72.94, 382.23	49.67, 74.00, 132.25	48.41, 73.67, 175.53
α, β, γ (°)	90, 90, 120	90, 90, 90	90, 90, 90
Resolution (Å)	41.31-2.28 (2.36-2.28)	39.71-173 (179-1.73)	46.67-1.86 (1.93-1.86)
R_{merge}	0.278 (3.14)	0.244 (1.74)	0.126 (1.30)
R_{meas}	0.286 (3.25)	0.256 (1.96)	0.132 (1.47)
R_{pim}	0.065 (0.827)	0.078 (0.873)	0.039 (0.659)
Total Reflections	101,1803 (76271)	476,507 (22328)	543,422 (22039)
Unique Reflections	53,455 (4892)	51,475 (4835)	53,166 (4812)
$CC_{1/2}$	0.988 (0.527)	0.972 (0.33)	0.996 (0.397)
I / sI	7.27 (0.98)	7.39 (1.25)	12.05 (1.18)
Completeness (%)	97.8 (81.3)	99.3 (94.0)	99.0 (90.1)
Redundancy	18.9 (15.6)	9.3 (4.6)	10.2 (4.6)
Refinement			
Resolution (Å)	41.31-2.28 (2.362-2.28)	39.71-1.73(1.79 -1.73)	46.67 -1.86 (1.926 -1.86)
No. reflections	52,716 (4313)	51,434 (4804)	53,130 (4780)
Reflections in R_{free}	2631 (237)	2522 (232)	2655 (246)
R_{work} / R_{free}	0.239/0.279	0.184/0.215	0.187/0.219
No. atoms	7182	3832	3818
Protein	6987	3459	3445
Ligand/ion	0	4	0
Water	195	369	373
B-values (Å^2)			
Average B-factors	56	32	35
Protein	56	31	34
Ligand/ion	0	32	0
Water	53	39	43
Wilson B-value	48	29	31
R.m.s. deviations			
Bond lengths (Å)	0.02	0.007	0.007
Bond angles (°)	1.02	0.89	0.84
Ramachandran Plots(%)			
Favoured	95.59	97.95	97.94
Allowed	4.3	2.05	2.06
Outliers	0.11	0	0
Clashscore	2.47	2.64	2.92

Numbers in parentheses refer to the highest resolution shell.

$R_{merge} = \Sigma_{hkl} \Sigma_i | I_{hkl,i} - \langle I_{hkl} \rangle | / \Sigma_{hkl} \Sigma_i I_{hkl,i}$ and $R_{meas} = \Sigma_{hkl} (n/(n-1))^{1/2} \Sigma_i | I_{hkl,i} - \langle I_{hkl} \rangle | / \Sigma_{hkl} \Sigma_i I_{hkl,I}$ and $R_{pim} = \Sigma_{hkl} (1/(n-1))^{1/2} \Sigma_i | I_{hkl,i} - \langle I_{hkl} \rangle | / \Sigma_{hkl} \Sigma_i I_{hkl,i}$, where $I_{hkl,i}$ is the scaled intensity of the ith measurement of reflection h, k, l, $\langle I_{hkl} \rangle$ is the average intensity for that reflection, and n is the redundancy.

$CC_{1/2}$ = Pearson correlation coefficient between two random half datasets.

$R_{work} = \Sigma_{hkl} | F_o - F_c | / \Sigma_{hkl} | F_o |$ x 100, where F_o and F_c are the observed and calculated structure factors, respectively.

R_{free} was calculated as for R_{work}, but on a test set comprising 5% of the data excluded from refinement.

2.7 References

1. Chatterjee, D. & Cockburn, I. A. The challenges of a circumsporozoite protein-based malaria vaccine. *Expert Rev Vaccines* **20**, 113–125 (2021).
2. Julien, J. P. & Wardemann, H. Antibodies against *Plasmodium falciparum* malaria at the molecular level. *Nat Rev Immunol* **19**, 761–775 (2019).
3. Zhao, J., Bhanot, P., Hu, J. & Wang, Q. A Comprehensive Analysis of *Plasmodium* Circumsporozoite Protein Binding to Hepatocytes. *PLoS One* **11**, e0161607 (2016).
4. Rathore, D., Sacci, J. B., De La Vega, P. & McCutchan, T. F. Binding and Invasion of Liver Cells by *Plasmodium falciparum* Sporozoites: Essential Involvement of the Amino Terminus of Circumsporozoite Protein. *J Biol Chem* **277**, 7092–7098 (2002).
5. Coppi, A. *et al.* Heparan Sulfate Proteoglycans Provide a Signal to *Plasmodium* Sporozoites to Stop Migrating and Productively Invade Host Cells. *Cell Host Microbe* **2**, 316–327 (2007).
6. Ying, P. *et al.* The malaria circumsporozoite protein: Interaction of the conserved regions I and II-plus with heparin-like oligosaccharides in heparan sulfate. *Exp Parasitol* **85**, 168–182 (1997).
7. Frevert, U. *et al.* Malaria circumsporozoite protein binds to heparan sulfate proteoglycans associated with the surface membrane of hepatocytes. *J Exp Med* **177**, 1287 (1993).
8. Coppi, A. *et al.* The malaria circumsporozoite protein has two functional domains, each with distinct roles as sporozoites journey from mosquito to mammalian host. *J Exp Med* **208**, 341–356 (2011).
9. Herrera, R. *et al.* Reversible Conformational Change in the *Plasmodium falciparum* Circumsporozoite Protein Masks Its Adhesion Domains. *Infect Immun* **83**, 3771 (2015).
10. Yoshida, N., Potocnjak, P., Nussenzweig, V. & Nussenzweig, R. S. Biosynthesis of Pb44, the protective antigen of sporozoites of *Plasmodium berghei*. *J Exp Med* **154**, 1236 (1981).
11. Coppi, A., Pinzon-Ortiz, C., Hutter, C. & Sinnis, P. The *Plasmodium* circumsporozoite protein is proteolytically processed during cell invasion. *J Exp Med* **201**, 27–33 (2005).
12. Nadeem, A. Y., Shehzad, A., Islam, S. U., Al-Suhaimi, E. A. & Lee, Y. S. Mosquirix^{TM} RTS, S/AS01 Vaccine Development, Immunogenicity, and Efficacy. *Vaccines (Basel)* **10**, 1033–1039 (2022).
13. Gordon, D. M. *et al.* Safety, Immunogenicity, and Efficacy of a Recombinantly Produced *Plasmodium falciparum* Circumsporozoite Protein-Hepatitis B Surface Antigen Subunit Vaccine. *J Infect Dis* **171**, 1576–1585 (1995).
14. Chatterjee, D. *et al.* Avid binding by B cells to the *Plasmodium* circumsporozoite protein repeat suppresses responses to protective subdominant epitopes. *Cell Rep* **35**, 108996 (2021).
15. Rathore, D. *et al.* An Immunologically Cryptic Epitope of *Plasmodium falciparum* Circumsporozoite Protein Facilitates Liver Cell Recognition and Induces

Protective Antibodies That Block Liver Cell Invasion. *Journal of Biological Chemistry* **280**, 20524–20529 (2005).
16. Espinosa, D. A. *et al.* Proteolytic Cleavage of the *Plasmodium falciparum* Circumsporozoite Protein Is a Target of Protective Antibodies. *J Infect Dis* **212**, 1111–1119 (2015).
17. Thai, E. *et al.* A high-affinity antibody against the CSP N-terminal domain lacks *Plasmodium falciparum* inhibitory activity. *J Exp Med* **217**, e20200061 (2020).
18. Tan, J. *et al.* Functional human IgA targets a conserved site on malaria sporozoites. *Sci Transl Med* **13**, eabg2344 (2021).
19. Kisalu, N. K. *et al.* A human monoclonal antibody prevents malaria infection and defines a new site of vulnerability on *Plasmodium falciparum* circumsporozoite protein. *Nat Med* **24**, 408 (2018).
20. Flores-Garcia, Y. *et al.* The P. falciparum CSP repeat region contains three distinct epitopes required for protection by antibodies in vivo. *PLoS Pathog* **17**, e1010042 (2021).
21. Wang, L. T. *et al.* A potent anti-malarial human monoclonal antibody targets circumsporozoite protein minor repeats and neutralizes sporozoites in the liver. *Immunity* **53**, 733 (2020).
22. Barbas, C. F., Kang, A. S., Lerner, R. A. & Benkovic, S. J. Assembly of combinatorial antibody libraries on phage surfaces: the gene III site. *Proc Natl Acad Sci* **88**, 7978–7982 (1991).
23. Gao, C., Brummer, O., Mao, S. & Janda, K. D. Selection of human metalloantibodies from a combinatorial phage single- chain antibody library. *J. Am. Chem. Soc.* **121**, 6517–6518 (1999).
24. Lieu, R. *et al.* Rapid and robust antibody Fab fragment crystallization utilizing edge-to-edge beta-sheet packing. *PLoS One* **15**, e0232311 (2020).
25. Mohamed, N. S. *et al.* Genetic polymorphism of the N-terminal region in circumsporozoite surface protein of *Plasmodium falciparum* field isolates from Sudan. *Malar J* **18**, 333 (2019).
26. Lê, H. G. *et al.* Genetic polymorphism and natural selection of circumsporozoite surface protein in *Plasmodium falciparum* field isolates from Myanmar. *Malar J* **17**, 361 (2018).
27. He, Z. quan *et al.* Genetic polymorphism of circumsporozoite protein of *Plasmodium falciparum* among Chinese migrant workers returning from Africa to Henan Province. *Malar J* **21**, 248 (2022).
28. Huang, H. Y. *et al.* Genetic polymorphism of *Plasmodium falciparum* circumsporozoite protein on Bioko Island, Equatorial Guinea and global comparative analysis. *Malar J* **19**, 245 (2020).
29. Kurtovic, L., Drew, D. R., Dent, A. E., Kazura, J. W. & Beeson, J. G. Antibody Targets and Properties for Complement-Fixation Against the Circumsporozoite Protein in Malaria Immunity. *Front Immunol* **12**, 775659 (2021).
30. Healer, J. *et al.* Complement-mediated lysis of *Plasmodium falciparum* gametes by malaria-immune human sera is associated with antibodies to the gamete surface antigen Pfs230. *Infect Immun* **65**, 3023 (1997).

31. Kurtovic, L. *et al.* Induction and decay of functional complement-fixing antibodies by the RTS,S malaria vaccine in children, and a negative impact of malaria exposure. *BMC Med* **17**, 1–14 (2019).
32. Kurtovic, L. *et al.* Human antibodies activate complement against *Plasmodium falciparum* sporozoites, and are associated with protection against malaria in children. *BMC Med* **16**, 1–17 (2018).
33. Khattab, A. *et al.* Hijacking the human complement inhibitor C4b-binding protein by the sporozoite stage of the *Plasmodium falciparum* parasite. *Front Immunol* **13**, (2022).
34. Langowski, M. D. *et al.* Optimization of a *Plasmodium falciparum* circumsporozoite protein repeat vaccine using the tobacco mosaic virus platform. *Proc Nat Acad Sci* **117**, 3114–3122 (2020).
35. Noe, A. R. *et al.* Bridging Computational Vaccinology and Vaccine Development Through Systematic Identification, Characterization, and Downselection of Conserved and Variable Circumsporozoite Protein CD4 T Cell Epitopes From Diverse Plasmodium falciparum Strains. *Front Immunol* **12**, (2021).
36. Sinigaglia, F. *et al.* A malaria T-cell epitope recognized in association with most mouse and human MHC class II molecules. *Nature* **336**, 778–780 (1988).
37. Aliprandini, E. *et al.* Cytotoxic anti-circumsporozoite antibodies target malaria sporozoites in the host skin. *Nature Microbiology 2018 3:11* **3**, 1224–1233 (2018).
38. Flores-Garcia, Y. *et al.* Antibody-Mediated Protection against *Plasmodium* Sporozoites Begins at the Dermal Inoculation Site. *mBio* **9**, e02194-18 (2018).
39. Schwenk, R. *et al.* IgG2 Antibodies against a Clinical Grade *Plasmodium falciparum* CSP Vaccine Antigen Associate with Protection against Transgenic Sporozoite Challenge in Mice. *PLoS One* **9**, e111020 (2014).
40. Oyen, D. *et al.* Structural basis for antibody recognition of the NANP repeats in *Plasmodium falciparum* circumsporozoite protein. *Proc Natl Acad Sci* **114**, E10438–E10445 (2017).
41. Otwinowski, Z. & Minor, W. Processing of X-ray diffraction data collected in oscillation mode. *Methods Enzymol* **276**, 307–326 (1997).
42. McCoy, A. J. *et al.* Phaser crystallographic software. *J Appl Crystallogr* **40**, 674 (2007).
43. Dunbar, J. *et al.* SAbPred: a structure-based antibody prediction server. *Nucl Acids Res* **44**, W474–W478 (2016).
44. Murshudov, G. N. *et al.* REFMAC5 for the refinement of macromolecular crystal structures. *Acta Crystallogr* **D67**, 367 (2011).
45. Afonine, P. V. *et al.* Towards automated crystallographic structure refinement with phenix.refine. *Acta Crystallogr* **D68**, 367 (2012).
46. Emsley, P. & Cowtan, K. Coot: model-building tools for molecular graphics. *Acta crystallogr* **D60**, 2126–2132 (2004).
47. Davis, I. W. *et al.* MolProbity: all-atom contacts and structure validation for proteins and nucleic acids. *Nucl Acids Res* **35**, W375–W383 (2007).

CHAPTER 3:

Structural Basis for High Avidity Binding of Monoclonal Antibodies from the MAL071 Trial to the αTSR domain

3.0 Abstract

The αTSR domain of *Plasmodium falciparum* was originally included in the RTS,S vaccine design due to its T-cell epitopes. Since then, little interest has been expressed towards the immune response to αTSR in favour of the highly protective repeat domain of CSP. However, the MAL071 trial reignited interest in CtCSP-based immunity when it appeared to be a key correlate of protection across both vaccine arms in multiple analyses. From X-ray crystal structures of 10 monoclonal antibodies from the MAL071 trial in complex with the αTSR domain, we show that antibodies targeting the conserved β-epitope of αTSR use a variety of antibody germline lineages to achieve heterogeneous binding poses and interactions, while those that target the variable α-epitope bind with similar angles of approach and binding interactions. We further characterized the binding epitope of mAb 1504, which targets a novel conserved epitope on the αTSR surface. Monoclonal antibodies targeting conserved epitopes on the αTSR domain bind a broad range of αTSR haplotypes, while mAbs that bind the polymorphic α-epitope are much more restricted in their haplotype recognition. In a total panel of fifteen mAbs, those targeting conserved epitopes show significantly higher avidity, linking two separately observations of anti-CtCSP avidity index and a strain-transcending CtCSP binding correlating to protection in RTS,S sera. Even so, mAbs targeting the αTSR domain do not provide sterilizing protection in an *in vivo* mouse model, highlighting a potential gap in the ability of the mouse model to mimic protection correlates observed in human RTS,S vaccination.

3.1 Introduction

The *Plasmodium falciparum* liver-stage vaccine RTS,S gained WHO approval in 2021 (1). Targeting the *P. falciparum* circumsporozoite protein, RTS,S contains 19 NANP repeats followed by the CSP C-terminal peptide (CtCSP), fused onto the HbsAg. The C-terminal domain of PfCSP is a thrombospondin-like type-1 repeat (αTSR) domain, an evolutionarily ancient domain across eukaryotes with multiple roles in cell adhesion and migration (2). Three key T-cell epitopes, Th2R, Th3R, and CS.3T, have been shown to boost lymphocyte proliferation, and are the rational for their inclusion in the RTS,S design(3–5). Following over 30 years of research and clinical trials since its inception, a key drawback has become apparent: antibody titres and protection wane rapidly in the six months following the last booster dose (6). Much of the structural work pertaining to antibody recognition of CSP epitopes has since focused on underpinning the structural basis for antibody protection for improvements in design of future vaccines and therapeutic antibodies.

3.1.1 Correlates of protection of antibodies targeting the CSP C-terminal domain

The MAL071 phase 2 trial demonstrated that a delayed third fractional dose of RTS,S provided significantly higher (86%) protection than the standard dose (64%) from CHMI (7). Surprisingly, anti-NANP titres between protected and unprotected individuals do not differ. Instead, protection best correlates with anti-CtCSP and anti-NANP avidity index, measured through the dissociation of bound mAb using a chaotropic agent. Whereas extensive structural characterization of antibody binding to repeat domains in recent years have provided a structural basis for their affinity as well as avidity through Fab-Fab

homotypic interactions (8–12), far less attention has been devoted to exploring the mechanisms of antibody affinity or protection towards CtCSP. Recent work suggests important roles in antibody-mediated protection towards CtCSP: antibodies targeting CtCSP have been shown to fix complement factor C1q(13), a correlate of protection in PNG children(14) and from CHMI in malaria naïve adults(15). Multi-variable serological analysis of MAL071 samples coupled with computational modelling approach have been used to identify CtCSP-specific antibody-mediated phagocytosis in monocytes and CSP-specific NK cell-activating antibodies as minimal markers to differentiate delayed fractional dose from standard dose regimens(16). Both are higher in delayed fractional dose and correlate with anti-CtCSP avidity index, suggesting potential co-evolution of anti-CtCSP avidity and effector functions. Both studies further associate serum polyfunctionality with increased protection.

3.1.2 Polymorphic epitopes of the CSP C-terminal domain

The Th2R and Th3R T-cell epitopes are also the location of extensive polymorphism across *P. falciparum* haplotypes(17–19). In one study, only 5.2% of sequenced isolates match the reference 3D7 strain of the RTS,S vaccine (20). When taking into account the infecting strain, 1-year cumulative vaccine efficacy increases from 33.4% to 50.3%(21). While there are a variable number of NANP repeats (and interspersed NVDP repeats) in the major repeat region of CSP, most polymorphisms occur in the αTSR domain T-cell epitopes. It is possible that decrease in vaccine efficacy due to strain mismatch suggests a role for antibodies targeting CtCSP polymorphic epitopes.

3.1.3 Monoclonal antibody binding to the CSP C-terminal domain

Compared to the major repeat epitope of CSP, there has been relatively little structural characterization of antibodies targeting the αTSR. The first X-ray crystal structure of a monoclonal antibody binding to the αTSR domain was mAb 1710 isolated from whole sporozoite immunization(22). The structure of Fab 1710 in complex with αTSR showed binding across the Th2R α-helix and CS-flap, with CDRH3 of 1710 inserting into the hydrophobic pocket between the two polymorphic epitopes (**Figure 3.1**). Failure of mAb 1710 to inhibit sporozoite cell traversal *in vitro* or parasitaemia *in vivo* suggested that it is non-protective.

Through collaboration with the PATH Malaria Vaccine Initiative, our group has characterized monoclonal antibodies targeting CtCSP isolated from the MAL071 trial(23). The X-ray crystal structures of three V_H3-21 and one (closely related) V_H3-48 monoclonal antibodies revealed remarkably similar binding to the epitope defined by mAb 1710, which was termed the α-epitope (**Figure 3.1**). An X-ray crystal structure of V_H3-21 mAb 1512 surprisingly illustrated binding to the opposite and highly conserved face of the domain, defining a new β-epitope. Both α-epitope binder mAb 236 and β-epitope binder mAb 1512 significantly protect from *P. berghei-P. falciparum* CSP transgenic parasite infection in a mouse liver burden assay, providing the first report of anti-CtCSP mediated protection by monoclonal antibodies.

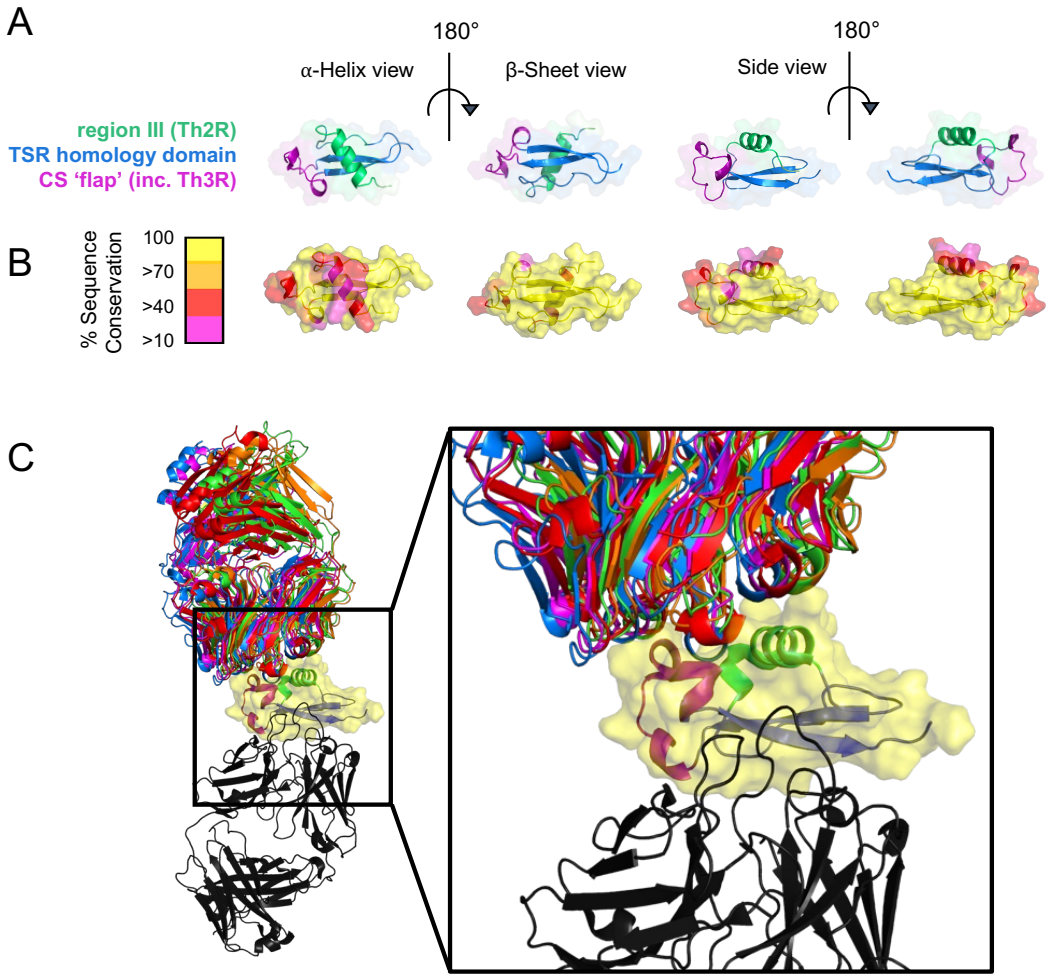


Figure 3.1. Structure of the C-terminal αTSR domain and antibody epitopes. (A) The structure of the αTSR epitope is composed of an amphipathic α-helix containing the Th2R T-cell epitope (green). The TSR homology region (blue) is composed of a pseudo-β-strand and the CS.T3 T-cell epitope, and two beta strands connected by the CS-flap (purple) which contains the Th3R T-cell epitope. (B) The surface of the αTSR domain is colored by sequence polymorphism across a panel of 15 haplotypes, showing a concentration of polymorphic residues across both Th2R and Th3R epitopes. (C) Structural alignment of antibodies that bind to the αTSR domain defining the α-epitope (1710 in blue, 234 in orange, 236 in red, 352 in green, 1488 in magenta) and mAb 1512 (black) highlighting the conserved β-epitope. (1710 PDB: 6B0S, 234 PDB:7RXI, 236 PDB: 7RXJ, 1512 PDB:7RXP, 1488 PDB:7RXL, 352 PDB:7S0X).

3.1.4 Aims

The novel characterization of RTS,S vaccination-elicited monoclonal antibodies provides an exciting opportunity for an expansion of our understanding of RTS,S-mediated anti-CtCSP immunity and its potential protective effects. In four of first five crystal structures of anti-CtCSP human mAbs that target the α-epitope, V_H3-21 encodes the heavy chain variable domain, which is reminiscent of the dominance of V_H3-30 and V_H3-33 responses to the NANP repeat domain. At that time, the only currently characterized monoclonal antibody to target the β-epitope was mAb 1512, also from the V_H3-21 lineage. Due to the effects of strain mismatch on vaccine efficacy, antibodies targeting the conserved face of CtCSP are more desirable, as they may provide strain-transcending protection. However, it is unclear whether these occur at a clinically relevant frequency. Further investigation into the immunological landscape presented by RTS,S vaccination-elicited CtCSP-targeting monoclonal antibodies is therefore essential to understand the importance and relevance of antibodies targeting conserved and polymorphic epitopes on CtCSP. In this chapter, I describe the X-ray crystal structures of ten monoclonal antibodies isolated from the MAL071 trial in complex with the CSP αTSR domain. These structures demonstrate the prevalence and breadth of antibodies targeting both conserved and polymorphic epitopes. The discovery of a novel epitopes and the diversity of antibodies targeting the conserved β-epitope can be now used to inform novel vaccine design as outlined in the next chapter.

3.2 Results

3.2.1 Determination of antibody epitopes by X-ray crystallography

Through our collaboration with PATH's Malaria Vaccine Initiative, we obtained a panel of CtCSP-binding mAbs isolated from MAL071 patients seven days after the final vaccine dose, already mapped by ELISA to bind CtCSP. To investigate the binding epitopes of the panel of CtCSP-targeting antibodies, antibody sequences were cloned into a mammalian expression vector for direct purification as Fabs as per standard lab protocol. Fabs were purified from clarified cell supernatants by protein G affinity chromatography and further purified by size-exclusion chromatography. Elution fractions corresponding to monomeric Fab were pooled and Fab-αTSR complex were formed in the presence of excess αTSR domain purified from bacterial expression. The Fab-αTSR complexes were additionally purified by size-exclusion chromatography to remove excess αTSR, and elution fractions corresponding to the Fab-αTSR complex concentrated for crystallization screens.

In all cases, crystals were screened for diffraction and full datasets were collected for crystals with diffraction maxima better than 3Å. All structures were solved by molecular replacement using separate search models for the αTSR domain, Fab variable domains, and Fab constant domains, and further built and refined using Coot and Phaser, respectively. Overall, we were able to determine the X-ray crystal structures of ten MAL071 mAbs in complex with the αTSR domain in resolutions ranging from 1.6-3.0Å, revealing, in high definition, the varied interactions that govern mAb binding to the αTSR domain. The CDR sequences and antibody lineages of previously characterized MAL07

mAbs and new MAL071 mAbs relevant to the following discussion are shown in **Figure 3.2**. All antibody amino acids follow Kabat numbering.

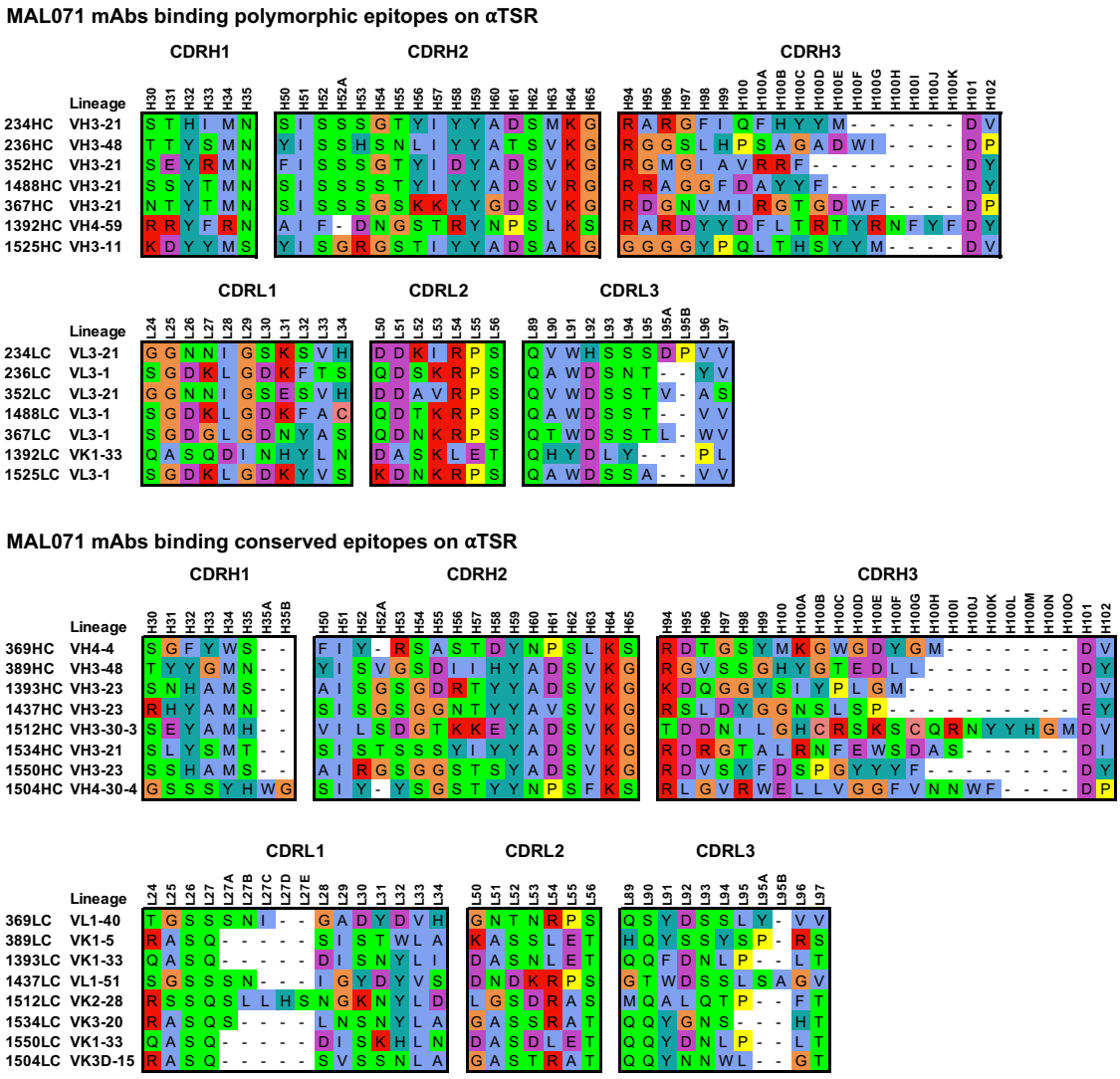


Figure 3.2. CDR sequences of MAL071 mAbs targeting the αTSR domain of CSP. Antibody VH and VL lineages are shown alongside CDR sequences as determined and aligned by AbYsis in clustal X default coloring, and in Kabat numbering. Hydrophobic (blue), positively charged (red), negatively charged (magenta) polar (green), aromatic (cyan), glycine (orange), proline (yellow), cysteine (pink), and unconserved gaps in white).

3.2.2 Fab 369, 1525, and 1392 bind the polymorphic α-epitope of αTSR

Out of ten Fabs for which crystal structures were obtained in complex with αTSR, Fab 367, 1392, and 1525 bound to the highly polymorphic face of the domain previously seen to bind both mAb 1710 and MAL071 mAbs 234, 236, 352, and 1488 **(crystallographic data table 3.1)**. To provide a general overview of the Fab-αTSR binding interface, the antibody binding sites (paratopes) are depicted on the surface of the αTSR domain in **Figure 3.3**. For illustrative purposes only, the paratopes are defined by residues which contribute over 20Å^2 of buried surface area, side chains or backbone segments forming direct hydrogen bonds and salt bridges, and interactions only mediated by a direct intermediate structured water.

3.2.2.1 Structural basis for Fab 367 binding to the αTSR domain

The X-ray crystal structure of Fab 367 (V_H3-21/V_L3-1) in complex with the αTSR domain was determined to 2.23Å resolution. The crystal asymmetric unit contained a single copy of the Fab-αTSR complex, and crystal lattice contacts are made between adjacent Fab constant domains, allowing for a large degree of flexibility in the variable domains and bound αTSR. This disorder within the crystal lattice is reflected by the individual B-factors shown in **Supplementary figure 3.1**; the electron density produced by refinement deteriorates substantially in the ligand binding region. As such, structured water molecules could only be assigned to the Fab constant domains, and some molecular details that would be expected from a 2.23Å structure are not interpretable in the antigen-binding site. This disparity between the structural model and data quality is further echoed by the R-work/R-free gap (0.236/0.288), which is slightly higher than might be expected

for a dataset of this resolution. Nevertheless, clear electron-density can be seen for key side-chains mediating contacts between Fab 367 and the αTSR domain, with a total buried surface area of 779Å^2.

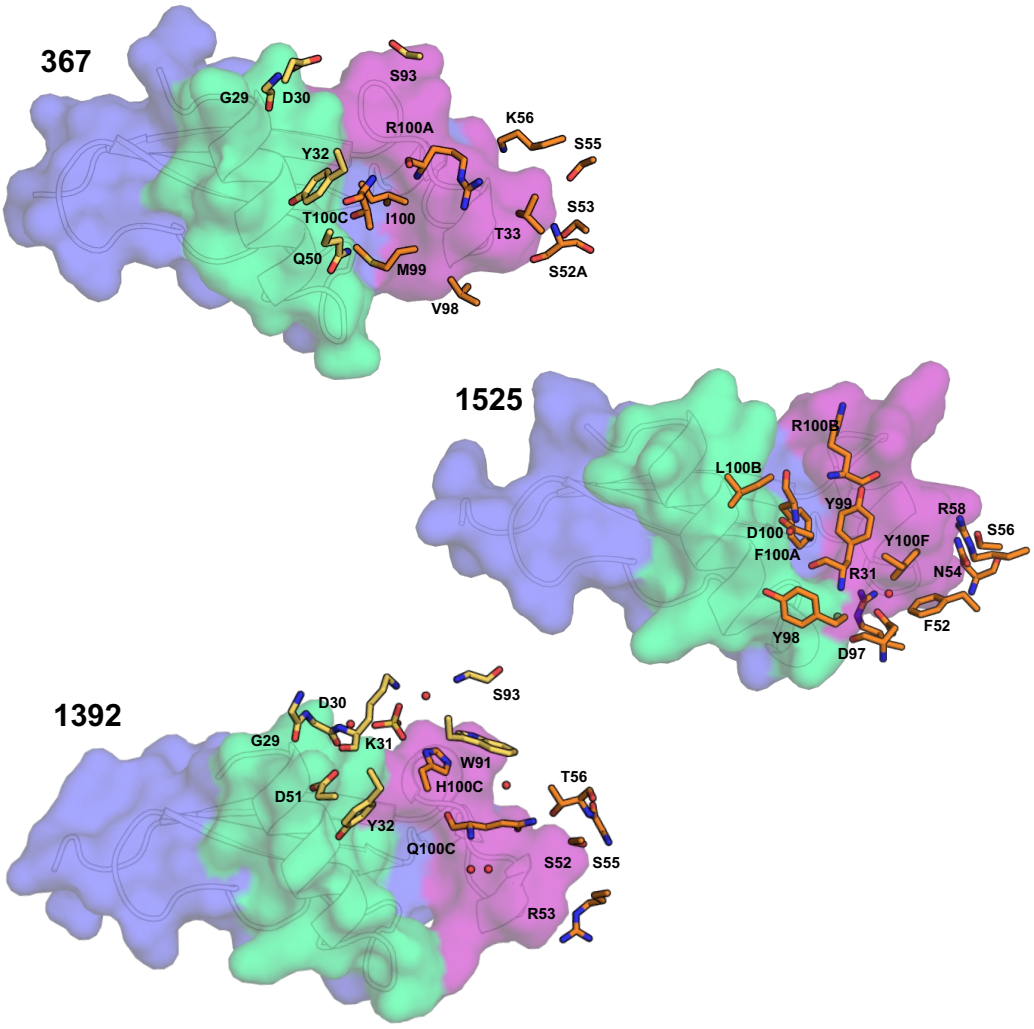


Figure 3.3. Paratopes of α-epitope binding Fabs 367, 1525, and 1392. Antibody paratope residues in sticks are superimposed on the αTSR surface colored by the CS-flap (purple), Th2R helix (green) and TSR homology domain (blue). Paratope residues are illustrated for heavy chain (orange) and light chain (yellow) residues that directly interact with the αTSR domain through hydrogen bonds, salt bridges, residues making over 20Å^2 of buried surface area, and residues interacting through a structured water (red sphere). Relevant residues side chains and backbones are shown as sticks and colored by element.

Alignment of the Fab 367 complex with previous MAL071 mAbs and mAb 1710 shows that the heavy and light chains are all positioned in proximity to interact with the CS-flap and Th2R helix, respectively, while its CDRH3 inserts into a hydrophobic core between these structural elements **(Figure 3.4A).**

3.2.2.2 Structural basis for Fab 1525 binding to the αTSR domain

The X-ray crystal structure of Fab 1525 (V_H3-11/V_L3-1) was also determined in complex with the αTSR domain to a resolution of 2.20Å. The asymmetric unit contains one Fab-αTSR complex, with clear electron density for all CDRs, allowing several networks of interactions mediating Fab 1525 binding to be identified, with a total buried surface area of 801Å^2. The crystallization condition which produced the best diffracting crystals (see Materials and Methods) contained 0.2 M magnesium sulphate. Several additional electron density features in the refinement difference map could be identified that could accommodate sulphate ions coordinated by nearby basic residues, one of which is on the periphery of the binding interface, coordinating CDRH3, CDRL1, CDRL3, and αTSR Th2R residues. Many other crystals that diffracted well grew in conditions not containing sulphate ions, and their binding may be simply due to a concentration of positively charged residues on the αTSR surface. Although mAb 1525 is from the V_H3-11 lineage, it binds the α-epitope in the αTSR domain with similar characteristics to V_H3-21 mAbs. Alignment of mAb1525 (V_H3-11) binding to αTSR shows the variable regions of

Fab1525 interact with the αTSR using a similar angle of approach as Fab367 (V_H3-21) **(Figure 3.4A, B).**

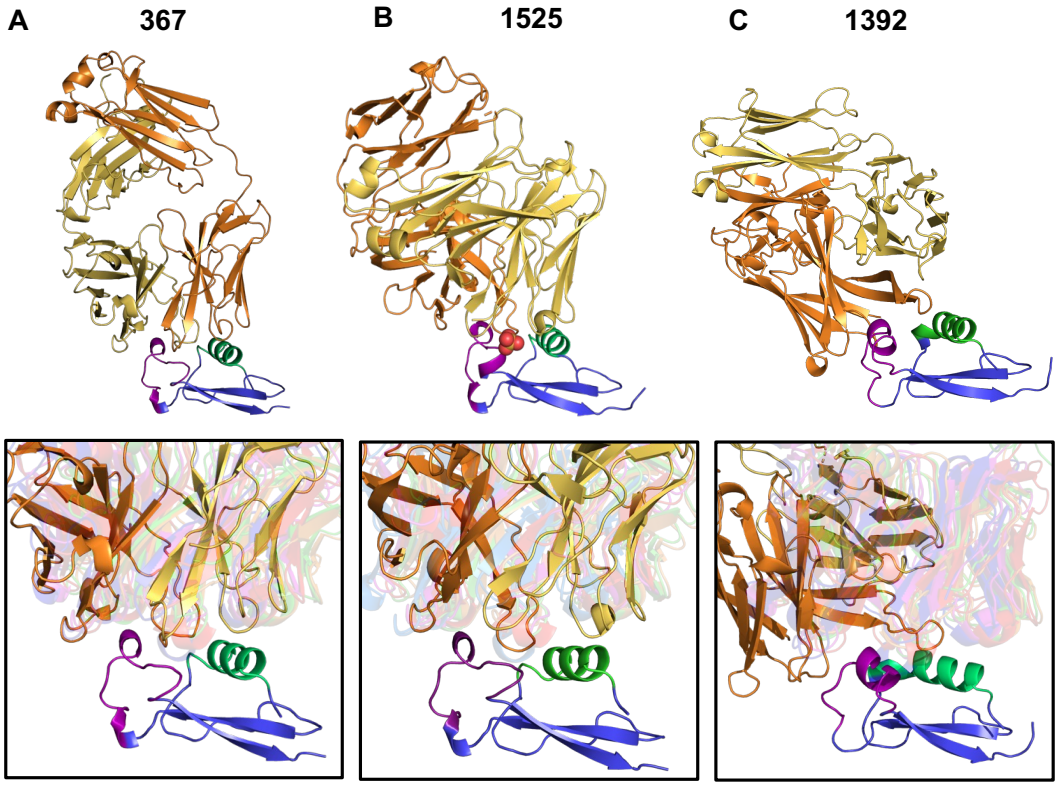


Figure 3.4. Structural basis for binding of Fabs 367, 1525, and 1392 to αTSR. Crystal structures of (A) Fab 367, (B) Fab 1525, and (C) Fab 1392 with the αTSR domain shows that these antibodies bind to the polymorphic CS-flap and Th2R helix. Structural alignment against other α-epitope binding mAbs shown in Figure 3.2 reveals that Fab 367 and 1525 bind from the same angle of approach, while Fab1392 is more tilted compared to these. Heavy chains (orange), light chain (yellow), CS-flap (purple), TSR homology domain (blue) are shown in cartoon ribbons. Alignment with other antibodies is shown in transparent cartoon representation.

3.2.2.3 Structural basis for Fab 1392 binding to the αTSR domain

The X-ray crystal structure of Fab 1392 (V_H4-59/V_K1-33) in complex with αTSR was determined to a resolution of 1.63Å. The asymmetric unit contained a single Fab-αTSR complex, with crystal lattice contacts mediated through all domains except the variable light chain domain. The 1392 Fab binds the αTSR domain solely through its heavy chain, forming a total buried surface area of 823Å^2. The mobility of the variable light domain due to lack of crystal contacts or antigen binding is apparent in the electron density difference map. Viewing the structure by B-factors further shows flexibility of this domain in the structure **(Supplementary figure 3.1)**. Due to its angle of approach, all CDRHs of mAb 1392 are within distance to interact with the CS-flap of the αTSR domain. The 20 amino acid CDRH3 of mAb 1392 contains eight aromatic residues, four arginine residues, and three aspartate residues, and forms an extended beta strand which extends further than the other CDRs to interact with both CS-flap, Th2R α-helix, and the hydrophobic pocket between them **(Figure 3.4B)**.

3.2.3 MAL071 mAbs target the α-epitope through conserved interactions

All previously characterized mAbs binding the polymorphic α-epitope are from the V_H3-21 or the closely related V_H3-48, which interact with the CS-flap (Th3R T-cell epitope). In their X-ray crystal structures, a stretch of serine and threonine in CDRH2 residues 52-55 form a hydrogen bond network with the side chains and backbones of Asp356, Glu357, or both, projecting outwards from the face of the domain. A nearby arginine residue contributes to the interaction in the Fab 352 and Fab 1488 structures. This interaction is maintained in the three new structures of Fab 367, Fab 1525, and Fab 1392 **(Figure 3.5A)**;

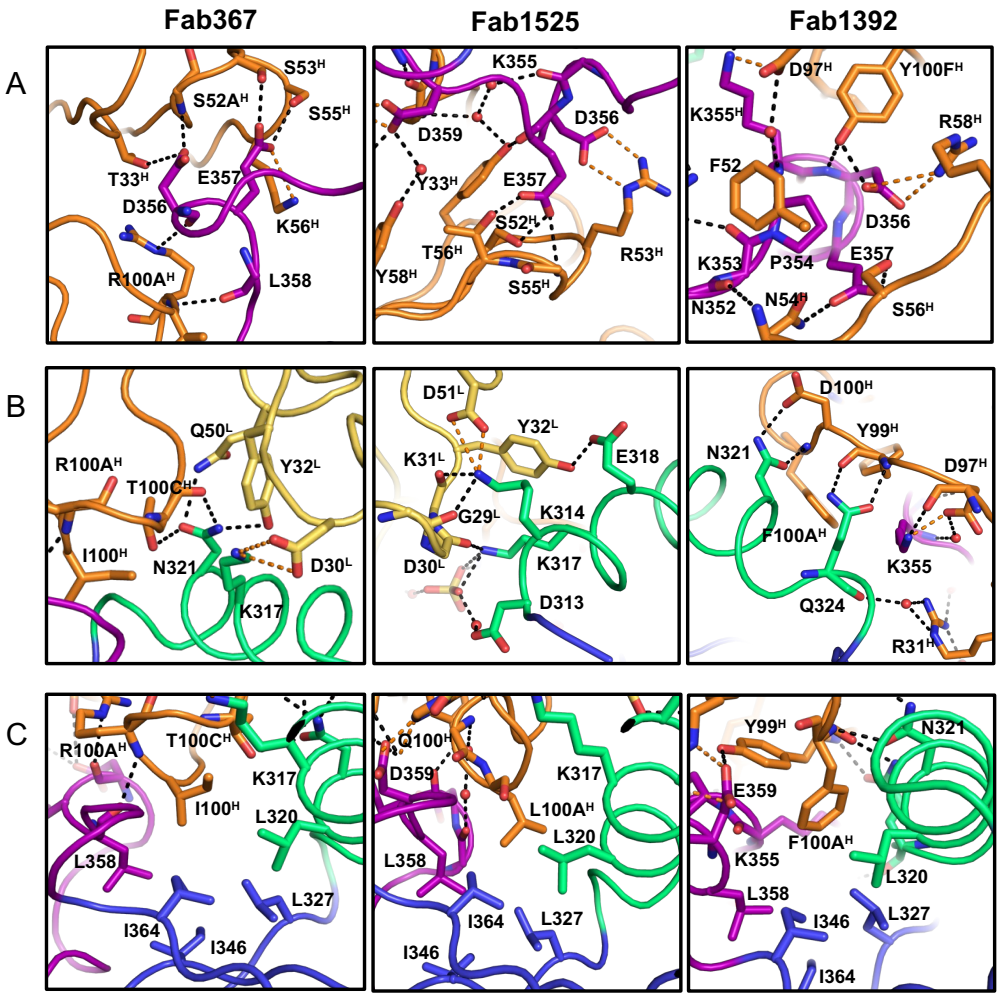


Figure 3.5. Conserved interactions mediating binding of Fab 367, 1525, and 1392 to the α-epitope. (A) Binding to the CS-flap residues Asp356 and Glu357 is mediated by serine and threonine residues of CDRH2. In the case of Fab 367, 1525, and 1392, this interaction is also supplemented by a nearby arginine for CDR H3 (Fab 367) or CDR H3 (Fabs 1525, 1392) . (B) Binding to the CS-flap is mediated through salt-bridge formation with Lys314 and Lys317, coordination of Asn 321 and Gln324, and hydrogen bond formation with Glu318. (C) All mAbs which bind the α-epitope insert a hydrophobic CDRH3 residue into the conserved pocket formed by Leu320, Leu327, Ile346, Leu358, and Ile364.

Fab367, also of the V_H3-21 lineage, utilizes CDRH2 to interact with both Asp356 and Glu357, with an additional hydrogen bond contributed by CDRH2 Lys53. Fab 1525 is of the V_H3-11 lineage, with substantial sequence similarity in CDRH2, except for Arg53,

which would be a serine in V_H3-21 mAbs. Fab 1525 CDRH2 Arg53 is still flanked by Ser52, Ser 55, and Thr56 which participate in a network of hydrogen bonds with Glu357, while Arg53 forms a salt bridge with Asp356. In Fab 1392, encoded by the V_H4-59 lineage, CDRH2 Asn54 and Ser56 interact with Glu357 while the nearby Arg58 forms a salt bridge with Asp356.

In addition to sharing closely related heavy chain lineages, previously characterized mAbs are of the V_L3-21 or V_L3-1 lineages. These lineages share sequence similarity in CDRL2, and to a lesser extent CDRL1. In the crystal structures of V_H3-21 and V_L3-1 Fabs in complex with αTSR, the light chain interacts with the side chains of Th2R α-helix residues that project out from the surface of the domain. Specifically, in Fabs 234, 235, 352 and 1488, CDRL2 Asp51 or 52 forms a salt-bridge with Lys314, Lys317 is coordinated through either salt bridge or hydrogen bonds, and Glu318 and Asn321 participate in a hydrogen bonding network with both CDRL1 and CDRL2 residues. Although this interaction is not identical in these newly characterized mAbs, several features are retained **(Figure 3.4B)**. Fab367 is also of the V_L3-1 lineage, forming a salt bridge between CDRL1 Asp30 and Lys317 as well as a hydrogen bonding network to Asn321 with its CDRL2 and CDRH3. Fab 1525 is also of the V_L3-1 lineage and forms a salt bridge with Lys314 through CDRL2 Asp51 and a hydrogen bond between CDRL1 backbone and Lys317. Fab 1392 approaches the domain from a different angle and does not bind through its light chain. Although CDRH3 of 1392 is longer than 90% of CDRH3s found in the natural human antibody repertoire(24), it does not extend far enough to interact with either Lys314 or Lys317 of Th2R. Instead, its CDRH3 forms a series of

hydrogen bonding interactions with Asn324 and Asn321, reminiscent of those seen in previous structures of Fabs bound to this domain.

Although varying significantly in both sequence and length, all CDRH3 of previously characterized mAbs insert a hydrophobic residue into the conserved core formed by Leu320, Leu 327, Ile346, Leu358, and Ile364 of the αTSR domain **(Figure 3.5C)**. Similarly, Fab367 CDRH3 inserts Ile100 into the hydrophobic pocket forming 110Å^2 of buried surface area, Fab1525 CDRH3 inserts Leu100A forming a BSA of 150Å^2, and Fab1392 CDRH3 inserts Phe100A forming a BSA of 149Å^2. It is possible that the conserved interactions mediating contacts with both the Th2R α-helix and the CS-flap produce a scaffold that provides the opportunity for substantial sequence diversity in the CDRH3.

3.2.4 Fabs 369, 389, 1393, 1437, 1534, and 1550 bind the β-epitope of αTSR

Out of the ten Fabs for which crystal structures were obtained in complex with αTSR, six Fabs bound to the opposite side of the domain, which was previously shown to bind MAL071 mAb 1512, and was termed the β-epitope **(crystallographic data tables 3.2 and 3.3)**. Their CDR sequences, together with previously characterized human mAbs from the MAL071 trial which bind this epitope, are shown in **Figure 3.2**. As before, the antibody binding sites (paratopes) have been identified from their interactions on the surface of the αTSR domain in **Figure 3.6 and Figure 3.7,** alongside previously characterized β-binder mAb 1512. The paratopes were defined as residues which contribute over 20Å^2 of buried surface area, side chains or backbone segments forming

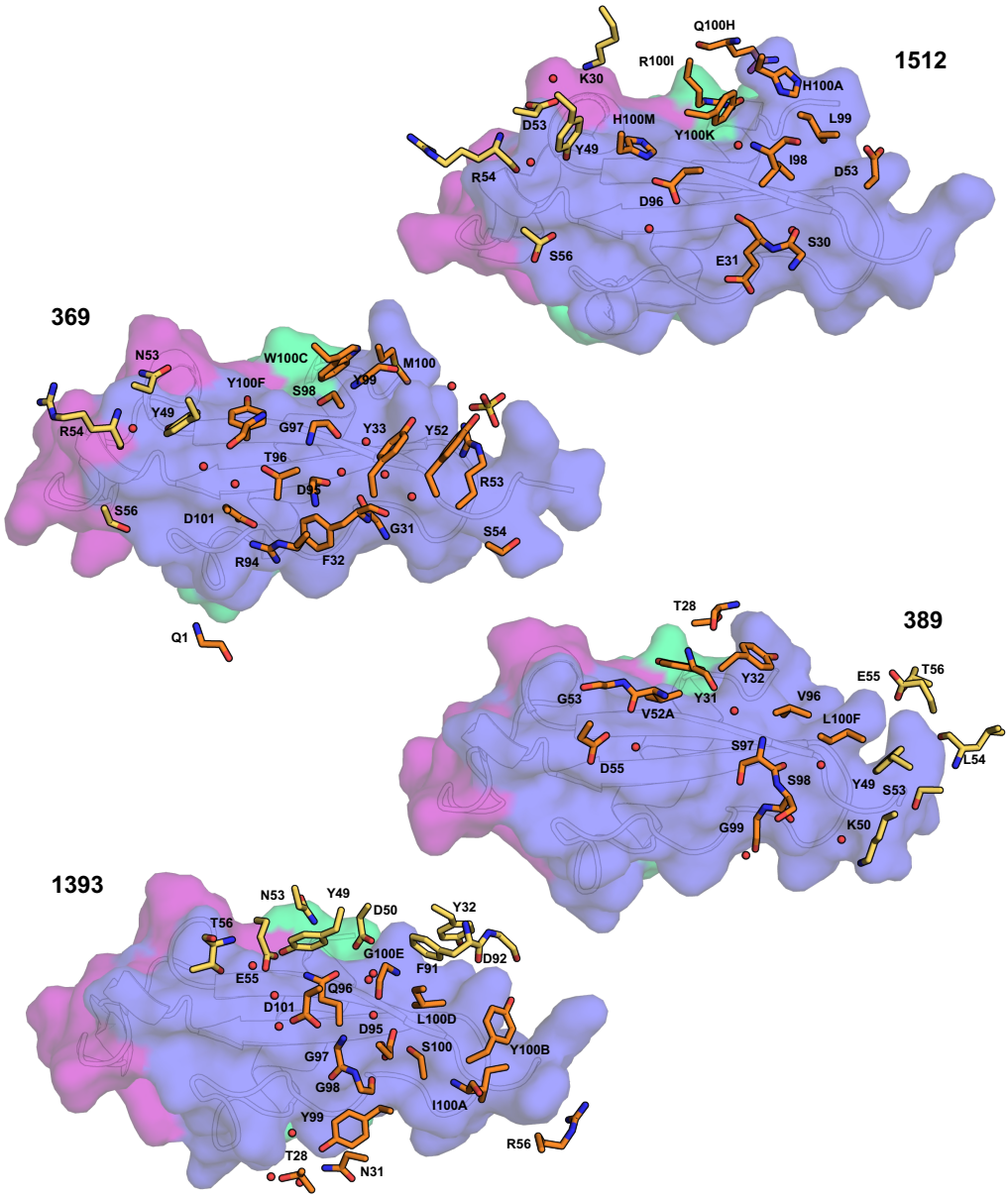


Figure 3.6. Paratopes of α-epitope binding Fabs 1512, 369, 389, and 1393. Antibody paratopes are shown superimposed on the αTSR surface colored by CS-flap (purple), Th2R helix (green) and TSR homology domain (blue). Paratopes are illustrated by their heavy chain (orange) and light chain (yellow) residues directly interacting with the αTSR domain through hydrogen bonds, salt bridges, residues making over 20Å^2 of buried surface area, and residues interacting through a structured water (red sphere). Relevant residues side chains and backbones are shown as sticks and colored by element.

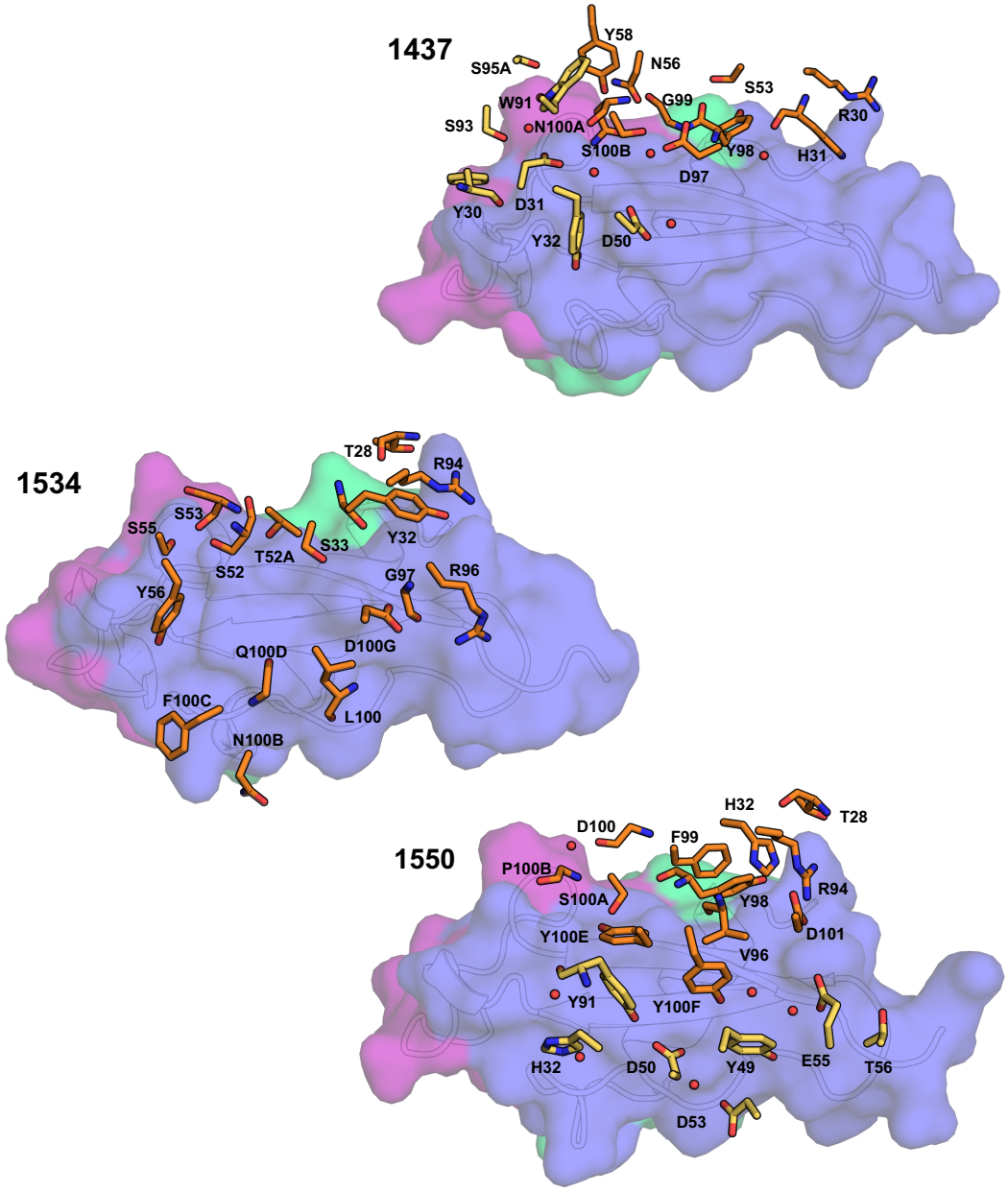


Figure 3.7. Paratopes of α-epitope binding Fabs 1437, 1534, and 1550. Antibody paratopes are shown superimposed on the αTSR surface colored by the CS-flap (purple), Th2R helix (green) and TSR homology domain (blue). Paratopes are illustrated by their heavy chain (orange) and light chain (yellow) residues directly interacting with the αTSR domain through hydrogen bonds, salt bridges, residues making over 20Å^2 of buried surface area, and residues interacting through a structured water (red sphered). Relevant residues side chains and backbones are shown as sticks and colored by element.

direct hydrogen bonds and salt bridges, and water-mediated interactions. In contrast to the largely conserved mode of interaction of α-epitope binding antibodies, the CDR sequences, angle of approach, and paratopes differ substantially amongst mAbs targeting the conserved β-epitope.

3.2.4.1 Structural basis for Fab 369 binding to the αTSR domain

The X-ray crystal structure of Fab 369 in complex with αTSR was determined to a resolution of 2.13Å. The asymmetric unit contains one copy of the Fab-αTSR complex and clear electron density can be visualized for all CDRs and relevant side-chains. Multiple ordered waters can be seen in the interface that mediate interactions between CDR residues and the αTSR domain. The crystallization condition that produced the best diffracting crystals contained 0.17M ammonium sulphate (see Materials and Methods). Following refinement, additional electron density could be seen for a sulphate ion on the periphery of the interface between the αTSR domain and Fab 369.

Fab 369 binds the C-terminal region of the αTSR domain, forming an overall buried surface area of 954Å^2 **(Figure 3.8A)**. The heavy chain of Fab369 produces 800Å^2 of BSA upon binding and mediates the majority of interactions. The only direct interaction made by a light-chain residue is a hydrogen bond between CDRL2 Tyr49 to the carboxylate side chain of Glu365 **(Figure 3.8B)**. Uniquely, the heavy chain N-terminal Gln1 forms a salt-bridge with Glu330, which is also coordinated by CDRH3 Arg94 **(Figure 3.8B).** The CDRH3 traverses the underside of the domain, forming a network of hydrogen bonds with Trp331, Arg345, Ile368 backbone, and Lys370 through tightly bound water molecules, while also directly coordinating the side chains of Lys370 and Glu310 **(Figure**

3.8C). Although the conserved Trp331 is sandwiched by Arg345 and Lys367, CDRH3 Tyr100F stacks perpendicularly to the indole group while simultaneously coordinating nearby residues through both its backbone and side chain hydroxyl **(Figure 3.8D)**.

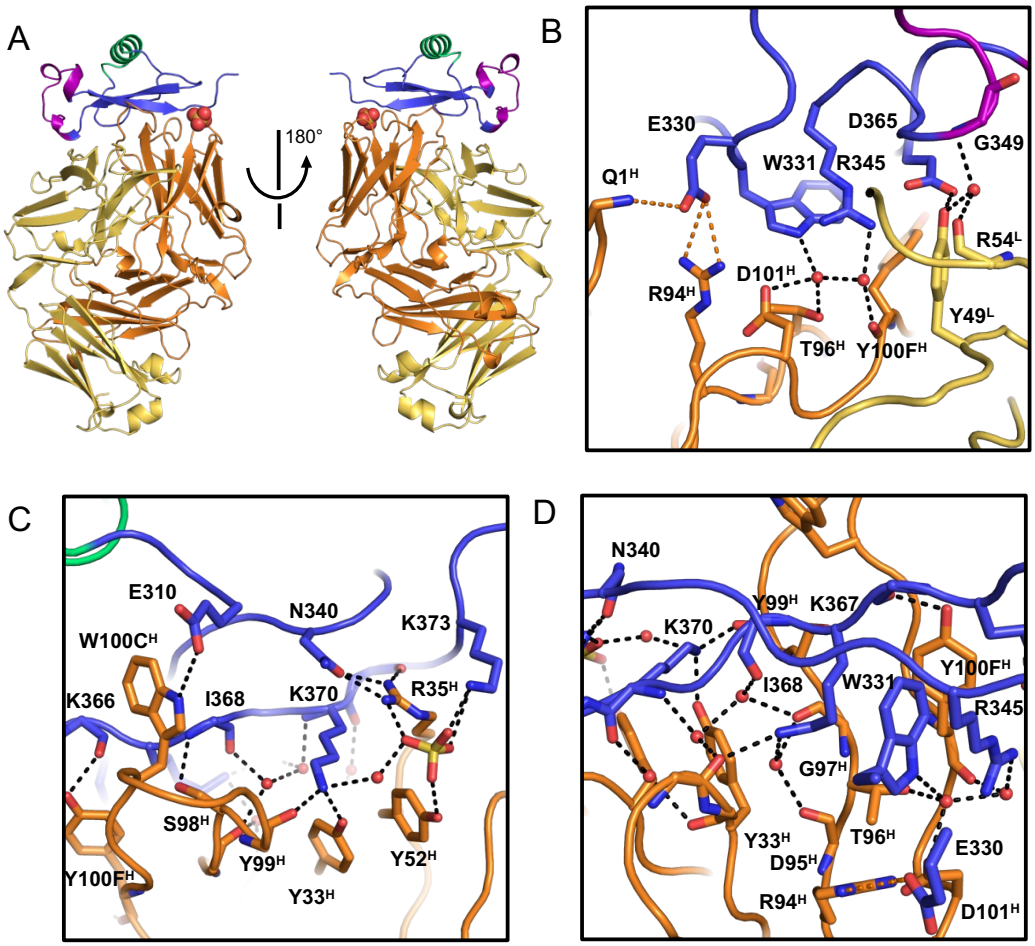


Figure 3.8. Structural basis for Fab 369 binding the αTSR domain of PfCSP. (A) Fab369 binds the conserved β-epitope of the αTSR domain, with a sulphate ion in the periphery of the binding interface. Antibody heavy chain (orange) and light chain (yellow) as well as αTSR (CS-flap in purple, TSR homology domain in blue, Th2R helix in green) are shown in cartoon representation. (B) CDRL2 Tyr49 forms a hydrogen bond with Asp365, and CDRH3 Arg94 forms a salt bridge with Glu330. (C) Fab369 forms a hydrogen binding network with the backbone of the TSR homology domain (D) Alternative view showing Tyr100F stacking against Trp331. Relevant side chains and backbone segments shown as sticks colored by element. Ordered waters relevant to binding are shown as red spheres. Dashes lines represent hydrogen bonds (black) and salt-bridges (orange).

3.2.4.2 Structural basis for Fab 389 binding to the αTSR domain

The X-ray crystal structure of Fab 389 in complex with αTSR was determined to a resolution of 2.09Å. The asymmetric unit contained two copies of Fab-αTSR complex, and, in each, the bound domain interacts in the same fashion. The crystallization condition that produced the best diffracting crystals contained 2.0 M ammonium sulphate and 0.2 M lithium sulphate, and electron density that could be attributed to sulphate ions can be seen in multiple parts of the structure. However, as they are not in the antibody binding interface, they are not shown and likely not functionally relevant.

Fab 389 binds the conserved face of the αTSR domain **(Figure 3.9A)**, forming a total buried surface area of 754Å^2, of which 532Å^2 is contributed by the heavy chain. The CDRH3 of Fab 389 binds to αTSR as an elongated β-strand making multiple backbone hydrogen bonds as it perpendicularly crosses the β-strands of the αTSR domain **(Figure 3.9B)**. CDRH2 Asp55 forms a salt-bridge interaction with Arg345 and coordinates a water molecule extending the interaction to the Trp331 indole. The nearby CDRH1 forms a network of hydrogen bonds with the backbone of Ile368 and the C-terminal Glu310 residue **(Figure 3.9C).** Through structured water molecules, CDRH1 Tyr31 carbonyl and CDRL2 Lys50 amine extend their interactions to the domain backbone **(Figure 3.9C and D)**. Although the majority of BSA is contributed by the heavy chain, CDRH2 of the light chain interacts with all four terminal residues of the domain (Lys370-Lys373) **(Figure 3.9D).**

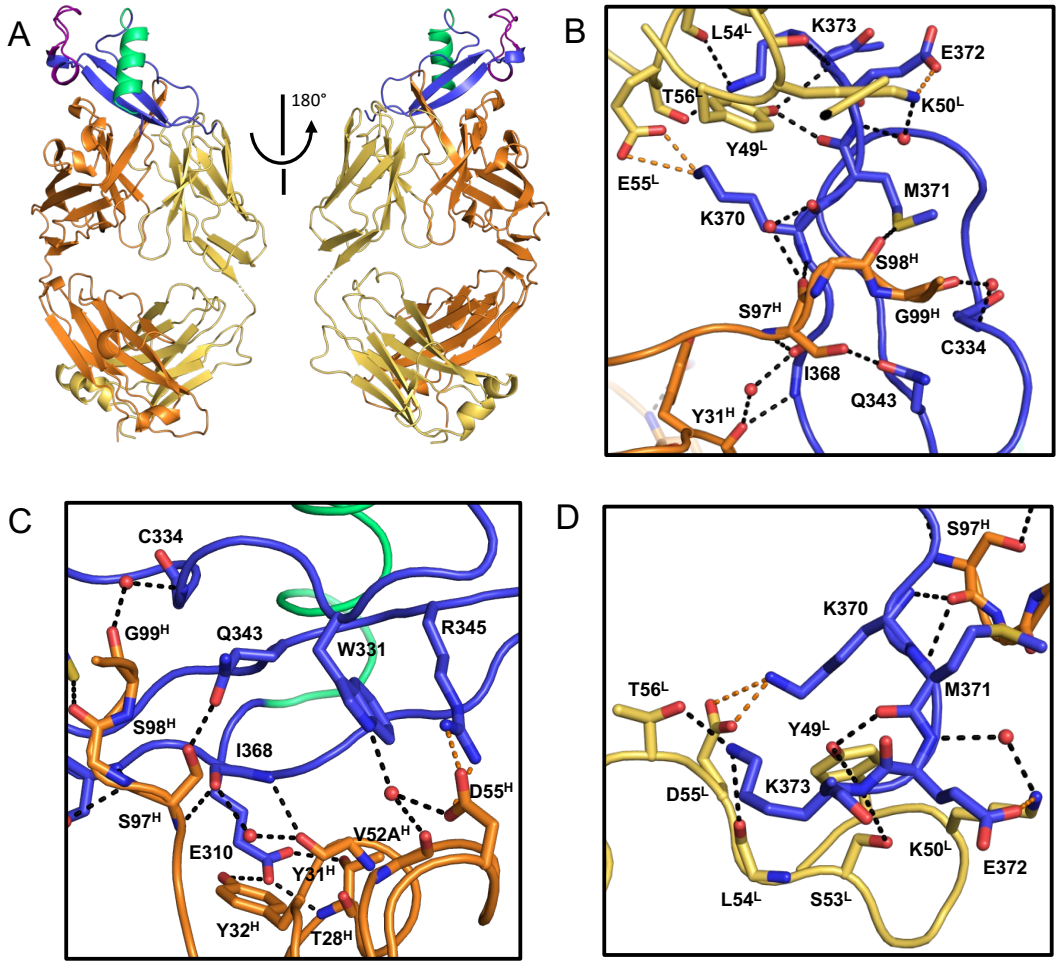


Figure 3.9. Structural basis for Fab 389 binding the αTSR domain of PfCSP. (A) Fab389 binds the conserved β-epitope of the αTSR domain interacting primarily through the heavy chain. Antibody heavy chain (orange) and light chain (yellow) as well as αTSR (CS-flap in purple, TSR homology domain in blue, Th2R helix in green) are shown in cartoon representation. (B) CDRH3 of Fab389 forms an elongated β-strand traversing the underside of the domain. (C) CDRH2 Asp55 forms a salt bridge with Arg345 and, together with Val52 backbone carbonyl, coordinates a structured water which interacts with Trp331 (D) CDRL2 forms an elaborate network of interactions with all four terminal residues of the domain. Relevant side chains and backbone segments shown as sticks colored by element. Ordered waters relevant to binding shown as red spheres. Dashes lines represent hydrogen bonds (black) and salt-bridges (orange).

3.2.4.3 Structural basis for Fab 1393 binding to the αTSR domain

The X-ray crystal structure of Fab 1393 in complex with αTSR was determined at a resolution of 1.80Å. The asymmetric unit contained a single copy of Fab and αTSR in complex, producing a buried surface area of 769Å^2. In Fabs 1525, Fab 369, and 389 interact with the underside of the αTSR domain through their CDRH3, thereby limiting the access of the light chain CDRs to bind the domain αTSR. In 1393, the αTSR domain is bound in the groove between the heavy and light chain, and both contribute to the interaction through all CDRs **(Figure 3.10A)**.

Overall, the binding of Fab 1393 to αTSR relies heavily on both hydrogen bonding interactions and water-mediated hydrogen bonds. CDRH1 and CDRH3 of Fab 1393 bind the αTSR Glu330 side chain and backbone through bridging water molecules, and together with CDRL2 bind the tightly stacked Trp311 and Arg345. The CDRH3 wraps under the domain and. together with CDRL2, Asp50 coordinates a network of four water molecules that mediate binding to Lys367, Gln343, and the backbone of Ile368 **(Figure 3.10B)**. The CDRL2 side chains coordinate the backbone of Ile368 and Lys366, as well as the side chains of Arg345 and Glu365, while on the other side of the domain the CDRH3 interacts with Lys 370 and Glu372, altogether strongly engaging the continuous stretch of residues between Glu365 and Glu372 **(Figure 3.10C and D)**. The binding to this region is further stabilized by CDRH2 Arg56, which forms a salt bridge with Glu372, the only salt-bridge interaction binding interface of Fab 1393 with αTSR **(Figure 3.10D)**.

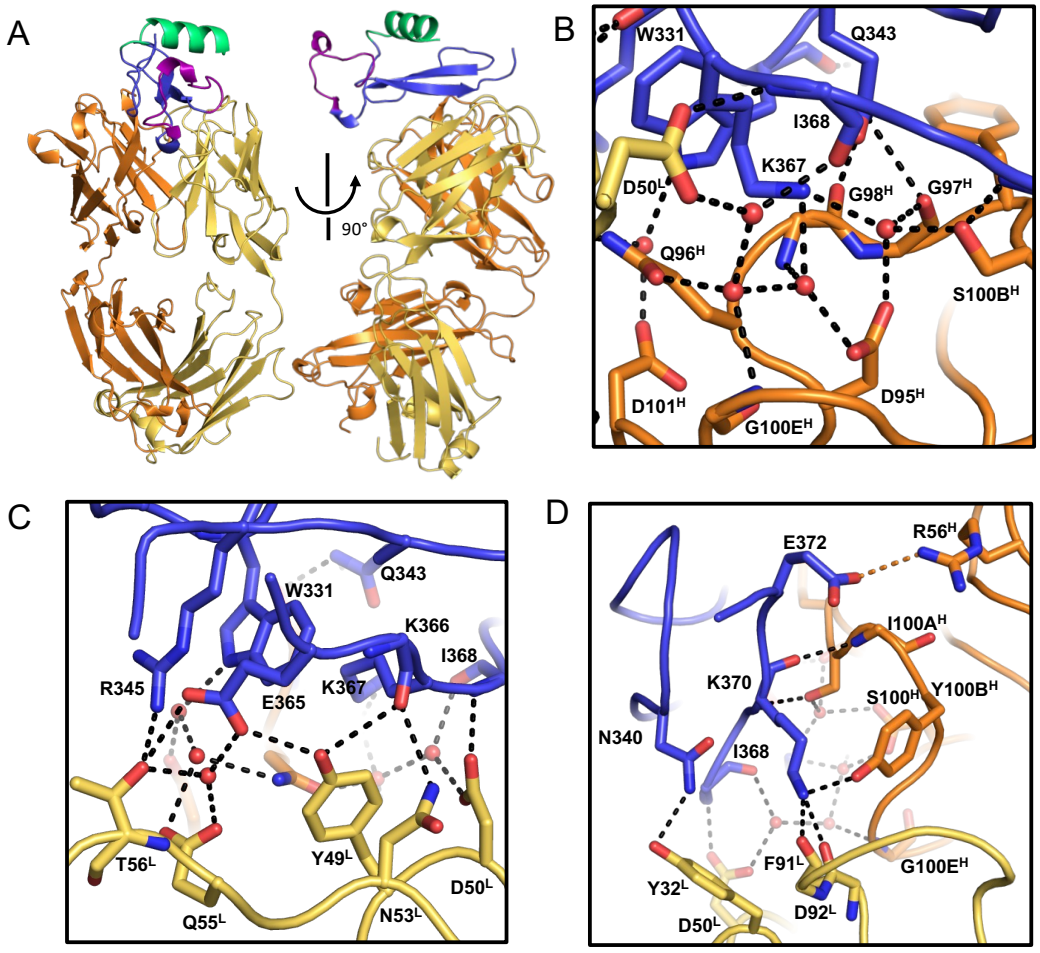


Figure 3.10. Structural basis for Fab 1393 binding the αTSR domain of PfCSP. (A) Fab1393 binds the conserved β-epitope with αTSR in the groove between the heavy and light chain. Antibody heavy chain (orange) and light chain (yellow) as well as αTSR (CS-flap in purple, TSR homology domain in blue, Th2R helix in green) are shown in cartoon representation. (B) CDRH3 binding to the underside of the domain coordinates a network of structured water molecules that extend the binding interaction with αTSR. (C) CDRL2 side chains interact with Arg345 and Glu365 side chains and the Ile368 and Lys366 backbones. (D) CDRH2 Arg56 forms the only salt bridge in the interface of Fab 1393 with Glu372, contributing to the stabilization of Glu365-Glu372 by CDRH3 and CDRL2. Relevant side chains and backbone segments are shown as sticks colored by element. Ordered waters relevant to binding shown as red spheres. Dashes lines represent hydrogen bonds

3.2.4.4 Structural basis for Fab 1437 binding to the αTSR domain

The X-ray crystal structure of Fab 1437 in complex with αTSR was determined at a resolution of 1.86Å. The asymmetric unit contains a single copy of Fab and αTSR, forming a total surface area of 840Å^2. Although the binding epitope of Fab 1437 is dominated by residues of the thrombospondin homology region, the angle of approach of Fab 1437 differs substantially from previous characterized Fabs, allowing interactions with both Th2R and Th3R residues on the side of the domain from both the heavy and light chains **(Figure 3.11A)**.

The CDRL1 of Fab 1437 closely interacts with Arg345-Ser350; the Tyr32 side chain hydroxyl interacts with both Arg345 and Ile346 through a structured water molecule, the adjacent CDRL1 Asp31 forms a salt bridge with Lys347, and Tyr30 coordinates Gly349 through its side backbone carbonyl and Ser350 through its side-chain hydroxyl **(Figure 3.11B)**. The Asp50 side chain of CDRL2 forms a salt bridge with Arg345 and coordinates Trp331 through a structured water molecule. Viewed facing the CS-flap, the CDRL3 interacts with the C-terminal portion of the CS-flap directly through Ser95, and via a structured water with Ser93 **(Figure 3.11C)**. The interaction with the CS-flap is also mediated by CDRH3 Asn100 and CDRH2 Tyr98 side chain on its other side. While the heavy chain CDRs binds the conserved Ile364, Lys366, and Ile368, they also form hydrogen bonds with Th2R Asp313 through the CDRH3 Tyr98 and CDRH2 Ser53 hydroxyl groups **(Figure 3.11D)**.

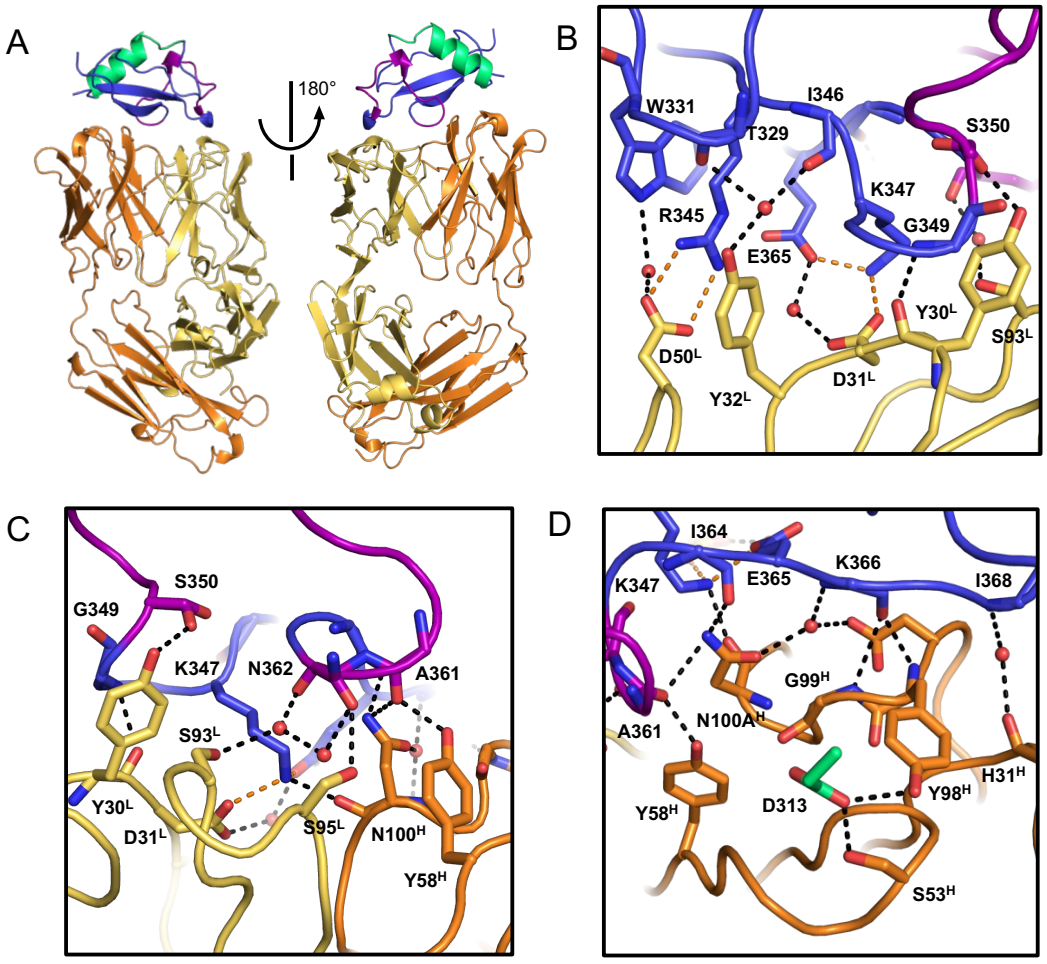


Figure 3.11. Structural basis for Fab 1437 binding the αTSR domain of PfCSP. (A) Fab 1347 binds the β-epitope from a side approach, interacting with both CS-flap and Th2R residues. Antibody heavy chain (orange) and light chain (yellow) as well as αTSR (CS-flap in purple, TSR homology domain in blue, Th2R helix in green) are shown in cartoon representation. (B) CDRL1 Asp31 forms a salt-bridge with Lys347 and CDRL2 Asp50 forms a salt-bridge with Arg345. (C) Both light and heavy chain residues interact with CS-flap residues Ser350, Asn362, and Ala361. (D) CDRH2 Ser53 and CDRH3 Tyr98 interact with the polymorphic Th2R helix Asp313, while the rest of CDRH3 makes several backbone contacts with the conserved TSR homology domain. Relevant side chains and backbone segments shown as sticks colored by element. Ordered waters relevant to binding shown as red spheres. Dashes lines represent hydrogen bonds (black) and salt-bridges (orange).

3.2.4.5 Structural basis for Fab 1534 binding to the αTSR domain

The X-ray crystal structure of Fab 1534 in complex with the αTSR domain was determined at a resolution of 2.8Å. The asymmetric unit contains a single copy of Fab and αTSR, with contacts entirely through the heavy chain, forming a buried surface area of 868Å^2. The higher R values and R_{work}/R_{free} gap of 5.4% (0.288/0.340) could suggest some disagreement between the model and the data. Zanuda(25) was used confirm whether the data were processed in the correct space group, with the results agreeing with the chosen space group of $P22_12_1$. The average B-factors of 85 Å^2 reflect some disorder or flexibility in the structure, as well as potential issues with the data collection. Nevertheless, clear electron density can be seen for the CDR loops and side chains, and multiple networks of interactions can be determined. Due to the lower resolution of this structure relative to those of the remaining beta binders, no ordered waters could be seen in the binding interface.

The αTSR domain binds Fab 1534 in a groove formed between CDRH3 and CDRH1-2, allowing the Fab CDRs to make hydrogen bonding interactions across the conserved face of the domain **(Figure 3.12A)**. In addition to making several backbone interactions, CDRH3 binds the Lys370 backbone through the Arg96 side-chain guanidinium, Glu330 hydrogen bonds with the side chain of Asn100B, and Lys367 forms a salt bridge with Asp100G **(Figure 3.12B-C)**. On the other side of the interface, CDRH2 residues interact with the Glu365 and the Lys366 backbone, and CDRH2 hydrogen bonds with Glu310, Ile368, and Lys370. Lastly, the guanidinium group of Arg345 is 4Å from the CDRH2 Tyr56 phenol ring, within distance to form a cation-pi interaction **(Figure 3.12C)**.

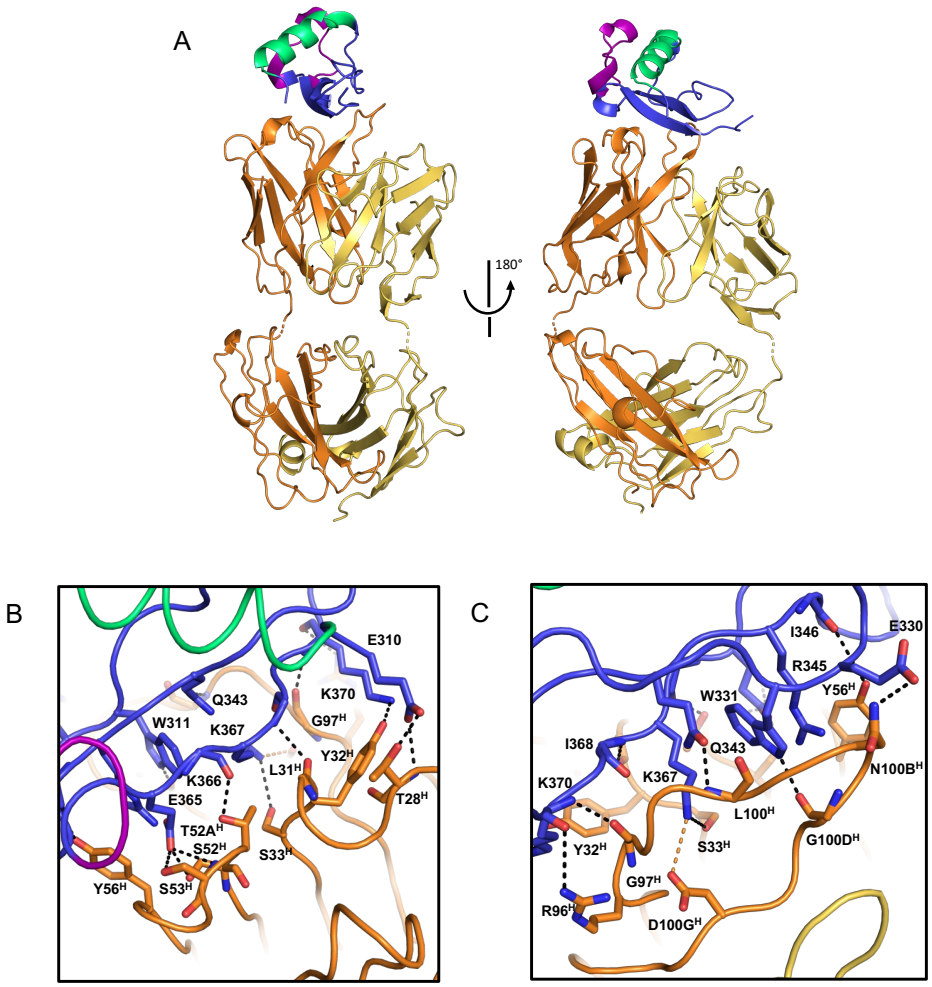


Figure 3.12. Structural basis for Fab 1534 binding the αTSR domain of PfCSP. (A) Fab1534 binds the β-epitope from a side approach solely through its heavy chain, with the αTSR in the groove between CDRH3 and CDRH1-2. Antibody heavy chain (orange) and light chain (yellow) as well as αTSR (CS-flap in purple, TSR homology domain in blue, Th2R helix in green) are shown in cartoon representation. (B) On one side of the interface, CDRH1 interacts with Glu310 and Lys370, and CDRH2 forms a hydrogen bonding network with Glu356 and the backbone of Lys366. (C) On the other side of the interface, CDRH3 tracks the side of the domain forming multiple hydrogen bonds and a salt bridge between Asp100G and Lys367. Relevant side chains and backbone segments shown as sticks colored by element. Ordered waters relevant to binding shown as red spheres. Dashes lines represent hydrogen bonds (black) and salt-bridges (orange).

3.2.4.6 Structural basis for Fab 1550 binding to the αTSR domain

The X-ray crystal structure of Fab 1550 in complex with the αTSR domain was determined at a resolution of 2.0Å. The asymmetric unit contains a single copy of Fab and αTSR, forming a complex with an interface buried surface area of 804Å^2, primarily by the heavy chain (546Å^2). The electron density in the structure clearly allows all CDRs, side-chain conformations, and many ordered waters to be assigned, revealing in detail the interactions that mediate Fab 1550 binding.

Fab 1550 approaches the αTSR domain from the opposite side to the CS-flap, binding the membrane-proximal portion of the β-epitope primarily through its CDRH3 and CDRL2 (**Figure 3.13A**). The heavy and light chains both interact with the domain through multiple salt-bridge interactions **(Figure 3.13)**. The CDRH1 His32 imidazole forms a salt bridge with Glu310, CDRH3 Tyr100F and CDRL2 Glu55 form a salt bridge network with Lys370, and CDRL2 Asp50 forms a salt bridge with Lys367 **(Figure 3.13B)**. As well as interacting with many of the side chains of the central β-strand of the domain, CDRH3 forms hydrogen bonds with both backbone amide and carbonyls of Lys366 and Ile368 **(Figure 3.13C)**. Although the conserved Trp331 is inaccessible for hydrophobic stacking as it is sandwiched between Arg345 and Lys 367, the binding of CDRH3 to the conserved face of the domain positions Tyr100E to stack perpendicular to Trp331, and CDRL3 Tyr91 to form a hydrogen bond with the Trp331 indole group **(Figure 3.13D)**. The backbone carbonyl of CDRL3 Tyr91 additionally coordinates a water molecule, which interacts with Arg345, also forming a hydrogen bond with CDRL1 His32.

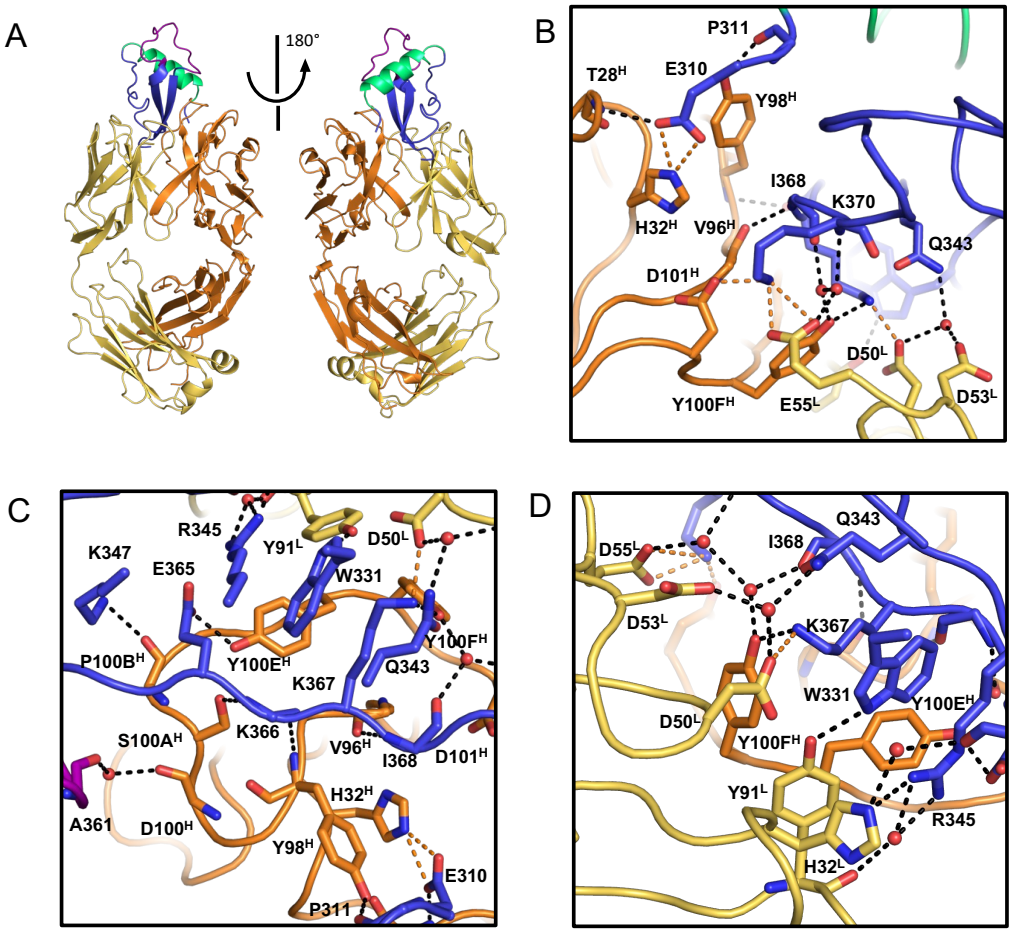


Figure 3.13. Structural basis for Fab 1550 binding the αTSR domain of PfCSP. (A) Fab1550 binds the β-epitope from the opposite direction to the CS-flap, engaging the membrane-proximal region of the domain. Antibody heavy chain (orange) and light chain (yellow) as well as αTSR (CS-flap in purple, TSR homology domain in blue, Th2R helix in green) are shown in cartoon representation. (B) CDRH1 His32 forms a hydrogen bond with Glu310, CDRH3 Asp101 and CDRL2 Glu55 form a salt bridge with Lys370, and CDRL2 Asp50 forms a salt-bridge with Lys366. (C) CDRH3 wraps around the TSR homology domain placing Tyr100E in position to perpendicularly stack against Trp311, while coordinating multiple contacts through its side chains and backbone. (D) CDRL1 and CDRL3 further coordinate the closely stacked Arg345 and Trp331. Relevant side chains and backbone segments shown as sticks colored by element. Ordered waters relevant to binding shown as red spheres. Dashes lines represent hydrogen bonds (black) and salt-bridges (orange).

3.2.5 mAb 1504 binds a novel epitope on the αTSR domain

The X-ray crystal structure of Fab 1504 in complex with αTSR was determined to a resolution of 3.0Å **(crystallographic data table 3.4)**. The dataset collected possessed pseudo-C2 symmetry; however, a molecular replacement solution can only be found in space group of P1, producing an asymmetric unit containing four Fabs and four αTSR molecules. Despite the relatively low completeness of the dataset, the electron densities for the backbone of the CDRs and αTSR domain were visible and, in all four Fab-αTSR complexes, the domain is bound in the same orientation. Due to the lack of side-chain detail, no specific side-chain interactions will be inferred, and further optimization of the crystallization conditions is required to obtain a higher resolution dataset or merge multiple datasets in P1.

The 1504 Fab binds the αTSR domain entirely through its heavy chain, encoded by the V_H3-30-4 lineage, which interacts with both the TSR homology domain and the Th2R α-helix on the opposite side to α-epitope binding mAbs **(Figure 3.14A)**. Although an accurate buried surface area formed by 1504 binding to αTSR requires a higher resolution structure, comparison of the BSA formed by 1504 binding in this structure shows that it produces a distinct footprint on the αTSR surface compared to both α-epitope and β-epitope binding mAbs **(Figure 3.14B)**. Fab 1504 binds directly to the RII+ region containing the conserved cell adhesion motif (EWSXCXVTCG)(26), and specifically to Thr336, which has been shown to be the target of O-fucosylation(27). Our αTSR protein is purified from bacterial sources, lacking O-fucosylation. Therefore, the effects of this post-translational modification on Fab 1504 binding remain to be investigated.

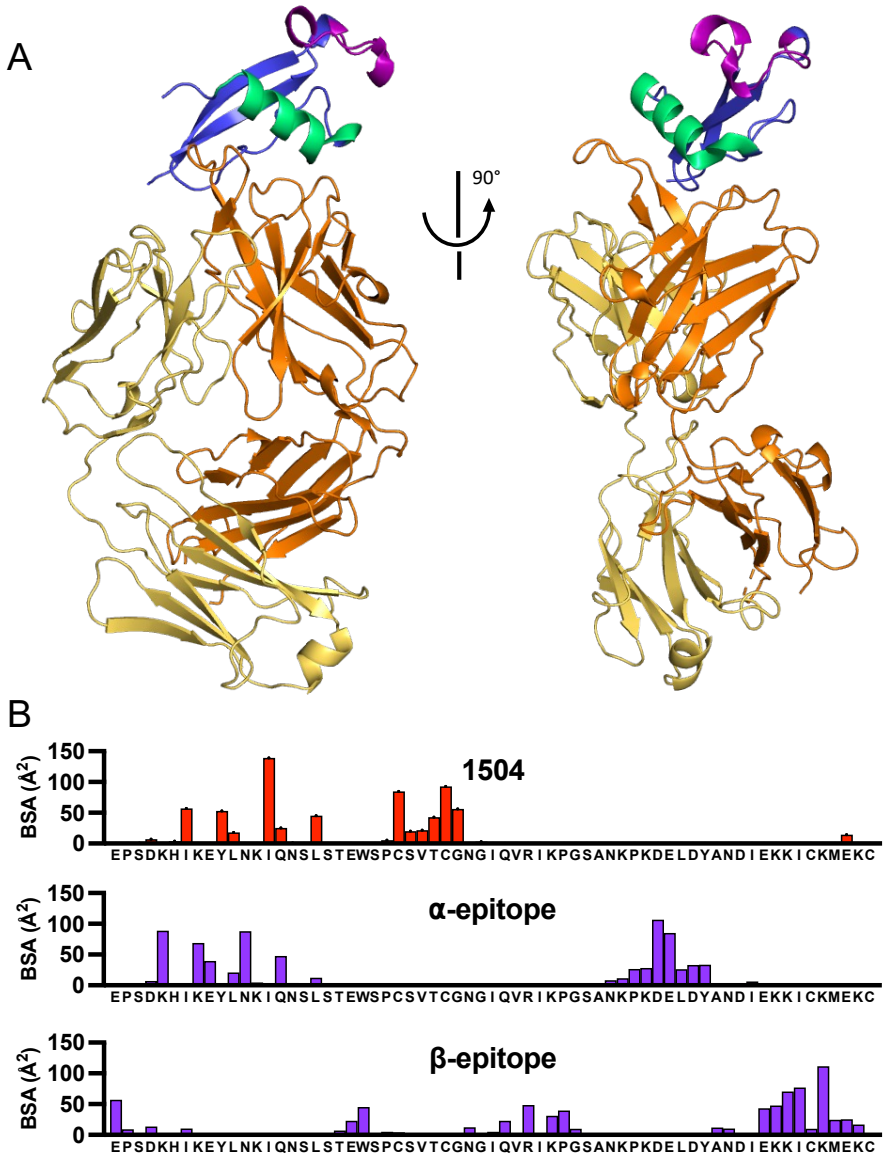
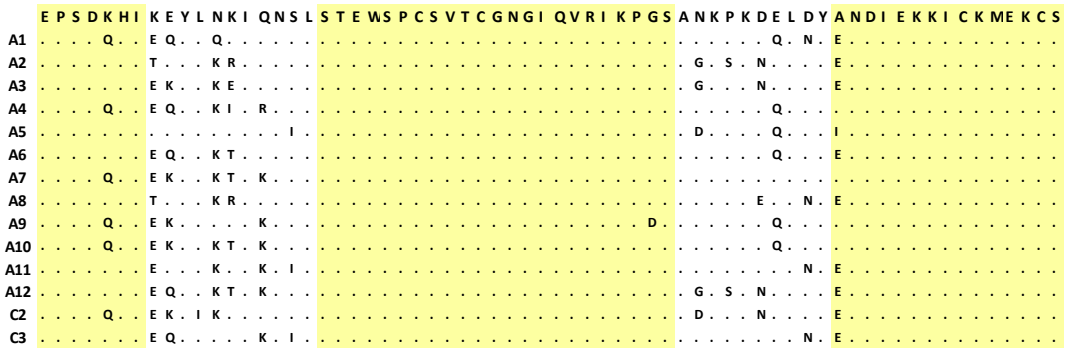


Figure 3.14. Fab 1504 binds a new epitope on αTSR. (A) Crystal structure of Fab 1504 in complex with αTSR shows binding of 1504 to a novel epitope on the αTSR domain containing residues of both Th2R helix and the RII+ conserved region of the TSR homology domain. Antibody heavy chain (orange) and light chain (yellow) as well as αTSR (CS-flap in purple, TSR homology domain in blue, Th2R helix in green) are shown in cartoon representation. (B) Buried surface area made by Fab 1504 binding to αTSR (red bars) reveals it produces a distinct footprint compared to the consensus epitope of all previously characterized α-epitope or β-epitope targeting mAbs (purple).

3.2.6 Antibodies binding the β-epitope provide cross-strain binding to a panel of αTSR haplotypes

CtCSP is the main locus of polymorphisms on CSP, which localize to the α-helix and the CS-flap formed by the Th2R and Th3R T-cell epitopes, respectively. CtCSP-binding mAbs previously characterized in our lab, which bind the polymorphic α-epitope encompassing both Th2R and Th3R, do not provide cross-strain binding to a panel of CtCSP haplotypes(23). In contrast, mAb 1512 binding the conserved β-epitope bound all CtCSP haplotypes tested(23). Out of the ten novel X-ray crystal structures of mAbs from the MAL071 trial, six mAbs bound the conserved face of the domain, while mAb 1504 defines a new conserved epitope on the domain surface. To determine whether these mAbs could provide strain-transcending binding to CSP, our collaborator Nathan Beutler in the Burton lab measured the binding affinities of anti-CtCSP mAbs to a panel of haplotypes by surface plasmon resonance (SPR) **(Figure 3.13)**.

Monoclonal antibody sequences were cloned into a mammalian expression vector for soluble expression in ExpiCHO cells. IgG was purified from cell culture supernatants by protein A affinity chromatography and size-exclusion chromatography. Eight monoclonal antibodies successfully expressed as IgG, including 1502, for which we did not obtain a crystal structure. mAb 1534 did not express as IgG and was not included in this assay. mAbs 1512, 1550 and 1504, with previously published affinities, were all included as positive controls.



KD	367	1392	1502	1525	KD	369	389	1393	1437	1504	1512	1550
A1	BT	BT	BT	BT	A1	BT	BT	BT	1.98E-10	6.19E-10	2.03E-10	7.53E-11
A2	BT	BT	BT	BT	A2	BT	BT	4.40E-11	BT	2.62E-08	4.38E-11	5.37E-07
A3	BT	BT	BT	BT	A3	3.80E-11	5.26E-10	2.31E-10	1.56E-09	BT	2.69E-09	3.33E-08
A4	BT	BT	BT	BT	A4	4.28E-11	3.64E-10	4.30E-10	6.56E-10	1.41E-07	1.08E-09	2.27E-07
A5	BT	BT	BT	3.25E-09	A5	BT	BT	BT	7.71E-10	8.59E-10	1.01E-10	7.19E-10
A6	BT	BT	BT	BT	A6	1.11E-11	6.73E-11	1.74E-10	4.13E-10	6.61E-08	2.81E-10	4.95E-07
A7	BT	BT	BT	BT	A7	7.71E-12	5.70E-11	2.10E-10	1.09E-10	3.26E-08	1.92E-10	1.14E-08
A8	BT	BT	BT	BT	A8	1.42E-11	6.55E-11	1.19E-10	2.22E-10	1.22E-08	1.60E-10	3.27E-08
A9	BT	BT	BT	BT	A9	BT	BT	BT	BT	1.51E-10	2.58E-10	3.03E-08
A10	BT	BT	BT	BT	A10	7.20E-12	6.56E-11	1.19E-10	1.95E-10	3.00E-08	2.69E-10	3.01E-08
A11	BT	BT	BT	BT	A11	8.14E-12	6.56E-11	8.83E-11	2.21E-10	3.90E-10	1.41E-10	3.42E-08
A12	BT	BT	BT	BT	A12	7.35E-12	5.65E-11	8.43E-11	4.92E-10	4.84E-10	2.06E-10	6.80E-10
C2	BT	BT	BT	BT	C2	BT	BT	BT	3.84E-10	5.72E-09	2.37E-10	1.18E-08
C3	BT	BT	BT	BT	C3	7.29E-12	6.11E-11	1.19E-10	7.48E-11	1.66E-10	2.11E-10	3.82E-11
3D7	BT	4.12E-12	6.49E-09	8.05E-11	3D7	5.03E-12	2.31E-11	2.79E-11	6.27E-11	1.03E-10	4.66E-11	3.85E-10

1E-7
1E-9
1E-11

Figure 3.15. Binding of MAL071 mAbs to a panel of CtCSP haplotypes. The sequences of haplotypes used correspond to a panel of diverse polymorphisms across both Th2R and Th3R domain, indicative of strong balancing selection. Residues bound by β-binding antibodies are highlighted in yellow. Surface plasmon resonance measurements were performed by Nathan Beutler in the Burton Lab using MAL071 mAb IgG1 purified from ExpiCHO cell supernatant, conjugated to a CM5 chip, and interpreted using a 1:1 Langmuir model. Binding affinities are color coded from high affinity (low KD) in red to low affinity (high KD) in green for each mAb.

mAb 367 did not bind any haplotypes, including the wild-type 3D7 RTS,S vaccine strain, suggesting that the protein is misfolded or aggregated. All mAbs except IgG 367 bound with sub-nanomolar affinity to the wild-type 3D7 RTS,S vaccine strain. As observed previously(23), mAbs 1512, 1550, and 1504 bound all haplotypes tested. Additionally, four mAbs bound most haplotypes: mAbs 1437, 1393, 389, and 369, bound 13, 12, 11,

and 11 out of 16 haplotypes, respectively. mAb 1525 only bound haplotype A5 in addition to the wild-type 3D7 haplotype, and mAbs 1502, and 1392 only bound the 3D7 vaccine strain haplotype.

In several cases, the binding patterns observed can be predicted from their epitopes as seen by X-ray crystal structure. The lack of strain-transcending binding from mAbs 1525 and 1392 is unsurprising as their crystal structure shows their binding to the highly polymorphic α-epitope. Similarly, mAbs 1512, 1550, and 1504 bind highly conserved epitopes and are not affected by sequence polymorphisms. Although the binding epitope of mAbs 369, 389, 1393 and 1437 as seen in their X-ray crystal structures is highly conserved, they do not bind all haplotypes, implying that conformational changes due to sequence polymorphisms can translate across the domain regardless of sequence conservation. Even so, mAbs targeting the conserved β-epitope bind across the majority of haplotypes tested.

3.2.7 Antibodies binding the β-epitope share a small consensus epitope

Deciphering common structural characteristics that mediate antibody binding to a vaccine can elucidate its antigenic potential and immunological breadth. By integrating knowledge of antibody protective efficacy and immunogenicity, definition of a consensus epitope can be used to guide future immunogen design to focus the immune response towards desirable epitopes. Although we have shown that sequence polymorphisms may

impact antibody binding to conserved regions of the domain, the β-epitope remains an attractive target for immunogen design due to its high sequence conservation across all *P. falciparum* strains.

With six new crystal structures of MAL071 mAbs binding the conserved face of the domain, and together with the previously X-ray crystal structure of mAb 1512, it is clear antibody lineages, angles of approach, and interaction residues are distinctly diverse compared to the α-epitope. Yet, a comparison of the buried surface areas formed by all MAL071 mAbs binding the β-epitopes show they still produce a highly similar footprint on the αTSR domain **(Figure 3.16)**.

To determine the consensus β-epitope across all of these structures, the binding interactions with which mAbs engage with each αTSR residue were tabulated to include salt bridges, hydrogen bonds, and interactions that are primarily mediated by structured water molecules **(Figure 3.17)**. Hydrophobic and van der Waals interaction still likely contribute to the overall affinity and shape complementarity to improve antibody binding. This comparison is therefore only looking at polar interactions which contribute to antibody specificity. The N-terminal Glu310, and C-terminal Glu365, Lys366, Lys367, Lys370, and Glu343 all engage in hydrogen bonds interactions in the majority of mAb interfaces. Lys366 and Lys 370, as well as Arg345, participate in salt-bridges in multiple mAb interfaces. Unexpectedly, the backbone of Ile368 is engaged in every mAb binding interface, and the indole side chain of Trp331 participates in hydrogen bonding interactions in all structures, mediated by ordered waters in five out of seven cases. On

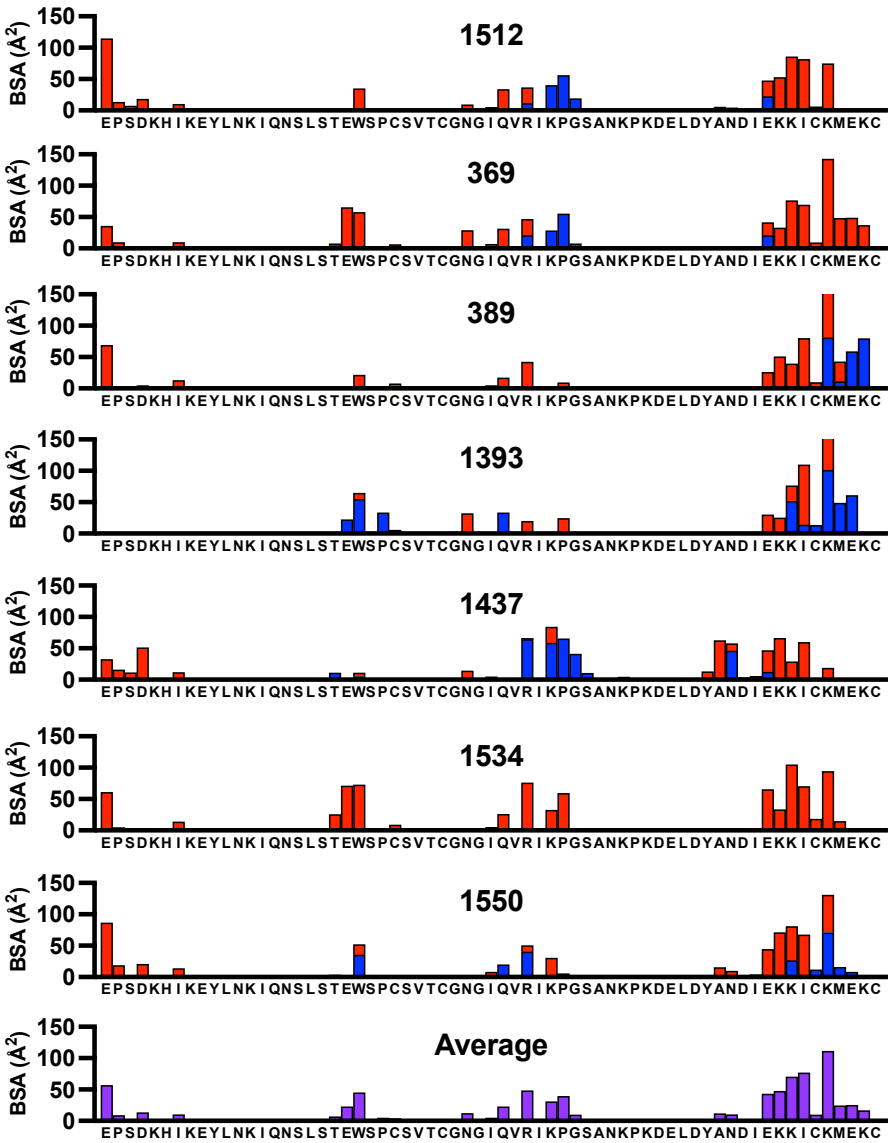


Figure 3.16. Summary of buried surface area formed by MAL071 mAb binding to the β-epitope. Buried surface area formed by binding of mAbs 1512, 369, 389, 1393, 1437, 1534, 1550, and the average buried surface area calculated as the mean across all seven structure interfaces. Buried surface area firmed by the heavy chain in red, and by light chain in blue, average in purple.

the surface of the domain, the combined representation showing only residues engaged in more than half of the structures produces a cluster at the center of the conserved face of the domain. This cluster overlaps strongly with the region of highest average buried

surface area, reiterating that the consensus β-epitope is a polar patch formed by Glu310, Trp331 stacked against Arg345, Gln343, Glu365, Lys366, Lys367, Ile368, and Lys370 **(Figure 5.17)**.

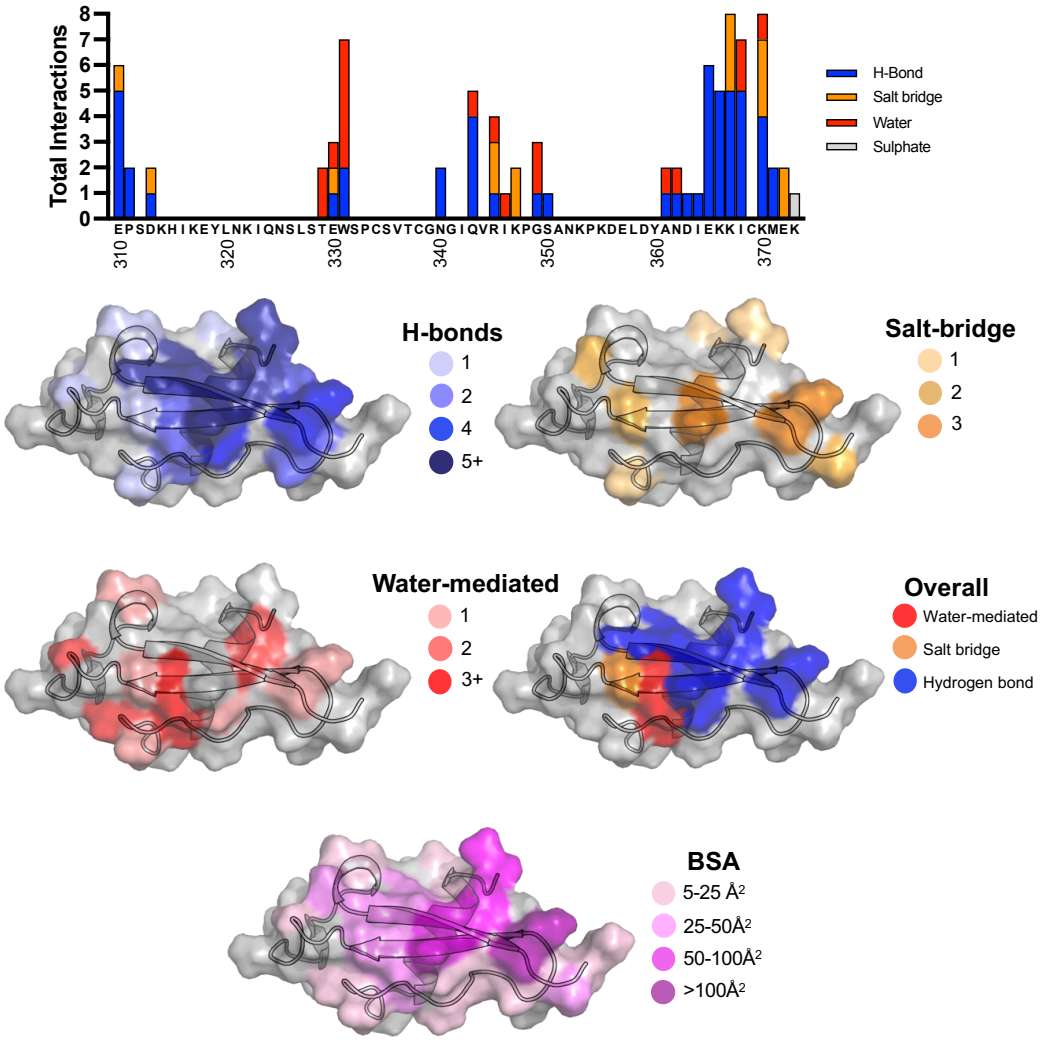
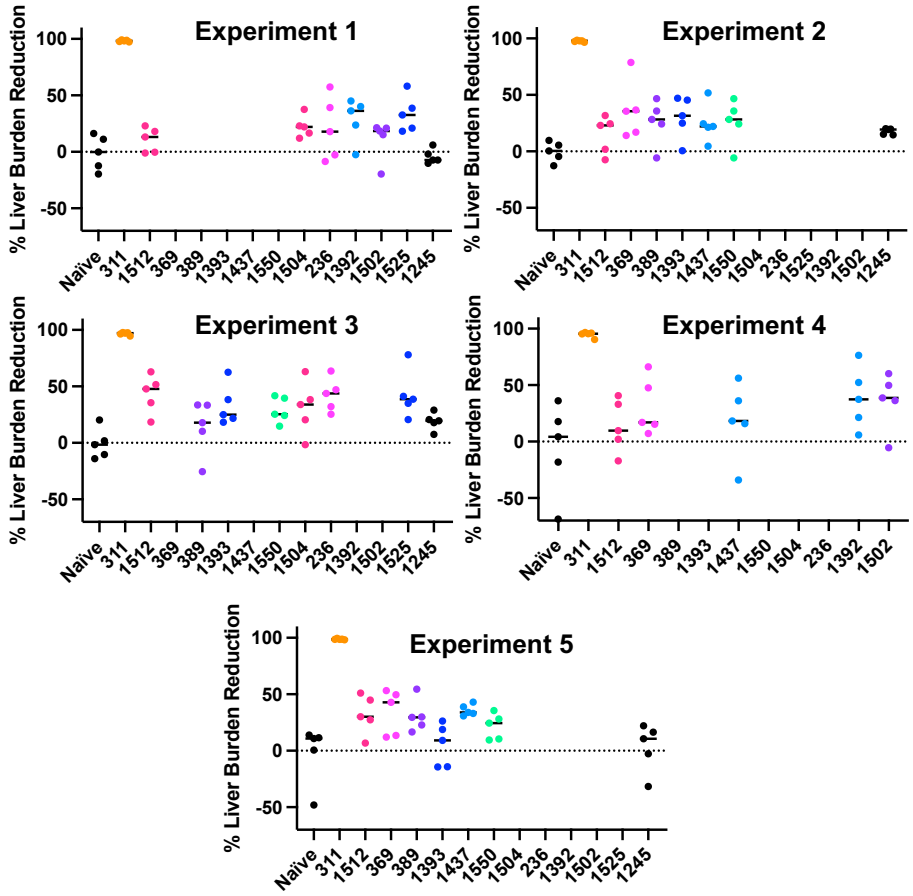


Figure 3.17. Defining a consensus β-epitope through interaction residues. Interactions mediating antibody binding to the β-epitope were tabulated to show both side-chain and backbone hydrogen bonds (blue), salt bridges (orange), water molecules bridging antibody-antigen interactions (red) and interfacial sulphates (gray) and plotted as bar chart. Each dominant interaction was plotted on the surface of the αTSR domain, and then combined by selecting only residues that contribute to binding in over half of the structures (overall). For comparison, the surface of the αTSR domain is shown with the consensus buried surface area formed by β-epitope binders as also shown in Figure **5.15** (pink and purple).

3.2.8 Antibodies targeting the αTSR domain provide weak protection in mouse *in vivo* model

The protective efficacy of mAbs was determined in collaboration with Fidel Zavala and performed by Yevel Flores Garcia (John Hopkins University). MAL071 mAbs were expressed as human IgG1 and purified from ExpiCHO cell culture supernatant by protein A affinity chromatography and size exclusion chromatography. IgG were then treated to remove endotoxin and sent to our collaborators for analysis. Five experiments were conducted, each with five mice (n=5) per group, treated with 300 ug of IgG. Each panel contained a negative control group of naïve untreated mice and a positive control group treated with the highly protective NANP-repeat targeting mAb 311. In four out of five groups, we also included a negative control mAb 1245, which is widely considered as non-inhibitory. Liver burden values are tabulated as percent liver burden reduction against the geometric mean of the naïve control group, and pairwise Mann-Whitney two-tailed test for significance was performed between each group and the naïve control **(Figure 5.18)**. In all five experiments, positive control mAb 311 showed significant protection of over 90% (P=0.0079). In experiment 2, the negative control mAb 1245 was significantly protective, albeit only modestly, at 17% (P=0.0079). Two anti-CtCSP mAbs provided significant protection in all experiments in which they were included; mAb 1525 provided 33.8% protection (P=0.0079) in experiment 1 and 42.7% protection (P=0.0079) in experiment 3; and mAb 1504 provided 22.3% protection (P=0.0159) in experiment 1 and 30.8% protection (P=0.0317) in experiment 3. All other mAbs were only protective in some experiments and not in the others.



% Reduction	311	1512	369	389	1393	1437	1550	1504	236	1392	1502	1525	1245
Expt 1	98.2	10.6						22.3	20.7	28.5	11.3	33.8	-4.1
Expt 2	97.7	14.7	36.4	25.8	29.9	24.8	25.8						17.8
Expt 3	96.7	43.3		13.9	33.2		29.2	30.8	42.4			42.7	18.9
Expt 4	94.8	13.7	30.7			18.5				38.7	35.9		
Expt 5	98.8	32.0	34.2	30.7	5.1	35.9	21.7						3.0

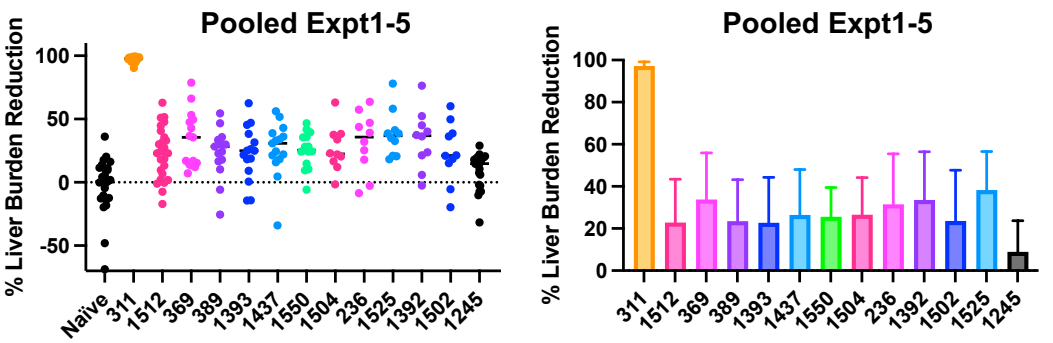
*
**

P value	311	1512	369	389	1393	1437	1550	1504	236	1392	1502	1525	1245
Expt 1	0.0079	0.3095						0.0159	0.2222	0.0556	0.2222	0.0079	0.8413
Expt 2	0.0079	0.2222	0.0079	0.0952	0.0317	0.0317	0.0952						0.0079
Expt 3	0.0079	0.0159		0.3095	0.0159		0.0159	0.0317	0.0079			0.0079	0.0556
Expt 4	0.0079	0.5476	0.2222			0.4206				0.0556	0.0556		
Expt 5	0.0079	0.0556	0.0317	0.0079	0.8413	0.0079	0.2222						0.8413

Figure 3.18. In vivo protection of MAL071 mAbs by mouse liver burden assay. Five different plots are shown corresponding to five separate experiments, N=5 per group, injected with 300ug IgG1. Positive control anti-NANP 311 IgG (300ug/mouse). Percent liver burden reduction is measured against the geometric mean of the naïve control, and significance calculated with the Mann-Whitney two-tailed test, with P values reported and summarized by color ($P<0.05$ in yellow, $P<0.01$ orange).

As can be seen from the individual percent liver burden measurements, mAbs targeting αTSR show high variability at low protective ranges. This is expected given the sensitivity of the liver burden assay model, which estimates protection best at higher levels. To decide whether we could increase the statistical power of our analysis, the standardized values were pooled across all panels, achieving N=25 for the naïve control, mAb 311, and mAb 1512, and N=15 for all mAbs binding the β-epitope, and N=10 for all other mAbs **(Figure 5.19)**.

All mAbs provided significant protection by Mann-Whitney two-tailed t-test, but to differing levels of statistical significance. Providing the highest significance, mAb 311 provided 96.9% protection ($P<0.0001$) and mAbs 369, 1392, 1437, 1525, and 1550 provided protection in the range of 25-38% protection ($P<0.0001$). mAbs 1512, 389, 1504, 236, and 1392 provided 22-34% protection ($P=0.0001$-0.0008). An order of significance lower, mAb 1393 provided 22.7% protection ($P=0.001$) and mAb 1502 provided 23.6% protection ($P=0.0039$). Lastly, negative control mAb 1245 provided 8.9% protection ($P=0.0317$). Although the negative control mAb provided the lowest average protection, it is still statistically significant, suggesting these results should be assessed taking that under consideration. At best, anti-CtCSP mAbs are mildly protective by liver burden assay, providing 20-40% protection at high doses of 300ug per mouse, but show high variability across measurements.



Combined	311	1512	369	389	1393	1437	1550	1504	236	1392	1502	1525	1245	
% Reduction	97.24	22.88	33.77	23.49	22.73	26.42	25.55	26.55	31.54	33.61	23.6	38.25	8.901	*
P value	<0.0001	0.0002	<0.0001	0.0002	0.001	<0.0001	<0.0001	0.0001	0.0008	0.0001	0.0039	<0.0001	0.0317	**
N	25	25	15	15	15	15	15	10	10	10	10	10	20	***
														****

Figure 3.19. Combined *in vivo* protection of MAL071 mAbs by liver burden assay. Previously shown experiments were combined into a single panel following standardization. All mice were treated with with 300ug IgG1. Positive control anti-NANP 311 IgG (300ug/mouse). Percent liver burden reduction is measured against the geometric mean of the naïve control, and significance calculated with the Mann-Whitney two-tailed test, with P values reported and summarized by color (P<0.05 in yellow, P<0.01 orange, P<0.001 red, P<0.0001 purple).

3.2.9 Antibodies binding conserved epitopes on αTSR have a higher avidity index

One hallmark of the MAL071 trial is the discovery that anti-CtCSP antibody avidity index correlates with protection across both vaccine arms. Antibody avidity index of patient sera is measured by the decrease in serum antibody following the addition of a chaotropic agent, often potassium thiocyanate (KSCN), as compared to PBS control wash. Although this is not indicative of any direct physiological function, avidity index has become a useful method for assessment of serum antibody quality. Therefore, we measured the antibody avidity index of all fifteen C-term MAL071 mAbs that we selected, which were

expressed as IgG across a range of KSCN concentrations, by ELISA. Results shown are averages of five ELISA curves from two independent experiments **(Figure 5.20A)**.

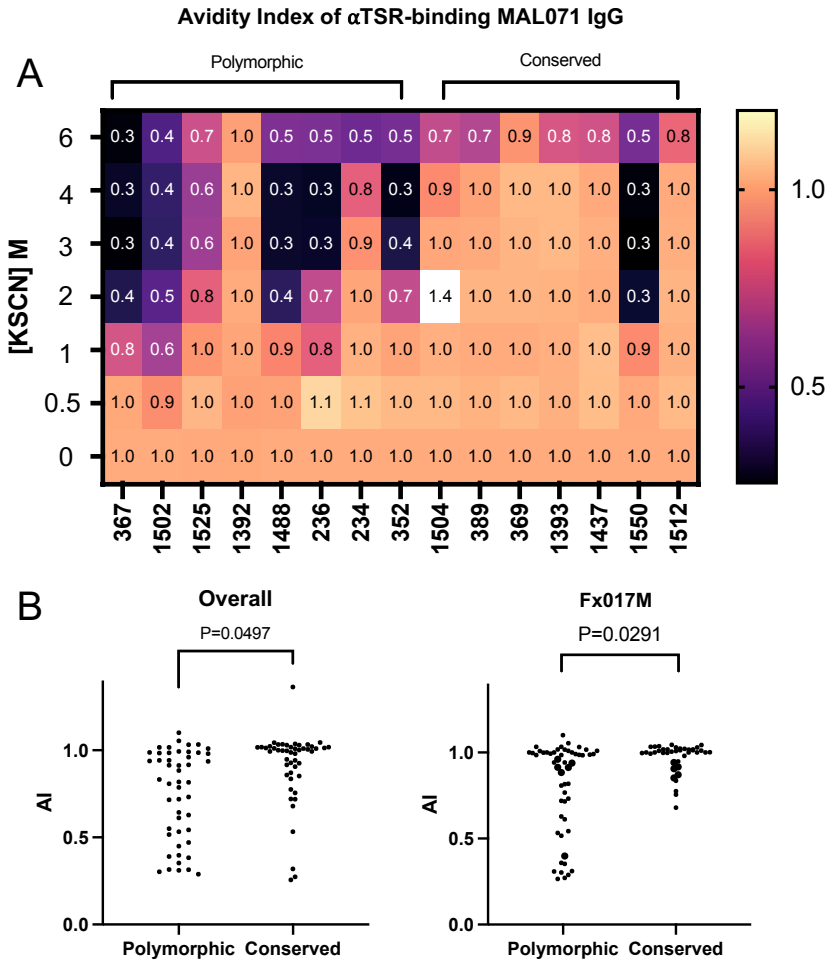


Figure 3.20. Binding to the conserved epitope on αTSR correlates with avidity. (A) Avidity index was measured by ELISA with a dissociation step including a dilution of potassium thiocyanate (KSCN) ranging from 0.5 to 6 M in PBS or PBS control (0 M). Avidity index was measured as reduction in binding compared to untreated PBS control and plotted as a heat map. (B) Two-way ANOVA with Bonferroni's multiple comparison test was used to measure significance between polymorphic and conserved epitope binding mAbs, accounting for matched measurements of each mAb across the range of concentrations. Results are plotted as grouped chart for illustrative purposes only. IgG 367 was excluded from the statistical analysis.

For the majority of mAbs tested, increasing KCSN concentration promoted mAb dissociation leading to a reduction in binding and therefore a lower avidity index. For several mAbs, such as 1512 and 369, no dissociation was seen for KSCN concentrations up to 4 M. As mAbs binding to conserved epitopes on αTSR and increase in CtCSP avidity index have both been separately correlated with protection(7,28), we next determined whether MAL071 mAbs binding conserved epitopes have a significantly higher avidity across a range of KSCN concentrations using a two-way ANOVA and Bonferroni's test for multiple comparisons. As mAb 367 did not bind in the SPR experiment (section 3.2.6), it is not included in the following statistical analysis.

Overall, MAL071 mAbs binding to conserved epitopes on αTSR have a significantly higher avidity index compared to those which bind polymorphic epitopes (P=0.0497) tested across 0.5 M to 6 M KSCN **(Figure 5.20B)**. When assessing only mAbs from the delayed fractional dose regimen (all but 1488, 1502, 1504, and 1550), the same results were obtained, but with a higher significance. mAbs binding conserved epitopes, now all β-epitope binding mAbs, show higher avidity (P=0.02) across all concentrations from 0.5 to 6 M KSCN. Together, these results would suggest that amongst our panel of MAL071 mAbs higher antibody avidity correlates with binding to conserved epitopes.

3.3 Discussion

3.3.1 RTS,S vaccination elicits a broad range of mAbs targeting conserved αTSR epitopes

Previous work in our lab has revealed the binding epitope of four V_H3-21 mAbs from the MAL071 trial targeting the polymorphic α-epitope, which was first seen to bind the non-protective mAb 1710 isolated from sporozoite immunization(22). The X-ray crystal structures of Fab 367, 1525, and 1392 further show that a variety of antibody lineages engage the α-epitope through insertion of CDRH3 hydrophobic residues into the conserved hydrophobic core of the domain, while other CDRs engage the nearby charged residues of the CS-flap and Th2R α-helix.

Although from the same V_H3-21 lineage as multiple mAbs mapped to the α-epitope, mAb 1512 was shown to bind the conserved face of the domain using its unusually long 23 amino acid CDRH3. The low frequency of long CDRH3 in the human antibody repertoire have been posed as a potential limiting factor in the humoral response to broadly neutralizing epitopes on the HIV envelope trimer(29). In the absence of any additional information on mAbs that bind the β-epitope, it was uncertain whether the antibody response to the conserved face of the αTSR may be restricted in the same way. The six novel X-ray crystal structures of MAL071 mAbs 369, 389, 1393, 1437, 1534, and 1550 bound to β-epitope confirm that RTS,S vaccination can elicit a broad antibody response to the conserved face of the domain through multiple heavy and light chain lineages, which utilize shorter CDR3s than mAb 1512. In contrast to the conserved interaction mode of mAbs targeting the α-epitope, β-binders approach the domain from a variety of

angles and engage the domain with substantial heterogeneity, only overlapping by a small number of conserved residues that form a polar patch on the domain surface.

Although they target conserved epitopes, the different binding approaches of β-epitope targeting mAbs may impact their ability to bind αTSR on the sporozoite surface. This is also the case for mAb 1504, which defines a new conserved epitope on the αTSR domain. The conserved cell adhesion motif bound by mAb 1504, known as Region II+, has been shown to be O-fucosylated on Thr336(30), and the effects of this post-translational modification on mAb binding to the sporozoite surface, and hence the ability to provide protection, should be further investigated.

3.3.2 High affinity mAbs targeting αTSR do not confer sterile protection in mice

As expected from their binding epitope, β-binding mAbs and mAb 1504 bound multiple CtCSP haplotypes by SPR with high affinity, demonstrating potential to provide strain-transcending neutralization of sporozoites. When assessed by liver burden assay in mice both α- and β-binding mAbs provided only modest protection between 20-40%. Although significantly higher than the negative control naïve mice, the protection granted by αTSR binding mAbs is much lower than protection from antibodies targeting the repeat epitopes of CSP. mAbs that target the NANP repeats can bind sporozoites at higher numbers per CSP molecule and avidity than C-terminal mAbs, which could provide them with higher protective efficacy. However, mAbs such as CIS43 which binds a single junctional epitope on CSP still provide higher protection than mAbs that bind CtCSP.

The weak protection of MAL071 mAbs *in vivo* by mouse liver burden assay contrasts with the identification of anti-CtCSP antibody avidity index in the MAL071 trial as a correlate of protection. Standard dose RTS,S sera from binding across a multiple αTSR haplotypes also correlates with protection, which would further implicate the β-epitope as a target of protective antibodies(28). Our data support that antibody avidity index, as measured using a concentration gradient of the chaotropic agent potassium thiocyanate, is higher for MAL071 mAbs binding conserved epitopes across both vaccine arms, providing a link between the two previously observed correlates. Characterization of more mAbs which bind αTSR, as well as analysis on the frequency at which they occur, will improve our understanding of the clinical relevance of these observations. Nevertheless, our results do not show that β-binders are more inhibitory than α-binders by mouse liver burden assay, although they are broader due to targeting conserved regions.

3.3.3 CtCSP-mediated immunity reveals a missing link in our understanding of vaccine-mediated protective efficacy against malaria infection

Our understanding of the potential mechanism of action produced by humoral responses targeting the different domains of CSP, including αTSR, are limited by the lack of understanding of the hepatocyte invasion mechanism of *P. falciparum* sporozoites. The N-terminal domain of CSP is a receptor for heparin sulphate proteoglycans on hepatocytes(31,32), and binding to hepatocytes initiates N-terminal domain cleavage at the RI cleavage sequence of the junctional region(33), providing a signal to switch to an invasive phenotype. Parasites expressing a CSP with a cleaved N-terminus are sensitized

to inhibition by antibodies targeting the αTSR domain, which would suggest invasion kinetics may limit the time for antibodies targeting αTSR to bind sporozoites(34). In a recent study, repeat-binding antibodies have been shown to facilitate unmasking of the αTSR domain on the surface of sporozoites, which could also increase their susceptibility to αTSR targeting antibodies(35). When combined with protective repeat-targeting mAbs, a panel of non-inhibitory antibodies targeting αTSR isolated from sporozoite immunization did not provide added protection *in vivo* by mouse challenge, despite the mAb combination significantly increasing binding to sporozoites *in vitro*.

These findings would suggest a potential shortcoming in the ability of the mouse model to correctly mimic correlates of protection observed in human trials. RTS,S sera binding to αTSR have been shown to fix complement C1q(15), a correlate of protection in PNG children and RTS,S adult vaccinees(14,36). Laboratory mice have been suggested to lack in complement activity(37), and further won't be able to activate complement by mAbs with a human Fc region. Other human Fc-mediated effector functions have too been identified as correlates from a multivariable serological analysis of MAL071 patient sera, in which C terminus-specific antibody-dependent cellular phagocytosis mediated by monocytes was selected as a minimal marker between delayed fractional dose and standard dose vaccine arms(16).

The current research gap extends further than the canonical subset of effector functions, which may mediate protection in conjunction with anti-CtCSP mAbs. The sequence conservation of the β-epitope suggests it is involved in a conserved interaction or activity

related to function. This is not the case for the nearby α-epitope, which is under strong selection pressure, as evident by its high degree of polymorphism(21). As antibody avidity correlates with protection, and antibodies targeting conserved epitopes on αTSR show higher avidity across vaccine arms, the missing causational link between an immune response towards the β-epitope and protection may require elucidation of the specific role it plays in the invasion process or immune evasion mechanisms. En route to the liver parenchyma, sporozoites traverse Kupffer cells, a class of phagocytes that reside in the liver sinusoids(38). CSP has been shown to suppress the oxidative burst which Kupffer cells use as a defensive mechanism against pathogens through its interaction with heparan sulphate proteoglycans and the low-density lipoprotein-like receptor(39). The αTSR domain has been shown to increase binding of CSP to heparin in conjunction with the N-terminal domain(31), and the TSR domain canonically contains heparan sulphate binding motifs(2). Specifically, the highly conserved RII+ of CSP (bound by mAb 1504) and the downstream basic residues (bound by the majority of β-binders) have been linked to heparin binding. Recent reports have shown that a central epitope in the N-terminal domain of CSP epitope binds the negative complement regulator C4b-binding protein(40). It is not unreasonable to consider that this or other epitopes of CSP could participate in *P. falciparum*-invasion-specific immune evasion mechanisms.

Therefore, future studies should seek to assess the effects of MAL071 α- and β-epitope binding antibodies on complement activation, phagocytosis, other Fc-mediated functions to better align with known correlates of protection. Even further, a true understanding of the potential of CtCSP-mediated immunity, or lack thereof, relies on an increased

understanding of the physiological role that the αTSR domain plays in the invasion process. Regardless of the role αTSR in the future of pre-erythrocytic malaria vaccination, establishment of an integrative model in which mouse liver burden data can be combined with an assessment of effector functions and immune evasion properties would provide a well-rounded platform for pre-clinical assessment of future vaccine antigens and therapeutic antibodies. By improving our understanding of the immunological landscape of the CtCSP αTSR domain through structural characterization of antibody epitopes, we have been able to produce a panel of antibodies with well-characterized epitopes that can help us investigate any epitope-specific mechanisms of protection on the main liver-stage vaccine antigen, CSP.

3.4 Materials and Methods

3.4.1 Sequences and Cloning

Sequences from the MAL071 vaccine trial were provided through our collaboration with the PATH Malaria Vaccine Initiative. Briefly, variable regions of heavy and light chain mRNA were sequences from peripheral blood mononuclear cells (PBMC)-sorted plasmablasts sampled seven days after the third immunization, and binding to CtCSP was determined by ELISA. From 369 antibodies screened, 20 bound CtCSP. Coding sequences of mAb heavy chain V_H-C_H1 and light chain V_L-C_L were synthesized as gBlocks (IDT) containing overlaps for cloning into pCMV3 vector backbone containing the Ig Kappa light chain leader peptide. For direct expression of Fabs, gBlocks were cloned into pCMV3 vector containing a stop codon immediately after the cysteine residue following the C_H1 EPKSC sequence.

3.4.2 Sequence Analysis

Antibody lineages and germline sequences were determined using IgBlast (NCBI). Sequence alignment of CDRs and relevant mutants was produced by AbYsis. Buried surface area analysis was performed using the PDBePISA server of EMBL-EBL.

3.4.3 Expression and purification of αTSR from *E. coli* (performed by Gonzalo Gonzales, Wilson lab)

The αTSR domain construct used for X-ray crystallography contains amino acids 311-375 of the *P. falciparum* 3D7 CSP, followed by a C-terminal 6xHis tag and cloned into the pET28a bacterial expression vector, as previously used in our lab (23). Purified

plasmid containing the αTSR construct was transformed into *E. coli* shuffle competent cells, and a single colony was used to start a 50 ml overnight culture, 25 ml of which were used to inoculate a 1L culture the following day. When cultures grown at 37°C reached an optical density of 0.6-0.8, they were induced with 1 mM isopropyl β-D-1-thiogalactopyranoside and grown at 18°C overnight. Cells were harvested and lysed by microfluidization in 50 ml lysis buffer containing 20 mM Na_2HPO_4 pH 7.2, 450 mM NaCl, 0.5% sarkosyl, and 1 Roche protease inhibitor tablet. Following centrifugation, 150 ml of 20 mM Na_2HPO_4 pH 7.2 supplemented with 450 mM NaCl was added, and the mixture was incubated overnight with 5 ml Roche Ni cOmplete resin. Beads were washed with 20 mM Na_2HPO_4 pH 7.2, 450 mM NaCl, 0.1% sarkosyl and then with 75 mM Tris pH 9.0, before the protein was eluted with 200 mM imidazole, 75 mM Tris pH 9.0, 150 mM NaCl, and concentrated for size exclusion on a Superdex200 16/90 column (GE healthcare).

DNA constructs of αTSR haplotypes were previously prepared by a previous member of the lab, David Oyen, and contain the coding sequence for αTSR haplotypes from a previous study (23) with a C-terminal strep tag in a pET28a vector backbone and transformed into *E. coli* Shuffle cells. Cultures were induced at OD 0.6-0.8 with 1 mM isopropyl β-D-1-thiogalactopyranoside and grown at 18°C overnight. Bacterial cell pellets centrifuged at 6000 xg for 8 minutes and pellets were resuspended with 50ml PBS, 0.5 M NaCl, Roche protease inhibitor tablet and 20 ul benzonase. Bacterial cells were ruptured using a EmultiFlex-C3 microfluidizer for 10 minutes on ice. Supernatants were then clarified by centrifugation at 26,000 xg for 30 mins at 4°C and loaded onto a 5 ml

StrepTrap HP column at 2ml/min, washed with PBS, and eluted with PBS supplemented with 2.5 nM D-desthiobiotin. Elution fractions were analyzed by SDS-PAGE and dialyzed in PBS overnight at 4°C, and purified by size exclusion chromatography on a Superdex75 16/90. Purified protein was aliquoted for storage at -80C.

3.4.4 Protein expression and purification in ExpiCHO cells

All IgG and Fabs were expressed in ExpiCHO mammalian cells. Heavy and light chain recombinant DNA were purified separately and co-transfected at a 1:2 (IgG) of 1:1 (Fab) heavy-to-light chain ratio using Expifectamine transfection reagent following manufacturer's protocol. Cells were cultured at 37°C, shaking at 125rpm, 8% CO_2 for 18-24 hours and then transferred to 32°C for an additional 10-12 days. Transfection enhancer and feed was added on day 1, and transfection feed was added again on day 5. Cell supernatants were harvested by centrifugation at 4,000-6,000 xg and filtered through 0.22 μM or 0.45 μM filter. Clarified Fab expression supernatants were loaded onto HiTrap™ protein G 5ml column (Cytiva), and IgG expression clarified supernatants loaded onto HiTrap™ protein A 5ml column (Cytiva). In both cases, the columns were washed with 5 column volume of PBS, eluted with 0.1M glycine pH 2.8, and neutralized with 1M Tris solution pH 9. Relevant elution fractions were pooled and further purified by size exclusion chromatography on a HiLoad™ Superdex75 16/600 column or a HiLoad™ Superdex200 16/600 column equilibrated with TBS pH 8.0. Size exclusion elution fractions corresponding to monomeric Fab or IgG were pooled and stored at 4°C.

For protection studies in mice, IgG fractions corresponding to monomeric IgG by size exclusion were pooled and re-bound the protein A column for endotoxin removal. To remove endotoxin, column-bound IgG was washed with 100ml 0.5 M arginine pH 7.4. Bound IgG was eluted from the protein A column with 0.1 M glycine pH 2.8, immediately neutralized with 1M Tris pH 9, and dialyzed in PBS overnight at 4° C. The following day, endotoxin levels were assayed on the Endosafe Nexgen-PTS using Limulus Amebocyte Lysate test cartridges, with endotoxin cutoff set to 50 EU/ml. Endotoxin-free IgG was diluted to 1mg/ml in PBS, flash frozen in liquid nitrogen, and stored at -80°C.

For crystallization trials, Fabs were purified as above, and Fab-αTSR complex formed by adding an excess of αTSR purified from *E. coli* as described above. If Fabs were already known to express poorly, a large excess of αTSR was added to clarified cell-culture supernatant and Fab-αTSR complexes were purified by protein G affinity chromatography as described previously, and additional αTSR was added following elution. Following complex formation for 30 mins at room temperature, excess αTSR was separated from the Fab-αTSR complex by a final step of size-exclusion chromatography on a HiLoad^{TM} Superdex75 16/600 column. Pooled elution fractions were then concentrated to 10-30mg/ml for crystallization.

3.4.5 Crystallization and structural determination

All Fab-αTSR complexes were expressed as detailed above and concentrated to 10-30mg/ml. For Fabs 1393, 1534, and 1550, equimolar amount of Protein G subdomain 3 with a C-terminal 6xHis tag was added to facilitate crystallization. Crystallization trials

were set up on our high-throughput robotic Rigaku CrystalMation system at TSRI by sitting drop vapor diffusion, combining 100ul of protein mixture with 100ul of well solution. Crystals were cryoprotected by adding cryoprotectant to well liquor and stored in liquid nitrogen for data collection. Diffraction data were collected at beamlines SSRL12-1 (Fabs 367, 1437, and 1550), APS 23ID-B (Fabs 1392, 1393, 1525, 1534, and 1504), APS 23ID-D (Fab 389) and ALS 501 (Fab 369). Crystallization conditions which produced the best diffracting crystals, and cryoprotectants are summarized below. Crystals were preliminarily screened for diffraction patterns, and those with diffraction maxima extending beyond 4Å were collected by rotating crystals 360° capturing 0.2° rotations every 1 second, producing full datasets comprised of 1800 frames.

The dataset for Fab369-αTSR was processed by XDS(41), and the remainder of datasets were processed using HKL2000(42). Structures were then determined by molecular replacement in Phaser(43) using search models for variable regions produced by AbPred(44), an appropriate search model for either lambda or kappa Fab constant regions, a search model for αTSR. In the case of Fabs 1393, 1534, and 1550, an additional search model for Protein G subdomain 3 was used. All datasets presented produced a molecular replacement solution with translation function Z-score of above 8, indicating a correct solution. In all cases, clear electron density was seen for all components of the complex. In the case of Fabs 1504 and 389, CCP4i Zanuda(25) was used to confirm the solution space groups of P1 and C2, respectively. Structures were built manually using Coot(45), refined by REFMAC5(46), PHENIX(47), and validated using MolProbity(48).

Structure figures were generated by PyMOL (Schrödinger). Graphical data were plotted using GraphPad Prism.

Fab367-αTSR

Crystallization condition: 40% PEG-400, 0.1 M acetate pH 4.5, final pH 5.4. Cryoprotectant: 30% glycerol.

Fab369-αTSR

Crystallization condition: 0.17 M ammonium sulphate, 15% glycerol, 25.5% PEG-4000. Cryoprotectant: 30% glycerol.

Fab389-αTSR

Crystallization condition: 2.0 M ammonium sulphate, 0.2 M lithium sulphate, 0.1 M Cyclohexyl-3-aminopropane sulfonic acid pH 10.5. Cryoprotectant: 30% glycerol.

Fab1392-αTSR

Crystallization condition: 30% PEG-600, 10% (v/v) glycerol, 0.5 M NH_4-sulfate, 0.1M Tris pH 7.0, final pH 5.6. Cryoprotectant: 30% glycerol.

Fab1393-αTSR

Crystallization condition: 20% PEG 3350, 0.2 M di-ammonium tartrate, pH 6.6. Cryoprotectant: 30% ethylene glycol.

Fab1437-αTSR

Crystallization condition: 8.5% isopropanol, 17% PEG-4000, 0.085 M HEPES pH 7.5, 15% glycerol. Cryoprotectant: 30% ethylene glycol.

Fab1504-αTSR

Crystallization condition: 65% MPD, 0.1 M Bicine pH 9.0. Cryoprotectant: no additional required.

Fab1525-αTSR

Crystallization condition: 20% PEG 3350, 0.2 M Mg-sulfate, pH 5.9.

Cryoprotectant: 30% ethylene glycol

1534-αTSR

Crystallization condition: 20% PEG 3350, 0.2 M K-iodide, pH 6.8.

Cryoprotectant: 30% ethylene glycol

Fab1550-αTSR

Crystallization condition: 20% PEG-6000, 1.0 M Li-chloride, 0.1 M citric acid pH 4.0

Cryoprotectant: 30% glycerol.

3.4.6 Surface Plasmon Resonance (performed by Nathan Beutler, Burton Lab, TSRI)

Affinity experiments were performed on a Biacore 8k at 25°C. All experiments were carried out with a flow rate of 30 µL/min in a mobile phase of HBS-EP+ [0.01 M HEPES (pH 7.4), 0.15 M NaCl, 3 mM EDTA, 0.0005% (v/v) Surfactant P20]. Anti-Human IgG (Fc) antibody was immobilized via standard NHS/EDC coupling to a Series S CM-5 sensor chip. Each mAb was injected over the chip followed by a wait period to normalize captured response units (RU). A concentration series of ctCSP peptides was injected across the antibody and control surface for 2 min, followed by 5000–8000 second dissociation phase. Regeneration of the surface in between injections of CtCSP peptides was achieved with a single, 120 s injection of 3 M MgCl2. Kinetic analysis of each reference subtracted injection series was performed using the BIAEvaluation software (Cytiva). All sensorgram series were fit to a 1:1 (Langmuir) binding model of interaction.

3.4.7 Liver Burden Assay (performed by Yevel Flores Garcia, Zavala Lab, JHU)

Mice were injected intravenously with 300 μg/mouse of monoclonal antibodies (human IgG1). Sixteen hours later, mice were challenged with $2x10^3$ chimeric sporozoites injected IV. Forty-two hours after challenge, mice were injected with 100 μl of D-Luciferin (30 mg/mL), anesthetized with isoflurane and imaged with the IVIS spectrum to measure the bioluminescence expressed by the chimeric parasites. Results were provided as Total Flux (photons/sec) and percent liver burden reduction was calculated as 100*(1-(VALUE/geomeanNaïve)). For pairwise analysis of significance, each mAb was compared to the naïve control by the Mann-Whitney two-tailed test. As well as reporting the individual P values, they were color coded by their P value summary *=yellow (P<0.05), **=orange (P<0.01), ***=red (P<0.001), and ****=purple (P<0.0001).

3.4.8 Antibody avidity enzyme-linked immunoassay

Corning high-binding half-well 96-well plates were coated with 1ug/ml αTSR in PBS overnight at 4°C. Plates were then blocked with 2% BSA in PBS for two hours at 37C. Plates were washed twice with PBST (PBS +0.005% Tween20), and monoclonal antibodies diluted to 1 ug/ml in PBST were added for 1 hour at RTM. ELISA plates were washed once with PBST, and multiple dilutions of potassium thiocyanate in PBS (6 M, 4 M, 3 M, 2 M, 1 M, 0.5 M, 0.25 M, and 0 M) were added to destabilize antibody binding. After 30 minutes at RTM, plates were washed thrice with PBST and secondary antibody diluted 1:20,000 in PBST with 1% BSA (Goat anti-Human IgG HRP, Fortis Life Sciences A80-104P) was added for 1 hour at RTM. Plates were washed five times with PBST and

developed using Thermo Scientific™ 1-Step™ Ultra TMB-ELISA Substrate Solution and quenched with 0.2 M sulfuric acid, and absorbances were read at 405 nm using SoftMax Pro 5.4 and a VersaMax microplate reader. Avidity index calculated as AI=1-(normOD405), where normOD405 is the normalized absorbance to the 0 M KSCN PBS absorbance. Statistical analysis conducted on GraphPad Prism using the ordinary two-way ANOVA, with Bonferroni's multiple comparisons test, with a single pooled variance.

3.5 Acknowledgements

We are thankful to PATH's Malaria vaccine initiative for providing us with the sequences for the MAL071 antibody sequences. Much of the protein samples were produced with the help of Gonzalo Gonzales (Wilson lab, TSRI) and H. Tien (Wilson lab, TSRI) set up the endless crystallization screens, without which none of these crystal structures would exist. We are also thankful to our collaborators Nathan Beutler (Burton Lab, TSRI) for performing the SPR experiments and discussion. We thank Yevel Flores Garcia and Fidel Zavala (JHU) for performing the mouse liver burden assay experiments and for their discussion. We would like to thank Robyn Stanfield, Xueyong Zhu, Meng Yuan and Rotimi Omorodion for their help with data collection, processing, and refinement, as well as sharing their expertise. We would like to acknowledge the great support staff in the Wilson Lab, Jeanne Matheson, Wenli Yu, and Beverly Ellis. This work was funded by PATH's Malaria Vaccine Initiative and The Bill & Melinda Gates Foundation. We are thankful to all beamline staff for their support in data collection.

3.6 Declaration

Antibody sequences were provided by PATH's Malaria Vaccine Initiative. Sequences for 1512, 236, 1550, 1504, 369, and 367 were cloned into expression vectors by David Oyen and Tossapol Pholcharee. DNA constructs for the expression of IgG 234 and 352 were provided by Nathan Beutler (Burton lab, TSRI). DNA constructs for the expression of αTSR for crystallization and αTSR haplotypes for SPR were made by a previous member of the Wilson Lab, David Oyen. αTSR for X-ray crystallography and αTSR haplotypes for SPR were expressed and purified by Gonzalo Gonzales (Wilson lab, TSRI). SPR measurements were performed and analyzed by Nathan Beutler (Burton lab, TSRI). Mouse liver burden assays were performed by our collaborators Yevel Flores Garcia and Fidel Zavala (John Hopkins University). Structure determination of Fab 1550-αTSR was assisted by Xueyong Zhu (Wilson lab, TSRI), and structure determination of Fab 1525-αTSR and Fab 1504-αTSR were assisted by Robyn Stanfield (Wilson lab, TSRI). Crystallization screens were set up by Henry (Hank) Tien in our high-throughput robotic crystallization facility (TSRI).

Table 3.1 Crystallographic data collection and refinement

Data collection	**367-αTSR**	**1392-αTSR**	**1525-αTSR**
Beamline	SSRL12-1	APS 23ID-B	APS 23ID-B
Wavelength (Å)	0.97946	1.03317	1.03317
Space group	P 2_1 2_1 2_1	C 2 2 2_1	P 6_1 2 2
Cell dimensions			
a, *b*, *c* (Å)	40.54, 69.02, 239.0	95.28, 150.15, 136.34	186.31, 186.31, 68.59
α, β, ɣ (°)	90, 90, 90	90, 90, 90	90, 90, 120
Resolution (Å)	35.0-2.23 (2.31-2.23)	42.1-1.63 (1.69-1.63)	46.6-2.20 (2.28-2.20)
R_{merge}	0.126 (1.66)	0.085 (1.18)	0.071 (0.39)
R_{meas}	0.138 (1.82)	0.088 (1.29)	0.072 (0.40)
R_{pim}	0.055 (0.74)	0.024 (0.50)	0.012 (1.00)
Total Reflections	19,7378 (17219)	1,422,447 (47230)	1,066,731 (28546)
Unique Reflections	33,115 (3035)	115,622 (8305)	31,636 (1894)
$CC_{1/2}$	0.996 (0.443)	0.999 (0.516)	1 (0.958)
I / sI	8.9 (1.5)	14 (1.2)	40 (7.8)
Completeness (%)	98.0 (92.5)	95.2 (69.1)	87.5 (53.73)
Redundancy	6.0 (5.7)	12.3 (5.7)	33.7 (15.1)
Refinement			
Resolution (Å)	35.0-2.23 (2.31-2.23)	42.1-1.63 (1.69-1.63)	46.58-2.20 (2.28-2.20)
No. reflections	33,110 (3035)	115,610 (8298)	31,536 (1896)
Reflections in R_{free}	1664 (146)	5652 (383)	1584 (102)
R_{work} / R_{free}	0.236/0.288	0.176/0.200	0.196/0.231
No. atoms	3887	4655	4434
Protein	3792	4018	4158
Ligand/ion	7	156	19
Water	91	481	257
B-values (Å^2)			
Average B-factors	62	34	47
Protein	62	32	48
Ligand/ion	47	44	55
Water	47	45	43
Wilson B-value	41	28	39
R.m.s. deviations			
Bond lengths (Å)	0.003	0.018	0.002
Bond angles (°)	0.65	1.63	0.58
Ramachandran Plots(%)			
Favoured	94.8	97.78	98.32
Allowed	4.6	2.22	1.68
Outliers	0.6	0	0
Clashscore	12.7	6.9	3.98

Numbers in parentheses refer to the highest resolution shell.

$R_{merge} = \Sigma_{hkl} \Sigma_i | I_{hkl,i} - \langle I_{hkl} \rangle | / \Sigma_{hkl} \Sigma_i I_{hkl,i}$ and $R_{meas} = \Sigma_{hkl} (n/(n-1))^{1/2} \Sigma_i | I_{hkl,i} - \langle I_{hkl} \rangle | / \Sigma_{hkl} \Sigma_i I_{hkl,I}$ and $R_{pim} = \Sigma_{hkl} (1/(n-1))^{1/2} \Sigma_i | I_{hkl,i} - \langle I_{hkl} \rangle | / \Sigma_{hkl} \Sigma_i I_{hkl,i}$, where $I_{hkl,i}$ is the scaled intensity of the ith measurement of reflection h, k, l, $\langle I_{hkl} \rangle$ is the average intensity for that reflection, and n is the redundancy.

$CC_{1/2}$ = Pearson correlation coefficient between two random half datasets.

$R_{work} = \Sigma_{hkl} | F_o - F_c | / \Sigma_{hkl} | F_o | \times 100$, where F_o and F_c are the observed and calculated structure factors, respectively.

R_{free} was calculated as for R_{work}, but on a test set comprising 5% of the data excluded from refinement.

Table 3.2 Crystallographic data collection and refinement

Data collection	**369-αTSR**	**389-αTSR**	**1393-αTSR**
Beamline	ALS-501	APS 23ID-D	APS 23ID-B
Wavelength (Å)	0.97741	1.0332	1.03317
Space group	C 1 2 1	C 1 2 1	P 1 21 1
Cell dimensions			
a, *b*, *c* (Å)	78.29, 71.10, 101.97	195.50, 63.66, 139.72	71.67, 61.12, 72.14
α, β, ɣ (°)	90, 102.81, 90	90, 101.76, 90	90, 106.21, 90
Resolution (Å)	49.7-2.13 (2.19-2.13)	45.6-1.75 (1.81-1.75)	43.7-1.80 (1.86-1.80)
R_{merge}	0.207 (1.53)	0.112 (1.67)	0.107 (0.964)
R_{meas}	0.225 (1.71)	0.129 (1.84)	0.127 (1.15)
R_{pim}	0.087 (0.741)	0.0521 (0.778)	0.0675 (0.610)
Total Reflections	201,828 (12239)	964,846 (78419)	187,183 (18238)
Unique Reflections	30,592 (2456)	166,878 (14246)	54,863 (5427)
$CC_{1/2}$	0.993 (0.322)	0.995 (0.376)	0.995 (0.439)
I / sI	8.2 (1.0)	6.6 (1.1)	8.9 (1.2)
Completeness (%)	99.7 (96.8)	98.3 (84.2)	98.5 (98.4)
Redundancy	6.6 (5.0)	5.8 (5.5)	3.4 (3.4)
Refinement			
Resolution (Å)	49.3-2.13 (2.21-2.13)	45.6-1.75 (1.81-1.75)	43.7-1.80 (1.86-1.80)
No. reflections	30,588 (2973)	166,800 (14215)	54,850 (5424)
Reflections in R_{free}	1521 (163)	8248 (759)	2628 (273)
R_{work} / R_{free}	0.185/0.227	0.189/0.218	0.180/0.214
No. atoms	4131	8779	4827
Protein	3808	7867	4297
Ligand/ion	65	61	0
Water	258	851	530
B-values (Å^2)			
Average B-factors	33	35	32
Protein	33	34	32
Ligand/ion	41	44	n/a
Water	36	44	35
Wilson B-value	29	29	22
R.m.s. deviations			
Bond lengths (Å)	0.008	0.017	0.004
Bond angles (°)	0.95	1.41	0.73
Ramachandran Plots(%)			
Favoured	96.6	98	97.46
Allowed	3.4	2	2.54
Outliers	0	0	0
Clashscore	2.74	4.59	4.35

Numbers in parentheses refer to the highest resolution shell.

$R_{merge} = \Sigma_{hkl} \Sigma_i | I_{hkl,i} - \langle I_{hkl} \rangle | / \Sigma_{hkl} \Sigma_i I_{hkl,i}$ and $R_{meas} = \Sigma_{hkl} (n/(n-1))^{1/2} \Sigma_i | I_{hkl,i} - \langle I_{hkl} \rangle | / \Sigma_{hkl} \Sigma_i I_{hkl,I}$ and $R_{pim} = \Sigma_{hkl} (1/(n-1))^{1/2} \Sigma_i | I_{hkl,i} - \langle I_{hkl} \rangle | / \Sigma_{hkl} \Sigma_i I_{hkl,i}$, where $I_{hkl,i}$ is the scaled intensity of the ith measurement of reflection h, k, l, $\langle I_{hkl} \rangle$ is the average intensity for that reflection, and n is the redundancy.

$CC_{1/2}$ = Pearson correlation coefficient between two random half datasets.

$R_{work} = \Sigma_{hkl} | F_o - F_c | / \Sigma_{hkl} | F_o |$ x 100, where F_o and F_c are the observed and calculated structure factors, respectively.

R_{free} was calculated as for R_{work}, but on a test set comprising 5% of the data excluded from refinement.

Table 3.3. Crystallographic data collection and refinement

Data collection	**1437-αTSR**	**1534-αTSR**	**1550-αTSR**
Beamline	SSRL12-2	APS 23ID-B	SSRL12-1
Wavelength (Å)	0.97946	1.03317	0.97946
Space group	C 2 2 21	P 2 21 21	C 1 2 1
Cell dimensions			
a, *b*, *c* (Å)	71.78, 106.14, 152.54	50.75, 118.26, 137.27	147.13, 61.06, 70.58
α, β, ɣ (°)	90, 90, 90	90, 90, 90	90, 106.64, 90
Resolution (Å)	38.64-1.86 (1.93-1.86)	46.6-2.77(2.87-2.77)	37.24-2.0 (2.07-2.0)
R_{merge}	0.197 (2.87)	0.133 (2.00)	0.227 (0.328)
R_{meas}	0.206 (3.14)	0.145 (2.16)	0.251 (0.394)
R_{pim}	0.0594 (1.21)	0.0562 (0.818)	0.105 (0.214)
Total Reflections	559,374 (25467)	140,941 (13871)	199,472 (6430)
Unique Reflections	48,308 (4062)	21,602 (2041)	36,662 (2166)
$CC_{1/2}$	0.995 (0.963)	0.996 (0.466)	0.949 (0.869)
I / sI	9.7 (0.7)	8.0 (1.2)	8.0 (6.4)
Completeness (%)	96.9 (73.1)	99.2 (96.3)	90.0 (53.4)
Redundancy	11.6 (6.3)	6.5 (6.8)	5.4 (3.0)
Refinement			
Resolution (Å)	38.64-1.86 (1.93-1.86)	46.6-2.77(2.87-2.77)	37.24-2.0 (2.07-2.0)
No. reflections	47,698 (3551)	21,588 (2035)	36,667 (2166)
Reflections in R_{free}	2358 (167)	1091 (103)	1860 (105)
R_{work} / R_{free}	0.218/0.260	0.288/0.340	0.172/0.211
No. atoms	4242	4320	4562
Protein	3824	4293	4257
Ligand/ion	6	0	0
Water	412	27	305
B-values (Å^2)			
Average B-factors	39	85	34
Protein	39	85	34
Ligand/ion	30	n/a	N/A
Water	42	71	38
Wilson B-value	30	77	29
R.m.s. deviations			
Bond lengths (Å)	0.006	0.003	0.008
Bond angles (°)	0.82	0.57	0.99
Ramachandran Plots(%)			
Favoured	97.2	92.91	97.46
Allowed	2.6	6.91	2.54
Outliers	0.2	0.18	0
Clashscore	5.39	8.25	3.58

Numbers in parentheses refer to the highest resolution shell.

$R_{merge} = \Sigma_{hkl} \Sigma_i \mid I_{hkl,i} - \langle I_{hkl} \rangle \mid / \Sigma_{hkl} \Sigma_i I_{hkl,i}$ and $R_{meas} = \Sigma_{hkl} (n/(n-1))^{1/2} \Sigma_i \mid I_{hkl,i} - \langle I_{hkl} \rangle \mid / \Sigma_{hkl} \Sigma_i I_{hkl,I}$ and $R_{pim} = \Sigma_{hkl} (1/(n-1))^{1/2} \Sigma_i \mid I_{hkl,i} - \langle I_{hkl} \rangle \mid / \Sigma_{hkl} \Sigma_i I_{hkl,i}$, where $I_{hkl,i}$ is the scaled intensity of the ith measurement of reflection h, k, l, $\langle I_{hkl} \rangle$ is the average intensity for that reflection, and n is the redundancy.

$CC_{1/2}$ = Pearson correlation coefficient between two random half datasets.

$R_{work} = \Sigma_{hkl} \mid F_o - F_c \mid / \Sigma_{hkl} \mid F_o \mid$ x 100, where F_o and F_c are the observed and calculated structure factors, respectively.

R_{free} was calculated as for R_{work}, but on a test set comprising 5% of the data excluded from refinement.

Table 3.4 Crystallographic data collection and refinement

Data collection	**1504-αTSR**
Beamline	APS 23ID-B
Wavelength (Å)	1.0337
Space group	P1
Cell dimensions	
a, *b*, *c* (Å)	73.47, 85.02, 105.11
α, β, ɣ (°)	95.57, 109.89, 114.55
Resolution (Å)	48.89-3.0 (3.108-3.0)
R_{merge}	0.121 (0.329)
R_{meas}	0.153 (0.423)
R_{pim}	0.092 (0.263)
Total Reflections	86029 (5429)
Unique Reflections	36167 (2636)
$CC_{1/2}$	0.963 (0.834)
I / sI	7.5 (3.1)
Completeness (%)	86.4 (62.9)
Redundancy	2.4 (2.1)
Refinement	
Resolution (Å)	48.89-3.0 (3.108-3.0)
No. reflections	36152 (2631)
Reflections in R_{free}	1662 (131)
R_{work} / R_{free}	0.289/0.318
No. atoms	14989
Protein	14989
Ligand/ion	0
Water	0
B-values (Å^2)	
Average B-factors	72
Protein	72
Ligand/ion	n/a
Water	n/a
Wilson B-value	60
R.m.s. deviations	
Bond lengths (Å)	0.004
Bond angles (°)	0.88
Ramachandran Plots(%)	
Favoured	89.9
Allowed	9.4
Outliers	0.67
Clashscore	10.8

Numbers in parentheses refer to the highest resolution shell.

$R_{merge} = \Sigma_{hkl} \Sigma_i | I_{hkl,i} - \langle I_{hkl} \rangle | / \Sigma_{hkl} \Sigma_i I_{hkl,i}$ and $R_{meas} = \Sigma_{hkl} (n/(n-1))^{1/2} \Sigma_i | I_{hkl,i} - \langle I_{hkl} \rangle | / \Sigma_{hkl} \Sigma_i I_{hkl,I}$ and $R_{pim} = \Sigma_{hkl} (1/(n-1))^{1/2} \Sigma_i | I_{hkl,i} - \langle I_{hkl} \rangle | / \Sigma_{hkl} \Sigma_i I_{hkl,i}$, where $I_{hkl,i}$ is the scaled intensity of the ith measurement of reflection h, k, l, $\langle I_{hkl} \rangle$ is the average intensity for that reflection, and n is the redundancy.

$CC_{1/2}$ = Pearson correlation coefficient between two random half datasets.

$R_{work} = \Sigma_{hkl} | F_o - F_c | / \Sigma_{hkl} | F_o |$ x 100, where F_o and F_c are the observed and calculated structure factors, respectively.

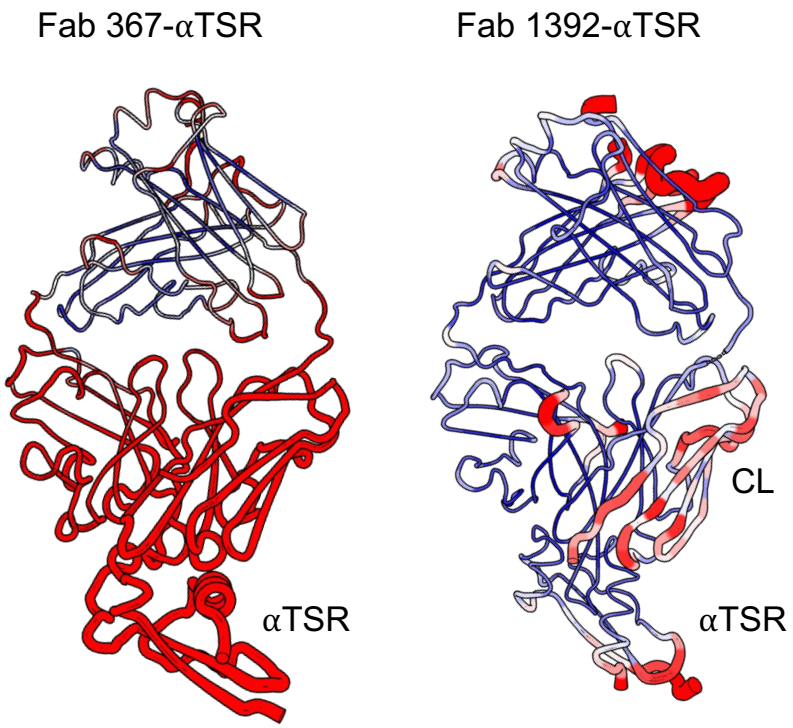
R_{free} was calculated as for R_{work}, but on a test set comprising 5% of the data excluded from refinement.

3.7 References

1. Nadeem, A. Y., Shehzad, A., Islam, S. U., Al-Suhaimi, E. A. & Lee, Y. S. Mosquirix™ RTS, S/AS01 Vaccine Development, Immunogenicity, and Efficacy. *Vaccines (Basel)* **10**, 1033–1039 (2022).
2. Adams, J. & Tucker, R. The Thrombospondin Type 1 Repeat (TSR) Superfamily: Diverse Proteins with Related Roles in Neuronal Development. **218**, 280–299 (2000).
3. Sinigaglia, F. *et al*. A malaria T-cell epitope recognized in association with most mouse and human MHC class II molecules. *Nature* **336**, 778–780 (1988).
4. Hoffman, S. L. *et al*. Human lymphocyte proliferative response to a sporozoite T cell epitope correlates with resistance to *falciparum* malaria. *J Immunol* **142**, 1299–1303 (1989).
5. Gordon, D. M. *et al*. Safety, Immunogenicity, and Efficacy of a Recombinantly Produced *Plasmodium falciparum* Circumsporozoite Protein-Hepatitis B Surface Antigen Subunit Vaccine. *J Infect Dis* **171**, 1576–1585 (1995).
6. White, M. T. *et al*. Immunogenicity of the RTS,S/AS01 malaria vaccine and implications for duration of vaccine efficacy: secondary analysis of data from a phase 3 randomised controlled trial. *Lancet Infect Dis* **15**, 1450–1458 (2015).
7. Regules, J. A. *et al*. Fractional Third and Fourth Dose of RTS,S/AS01 Malaria Candidate Vaccine: A Phase 2a Controlled Human Malaria Parasite Infection and Immunogenicity Study. *J Infect Dis* **214**, 762–771 (2016).
8. Martin, G. M. *et al*. Structural basis of epitope selectivity and potent protection from malaria by PfCSP antibody L9. *bioRxiv* (2022) doi:10.1101/2022.10.07.511358.
9. Kucharska, I. *et al*. High-density binding to *Plasmodium falciparum* circumsporozoite protein repeats by inhibitory antibody elicited in mouse with human immunoglobulin repertoire. *PLoS Pathog* **18**, e1010999 (2022).
10. Oyen, D. *et al*. Cryo-EM structure of *P. falciparum* circumsporozoite protein with a vaccine-elicited antibody is stabilized by somatically mutated inter-Fab contacts. *Sci Adv* **4**, 8529 (2018).
11. Oyen, D. *et al*. Structural basis for antibody recognition of the NANP repeats in *Plasmodium falciparum* circumsporozoite protein. *Proc Natl Acad Sci* **114**, E10438–E10445 (2017).
12. Martin, G. M. *et al*. Affinity-matured homotypic interactions induce spectrum of PfCSP-antibody structures that influence protection from malaria infection. *bioRxiv* 2022.09.20.508747 (2022) doi:10.1101/2022.09.20.508747.
13. Kurtovic, L., Drew, D. R., Dent, A. E., Kazura, J. W. & Beeson, J. G. Antibody Targets and Properties for Complement-Fixation Against the Circumsporozoite Protein in Malaria Immunity. *Front Immunol* **12**, 775659 (2021).
14. Kurtovic, L. *et al*. Human antibodies activate complement against *Plasmodium falciparum* sporozoites, and are associated with protection against malaria in children. *BMC Med* **16**, 61 (2018).
15. Kurtovic, L. *et al*. Multifunctional Antibodies Are Induced by the RTS,S Malaria Vaccine and Associated With Protection in a Phase 1/2a Trial. *J Infect Dis* **224**, 1138 (2021).

16. Das, J. *et al*. Delayed fractional dosing with RTS,S/AS01 improves humoral immunity to malaria via a balance of polyfunctional NANP6- and Pf16-specific antibodies. *Med* **2**, 1269-1286.e9 (2021).
17. Lê, H. G. *et al*. Genetic polymorphism and natural selection of circumsporozoite surface protein in *Plasmodium falciparum* field isolates from Myanmar. *Malar J* **17**, 361 (2018).
18. Huang, H. Y. *et al*. Genetic polymorphism of *Plasmodium falciparum* circumsporozoite protein on Bioko Island, Equatorial Guinea and global comparative analysis. *Malar J* **19**, 245 (2020).
19. He, Z. quan *et al*. Genetic polymorphism of circumsporozoite protein of *Plasmodium falciparum* among Chinese migrant workers returning from Africa to Henan Province. *Malar J* **21**, 248 (2022).
20. Pringle, J. C. *et al*. RTS,S/AS01 malaria vaccine mismatch observed among *Plasmodium falciparum* isolates from southern and central Africa and globally. *Sci Reports* **8**, 6622 (2018).
21. Neafsey, D. E. *et al*. Genetic Diversity and Protective Efficacy of the RTS,S/AS01 Malaria Vaccine. *N Engl J Med* **373**, 2025–2037 (2015).
22. Scally, S. W. *et al*. Rare PfCSP C-terminal antibodies induced by live sporozoite vaccination are ineffective against malaria infection. *J Exp Med* **215**, 63 (2018).
23. Beutler, N. *et al*. A novel CSP C-terminal epitope targeted by an antibody with protective activity against *Plasmodium falciparum*. *PLoS Pathog* **18**, e1010409 (2022).
24. Krawczyk, K., Buchanan, A. & Marcatili, P. Data mining patented antibody sequences. *bioRxiv* 2020.11.26.389866 (2020) doi:10.1101/2020.11.26.389866.
25. Lebedev, A. A. & Isupov, M. N. Space-group and origin ambiguity in macromolecular structures with pseudo-symmetry and its treatment with the program Zanuda. *Acta Cryst* **70**, 2430–2443 (2014).
26. Dame, J. B. *et al*. Structure of the Gene Encoding the Immunodominant Surface Antigen on the Sporozoite of the Human Malaria Parasite *Plasmodium falciparum*. *Science* **225**, 587–593 (1984).
27. Lopaticki, S. *et al*. Protein O-fucosylation in *Plasmodium falciparum* ensures efficient infection of mosquito and vertebrate hosts. *Nat Commun 2017 8:1* **8**, 561 (2017).
28. Chaudhury, S. *et al*. Breadth of humoral immune responses to the C-terminus of the circumsporozoite protein is associated with protective efficacy induced by the RTS,S malaria vaccine. *Vaccine* **39**, 968–975 (2021).
29. Yu, L. & Guan, Y. Immunologic Basis for Long HCDR3s in Broadly Neutralizing Antibodies Against HIV-1. *Front Immunol* **5**, 250 (2014).
30. Swearingen, K. E. *et al*. Interrogating the *Plasmodium* Sporozoite Surface: Identification of Surface-Exposed Proteins and Demonstration of Glycosylation on CSP and TRAP by Mass Spectrometry-Based Proteomics. *PLoS Pathog* **12**, e1005606 (2016).
31. Zhao, J., Bhanot, P., Hu, J. & Wang, Q. A Comprehensive Analysis of *Plasmodium* Circumsporozoite Protein Binding to Hepatocytes. *PLoS One* **11**, e0161607 (2016).

32. Pinzon-Ortiz, C., Friedman, J., Esko, J. & Sinnis, P. The Binding of the Circumsporozoite Protein to Cell Surface Heparan Sulfate Proteoglycans is Required for *Plasmodium* Sporozoite Attachment to Target Cells. *J Biol Chem* **276**, 26784–26791 (2001).
33. Coppi, A., Pinzon-Ortiz, C., Hutter, C. & Sinnis, P. The *Plasmodium* circumsporozoite protein is proteolytically processed during cell invasion. *J Exp Med* **201**, 27–33 (2005).
34. Coppi, A. *et al*. The malaria circumsporozoite protein has two functional domains, each with distinct roles as sporozoites journey from mosquito to mammalian host. *J Exp Med* **208**, 341–356 (2011).
35. Wang, L. T. *et al*. Protective effects of combining monoclonal antibodies and vaccines against the *Plasmodium falciparum* circumsporozoite protein. *PLoS Pathog* **17**, e1010133 (2021).
36. Kurtovic, L. *et al*. Induction and decay of functional complement-fixing antibodies by the RTS,S malaria vaccine in children, and a negative impact of malaria exposure. *BMC Med* **17**, 45 (2019).
37. Kurtovic, L. *et al*. Complement in malaria immunity and vaccines. *Immunol Rev* **293**, 38–56 (2020).
38. Pradel, G. & Frevert, U. Malaria sporozoites actively enter and pass through rat Kupffer cells prior to hepatocyte invasion. *Hepatology* **33**, 1154–1165 (2001).
39. Usynin, I., Klotz, C. & Frevert, U. Malaria circumsporozoite protein inhibits the respiratory burst in Kupffer cells. *Cell Microbiol* **9**, 2610–2628 (2007).
40. Khattab, A. *et al*. Hijacking the human complement inhibitor C4b-binding protein by the sporozoite stage of the *Plasmodium falciparum* parasite. *Front Immunol* **13**, 1051161(2022).
41. Kabsch, W. XDS. *Acta Cryst* **66**, 132 (2010).
42. Otwinowski, Z. & Minor, W. Processing of X-ray diffraction data collected in oscillation mode. *Methods Enzymol* **276**, 307–326 (1997).
43. McCoy, A. J. *et al*. Phaser crystallographic software. *J Appl Crystallogr* **40**, 674 (2007).
44. Dunbar, J. *et al*. SAbPred: a structure-based antibody prediction server. *Nucl Acids Res* **44**, W474–W478 (2016).
45. Emsley, P. & Cowtan, K. Coot: model-building tools for molecular graphics. *Acta Crystallogr* **D60**, 2126–2132 (2004).
46. Murshudov, G. N. *et al*. REFMAC5 for the refinement of macromolecular crystal structures. *Acta Crystallogr* **D67**, 355-367 (2011).
47. Afonine, P. V. *et al*. Towards automated crystallographic structure refinement with phenix.refine. *Acta Crystallogr* **D68**, 352-367 (2012).
48. Davis, I. W. *et al*. MolProbity: all-atom contacts and structure validation for proteins and nucleic acids. *Nucl Acids Res* **35**, W375–W383 (2007).



Supplementary Figure 3.1. Individual B-factors of Fab 367 and Fab 1392 in complex with αTSR. Crystal structures of Fab 367 and Fan 1392 in complex with αTSR are colored by B-factors in cartoon putty representation ranging from low B-factors (blue, thin) to high B-factors (red, wide), showing the disorder in the antigen binding region of Fab 367 bound to αTSR and in the VL domain of Fab 1392 bound to αTSR.

CHAPTER 4: Novel Immunogen Design Incorporating Protective CSP B-cell Epitopes into the αTSR Domain

4.0 Abstract

Improved second-generation vaccine design is required to overcome key problems identified by analysis of RTS,S patient sera, incorporate new epitopes, and use antigen display methods discovered in the last 30 years. Our previous work demonstrates the breadth of antibodies isolated from the MAL071 trial binding conserved epitopes on the αTSR domain with high affinity and a high avidity index. We produced a modified αTSR immunogen design that seeks to divert the response from polymorphic epitopes towards protective CSP epitopes by replacing the polymorphic CS-flap with major repeat, minor repeat, and junctional epitopes of CSP. Expressed on the surface of modified lumazine synthase nanoparticles, modified αTSR-based immunogens show decrease binding to polymorphic sequence targeting mAbs while maintaining binding to mAbs that bind conserved sequence on αTSR. In C57Bl/6 mice, immunogenicity ranges from EC_{50} values 1.5-fold higher to 4-fold lower than that of RTS,S, while still provide comparable protection to RTS,S. This is a first proof-of-concept study showing immunogens incorporating protective CSP B-cell epitopes into the αTSR structure can produce high anti-CSP antibody titres and achieve comparable protection to the benchmark RTS,S vaccination, thereby providing a useful design for further optimization for the display of protective CSP epitopes.

4.1 Introduction

In a landmark decision by the World Health Organisation, the RTS,S/AS01 circumsporozoite protein (CSP)-based vaccine was approved for use in high malaria transmission regions in 2021(1). Long before this decision, it was apparent that RTS,S vaccination suffers from a major problem: antibody titres fall sharply in the first 6 months from the final vaccination(2). Additionally, strain mismatch from the vaccine strain(3) and non-protective pre-exposure(4) both reduce vaccine efficacy. Recently, a rebound effect has been observed with malaria incidences increasing in RTS,S vaccinees as opposed to unvaccinated individuals three years post immunization(5). These highlight the need for a more cost effective and efficacious vaccine second generation vaccine.

Second-generation vaccine design focuses on implementing our advanced understanding of antibody-mediated for the generation of improved vaccines. In the 30 years since the inception of RTS,S, two specific paradigms have shifted to guide the next round of immunogen design: the discovery of potent mAbs targeting the minor repeat and junctional epitopes of CSP(6,7), isolated from sporozoite immunization, has revealed that the major repeat epitope is not the only target of highly protective antibodies on CSP. Multiple immunogen designs targeting the junctional epitope have shown to provide protection in mouse models (8–11). Secondly, the binding of major repeat antibodies to long repeat peptides through Fab-Fab homotypic interactions has been shown to increase mAb affinity through avidity(12–15). Antibody avidity to the major repeat epitope has been found as a better correlate of protection in multiple trials as opposed to anti-CSP

titres(16–18), shifting the focus from the production of higher anti-CSP titres to also producing high avidity antibodies.

The C-terminal αTSR domain of CSP was originally included in the RTS,S vaccination following the observation that the presence of T-cell epitopes increases anti-NANP antibody titres(19). The recent MAL071 delayed fractional dose RTS,S trial put further emphasis on anti-CtCSP antibody-mediated protection(18). Multiple analyses suggested that the delayed fractional dose regime is differentiated from standard dose regime by multiple anti-CtCSP antibody mediated effector function(20,21). Anti-CtCSP antibodies have also been shown to fix complement, another correlate of protection in RTS,S vaccination(22–24). Nevertheless, many second-generation vaccine designs have omitted the CtCSP αTSR domain from their designs.

Previous work in the Wilson lab led to determination of X-ray crystal structures of five mAbs isolated from RTS,S vaccination to define and α- and β- epitopes on the αTSR surface(25). In the previous chapter, we reiterate the similar modes of binding employed by mAbs targeting the α-epitope of αTSR, identifying six further mAbs binding to the highly conserved β-epitope, as well as mAb 1504 targeting a new conserved epitope on αTSR. We then showed that mAbs that target conserved epitopes on αTSR have a higher avidity index. A recent analysis of RTS,S sera shows that binding to conserved CtCSP peptides correlates with vaccine-mediated protection(20). We have also shown in the previous chapter that MAL071 mAbs targeting αTSR do not provide sterilising protection, echoing the observation made by recent analysis using a panel of mAbs from

sporozoite immunization(26). While we lack a mechanism of action for CtCSP-mediated immunity, the identification of anti-CtCSP avidity as an immune correlate should be further interrogated through future vaccine design. In this chapter, we propose an immunogen design that incorporates CSP major repeat, minor repeat, and junctional B-cell epitopes in the αTSR domain, eliminates polymorphic epitopes, and directs antibody production towards the highly conserved β-epitope.

4.2 Results

4.2.1 Immunogen design rationale

Previous work in the Wilson lab has revealed the conserved secondary structure elements adopted by repeat antigens and their stabilization by inhibitory RTS,S induced antibodies(27). Structural modelling of the RTS,S major repeat domain further suggests that it adopts a non-linear conformation(28). Decreasing the conformational flexibility of repeat epitopes through their stabilization in loops within immunogens produces increased antibody titres in mice(29). As opposed to incorporating linear epitopes as loops in carrier antigens such as the tobacco mosaic virus envelope, we can incorporate them as loops within existing CSP domains: while the Th2R polymorphic epitope of αTSR forms an α-helix likely key to the structural integrity of the domain, the Th3R polymorphic epitope forms a loop connecting two conserved β-strands and points in a solvent-exposed direction away from the membrane on parasite surface. We hypothesize that replacing the Th3R polymorphic epitope with conserved CSP B-cell epitopes could simultaneously reduce their conformational flexibility and destabilize binding of α-epitope binding mAbs. To test this hypothesis, eight αTSR variants were designed in which the Th3R domain was replaced with conserved B-cell epitopes corresponding to the major repeats, minor repeats, junctional epitope, and RI cleavage site. These epitopes were inserted between the conserved turn-inducing Pro348 and Asp363 residues of the conserved CS.T3 T-cell epitope. A panel of eight constructs were designed to include varying length and orientation major repeat (αTSR1-2), minor repeat (αTSR3-5), junctional (αTSR6-7), and RI cleavage (αTSR8) epitopes **(Figure 4.1)**. This immunogen design can provide useful information as to whether stabilization of protective CSP

epitopes within the αTSR structure can divert the antibody response away from polymorphic epitopes to conserved and protective epitopes of CSP, and whether elicited antibodies can bind those epitopes on sporozoites to protect from infection in a mouse challenge.

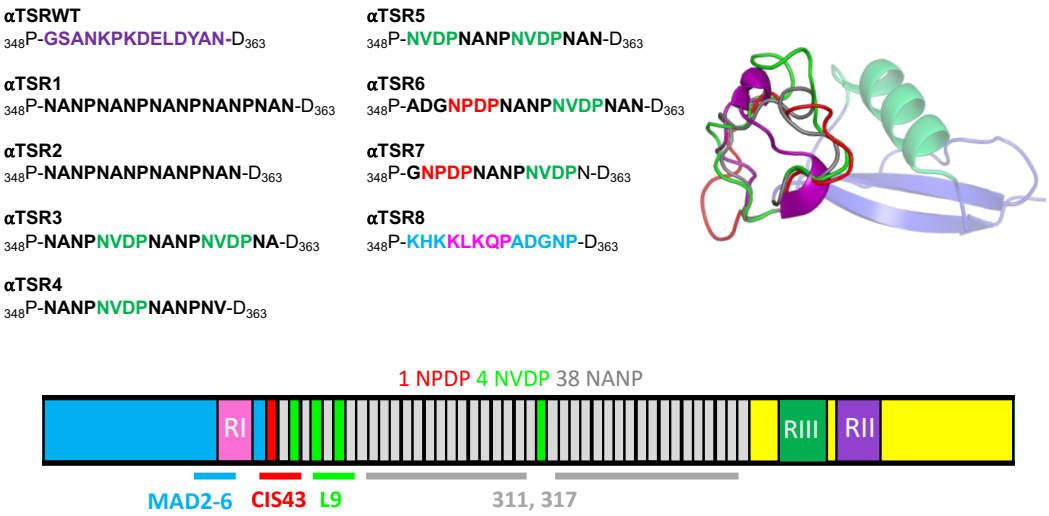


Figure 4.1. αTSR-based immunogen design. The CS-flap (purple) of the αTSR domain was replaced with eight sequences corresponding to four major repeats (αTSR1), three major repeats (αTSR2), minor repeats (αTSR3), shortened minor repeats (αTSR4), alternative shortened minor repeats (αTSR5), junctional epitope (αTSR6), short junctional epitope (αTSR7), and RI (αTSR8). Residues are colored according to the schematic shown to illustrate the different epitopes. Structural representation of the αTSR domain with loops of variable conformations and lengths is shown as cartoon, with the remaining domain in transparent cartoon (TSR homology domain in blue and Th2R helix in green).

4.2.2 Antibody binding to hybrid immunogens expressed on HEK cell surface

First, we assessed whether well-characterized antibodies retain binding to their relevant epitopes in the proposed immunogen design. Hybrid αTSR domains were expressed on HEK293F cell surface fused to the SARS-CoV-2 trimer transmembrane α-helix and assessed for antibody binding by flow cytometry. The gating strategy is shown in **Supplementary Figure 4.1.** Only weak background binding was seen by any mAb to the non-transfected control **(Figure 4.2A)** and negative control αHA IgG did not bind HEK293F cells expressing αTSR variants on their surface. Wild-type αTSR domain expressed on HEK cell surface bound β-epitope binding mAb 1512 and α-epitope binding mAbs 236 and 1525 **(Figure 4.2A)** suggesting that the domain is at least partially folded on the cell surface. While mAb 1512 bound to all cell-surface constructs, mAbs 236 and 1525 only bound αTSR-WT **(Figure 4.2B).** Due to the lack of positive transfection control, it is unclear whether decreased binding of mAb 1512 is due to differences in transfection efficiency or domain misfolding. Nevertheless, these results show that substitution of the CS-flap with non-CtCSP linear epitopes abrogates binding of the tested antibodies targeting polymorphic epitopes to modified αTSR domains expressed on HEK293F cell surface.

Major repeat, minor repeat, and junctional epitopes share sequence similarities and cross-reactivity to these domains has been documented (30). It is therefore unsurprising that mAb 311 with a short $(NANP)_2$ minimal epitope (31) binds all repeat-based hybrid domain designs **(Figure 4.2C).** Major-repeat binding mAb 317 has a longer $(NANP)_3$ minimal epitope (31) and produces differential binding across repeat-based αTSR

construct **(Figure 4.2C)**. Minor repeat-binding mAb L9 bound both minor repeat and junctional epitope-containing αTSR 3-7 with highest binding to minor repeat based αTSR3, but shows reduced binding to major repeat containing αTSR1-2, suggesting that it is more specific to minor repeat sequences (**Figure 4.2D).**

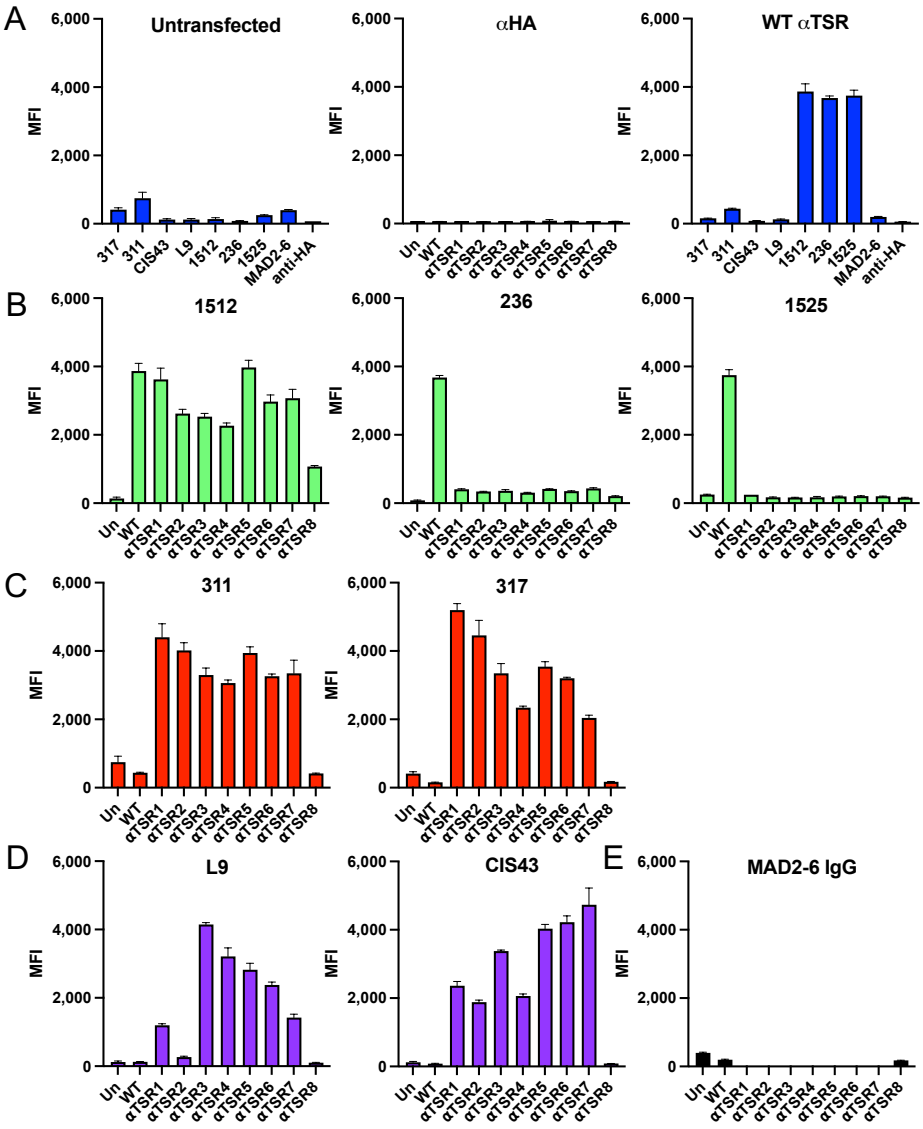


Figure 4.2. Monoclonal antibody binding to αTSR variants expressed on HEK cell surface. HEK293F cells expressing αTSR variants or non-transfected control (Un) were stained with monoclonal mAbs targeting CSP epitopes or negative control αHA. 20,000 events were counted per sample and mean fluorescent intensity (MFI) values shown are calculated as the mean of triplicates with standard deviation shown as error bars.

Junctional epitope-binding CIS43 bound all repeat-based constructs, with high binding to junctional epitope-based constructs TSR6-7 **(Figure 4.2D)**. While all repeat-based constructs bound antibodies targeting their respective epitopes, mAb MAD2-6(32) IgG did not bind any constructs including αTSR8 **(Figure 4.2E).** With the exception of the Region I epitope, these results validate that linear epitopes conformationally restricted within a loop in the αTSR domain retain binding to their respective targeting mAbs. Due to the lack of binding of αTSR8 to its respective epitope, it was not taken forward for soluble expression.

4.2.3 Nanoparticle expression and purification

Hybrid domain constructs were expressed as N-terminal fusions to modified lumazine synthase, which self-assembles into 60-mer nanoparticles. NP1-7 were expressed in HEK293F cells and purified by lectin affinity chromatography, producing a dominant peak by reducing SDS-PAGE (representative purification in **Figure 4.3A**). Elution fractions were further purified by size-exclusion chromatography on a Superose6 column producing a single dominant peak **(Figure 4.3B)**. All Superose6 purified NP1-7 produced a single major band on reducing SDS-PAGE at the expected molecular weight of 27 kDa, with very slight impurities which may correspond to non-reduced multimeric assemblies **(Figure 4.3C)**. To ensure correct self-assembly of all nanoparticles, NP1-7 were inspected by negative-stain electron microscopy **(Figure 4.4)**. Most nanoparticles form uniformly sized rounded shapes with hollow centres, as expected from a correctly formed nanoparticle assembly.

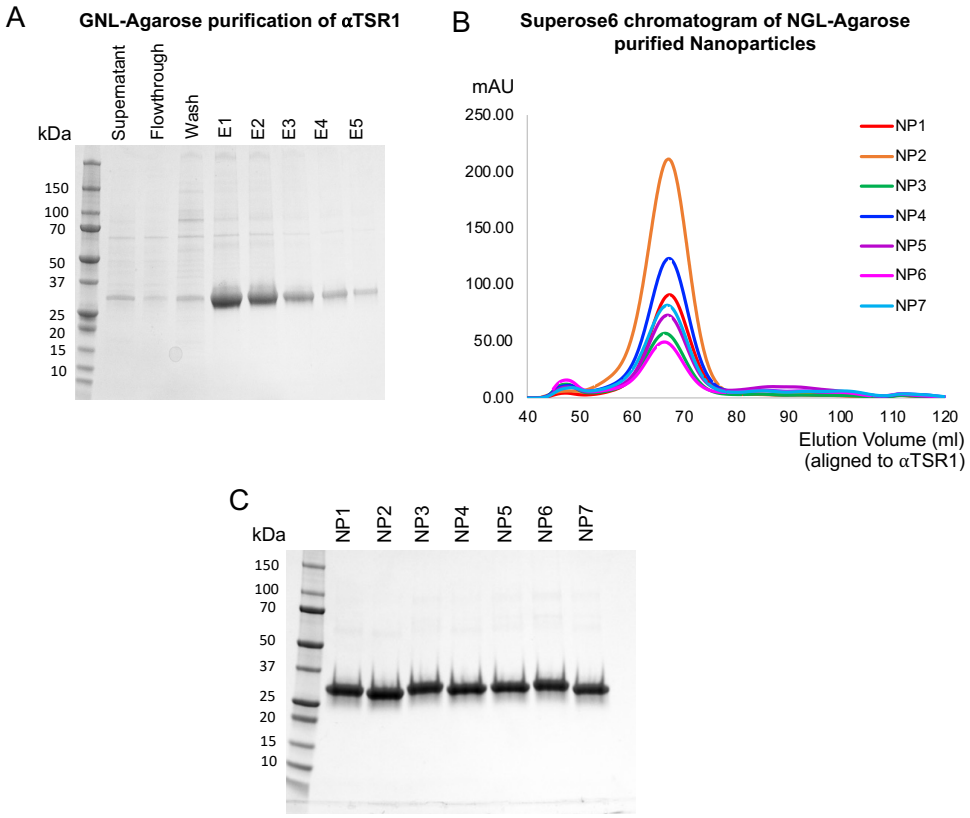


Figure 4.3. Expression and purification of nanoparticles in HEK293F cells. (A) Purification of NP1 from HEK293F cell supernatant by GNL lectin affinity chromatography visualized by SDS-PAGE, showing a single major band at the expected MW of 27 kDa. (E=elution) (B) SEC chromatogram of NP1-7 purified on a Superose6 GL column. Nanoparticles were purified by tandem injections, and chromatograms were aligned to the NP1 chromatogram for comparison purposes. (C) Purified NP1-7 produce a single major band at 27 kDa by SDS-PAGE.

4.2.4 Antigenicity of αTSR-based nanoparticles

The antigenicity of NP1-7 was assessed by ELISA using a panel of mAbs targeting αTSR and repeat epitopes. All nanoparticles bound β-epitope binding mAbs 1512 and 369 with a similar EC_{50} ranging from $6.2x10^{-3}$ to $9.9x10^{-3}$ ug/ml **(Figure 4.5)**. In contrast, α-epitope binding mAb 236 and 1525 bound to nanoparticle with WT-αTSR with EC_{50} of

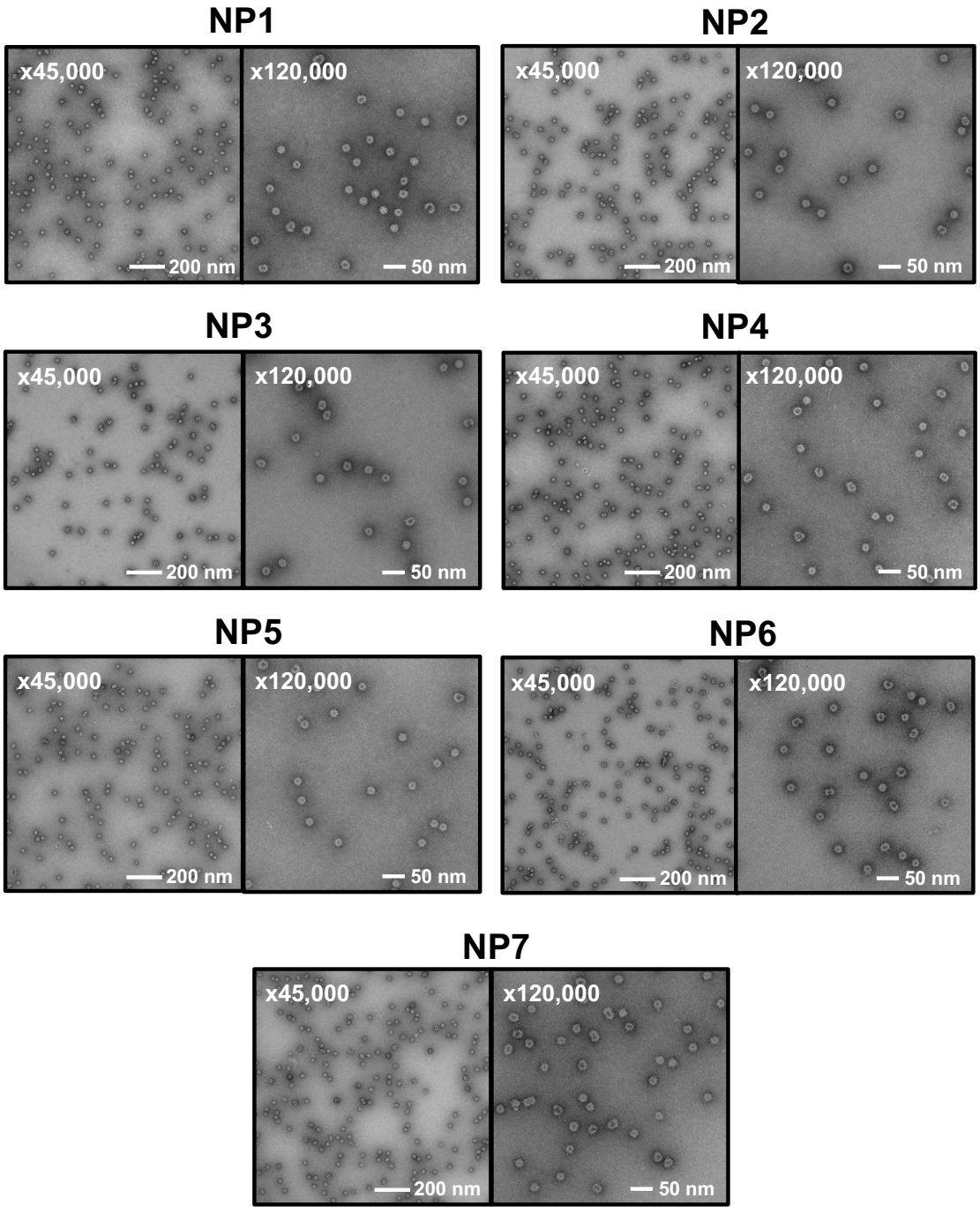
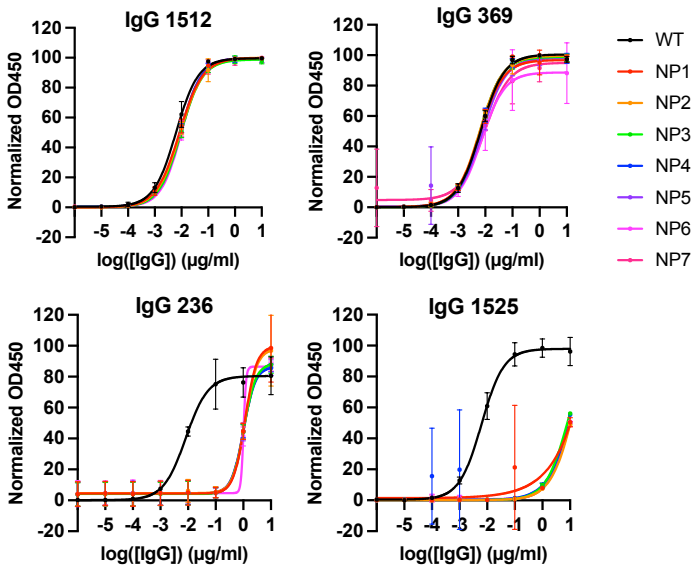


Figure 4.4. Negative-stain electron microscopy of purified nanoparticles. Nanoparticles were stained with uranyl formate and imaged at magnification of x45,000 and x120,000, with bars for scale showing the nanoparticles form spheres with hollow centers.

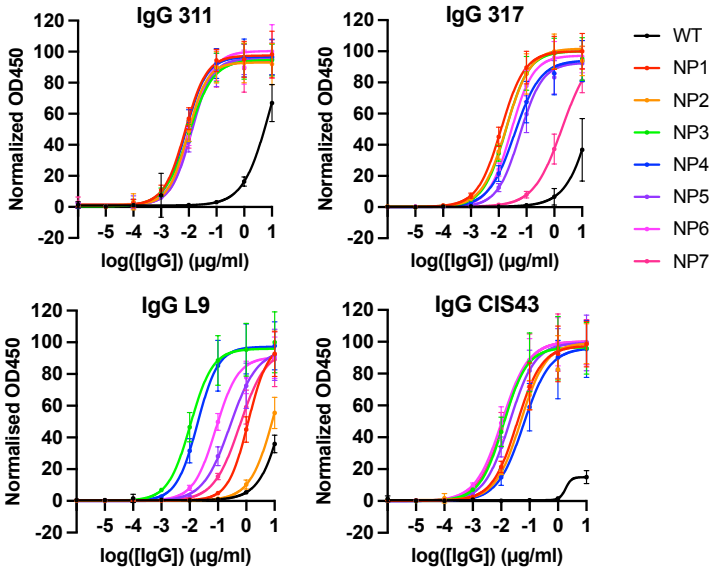


EC50 g/ml	αTSR-WT	NP1	NP2	NP3	NP4	NP5	NP6	NP7
IgG 1512	6.2E-09	8.4E-09	9.0E-09	9.4E-09	8.9E-09	9.6E-09	9.9E-09	8.8E-09
IgG 369	6.8E-09	6.3E-09	6.2E-09	6.2E-09	6.6E-09	7.7E-09	7.4E-09	9.4E-09
IgG 236	8.3E-09	1.2E-06	1.2E-06	1.1E-06	1.0E-06	1.0E-06	1.0E-06	1.0E-06
IgG 1525	6.2E-09		1.7E-05	7.7E-06	1.9E-05	1.3E-05	6.8E-06	1.1E-05

1E-5
1E-7
1E-9

Figure 4.5 Antigenicity of modified αTSR nanoparticles to CtCSP binding mAbs. Binding of mAb 1512 and 369 to the conserved β-epitope and mAbs 236 and 1525 to the polymorphic α-epitope were assessed by ELISA, with results shown from four ELISA curves from two separate experiments. EC_{50} values (g/ml) were produced by non-linear regression using a sigmoidal four parameter logistic curve and are color coded from high (weak binding, red) to low (strong binding, green) for each mAb.

$6.2x10^{-3}$ ug/ml, while binding to the remainder of nanoparticles with EC_{50} ranging from 1-19 ug/ml, three orders of magnitude higher than the wild-type **(Figure 4.5)**. Together, these results would suggest that the conformation of the β-epitope is less impacted by the substitution of the CS-flap with conserved CSP epitopes, while the α-epitope is sufficiently altered to abrogate antibody binding. Next, we assessed the nanoparticle antigenicity to mAbs targeting the B-cell epitopes replacing the CS-flap **(Figure 4.6)**. IgG 311 (minimal epitope $(NPNA)_2$) bound NP1-7 with EC_{50} of 10^{-3} to 10^{-2} ug/ml, and



EC50 g/ml	αTSR-WT	NP1	NP2	NP3	NP4	NP5	NP6	NP7
IgG 311	8.05E-06	7.40E-09	9.28E-09	9.97E-09	7.80E-09	1.26E-08	1.21E-08	1.12E-08
IgG 317	4.05E-05	1.22E-08	1.87E-08	1.85E-08	3.73E-08	5.75E-08	2.79E-08	1.89E-06
IgG L9	3.42E-05	1.17E-06	1.09E-05	1.06E-08	1.88E-08	2.70E-07	8.40E-08	5.93E-07
IgG CIS43	1.84E-06	3.59E-08	4.85E-08	1.21E-08	6.13E-08	2.00E-08	1.06E-08	1.25E-08

1E-5
1E-7
1E-9

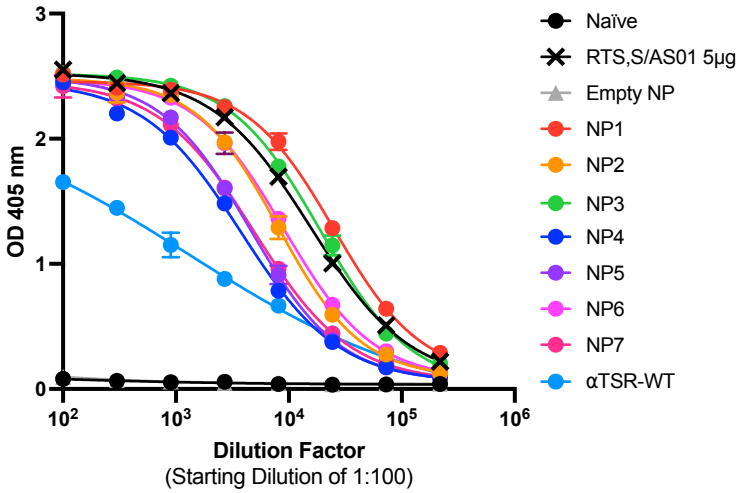
Figure 4.6 Antigenicity of modified αTSR nanoparticles to repeat and junctional epitope binding mAbs. Binding of mAb 311, 317, L9, and CIS43 were assessed by ELISA, with results shown from four ELISA curves from two separate experiments. EC_{50} values (g/ml) were produced by non-linear regression using a sigmoidal four parameter logistic curve and are color coded from high (weak binding, red) to low (strong binding, green) for each mAb.

bound WT-αTSR with a substantially reduced EC_{50} of 8.05 ug/ml. Except WT-αTSR, the difference in binding between the strongest binder NP1 and the weakest binder NP7 is only 2-fold, showing mAb 311 is highly cross-reactive and barely differentiates between the different CS-flap inserts (EC_{50} of $7.4x10^{-3}$ and $1.12x10^{-2}$ ug/ml, respectively). IgG 317 (minimal epitope $(NPNA)_3$) produced even weaker binding to WT-αTSR with an EC_{50} of 40.5 ug/ml. Amongst the remaining nanoparticles, IgG 317 bound with the lowest

EC_{50} to NP1-3 (EC_{50} $1.22x10^{-3}$ to $1.87x10^{-3}$ ug/ml), showed slightly weaker binding to NP4-6 ($2.79x10^{-3}$ to $5.75x10^{-2}$ ug/ml) and only weakly bound NP7 (EC_{50} of 1.89 ug/ml). Despite having a longer minimal epitope than mAb 311, mAb 317 also showed cross reactivity to most nanoparticles, and surprisingly bound NP6 despite the large difference in sequence compared to its canonical epitope. The largest difference in binding across the panel of nanoparticles was produced by minor repeat binding mAb L9. As expected, L9 bound best to NP3 and NP4, which contain minor repeat epitopes instead of the CS-flap (EC_{50} $1.06x10^{-2}$ and $1.88x10^{-2}$ ug/ml, respectively). While also containing a minor repeat sequence, NP5 bound L9 with an over 10-fold increase in EC_{50} (0.27 ug/ml), showing that the specific conformation and orientation at which the minor repeat epitope is presented substantially impacts L9 binding. The weak binding of L9 to both NP1 and NP2 (1.17 and 1.09 ug/ml respectively) further shows its specificity to minor repeat epitopes. Lastly, junctional epitope binding mAb CIS43 showed little binding to WT-αTSR even at the highest concentration used (EC_{50} 18.4 ug/ml). Surprisingly, CIS43 bound to all other nanoparticles with EC_{50} in the range of $1.06\text{-}6.13x10^{-2}$ ug/ml, showing only mild preference for junctional epitope containing NP6 and NP7 (EC_{50} $1.06x10^{-2}$ and $1.25x10^{-2}$ ug/ml, respectively).

4.2.5 Immunogenicity of αTSR-based nanoparticles

The immunogenicity of NP1-7 adjuvanted with AS01B in C57Bl/6 mice (n=5) was assessed following a prime-boost-boost immunization with two weeks between each 15ug dose. An empty nanoparticle which does not have any conjugated domain on its surface was included as a negative control, as well as nanoparticle expressing wild-type



	Naïve	RTS,S	Empty-NP	NP1	NP2	NP3	NP4	NP5	NP6	NP7	αTSR-WT
EC_{50}	54.8	15600	64.8	25000	8100	19000	3800	4550	9100	4900	1300
R^2	0.8495	0.9992	0.9365	0.9978	0.9975	0.998	0.998	0.9988	0.9984	0.999	0.9935

EC_{50} dilution: 0 – 1E4 – 2.5E4

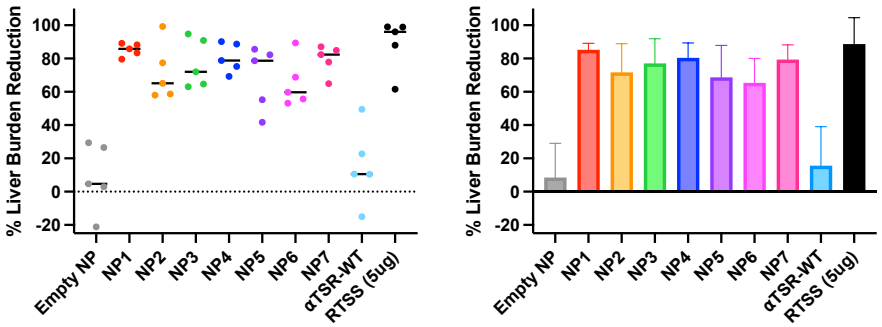
Figure 4.7. Immunogenicity of NP1-7 adjuvanted with AS01B in C57Bl/6 mice. Mice (n=5) were immunized three times, three weeks apart, with 15ug NP1-7, empty NP control, NP displaying wild-type αTSR, with a positive control of RTS,S/AS01E (5ug). Terminal bleeds were collected three weeks after the final boost immunization and immunogenicity assessed against rsCSP by ELISA using pooled sera. EC_{50} values (50% neutralizing titer) obtained by non-linear regression with a four-parameter logistic curve. EC_{50} dilutions are color coded from high titer (red) to low titer (green).

αTSR (NP-WT). As a positive control, another group of mice (n=5) was immunized with 5ug RTS,S adjuvanted with AS01E following the same immunization schedule. Immunogenicity was assessed by ELISA using pooled sera against rsCSP, a recombinant CSP construct containing 19 NANP repeats **(Figure 4.7)**.

Pooled sera both naïve mice and mice immunized with empty NP control showed minimal binding to rsCSP at the highest dilution used, while RTS,S produced strong binding with an EC_{50} dilution of 1:15600. Sera from mice immunized with nanoparticles displaying wild-type αTSR produced a 10-fold lower EC_{50} titer of 1:1300. Containing four tetrapeptide repeats, NP1 and NP3 produced higher EC_{50} titres than RTS,S (1:25,000 and 1:19,000, respectively). Sera from mice immunized with NP2 and NP6 both produced an EC_{50} titre ~2-fold lower than that of RTS,S (1:8,100 and 1:9,100 respectively), and lastly NP4, NP5, and NP7 all produced EC_{50} titres ~3-4-fold lower than RTS,S, ranging from 1:4900 to 1:3800.

4.2.6 Hybrid-domain αTSR-based immunogens provide protection in mice

To determine whether antibodies elicited by immunization with NP1-7 provide protection, the parasite liver burden of mice (n=5) was assessed 42 hours after transgenic *B. berghei* -PfCSP sporozoite challenge. Results are shown as percent liver burden reduction compared to naïve control mice, and the statistical significance of liver burden reduction was determined by Mann-Whitney two-tailed test against the naïve group. Mice immunized with RTS,S/AS01 (5ug) showed 88.7% decrease in liver burden (P=0.0079), while the negative control empty NP and NP-WT immunized mice showed a non-significant liver burden reduction of 8.5% (P=0.5476) and 15.7% (P=0.0952), respectively. All hybrid-domain immunogens provided significant protection in the range of 65-85% (P=0.0079), with the highest protection from NP1 (85.3%) and lowest from NP6 (65.4%).



	Empty NP	NP1	NP2	NP3	NP4	NP5	NP6	NP7	αTSR-WT	RTS,S
% Reduction	8.5	85.3	71.7	77.1	80.4	68.7	65.4	79.4	15.7	88.7
P value	0.5476	0.0079	0.0079	0.0079	0.0079	0.0079	0.0079	0.0079	0.0952	0.0079
Summary	ns	**	**	**	**	**	**	**	ns	**

0%
50%
100%

Figure 4.8. NP1-7 provide protection in C57Bl/6 mouse sporozoite challenge. Mice (n=5) were challenged with transgenic *P. berghei* parasites expressing PfCSP three weeks after the final boost immunization. Liver burden was measured after 42 hours and results shown as percent liver burden reduction compared to the geometric mean of the naïve group, color coded from highest (red) to lowest (green). Statistical significance was assessed using the Mann-Whitney two-tailed test. P values reported together with P value summary: ns= not significant, *=P<0.05, **=P<0.001.

4.3 Discussion and future work

The increase of antibody titres generated by restricting repeat antigen conformation within loops in proteins(9) builds upon previous observations that repeat epitopes have preferred secondary structural motifs(27), and that increased antibody titers can be induced by reducing CSP epitope flexibility in loops within proteins(33). We show that when the CS-flap of αTSR is replaced with protective CSP B-cell epitopes, mAbs canonically targeting these epitopes retain binding. However, the differential binding to these epitopes by these mAbs confirms that their epitope selectivity is both sequence and conformation based. Compared to mAb 311, 317, and CIS43 that show cross-reactivity to multiple immunogens in our panel, L9 is sensitive to small changes in the positioning of the minor repeat sequence. Therefore, optimization of the position of the epitopes inserted into the CS-flap could further improve immunogenicity. Previous designs in which CSP epitopes are restricted within loops have found that five tetrapeptide inserts produce the highest avidity and protection compared to both shorter and longer loops(33), and future rounds of design could further improve antigenicity as well as immunogenicity by including higher valency repeat epitopes.

Despite differences in antigenicity, all seven tested immunogens provided significant protection from sporozoite challenge from 65.4% for NP6 to 85.3% for NP1 (P=0.0079), comparable to an 88.8% reduction in liver burden from RTS,S (5ug) immunization (P=0.0079), and substantially higher than WT αTSR (P=0.0952). In addition to producing a higher reduction in liver burden assay, all seven immunogens produced EC_{50} titres 3-20-fold higher than WT αTSR. Specifically, NP1 and NP3 produced EC_{50} titers of

1:25,000 and 1:19,000, higher than RTS,S with an EC_{50} titer of 1:15,600. This suggests that the protection by our immunogens is mediated primarily through an antibody response directed at the major repeat, minor repeat, and junctional epitopes of CSP. Therefore, this study provides a proof-of-concept to show that the conjunction between the nanoparticle platform and our immunogen design displays protective epitopes in an immunogenic conformation, which then elicit protective mAbs in mice. Furthermore, the 3-fold lower EC_{50} titres of NP4, NP5, and NP7 compared to RTS,S do not translate to a proportional decrease in protection, as they still provide comparable protection against sporozoite challenge, suggesting they elicit more potent antibodies, or fewer antibodies non-inhibitory antibodies. Future work should therefore assess the epitope specific antibody titres and avidity produced by these immunogens to identify any correlates between epitope specific immunogenicity, antigenicity, and protection, to guide forward the next round of immunogen design. Structural characterization of immunogens by X-ray crystallography could also direct immunogen design by revealing whether the epitopes inserted into the αTSR domain form stable secondary structural elements, such as the common motifs seen in monoclonal antibody binding to CSP epitopes(34,35).

One key objective of this immunogen design was to divert humoral response away from polymorphic epitopes of αTSR. In Chapter 3, our collaborator's work reveals that polymorphisms in the CS-flap and Th2R helix can impact binding of mAbs targeting conserved epitopes. The binding of mAbs 1512 and 369 to modified αTSR immunogens suggests that the conformation of the β-epitope is not altered enough to appreciably alter their binding, while binding of α-epitope targeting mAbs 236 and 1525 is significantly

diminished. However, this may be due to induced fit, we have yet to determine if the antibody response following immunization with αTSR variants successfully mimics their antigenicity profile to elicit a high affinity antibody response to conserved epitopes while decreasing binding to polymorphic epitopes. As discussed in Chapter 3, our complete understanding of the potential for CtCSP-mediated immunity hinges on our understanding of the specific mechanisms of action of anti-CtCSP antibodies which have led to their identification as immune correlates in humans but not in mice. Therefore, sera from immunization of humanized mice could provide insight towards the inhibitory potential of monoclonal antibodies elicited by our αTSR variant immunogens through Fc-mediated effector functions, as well as determining if their immunogenicity in the mouse antibody repertoire successfully translates to the human antibody repertoire.

4.4 Materials and methods

4.4.1 Flow Cytometry

For preliminary flow cytometric analysis of nanoparticle constructs, HEK293F cells were transfected with wild-type αTSR and αTSR1-8 with a C-terminal SARS-CoV-2 spike protein TM-helix for display on cell surface (provided by Nelson Wu, Schief lab) using Lipofectamine (Invitrogen) transfection reagent following manufacturer's protocol. Transfected cells, together with un-transfected control cells, were harvested on day 3 by centrifugation at 2000 rpm and resuspended in PBS + 1% BSA to block on ice for 1 hour. Cells were diluted to $6x10^6$ cells/ml in PBS +1% BSA and 50ul of cells ($3x10^5$ cells) per well were added to Gibco 96-well U-bottom cell culture plate. Primary antibody was added to a final concentration of 10 ug/ml for 1 hour on ice. Cells were pelleted by centrifugation at 2000 rpm for 5 minutes at 4°C, supernatant aspirated, and resuspended in PBS + 0.5% BSA. This process was repeated once more before addition of secondary antibody diluted 1:200 (Goat anti-human IgG AlexaFluor-488 A11013, Invitrogen) for 1 hour on ice. Cells were washed x3 as described above and resuspended in 4% PFA in PBS for 15 mins at room temperature, and washed x2 with PBS to remove excess PFA. The following day, cells were analyzed on a ZE5 cell analyzer (BioRad) with a 488 nm laser, counting 20,000 events per sample. Samples were analyzed in triplicate in a single experiment.

4.4.2 Nanoparticle design (by Nelson Wu, Schief lab)

Nanoparticles expressing αTSR immunogens contain the αTSR domain of PfCSP followed by a linker containing the PADRE T-cell epitope, fused to the N-terminus of

modified lumazine synthase. *A. aeolicus* lumazine synthase (PDB:1hqk) was modified to mutate away an unpaired cysteine at position 37 and a buried glycosylation site at position 102. Four cysteines were introduced to design two extra disulfide bridges. Three mutations were introduced to knock out the active sites of the nanoparticle. And finally, one extra glycosylation site was introduced at position 71 and two glycosylation sites are added to the C-terminus.

4.4.3 **Nanoparticle expression and purification in HEK239F cells**

Nanoparticles displaying αTSR-based immunogens were expressed in HEK293F cells. 1mg DNA and 3mg PEI-MAX were separately diluted in 25ml DMEM and incubated at RTM for 5 minutes before being mixed and allowed to incubate at RTM for 30 mins. DNA-PEI complex mixture was added dropwise to 1L HEK293F cells at a concentration of $1.5x10^6$ cells/ml, and cells. Day 7 supernatant was harvested by centrifugation at 2000 rpm for 20 minutes and filtered through a 0.45 μM PES membrane (Millipore). 5ml GNL-agarose beads were added to the clarified supernatant to stir overnight at 4°C. The following day, beads were collected and washed twice with 50ml PBS and nanoparticles were eluted with 50 ml PBS + 0.5 M α-methyl-D-mannopyranoside. Eluted nanoparticles were dialyzed overnight at 4C in 4 L PBS, and purified by size exclusion chromatography on a HiLoad 16/600 Superose 6 PG column (GE Healthcare). Elution fractions corresponding to correctly assembled nanoparticles were pooled and concentrated to 1 mg/ml. Endotoxin levels were assayed on the Endosafe Nexgen-PTS using Limulus Amebocyte Lysate test cartridges, with endotoxin cutoff set to 50 EU/ml. Endotoxin-free nanoparticles were diluted to 0.5 mg/ml in PBS with 20% sucrose (final concentration of

10% sucrose) and flash-frozen for storage at -80°C. Throughout the purification, relevant fractions were collected and analyzed by SDS-PAGE.

4.4.4 Negative stain electron microscopy (EM) (performed by Theresa Fassel, TSRI)

Carbon-coated copper grids (400 mesh) were glow-discharged and 10 µL of each sample was adsorbed for 2 minutes. Excess sample was wicked away and grids were negatively stained with 2% uranyl formate for 2 minutes. Excess stain was wicked away and the grids were allowed to dry. Samples were analyzed at 120 kV with a ThermoFisher Talos L120C transmission electron microscope and images were acquired with a CETA 16M CMOS camera.

4.4.5 Antigenicity ELISA

To assess nanoparticle antigenicity, Costar 96 well high-binding plates were coated with nanoparticles diluted to 1 ug/ml in PBS at 4C overnight. Plates were washed once with PBST (PBS + 0.005% Tween20) and blocked with 5% milk in PBST for 2 hours at 37°C. Plates were washed once with PBST, and primary antibody dilution in PBST (starting at 10 ug/ml) was added to plates for 1 hour at RTM. Plates were washed x3 with PBST and secondary antibody Goat anti-Human IgG HRP (Fortis Life Sciences A80-104P) diluted 1:20000 in PBST was added for 1 hour at RTM. Plates were washed x3 with PBST and developed using Thermo Scientific™ 1-Step™ Ultra TMB-ELISA Substrate Solution and quenched with 0.2 M sulfuric acid, and absorbances were read at 405 nm using SoftMax Pro 5.4 and a VersaMax microplate reader. Results shown are from 4 ELISA

curves from two separate experiments. Values were normalized against highest absorbance reading for each plate and EC50 values were calculated on Prism using non-linear regression (sigmoidal, 4PL, X is log concentration).

4.4.6 Mouse immunization (performed by Yevel Flores-Garcia, Berenice Salgado-Jimenez, John Hopkins University)

C57Bl/6 mice were immunized intramuscularly x3 at 3-week intervals, then evaluated for parasite liver burden following IV challenge with tg*Pb*-*Pf*CSP. RTS,S/AS01 was administered at 5 μg (2.5 μg AS01) per mouse as the established benchmark and positive control. All αTSR NP were dosed at 15 μg formulated in AS01B, also at 2.5 μg/mouse. AS01B is being used just as a clinically relevant adjuvant, not as a proposed final formulation. Mice were challenged IV with 2000 tg*Pb*-*Pf*CSP 3 weeks after the final boost immunization with RTS,S/AS01 or nanoparticles. Forty-two hours after challenge, mice were injected with 100 μl of D-Luciferin (30 mg/mL), anesthetized with isoflurane and imaged with the IVIS spectrum to measure the bioluminescence expressed by the chimeric parasites. Results were provided as Total Flux (photons/sec) and percent liver burden reduction was calculated as 100*(1-(VALUE/geomeanNaïve)). For pairwise analysis of significance, each mAb was compared to the naïve control by the Mann-Whitney two-tailed test.

4.4.7 Immunogenicity ELISA (performed by Yevel Flores-Garcia, Berenice Salgado-Jimenez, Zavala lab, John Hopkins University)

To assess the immunogenicity of mouse sera, 100 µL of recombinant circumsporozoite protein (rCSP) was plated at a concentration of 50 ng/mL into a 96 well MaxiSorp plate and incubated overnight at room temperature. Plates were washed three times with 1X PBS and blocked in 1X PBS-1% BSA) for 1 hour. After blocking, plates were washed x3 with 1X PBS, followed by a one-hour incubation with 100 µL of serially diluted serum samples, starting at a dilution of 1:100. Plates were then washed twice with 1X PBS-0.5% Tween-20 and three times with 1X PBS. After washing, each well was incubated with 100 µL of peroxidase-labeled goat α-mouse IgG (H+L) at a concentration of 250 ng/mL for 1 hour. This was followed by three washes with 1X PBS-0.5% Tween-20 and three washes with 1X PBS. 100 µL of horseradish peroxidase substrate was added to each well with plates allowed to develop in the dark. The reaction was stopped by adding 50 µL of 1% SDS to each well. Each plate was read in a spectrophotometer at OD 405 nm.

4.5 Acknowledgements

We would like to thank PATH's Malaria Vaccine Initiative for the funding, and in specific Randall McGill for their support and discussion. We could not have done this study without the help of Yevel Flores Garcia and Berenice Salgado-Jimenez under the supervision of Fidel Zavala, and we are grateful for their undertaking this study under the time restraints of this project. We are very grateful to Nelson Wu (Schief lab) for their collaboration, as their previous design and validation of the nanoparticle design greatly expedited this project. We acknowledge the expert assistance of Scott Henderson,

Kimberly Vanderpool, and Theresa Fassel of The Core Microscopy Facility at The Scripps Research Institute.

4.6 Declaration

The modified nanoparticle used as display platform in this study as well as the vector for cell-surface display of αTSR immunogens was designed and validated by Nelson Wu, Schief lab. Mouse immunizations and immunogenicity assessment are a collaboration with Fidel Zavala, John Hopkins University, and were performed by Yevel Flores-Garcia and Berenice Salgado-Jimenez. Theresa Fassel conducted the negative stain EM imaging.

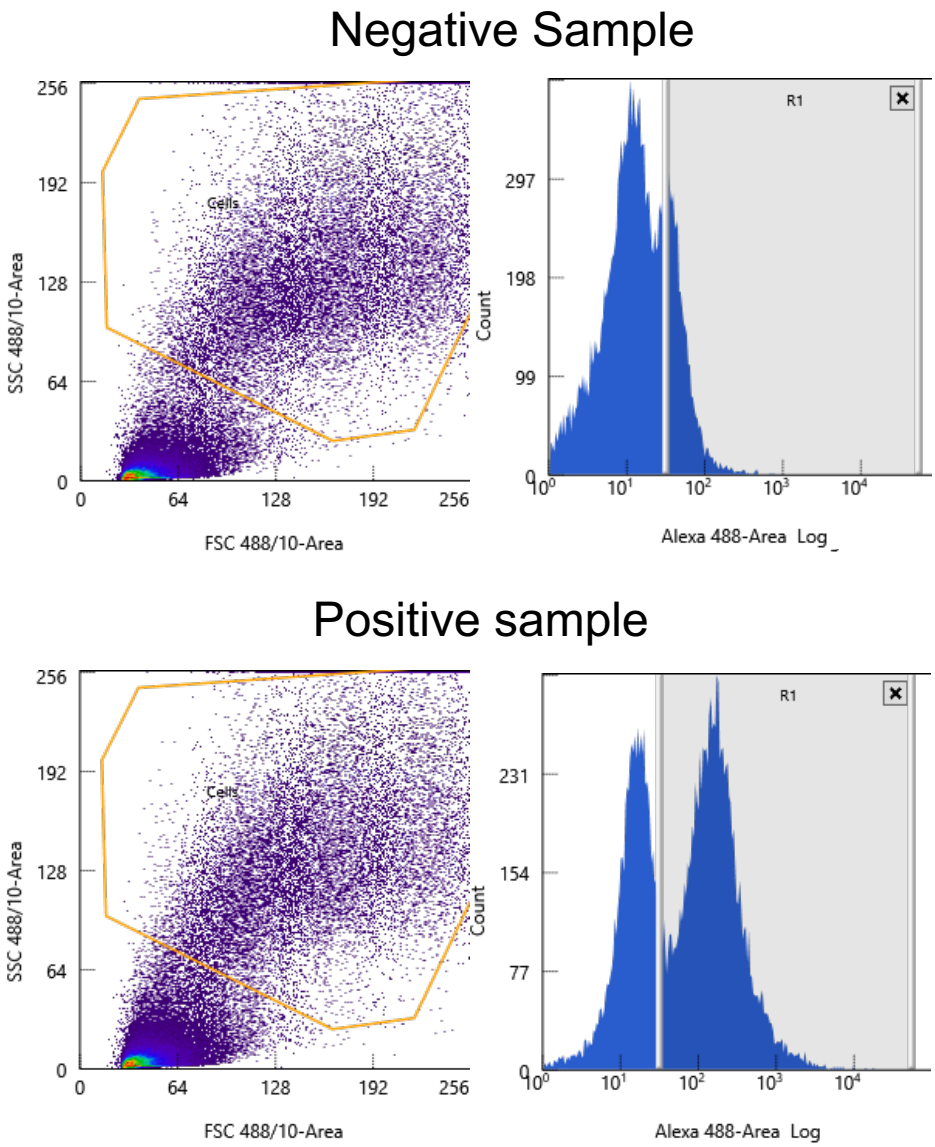
4.7 References

1. Nadeem, A. Y., Shehzad, A., Islam, S. U., Al-Suhaimi, E. A. & Lee, Y. S. Mosquirix^{TM} RTS, S/AS01 Vaccine Development, Immunogenicity, and Efficacy. *Vaccines (Basel)* **10**, 1033–1039 (2022).
2. White, M. T. *et al.* Immunogenicity of the RTS,S/AS01 malaria vaccine and implications for duration of vaccine efficacy: secondary analysis of data from a phase 3 randomised controlled trial. *Lancet Infect Dis* **15**, 1450–1458 (2015).
3. Neafsey, D. E. *et al.* Genetic Diversity and Protective Efficacy of the RTS,S/AS01 Malaria Vaccine. *N Engl J Med* **373**, 2025–2037 (2015).
4. Polhemus, M. E. *et al.* Evaluation of RTS,S/AS02A and RTS,S/AS01B in Adults in a High Malaria Transmission Area. *PLoS One* **4**, e6465 (2009).
5. Bell, G. J. *et al.* Malaria Transmission Intensity Likely Modifies RTS, S/AS01 Efficacy Due to a Rebound Effect in Ghana, Malawi, and Gabon. *J Infect Dis* **226**, 1646–1656 (2022).
6. Wang, L. T. *et al.* A potent anti-malarial human monoclonal antibody targets circumsporozoite protein minor repeats and neutralizes sporozoites in the liver. *Immunity* **53**, 733 (2020).
7. Kisalu, N. K. *et al.* A human monoclonal antibody prevents malaria infection and defines a new site of vulnerability on *Plasmodium falciparum* circumsporozoite protein. *Nat Med* **24**, 408 (2018).
8. Jelínková, L. *et al.* An epitope-based malaria vaccine targeting the junctional region of circumsporozoite protein. *NPJ Vaccines* **6**, (2021).
9. Langowski, M. D. *et al.* Restricted valency (NPNA)n repeats and junctional epitope-based circumsporozoite protein vaccines against *Plasmodium falciparum*. *NPJ Vaccines* **7**, 13 (2022).
10. Atcheson, E., Hill, A. V. S. & Reyes-Sandoval, A. A VLP for validation of the *Plasmodium falciparum* circumsporozoite protein junctional epitope for vaccine development. *npj Vaccines* **6**, 46 (2021).
11. Francica, J. R. *et al.* Design of Alphavirus Virus-Like Particles Presenting Circumsporozoite Junctional Epitopes That Elicit Protection against Malaria. *Vaccines (Basel)* **9**, 287 (2021).
12. Oyen, D. *et al.* Cryo-EM structure of *P. falciparum* circumsporozoite protein with a vaccine-elicited antibody is stabilized by somatically mutated inter-Fab contacts. *Sci Adv* **4**, 8529 (2018).
13. Kucharska, I. *et al.* High-density binding to *Plasmodium falciparum* circumsporozoite protein repeats by inhibitory antibody elicited in mouse with human immunoglobulin repertoire. *PLoS Pathog* **18**, e1010999 (2022).
14. Martin, G. M. *et al.* Affinity-matured homotypic interactions induce spectrum of PfCSP-antibody structures that influence protection from malaria infection. *bioRxiv* 2022.09.20.508747 (2022) doi:10.1101/2022.09.20.508747.
15. Imkeller, K. *et al.* Antihomotypic affinity maturation improves human B cell responses against a repetitive epitope. *Science* **360**, 1358–1362 (2018).
16. Seaton, K. E. *et al.* Subclass and avidity of circumsporozoite protein specific antibodies associate with protection status against malaria infection. *NPJ Vaccines* **6**, 110 (2021).

17. Dobaño, C. *et al.* Concentration and avidity of antibodies to different circumsporozoite epitopes correlate with RTS,S/AS01E malaria vaccine efficacy. *Nat Commun* **10**, 2174 (2019).
18. Regules, J. A. *et al.* Fractional Third and Fourth Dose of RTS,S/AS01 Malaria Candidate Vaccine: A Phase 2a Controlled Human Malaria Parasite Infection and Immunogenicity Study. *J Infect Dis* **214**, 762–771 (2016).
19. Sinigaglia, F. *et al.* A malaria T-cell epitope recognized in association with most mouse and human MHC class II molecules. *Nature* **336**, 778–780 (1988).
20. Chaudhury, S. *et al.* Breadth of humoral immune responses to the C-terminus of the circumsporozoite protein is associated with protective efficacy induced by the RTS,S malaria vaccine. *Vaccine* **39**, 968–975 (2021).
21. Das, J. *et al.* Delayed fractional dosing with RTS,S/AS01 improves humoral immunity to malaria via a balance of polyfunctional NANP6- and Pf16-specific antibodies. *Med* **2**, 1269-1286.e9 (2021).
22. Kurtovic, L. *et al.* Induction and decay of functional complement-fixing antibodies by the RTS,S malaria vaccine in children, and a negative impact of malaria exposure. *BMC Med* **17**, 1–14 (2019).
23. Kurtovic, L. *et al.* Induction and decay of functional complement-fixing antibodies by the RTS,S malaria vaccine in children, and a negative impact of malaria exposure. *BMC Med* **17**, 1–14 (2019).
24. Kurtovic, L. *et al.* Human antibodies activate complement against *Plasmodium falciparum* sporozoites, and are associated with protection against malaria in children. *BMC Med* **16**, 61 (2018).
25. Beutler, N. *et al.* A novel CSP C-terminal epitope targeted by an antibody with protective activity against *Plasmodium falciparum*. *PLoS Pathog* **18**, e1010409 (2022).
26. Wang, L. T. *et al.* Protective effects of combining monoclonal antibodies and vaccines against the *Plasmodium falciparum* circumsporozoite protein. *PLoS Pathog* **17**, e1010133 (2021).
27. Pholcharee, T. *et al.* Structural and biophysical correlation of anti-NANP antibodies with in vivo protection against *P. falciparum*. *Nat Commun* **12**, 1063 (2021).
28. Plassmeyer, M. L. *et al.* Structure of the *Plasmodium falciparum* Circumsporozoite Protein, a Leading Malaria Vaccine Candidate. *J Biol Chem* **284**, 26951–26963 (2009).
29. Langowski, M. D. *et al.* Optimization of a *Plasmodium falciparum* circumsporozoite protein repeat vaccine using the tobacco mosaic virus platform. *Proc Natl Acad Sci U S A* **117**, 3114–3122 (2020).
30. Tan, J. *et al.* A public antibody lineage that potently inhibits malaria infection through dual binding to the circumsporozoite protein. *Nat Med* **24**, 401–407 (2018).
31. Oyen, D. *et al.* Structural basis for antibody recognition of the NANP repeats in *Plasmodium falciparum* circumsporozoite protein. *Proc Natl Acad Sci* **114**, E10438–E10445 (2017).
32. Tan, J. *et al.* Functional human IgA targets a conserved site on malaria sporozoites. *Sci Transl Med* **13**, eabg2344 (2021).

33. Langowski, M. D. *et al.* Optimization of a *Plasmodium falciparum* circumsporozoite protein repeat vaccine using the tobacco mosaic virus platform. *Proc Nat Acad Sci* **117**, 3114–3122 (2020).
34. Martin, G. M. *et al.* Structural basis of epitope selectivity and potent protection from malaria by PfCSP antibody L9. *bioRxiv* (2022) doi:10.1101/2022.10.07.511358.
35. Pholcharee, T. *et al.* Diverse Antibody Responses to Conserved Structural Motifs in *Plasmodium falciparum* Circumsporozoite Protein. *J Mol Biol* **432**, 1048–1063 (2020).

Supplementary figure 4.1 Flow cytometry gating strategy



Supplementary figure 4.1. Flow cytometry gating strategy. Flow cytometry gates selecting for non-debris cells, and a secondary gate selecting for positively stained cells was placed using the negative control non-transfected cells stained with αHA IgG. Plots on left show side scatter vs front scatter, and plots on right show event count vs. log Alexa-488 mean fluorescent intensity.

CHAPTER 5:

Structural Basis for Engagement of the DARC Ectodomain with the Minimal Binding Region of Plasmodium vivax DBP

5.0 Abstract

Plasmodium vivax malaria has long been considered benign compared to the more virulent *P. falciparum*. Yet its broad geographical range and relapse due to dormant liver-stage hypnozoite comprise a large global healthcare burden. The best characterized merozoite invasion ligand of *P. vivax* is the Duffy Binding Protein (PvDBP) binding to erythrocytic receptor Duffy Antigen Receptor for Chemokines (DARC). The minimal binding region PvDBP-RII is a promising vaccine antigen, with vaccination of mice, non-human primates, and humans providing protection from *P. vivax* infection. The X-ray crystal structure of bacterially produced PvDBP-RII in complex with DARC ectodomain peptide reveal how PvDBP-RII binds DARC19-30 and how it dimerizes. The existing structure-guided model for PvDBP binding to DARC fails to provide mechanistic detail for the observed effects of tyrosine sulphation and allele polymorphism in the DARC ectodomain on merozoite invasion of erythrocytes. The X-ray crystal structure of PvDBP-RII expressed from mammalian sources reveals in molecular detail binding of the sulphated Tyrosine 41 in a positively charged binding pocket, and the binding epitope of vaccine-elicited monoclonal antibody DB1. Together with the preliminary characterization of the full-length PvDBP ectodomain, the results herein provide a substantial improvement of our understanding of the DARC-PvDBP-RII interaction to be used to guide future vaccine and immunogen design.

5.1 Introduction

Plasmodium vivax remains a global health burden with over 2.5 billion individuals at risk of infection world-wide (1). Although less virulent than *Plasmodium falciparum*, there have been several recent reports of severe malaria disease resulting from *P. vivax* infection (2,3). Unique to *P. vivax* is the hypnozoite, a dormant liver-stage life form which can cause disease relapse upon reactivation (4,5). While it unclear what causes *P. vivax* hypnozoite re-activation, one study suggests 80% of *Plasmodium vivax* infections are due to relapse (6). Therapeutics capable of killing hypnozoites are incompatible with patients with glucose-6-phosphate dehydrogenase deficiency as they cause fatal haemolytic anaemia. In some areas endemic to *P. vivax*, over 5% of the population may have G6PD deficiency, preventing widespread therapeutic distribution (7). As the *P. vivax* hypnozoite is established following successful liver-stage infection, a blood-stage vaccination is most likely to provide protection from relapse. Similarly, blood-stage vaccination to prevent *P. vivax* merozoite invasion of erythrocytes will decrease clinical symptoms of both primary and relapse infection and reduce parasite burden.

5.1.1 The *Plasmodium vivax* Duffy-binding protein (PvDBP)

The current leading blood-stage malaria vaccine candidate for *P. vivax* malaria is the Duffy binding protein (PvDBP). First discovered as a single gene in *P. vivax* and three genes in *P. knowlesi*, DBP proteins share a common architecture based on seven homologous regions (Region I-VII) **(Figure 5.1A)** and 70% sequence identity in the cysteine-rich Region II (8). The X-ray crystal structure of PvDBP-RII shows an α-helical secondary structure, composed of three subdomains containing intra-subdomain

disulphide bonds **(Figure 5.1B)**, Region II contains the minimal binding region for engagement of PvDBP receptor Duffy-antigen and receptor for chemokines (DARC) on human erythrocytes **(Figure 5.1C)**. The crystal structure of the orthologous PkDBPα-RII shows a sulphate ion bound in pocket of positively-charged residues (9). However, the importance or relevance of this sulphate-binding pocket has not been demonstrated. A single amino-acid mutation of the homologous Region VI of the *P. yoleii* invasion ligand PyEBL affects both the intracellular localization and the erythrocyte-type preference of the parasite (10). It is highly likely that other regions of PvDBP cause *P. vivax* host-pathogen interactions and may contribute to the complete DARC-PvDBP interaction.

5.1.2 Duffy-antigen receptor for chemokines (DARC)

DARC is a homodimeric membrane protein with a seven transmembrane pass G-protein coupled receptor architecture and a short 60-amino acid extracellular domain (11) **(Figure 5.2A)**. A single polymorphism in position 42 of the DARC ectodomain separates the codominant FY*A (G42) and FY*B (D42) alleles, the latter of which renders erythrocytes more susceptible to PvDBP-RII binding and *P. vivax* merozoite invasion (12,13). One polymorphism in the promoter region of the FY*B allele produces the FY*B^{ES} (erythrocyte silent) phenotype in which expression of DARC on the surface of erythrocytes is abrogated. Duffy negative individuals homozygous for the FY*B^{ES} allele, known as duffy-negative individuals, have long been known to be refractory to P. vivax infection (14). An additional binding determinant has been identified with observation that binding of recombinant PvDBP-RII to recombinant DARC is impacted affected by

mutation of DARC Tyr30 and Tyr41 to Phe, both targets of tyrosine sulphation (15) **(Figure 5.2A).**

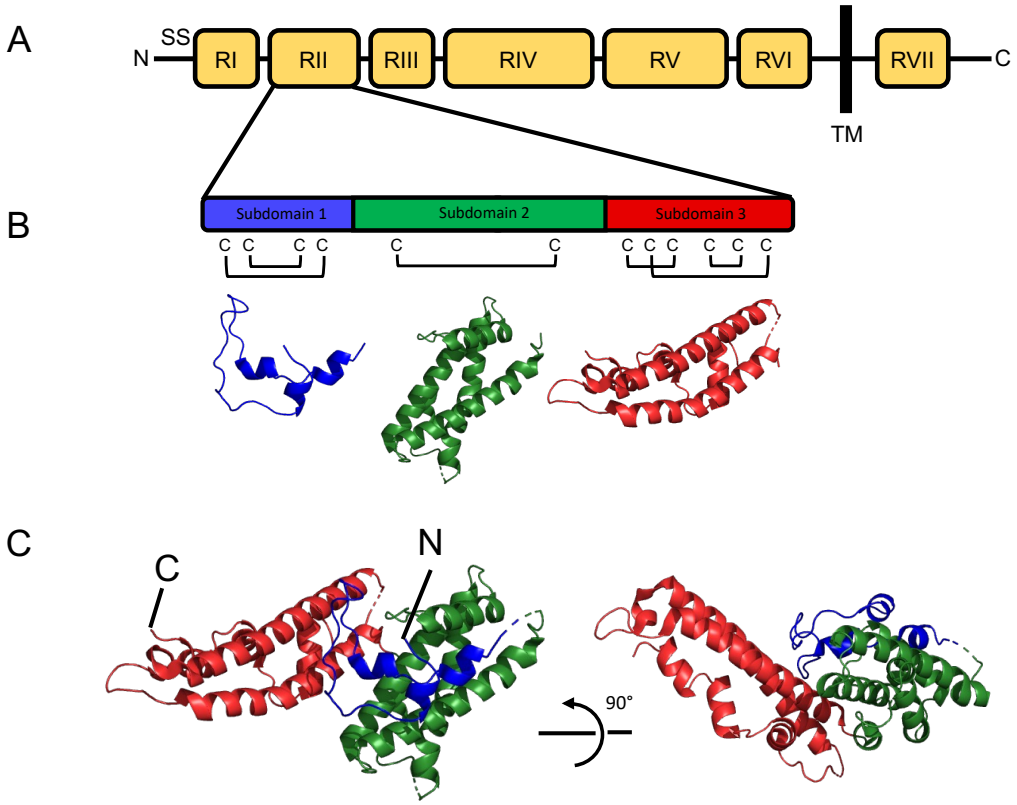


Figure 5.1. PvDBP domain architecture and PvDBP-RII X-ray crystal structure. (A) Schematic of PvDBP domain organization as suggested by alignment with PkDBP and PfDBL protein structure (Adams et al. 1992). The N-terminal signal sequence is followed by RI-RVII correspond the region 1-6, followed by a transmembrane region, and the C-terminal region 7. (B) Schematic of the cysteine-rich RII domain of PvDBP showing subdomains and disulphide bong arrangement. Subdomain 1 in blue, subdomain 2 in green, and subdomain 3 in red. (C) The entire PvDBP-RII domain is shown from two different angles. DBP: 4NUV.

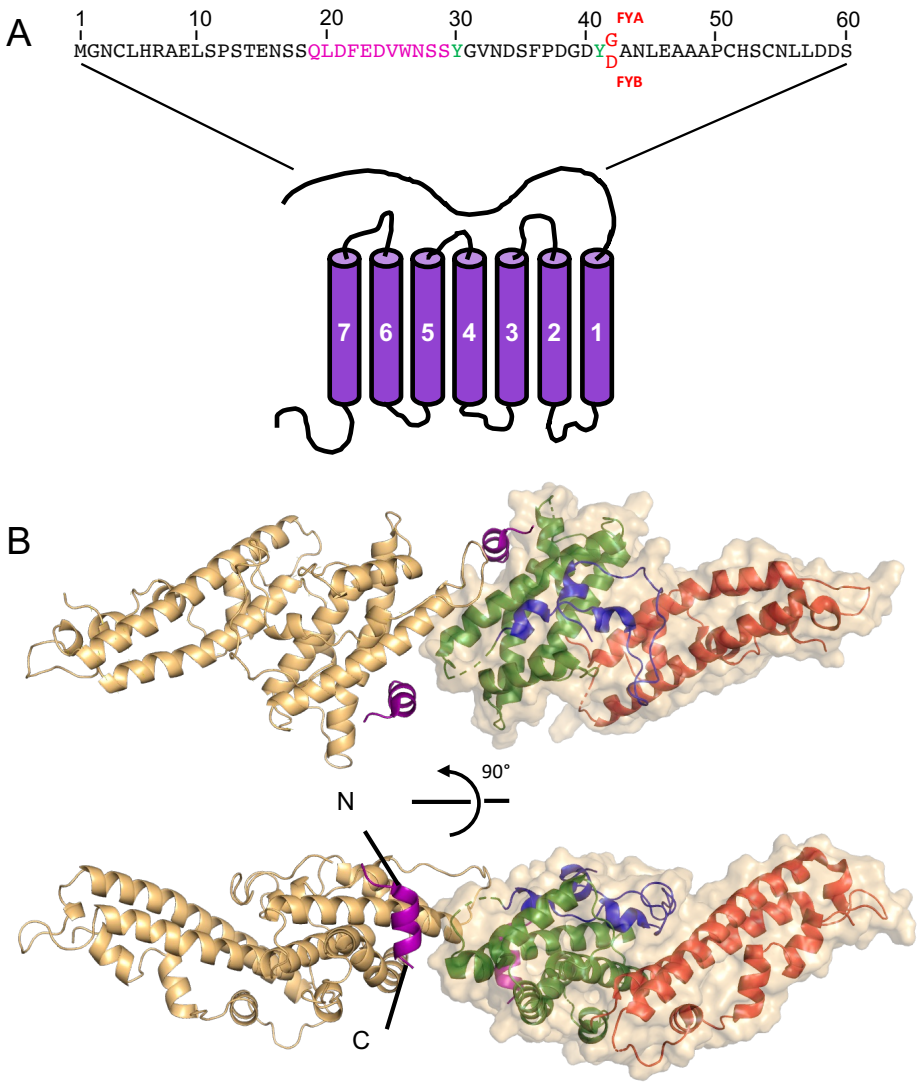


Figure 5.2. Structural basis for engagement of PvDBP-RII with DARC and monoclonal antibodies. (A) Schematic of DARC structure, a seven-pass transmembrane protein with G-protein coupled receptor architecture and an N-terminal 60 amino acid extracellular domain. Residues corresponding to the bound peptide in the DARC-PvDBP-RII complex structure are in pink, sulphated tyrosine Y30 and Y41 residues are in green, and FY*A/FY*B polymorphic residue G42/D42 in red. (B) Crystal structure of PvDBP-RII in complex with DARC ectodomain peptide residues 19-30 (purple ribbon cartoon). One PvDBP-RII monomer is shown in light yellow, whereas the other monomer is colored by subdomain (subdomain 1 in blue, subdomain 2 in green, subdomain 3 in red) with transparent yellow surface. PDB: 4NUV.

5.1.3 PvDBP-RII binds the DARC extracellular domain

Currently, only the minimal interaction between DARC and PvDBP-RII has been described in structural studies. NMR studies using the DARC ectodomain and PvDBP-RII purified from bacterial sources identified DARC14-43 to be the minimal binding residues(16). Bacterial expression systems are not capable of tyrosine sulphation, and therefore the DARC ectodomain peptide used is not sulphated. X-ray crystal structures of DARC ectodomain in complex with PvDBP-RII only shows binding of DARC19-30 to PvDBP-RII subdomain 2 in an α-helical conformation (16) **(Figure 5.2B).** Using two X-ray crystal structures of PvDBP-RII dimer in complex with one (heterodimer) or two (heterotetramer) DARC ectodomain bound, a stepwise binding mechanism was suggested in which DARC binding facilitated PvDBP-RII dimerization (16). This mechanism is supported by small-angle X-ray scattering measurements of PvDBP-RII and DARC ectodomain peptide purified from bacterial cultures, showing that PvDBP-RII dimerizes at high concentrations in the presence of DARC ectodomain peptide. However, it is not supported by *in vivo* evidence. Whether stepwise binding or concerted dimerization upon DARC binding occurs, no currently proposed mechanism accounts for the effects of allelic polymorphisms and tyrosine sulphation on DARC binding to PvDBP-RII.

5.1.4 PvDBP-RII as a promising vaccine candidate

Immunization of mice (17), rabbits (18), non-human primates (19), and humans (20,21) produce antibody responses able to disrupt the DARC-PvDBP-RII interaction. Much like natural *P. vivax* infection in humans, multiple exposures are required to produce a robust

immune response. Multiple exposures or immunizations are also necessary to produce a strain-transcending immune response to overcome the effects of high sequence polymorphism across *P. vivax* isolates. Two immuno-focusing strategies, removal of polymorphic epitopes and glycan masking, have been successfully used to direct antibody response to PvDBP-RII vaccination away from polymorphic epitopes (22–25). To best implement these in a second-generation PvDBP-RII vaccine, characterization of individual epitopes and the monoclonal antibodies which target them are required. Structural characterization of monoclonal antibodies targeting PvDBP-RII has demonstrated binding of multiple antibodies from both mouse immunization and human vaccination to subdomain 3 (26,27). Although binding away from the known DARC-PvDBP-RII interface, monoclonal antibodies binding to subdomain 3 can sterically inhibit PvDBP-RII binding to DARC to prevent merozoite invasion of erythrocytes (26). In contrast, most human monoclonals isolated from natural infection bind subdomain 2 and inhibit dimerization through direct competition for DARC binding (28) **(Figure 5.3).** This may simply be due to the small number of mAbs characterized to bind PvDBP-RII, and more structural characterization of monoclonal antibody binding to PvDBP-RII is required to determine any differences in epitope preference in antibody responses from vaccination and natural infection.

Herein I will describe the expression and purification of PvDBP-RII and full length PvDBP ectodomain from mammalian cell culture supernatant as tools to investigate the aforementioned interactions, and the crystallization of the triple complex of PvDBP-RII with DARC ectodomain and antigen-binding fragment of highly inhibitory antibody DB1

isolated from human vaccination. In this crystal structure, PvDBP-RII binding to DARC ectodomain clearly illustrates binding of Tyr41 in the proposed sulphated tyrosine binding pocket, providing a clear explanation enhanced binding with sulphation of Tyr41, and additional molecular basis for increased susceptibility of FY*B erythrocytes for invasion by *P. vivax* merozoites.

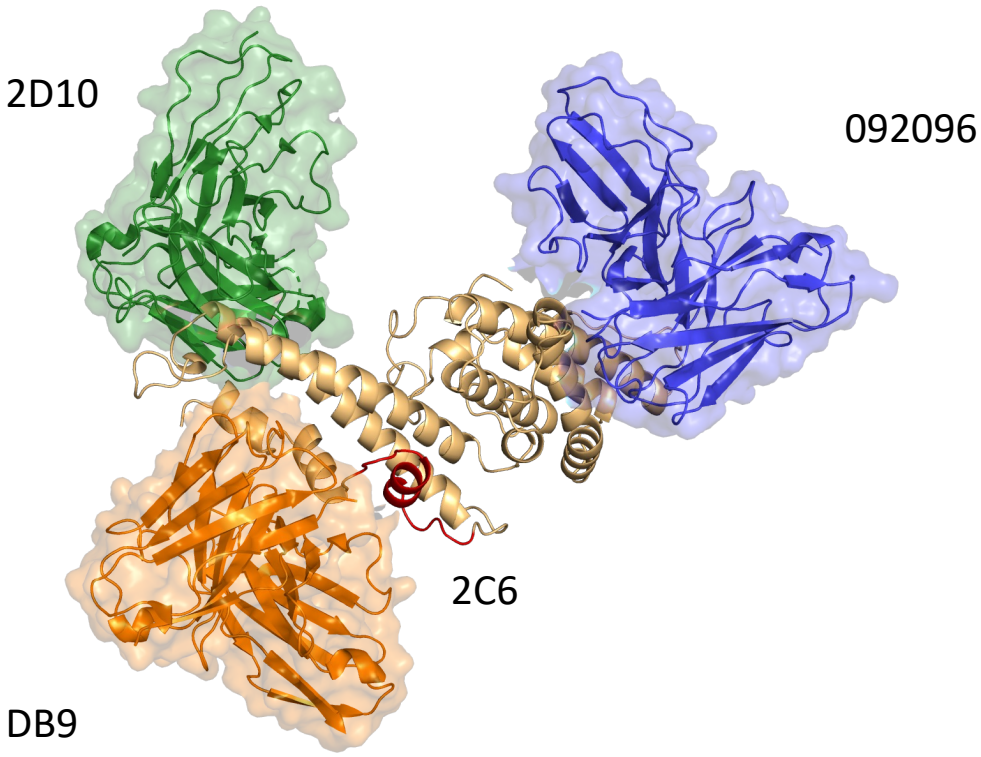


Figure 5.3. Binding epitopes of monoclonal antibodies on PvDBP-RII. The surface of PvDBP-RII is shown in light orange, with the epitope of murine mAb 2C6 in red. The binding epitopes of mAb 092096 (blue), 2D10 (green) and DB9 (orange) are shown by alignment of their respective X-ray crystal structures, showing the variable region of each mAb.

5.2 Results

5.2.1 Purification of PvDBP-RII from *Escheria coli* inclusion bodies

Previous structural characterizations of PvDBP-RII were conducted with protein obtained from refolding of bacterial inclusion bodies (26). The vast majority of attempts to purify PvDBP-RII following the previously used protocol did not produce any monomeric protein, and the protein aggregated during or prior to the final size-exclusion purification step. **Figure 5.4** shows a unique preparation which produced correctly folded monomeric PvDBP-RII. Assessing the purity of PvDBP-RII by SDS-PAGE, the NiNTA elution fraction contains a distinct band at ~35-40 kDa, corresponding to the expected molecular weight of PvDBP-RII (39kDa) **(Figure 5.4A)**. Purification of this fraction by size exclusion chromatography produces a single symmetrical peak at elution volume 18-20ml on a Superdex200 10/300 column **(Figure 5.4B)**. A clear band can be seen with little contaminants on an SDS-PAGE gel of the corresponding elution fractions **(Figure 5.4C)**. Next, circular dichroism measurements of the protein sample were obtained to confirm the folding state of the purified protein. CD spectra taken between 190-260 nm shows the characteristic peaks at 208 nm and 222 nm typical of an α-helical protein **(Figure 5.D)**. Nevertheless, the purified protein aggregated after a single freeze-thaw cycle. The extremely time consuming and rarely successful process of refolding PvDBP-RII from inclusion bodies is undesirable due to its lack of reproducibility. In attempts to improve this protocol, several changes were attempted, including solubilizing bacterial cell pellets directly into guanidine hydrochloride, on-column refolding, purification of solubilized PvDBP-RII by NiNTA chromatography prior to refolding, solubilizing inclusion bodies in urea, refolding in presence of glycerol

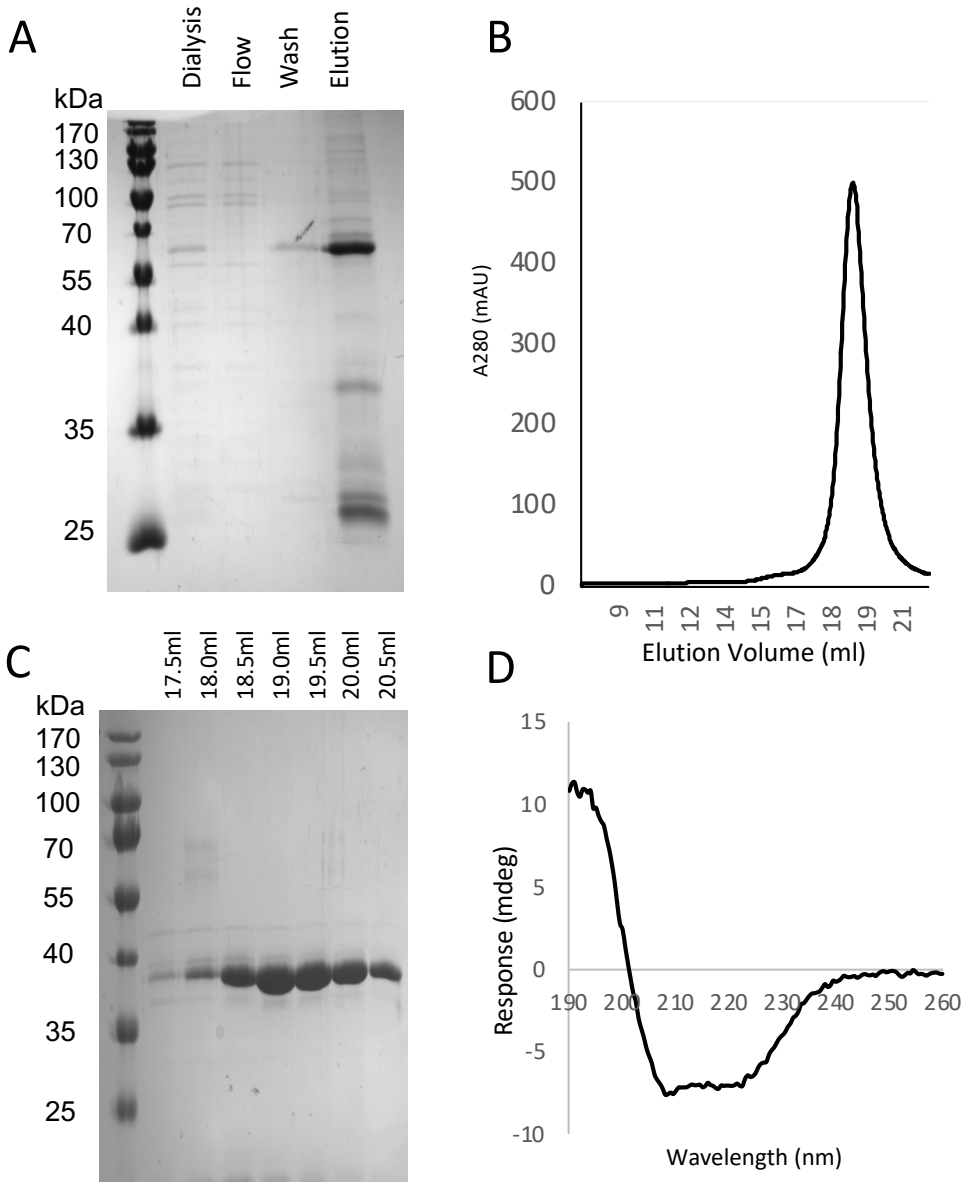


Figure 5.4. Purification of PvDBP-RII after refolding of *E. coli* inclusion bodies. (A) NiNTA affinity chromatography purification steps visualized by SDS-PAGE, with band corresponding to PvDBP-RII (35-40 kDa) seen in the elution fraction. (B) Size exclusion chromatography trace of PvDBP-RII on an Superdex200 10/300 GL column, with peak at elution volume of 19 ml corresponding to monomeric PvDBP-RII. (C) Size exclusion chromatography elution fractions visualized by SDS-PAGE showing a band at the expected molecular weight for PvDBP-RII. (D) CD spectrum of PvDBPRII at 0.1 mg/ml. Peaks at 208 nm and 222 nm typical of an α-helical structure.

and/or TritonX-100 and β-cyclodextrin, altering ionic strength of refolding buffer, and a range of dialysis volumes and flash-dilution methods. None of the attempts to improve the refolding protocol produced any correctly folded protein. Instead, expression of PvDBP-RII and various other PvDBP domain constructs were tested for soluble expression in HEK293 mammalian cells.

5.2.2 Construct design for expression of PvDBP in mammalian cells

Alongside expression trials of PvDBP-RII for soluble expression in mammalian cells, a panel of larger PvDBP constructs was designed to investigate the broader PvDBP-DARC interaction. Structure prediction server RaptorX assigns Region VI as 5-helical bundle due to its homology to PfEBA-175 Region VI (29), a further two-helical bundle at RI, Region III-V as disordered, and region VII as a TM α-helix **(Figure 5.5A)**. Following this domain assignment and using multiple boundaries for RII from previous publications (16,22,27), a panel of expression constructs of varying lengths were subcloned into pHLSec vector for mammalian expression **(Figure 5.5B)**. The largest construct in the panel contains the entire PvDBP ectodomain (RI-RVI), while the smallest constructs in the panel are of PvDBP-RII by itself. All other constructs include RII as it is the minimal binding region of PvDBP-RII. Due to its proximity to RII and predicted secondary structure, RI was included in three constructs of RI-RII fusion. Although RVI is also predicted to have secondary structure, it is separated from RII by the large region of predicted disorder in RIII-RV. Large regions of disorder are susceptible to degradation and may cause aggregation when over-expressed in non-native expression systems, and so four constructs were designed in which RIII-RV were truncated.

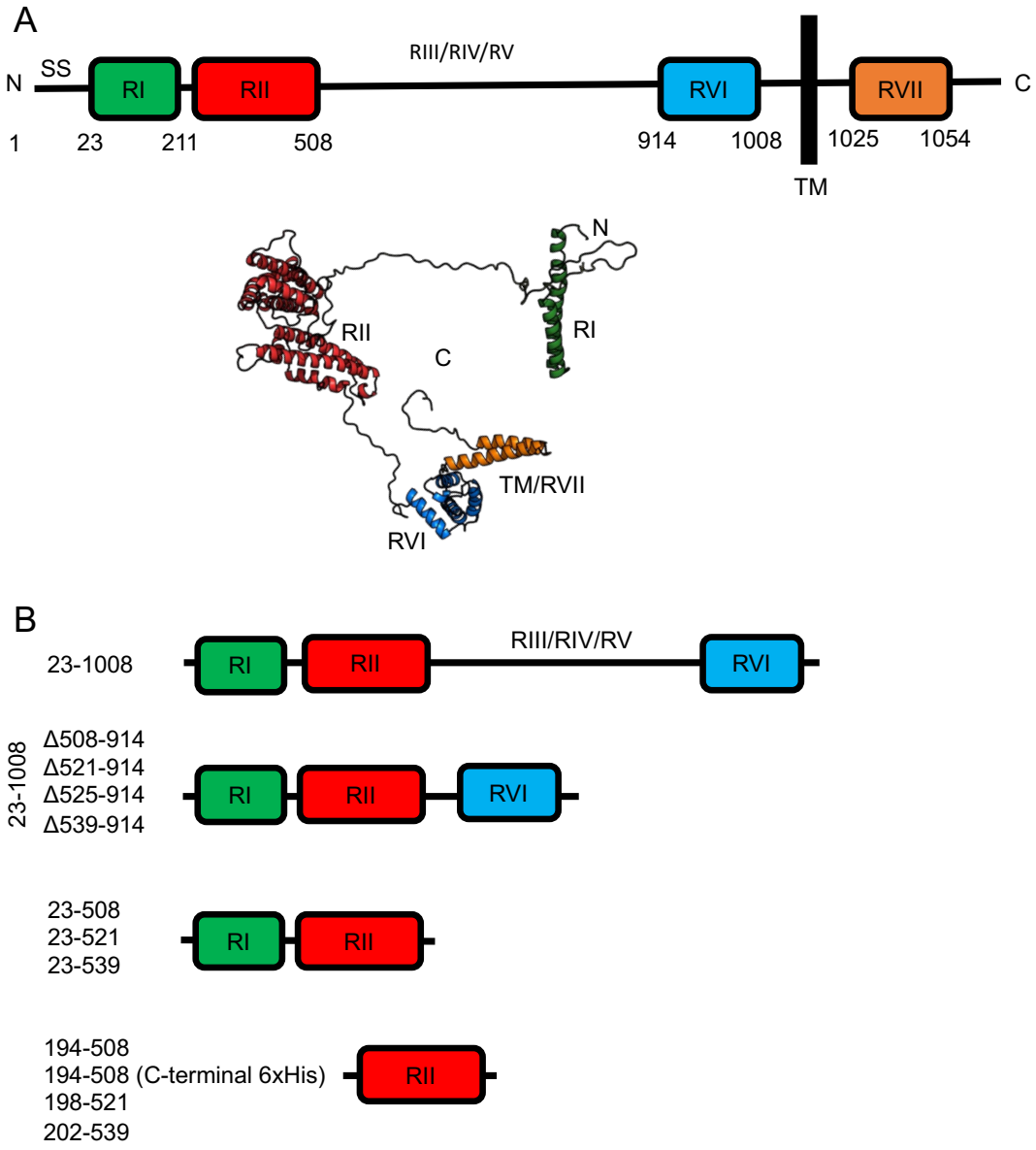


Figure 5.5. Expression Construct Design for PvDBP Expression In Mammalian Cell Culture. (A) Schematic representation of domain boundaries produced by structural prediction with RaptorX, with cartoon representation of the predicted structure. (B) Schematic representation and domain boundaries for the panel of constructs designed for expression in mammalian cells. RI in green, RII in red, RVI in blue, and RVII in orange. Number following Δ are truncated.

Small-scale expression from culture supernatant was then visualized by SDS-PAGE of NiNTA elution fractions **(Figure 5.6A)**. For both Region II 194-508 constructs, a weak band can be seen at ~40 kDa, corresponding to the expected molecular weight of PvDBP-RII. Similarly, very faint expression can be seen for all PvDBP ectodomain constructs with truncation of RIII-RV (ΔRIII-RV). Although it was initially thought that the large regions of disorder will prevent successful expression of the full-length PvDBP ectodomain, a clear band is seen corresponding to a protein of around 170 kDa, much higher than expected for the PvDBP ectodomain (110 kDa). To determine whether this increase in molecular weight may be due to glycosylation, all constructs which showed preliminary expression were deglycosylated overnight. As can be seen from the SDS-PAGE gel, all PNGase F-treated samples show a shift in migration on SDS-PAGE **(Figure 5.6B)**. This decrease in molecular weight does not lower the apparent molecular weight of PvDBP full-length ectodomain to the expected 110 kDa. The PvDBP ectodomain contains large sections of polar and negatively charged residues, which can affect the ability of the peptide to be coated with SDS, altering the charge density of the protein thereby increasing its apparent molecular weight by SDS-PAGE. Nevertheless, PvDBP ectodomain is homogenous and provides new opportunities for the characterisation of the interaction full-length PvDBP with DARC. Additionally, the expression of PvDBP-RII with a C-terminal 6xHis tag in mammalian cells provides an effective solution for X-ray crystallography studies as shown in section **5.2.3**, which require a reproducible and scalable source of recombinant protein.

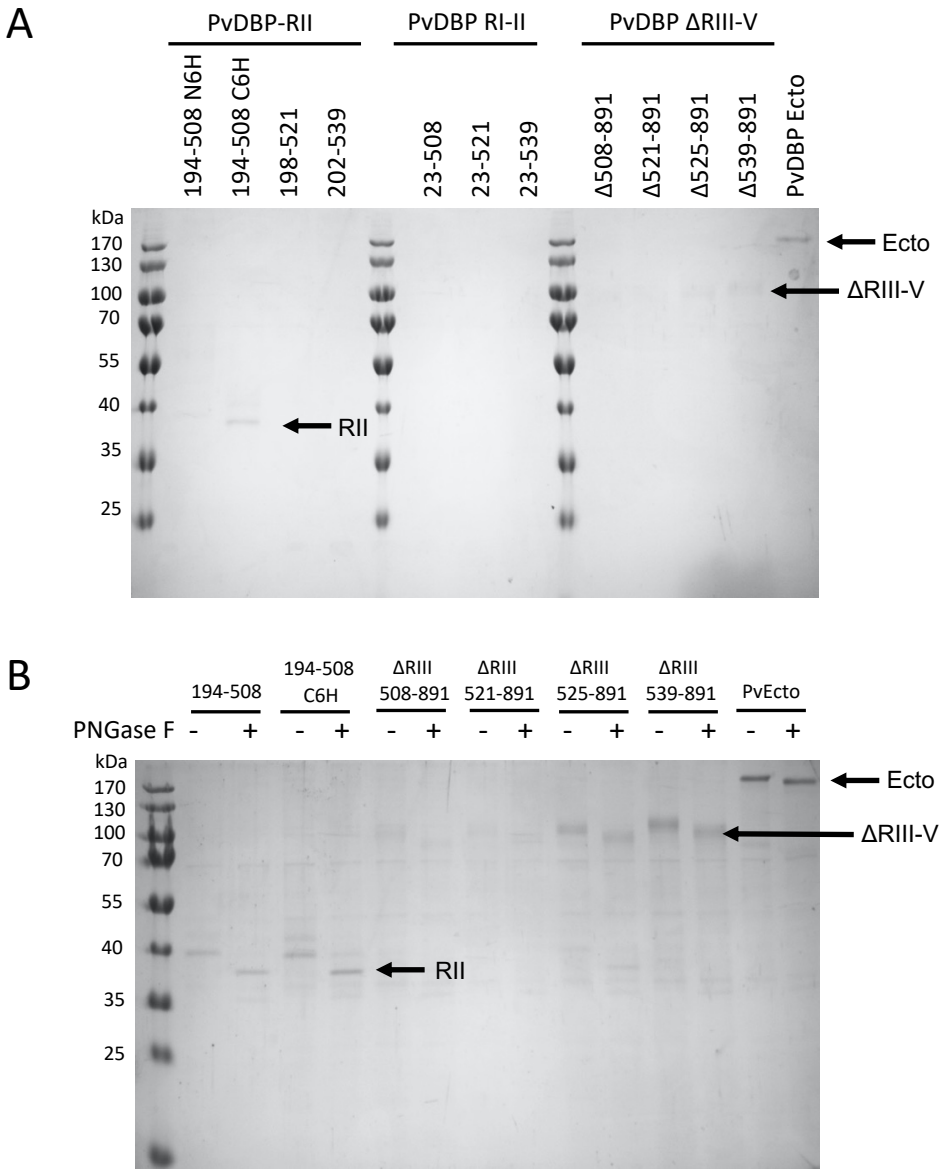


Figure 5.6. Expression trial of PvDBP constructs in HEK293F cells. (A) Reducing SDS-PAGE of NiNTA elution fraction from small-scale mammalian cell expression of PvDBP-based cosntructs, showing weak expression of PvDBP-RII 194-508 C6H (C-terminal 6xHis tag), PvDBP ΔRIII-V , and PvDBP Ecto. (B) Reducing SDS-PAGE of PNGase F treatment of selected elution fractions. Numbers following Δ are truncated. Arrows show relevant bands corresponding to PvDBP-Ecto, PvDBP-ΔRIII-V, and PvDBP-RII.

5.2.3 Purification and crystallization of PvDBP-RII in complex with DARC ectodomain and DB1

Previous X-ray crystal structures contain DARC ectodomain peptide expressed in bacterial sources which are not capable of tyrosine sulphation (16). The peptide used is therefore lacking in sulphation of tyrosine 30 and 41, which increase the affinity of PvDBP-RII binding to DARC and increases merozoite invasion(15). The $DARC_{Ecto}$ construct previously used in our lab contains DARC1-60 with an N-terminal TEV cleavage site and a 6xHis tag for NiNTA affinity purification. Expressed in mammalian Expi293F cells, it has been previously shown in our lab to be sulphated by mass spectrometry. $DARC_{Ecto}$ was purified from mammalian cell culture supernatant by NiNTA affinity chromatography and deglycosylated with PNGase F **(Figure 5.7A)**. The SEC chromatogram of $DARC_{Ecto}$ shows a single peak with a significant shoulder **(Figure 5.7B)**. To elucidate the structural basis for the interaction of PvDBP-RII with the sulphated DARC ectodomain, PvDBP-RII was co-purified with $DARC_{Ecto}$ for crystallization trials, with an additional deglycosylation and TEV protease cleavage step following co-purification. Following multiple attempts, no crystals were produced. We therefore attempted to use Fab from monoclonal antibodies as crystallisation chaperones.

Monoclonal antibody DB1 was isolated by our collaborators following human vaccination with PvDBP-RII(26). Although it is highly inhibitory to merozoite invasion, DB1 does not inhibit the binding of DARC ectodomain peptide on ELISA plate with recombinant PvDBP-RII. For crystallization, DB1 IgG was purified from mammalian cell

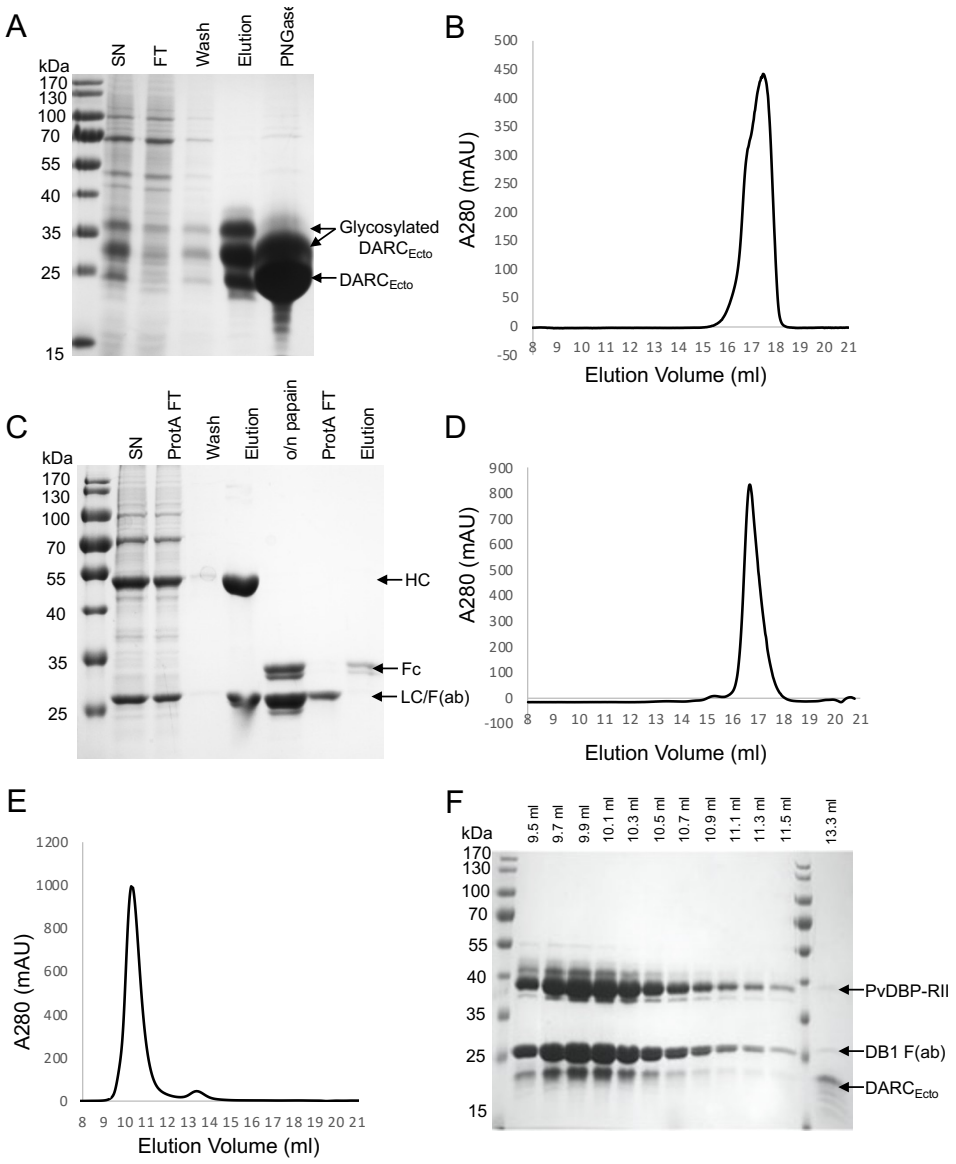


Figure 5.7. Purification of DARC ectodomain, DB1 F(ab), and the PvDBP-RII-DARC-DB1 triple complex. (A) Reducing SDS-PAGE of $DARC_{Ecto}$ NiNTA affinity chromatography. (B) SEC chromatogram of $DARC_{Ecto}$ on an Superdex75 10/300 GL column, showing a monomeric peak with a shoulder. (C) Reducing SDS-PAGE of DB1 IgG protein A affinity chromatography and papain treatment to produce DB1 F(ab). Bands corresponding to F(ab) heavy and light chain are seen at the expected 25 kDa molecular weight in the second protein A flow-through. (D) SEC chromatogram of DB1 F(ab) on a Superdex200 10/30 GL column. (E) SEC chromatogram of PvDBP-RII-DARC-DB1 triple complex on a Superdex200 10/30 GL column, with triple complex peak at elution volume 10-11ml. (F) Reducing SDS-PAGE of size exclusion chromatography elution fractions corresponding to the major triple complex peak. SN=supernatant, FT=flow through, ProtA= protein A, o/n=overnight.

culture supernatant by Protein A affinity chromatography and Fab produced by enzymatic digestion with papain **(Figure 5.7C).** Following removal of Fc fragments with Protein A, the Fab of DB1 can be seen to migrate as a single band by size-exclusion **(Figure 5.7C).** To improve stability of PvDBP-RII in solution during the purification process, the triple complex of PvDBP-RII in complex with DB1 Fab and $DARC_{ecto}$ was co-purified by NiNTA affinity chromatography and further purified by size-exclusion chromatography **(Figure 5.7E)**. Visualization of the elution fractions by SDS-PAGE clearly shows the major peak to contain all three components of the triple complex **(Figure 5.7F)**.

One crystal produced diffraction maxima up to 2.5Å and a full dataset was collected by capturing 0.2° of a full 360° rotation, producing a dataset of 1800 diffractions at Beamline I24 of the Diamond Light Source Synchrotron **(Crystallographic data table 5.1)**. The dataset was processed by autoPROC to a resolution of 2.49Å, suggesting a space group of $P2_12_12_1$. The overall $R_{\underline{pim}}$ value of 0.07 overall and 0.703 for the highest resolution shell are within the generally accepted limits of data quality and would suggest a correct space group assignment. Through molecular replacement with Phaser MR, one copy of PvDBP search model, one copy of Fab variable domain search model, and one copy of Fab constant domain search models were found in the asymmetric unit cell. The molecular replacement solution positions the Fab constant and variable domain models put back together to form a complete Fab molecule, with the variable domain facing the PvDBP search model.

Following refinement of the molecular replacement solution with BUSTER, the electron density difference map (F_o-F_c) was used to build any missing loops in the PvDBP-RII structure and the CDRs of DB1. After several more rounds of building and refinement using Coot and BUSTER, respectively, side chain densities could be easily assigned, and missing electron density was seen in the region previously seen to bind DARC. The DARC ectodomain peptide was manually built into the structure as a polyalanine model, and residues assigned with the known DARC ectodomain sequence and clear missing electron density for the side chains. The refinement factors of R_{work}/R_{free} of 0.198 / 0.225 would suggest the final model is in good agreement with the data.

After building the DARC ectodomain peptide into the electron density map refined with the PvDBP-RII-DB1 complex, we were able to see electron density for the backbone and majority of side chains for DARC19-47. An alignment of PvDBP-RII in the structure with that of the previously published PvDBP-RII-DARC homodimer (PDB:4NUV) produces a root mean square difference (RMSD) of 0.9Å for the two PvDBP-RII molecules **(Figure 5.8A)**. Residues 254-261, previously missing from the heterotetramer and heterotrimer structures, are seen in the structure, and PvDBP-RII purified from mammalian culture has the same fold as that produced from bacterial refolding. The DARC19-30 peptides bound in both structures assume an α-helical conformation, supporting the previously discerned minimal DARC binding region **(Figure 5.8B).** Additionally, clear electron density reveals DARC31-47 binding, with clear side chain detail for sulphation of Tyr41, but not of Tyr30. As well, the polymorphic residue Asp42 corresponding to FY*B allele, can also be seen. Together, this structure provides a

rational for the observed effects of tyrosine sulphation and polymorphisms on merozoite invasion. **(Figure 5.8C).**

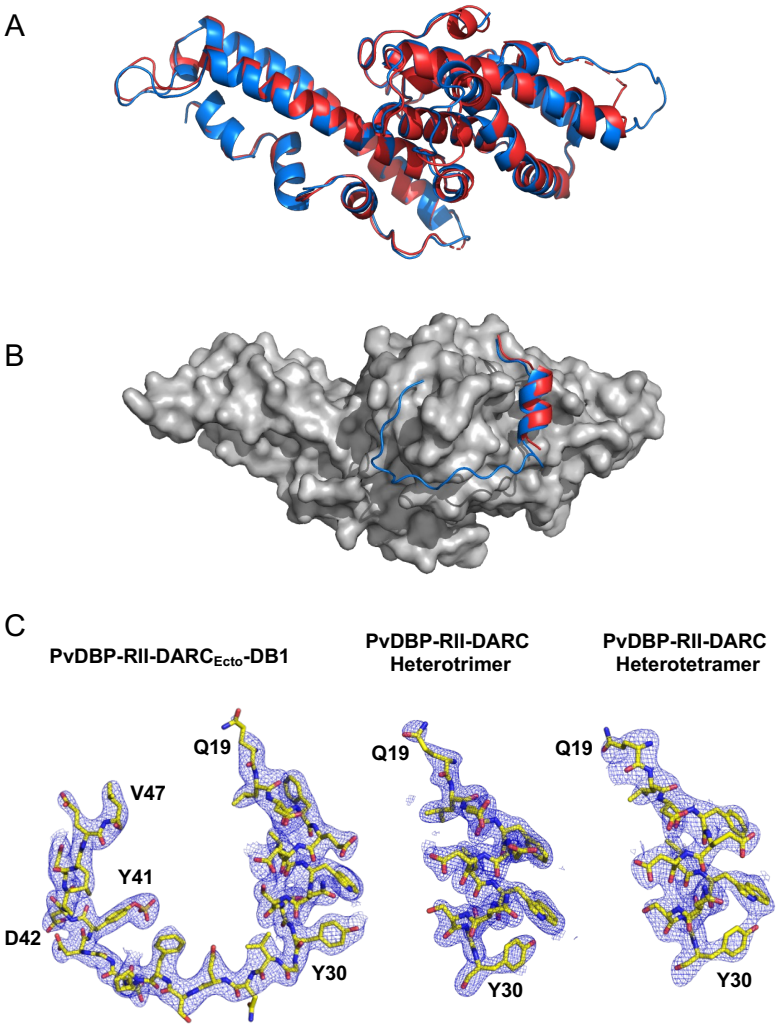


Figure 5.8. Comparison of PvDBP-RII-DARC X-ray crystal structures. (A) Alignment of PvDBP-RII from mammalian cell culture in the triple complex crystal structure (blue) and from bacterial refolding from homotetramer crystal structure (red) (PDB:4NUV). (B) Alignment of DARC ectodomain peptide in triple complex structure (blue) and homotetramer structure (red) (PDB:4NUV). (C) DARC ectodomain peptide in the triple complex structure, PvDBP-RII-DARC heterodimer (PDB:4NUU), and PvDBP-RII-DARC homotetramer (PDB:4NUV) represented as yellow cartoon (up) and sticks (down) colored by element. Electron density maps of peptides are shown in blue mesh and contoured to sigma=1.

5.2.4 DARC binding is mediated by positively charged residues on subdomain 2

The DARC ectodomain binds to PvDBP-RII in a horse-shoe shape, wrapping around a protrusion of Subdomain II formed by the C-terminal portion of the α-helix formed by subdomain 2 residues 341-369 and residues 369-385 that link subdomain 2 and subdomain 3 **(Figure 5.9A)**. Approaching the interface between subdomain II and III, the sulphated Tyr41 can be seen binding in a pocket of basic residues, before the peptide continues to wrap around subdomain II **(Figure 5.9B)**. Beyond shape complementarity, binding of the acidic DARC ectodomain peptide to the highly positively charged PvDBP-RII is largely facilitated by charge interactions. The α-helical DARC19-30 is stabilized in part by a cation-pi interaction of $Trp26^{DARC}$ with $Arg274^{DBP}$ and a salt bridge between $Asp24^{DARC}$ with $Lys367^{DBP}$ **(Figure 5.10A)**. The downstream $Asp34^{DARC}$ forms a salt-bridge with $Lys366^{DBP}$, followed by $Phe36^{DARC}$ hydrophobically stacking perpendicular to $Phe373^{DBP}$, anchoring the peptide in its horse-shoe trajectory towards the sulphate binding pocket **(Figure 5.10A)**.

The site of sulphated tyrosine binding was previously hypothesised due to the binding of a sulphate in a pocket of positively charged residues in the crystal structure of the homologous PkDBPα crystal structure (9). Indeed, the crystal structure of PvDBP in complex with sulphated DARC ectodomain shows sulphated Tyr41 bound in the pocket of positively charged residues **(Figure 5.10C)**. While the sulphate group is stabilized by the formation of a salt bridge with the positively charged side chains of $Lys301^{DBP}$ and $Arg304^{DBP}$, the hydrocarbon chains of $Lys297^{DBP}$ and $Lys378^{DBP}$ stabilize the aromatic

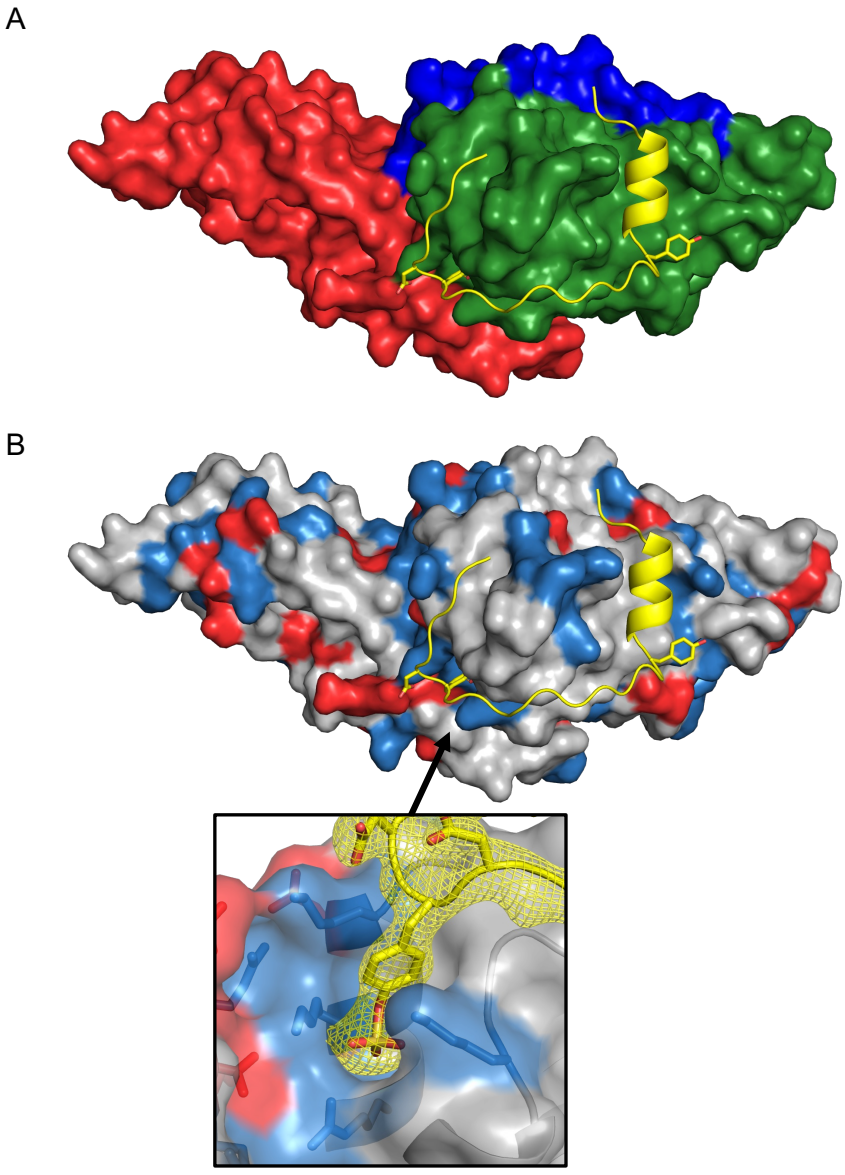


Figure 5.9. DARC ectodomain wraps around a protrusion in PvDBP-RII subdomain 2. PvDBP-RII bound to DARC19-47 shown in yellow cartoon with relevant side-chains in sticks colored by element. (A) PvDBP-RII surface colored by subdomain, with subdomain 1 in blue, subdomain 2 in green, subdomain 3 in red. (B) PvDBP-RII surface colored by charge at pH 7, with positive in blue and negative in red. Detail showing sulphates Tyr41 binding in a pocket of positively charged residues, with electron density as a yellow mesh contoured to sigma=1.

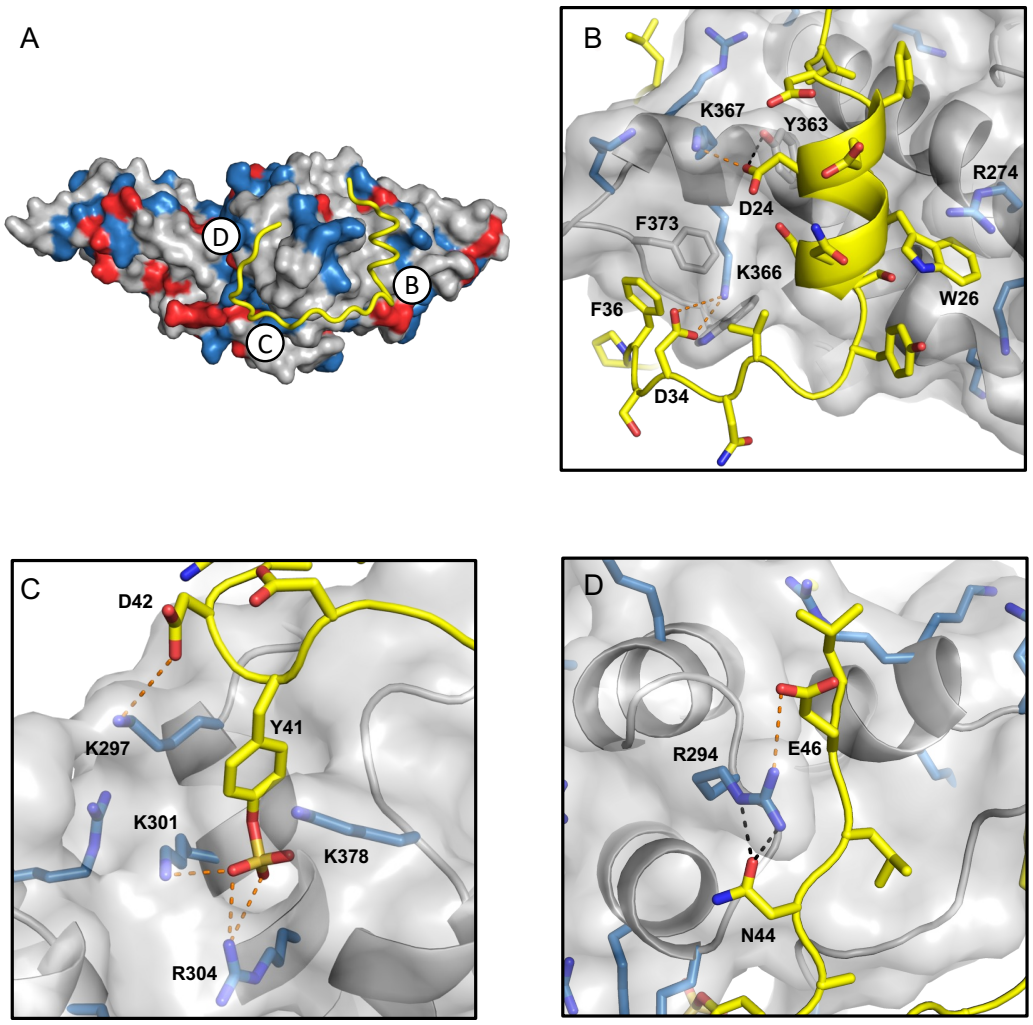


Figure 5.10. DARC ectodomain binds PvDBP-RII through electrostatic interactions. (A) Surface of PvDBP-RII colored by electrostatic charge (neutral=grey, positive=blue, negative=red), and DARC ectodomain shown as yellow tube. Location of details shown in white circles. (B) Binding of the DARC19-30 α-helix is mediated by charge interactions of Asp24 with Lys367, and cation-pi interaction of Trp26 with Arg274. The horse-shoe trajectory of the peptide is stabilized by a salt-bridge between Asp34 and Lys366 and stacking of Phe36 with Phe373. (B) Sulphated Tyr42 binds in a pocket of basic residues, and the FY*B allele Asp42 forms a salt-bridge with the nearby Lys297. (C) The C-terminal region of the visible DARC ectodomain is anchored by Arg294 hydrogen bonding Asn44 and forming a salt-bridge with Glu46. Backbone is shown in grey, cartoon, and select positive residues in sticks colored by element.

Tyr41^{DARC} phenol ring **(Figure 5.10C)**. The proceeding Asp42^{DARC}, corresponding to the FY*B allele, is facing towards Lys297^{DBP}, and the carboxylate oxygen of Asp42^{DARC} is 3.9Å away from the amine group of Lys297^{DBP} side chain, within distance to form a salt bridge. This interaction would not be possible with FyA Gly42^{DARC}, providing a potential molecular basis for the observed susceptibility of FY*B erythrocytes to merozoite invasion by *P. vivax* and increase binding of FyB DARC to PvDBP-RII as compared to FyA (Asp42→Gly)([12]). Upstream of this lysine, Arg294^{DBP} doubly interacts with the Asn44^{DARC} side chain carbonyl and Glu46^{DARC}, stabilizing the last portion of the bound peptide with visible electron density **(Figure 5.10D)**.

5.2.5 Binding epitope of inhibitory monoclonal antibody DB1 to PvDBP-RII

The X-ray crystal structure of PvDBP-RII bound to DARC$_{Ecto}$ also reveals the epitope of inhibitory monoclonal antibody DB1, which can be seen binding to the termini of two Subdomain 2 α-helices and their connecting loops **(Figure 5.11A)**. Facing the DB1 complementarity defining region, PvDBP-RII Asn330-Arg35 interacts in the groove formed by the heavy-chain CDRs and CDRL3, while PvDBP-RII Asn55-Leu270 binds on the other side of CDRH3 in close proximity to CDRL2 **(Figure 5.11B).** This insertion of CDRH3 into the PvDBP-RII structure contributes to shape complementarity and the formation of multiple interaction networks that stabilize DB1 binding. In the first interaction network, CDRL2 Ser56 forms a hydrogen bond with Asn260, the adjacent Phe261 stacks perpendicular to the aromatic light-chain framework residue Tyr49 while its backbone carbonyl forms a hydrogen bond with CDRL2 Gln55 **(Figure 5.11C).** Both

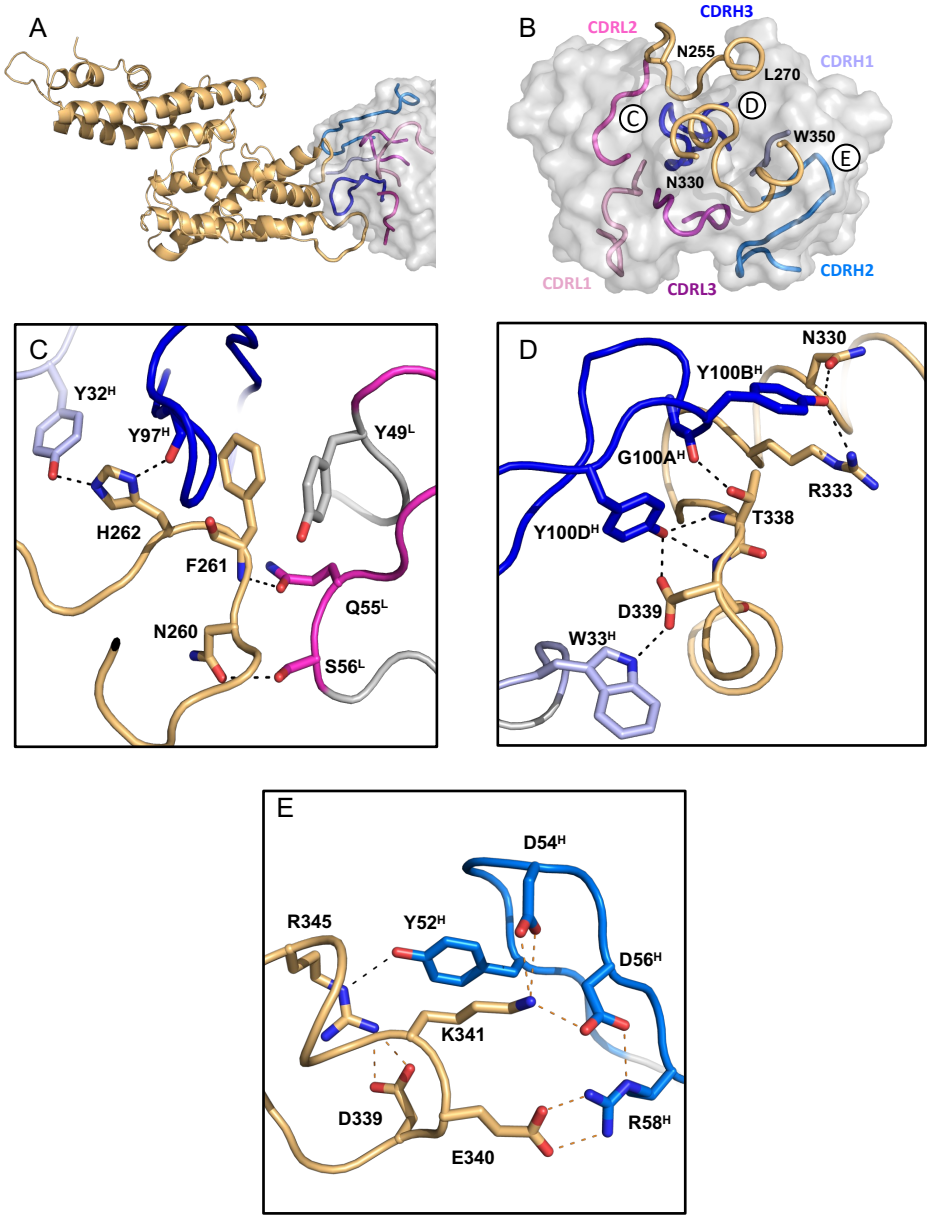


Figure 5.11. Structural basis for DB1 binding to PvDBP-RII. (A) DB1 (grey surface) binds two loops in subdomain 2 of PvDBP-RII (light orange). (B) Birds-eye view of the DB1 CDRs showing the location specific molecular interactions discussed in C, E, and F in white circles. (C) CDRL2, CDRH1, and CDRH3 stabilize the binding of PvDBP-RII 260-262 on one side of CDRH3 (D) while the other side of CDRH3 binds PvDBP-RII 330-339. (F) CDRL2 forms a network of salt-bridges with the polymorphic $_{339}$DEK$_{341}$ motif of PvDBP-RII. CDRH1 in light blue, CDRH2 in marine, CDRH3 in blue, CDRL1 in pink, CDRL2 in magenta, and CDRL3 in purple, framework residues in grey assigned by AbYsis. Backbone shown as cartoon tube and select side-chains shown as sticks colored by atom.

imidazole nitrogens of the proceeding His262 are stabilized through hydrogen bonding interactions with CDRH1 Tyr32 hydroxyl and CDRH3 Tyr97 backbone carbonyl **(Figure 5.11C)**. On the other side of CDRH3, the incoming α-helix is stabilized by CDRH3 Tyr100B forming a hydrogen bond with Asn330 and Arg333 of the following helical turn **(Figure 5.11D)** The nearby backbone carbonyl of CDRH3 Gly100A forms a hydrogen bond with the side-chain hydroxyl of Thr338, further held in position by CDRH3 Tyr100D, poised to interact with the backbone amides of Thr338, Asp339, and the side chain carboxylate of Asp339. Simultaneously interacting with CDRH3 Tyr100D and the indole group of CDRH1 Trp33 **(Figure 5.11D)** Asp339 also forms a salt-bridge with Arg345, positioning the connecting loop to form an extensive network of salt-bridges with CDRH2 **(Figure 5.11E)**. The side-chain of Glu340 faces directly towards the guanidino group of CDRH2 Arg48, which itself interacts with CDRH2 Asp56. Together with CDRH2 Asp54, CDRH2 Asp56 binds the positively charged Lys341 amine **(Figure 5.11E)**.

Owing to the extreme selection pressure on PvDBP and the rapid cycle of *P. vivax* merozoite invasion of reticulocytes, close to 20% of PvDBP-RII residues are polymorphic across isolated strains. Representing the PvDBP-RII surface by sequence entropy amongst a panel of isolates, the DB1 binding site can be clearly seen to overlap with a polymorphic hot spot **(Figure 5.12)**. The elaborate network of salt-bridge interactions formed by DB1 CDRH2 directly engages the polymorphic $_{339}$DEK$_{341}$ motif, providing a structural basis for the previous observation that DB1 fails to provide strain-transcending inhibition of merozoite invasion across a panel of *P. vivax* isolates(26).

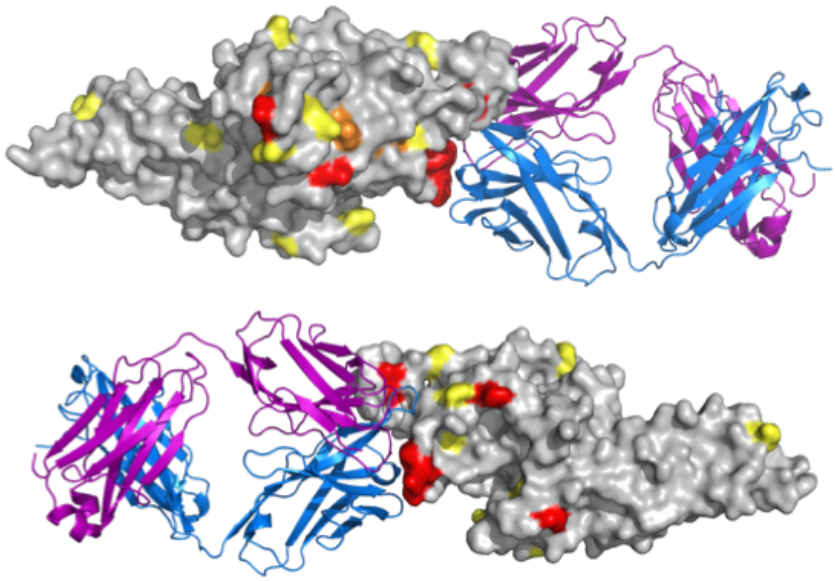


Figure 5.12. DB1 binds a polymorphic hot-spot on PvDBP-RII Subdomain 2. The PvDBP-RII surface is represented by specific residue sequence entropy from a panel of 383 isolates. Sequence entropy of 0-0.15 in grey, 0.15-0.3 in yellow, 0.3-0.45 in orange, and >0.45 in red. PvDBP-RII, shown in cartoon representation can be seen to bind a cluster of residues with high sequence entropy using both its heavy (blue) and light (purple) chains.

Comparison of the epitope bound by DB1 to other epitopes of inhibitory mAbs shows that while DB1 and human mAbs 092096 bind to subdomain 2, DB1 does not directly bind the conserved DARC binding site, whereas 092096 binds the conserved DARC binding region **(Figure 5.13)**. In agreement with previous binding studies[26] the full triple complex structure confirms that DB1 binding to PvDBP-RII does not affect the binding of DARC **(Figure 5.14A).** By alignment of PvDBP-RII with that of the previously published PvDBP-RII-$DARC_{Ecto}$ heterotetramer structure (PDB: 4NUV), DB1 is clashing with both the second bound $DARC_{Ecto}$ and PvDBP-RII **(Figure 5.14B)**. In previous

studies, DARC and PvDBP-RII from bacterial sources were shown to dimerize in solution at a high concentration (16), as well as making dimer contacts in crystal structure, providing a proposed mechanism by which concerted DARC binding and PvDBP-RII dimerization drive erythrocyte recognition.

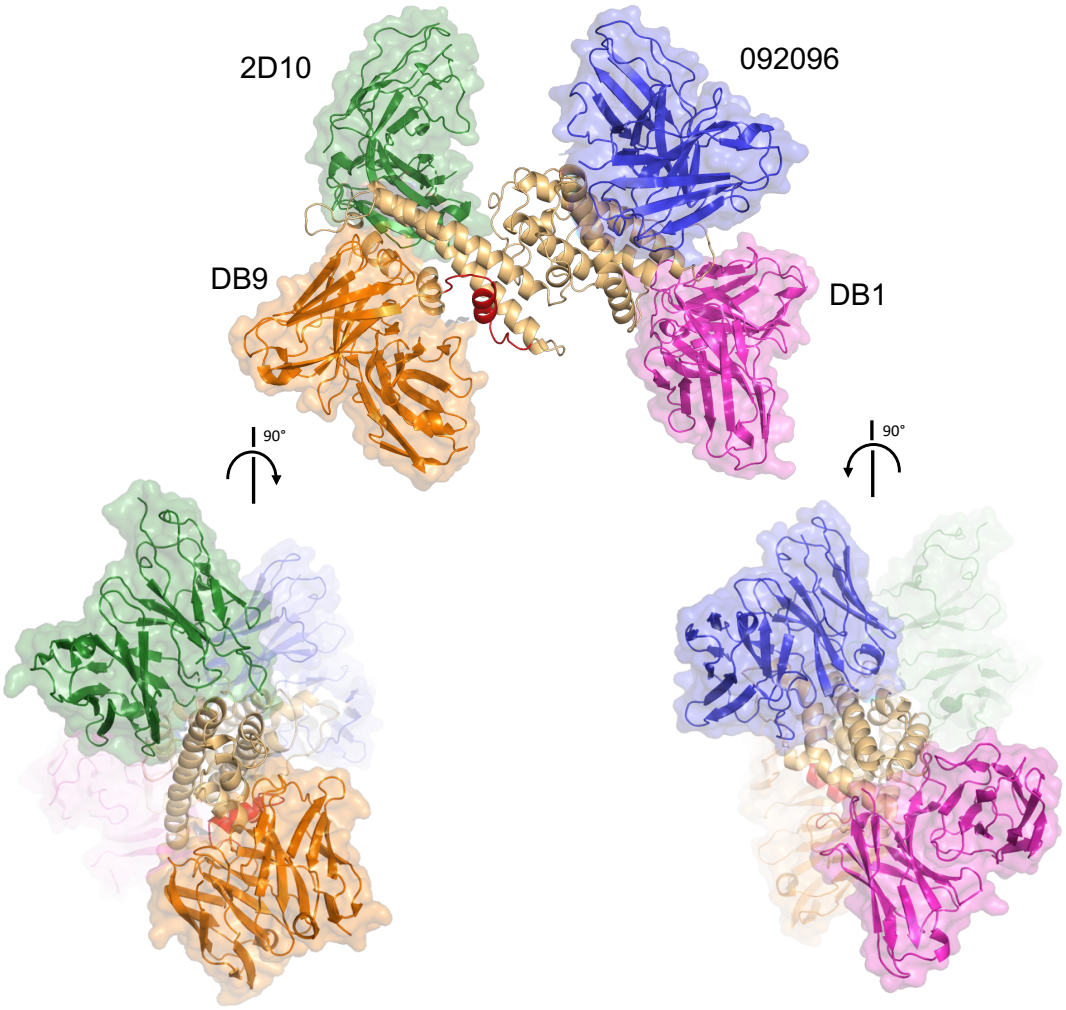


Figure 5.13. DB1 binds a different epitope to previously characterized mAbs. The binding epitope of DB1 (pink) on PvDBP-RII (light orange) is not overlapping with the nearby 092096 (blue), while DB9 (orange) and 2D10 (green) bind on opposite ends of subdomain 3. The footprint of 2C6 occupies an overlapping epitope with DB9 on subdomain 3.

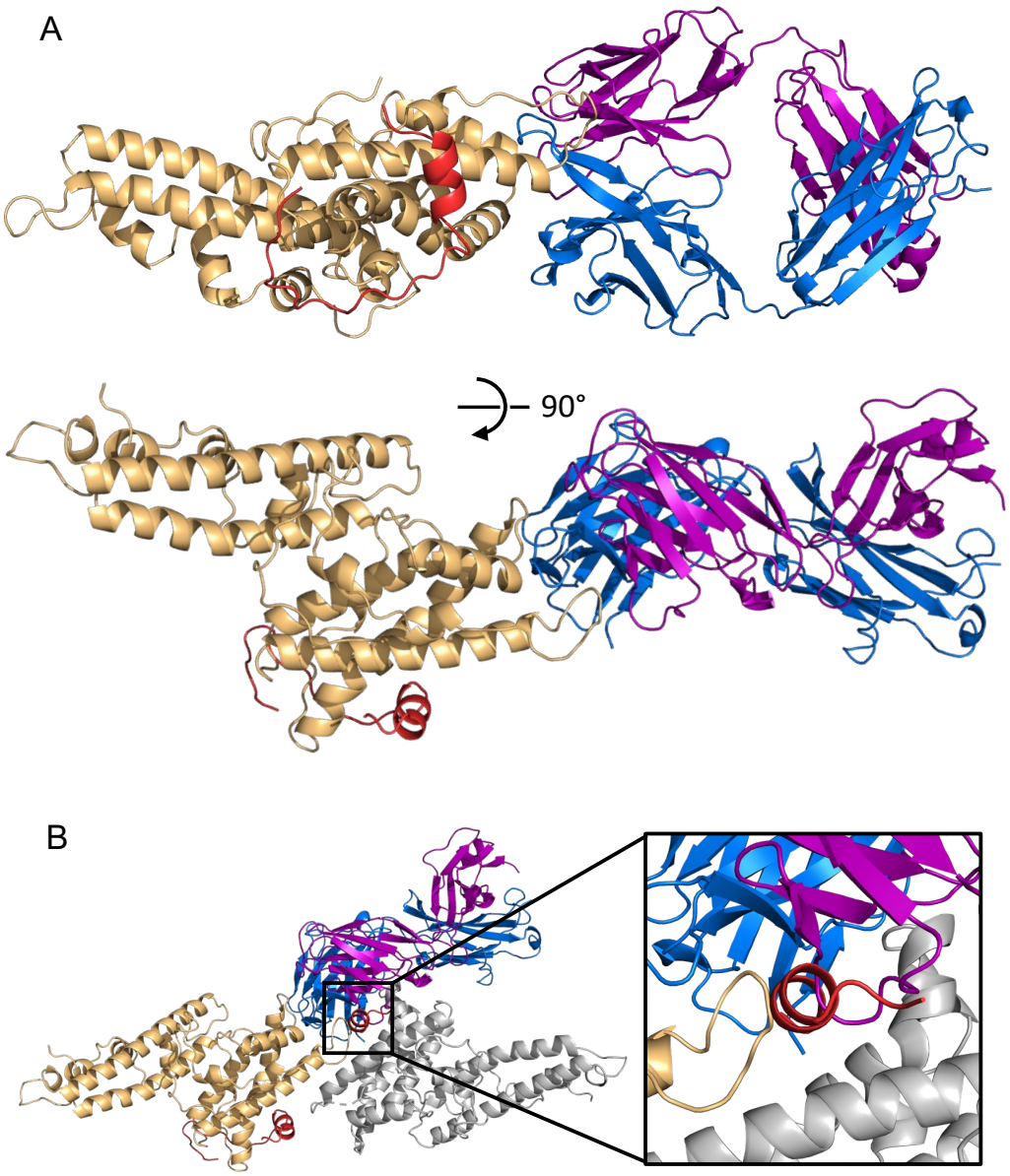


Figure 5.14. Binding site of human monoclonal antibody DB1. (A) PvDBP-RII-DARC-DB1 triple complex structure in cartoon representation, PvDBP-RII light orange, DARC ectodomain in red, DB1 in blue (heavy chain) and purple (light chain). (B) Alignment of PvDBP-RII-DARC-DB1 triple complex structure with PvDBP-RII-DARC homotetramer crystal structure, revealing that DB1 directly clashes with the second PvDBP-RII and DARC ectodomain.

5.2.6 Molecular dynamics simulation of DARC ectodomain binding to PvDBP-RII

Although the triple complex structure provides molecular detail for sulphated Tyr41 binding, no sulphation can be seen for Tyr30, either due to lack of sulphation of disorder in the structure. To assess the stability of Tyr41 and Tyr30, metadynamic simulations were performed by our collaborator Bora Guloglu (Higgins Group) to determine the relative free energy landscapes of sulphated and non-sulphated Tyr30 and Tyr41 **(Figure 5.15)**.

Sulphation of Tyr41 leads to an average free energy decrease of 7.63 kJ/mol, with a maximal energy decrease of 17.87 kJ/mol at the existing energetic global minimum of χ_1=-180° **(Figure 5.15A),** producing a single preferred conformation for sulphated Tyr41 **(Figure 5.15B)**. Sulphation of Tyr30 leads to a similar average free energy decrease of 8.75 kJ/mol, but the disappearance the free energy barrier at χ_1=-120° does not produce a new global minimum **(Figure 5.15C)**. Therefore, while sulphation of Tyr41 provides a new free energy minimum to stabilize the bound peptide at a specific conformation, the sulphated Tyr30 occupies a larger conformational landscape **(Figure 5.15D)**. The average number of interactions formed by each side chain was also calculated by weighing the number of interactions to the fraction of the simulation during which the interaction occurs **(Figure 5.15E)**. Whereas the number of interactions formed with PvDBP-RII upon Tyr30 sulphation increases modestly from 1.30 to 1.87, the number of interactions with PvDBP-RII upon sulphation of Tyr41 more than doubles from 3.64 to 7.46. This is partially explained by the ability of the sulphated Tyr41 to form electrostatic interactions with the guanidino group of Arg304, which it is unable to reach in the non-sulphated

form, stabilizing it in a specific conformation, as suggested by the free energy landscape **(Figure 5.15F)**.

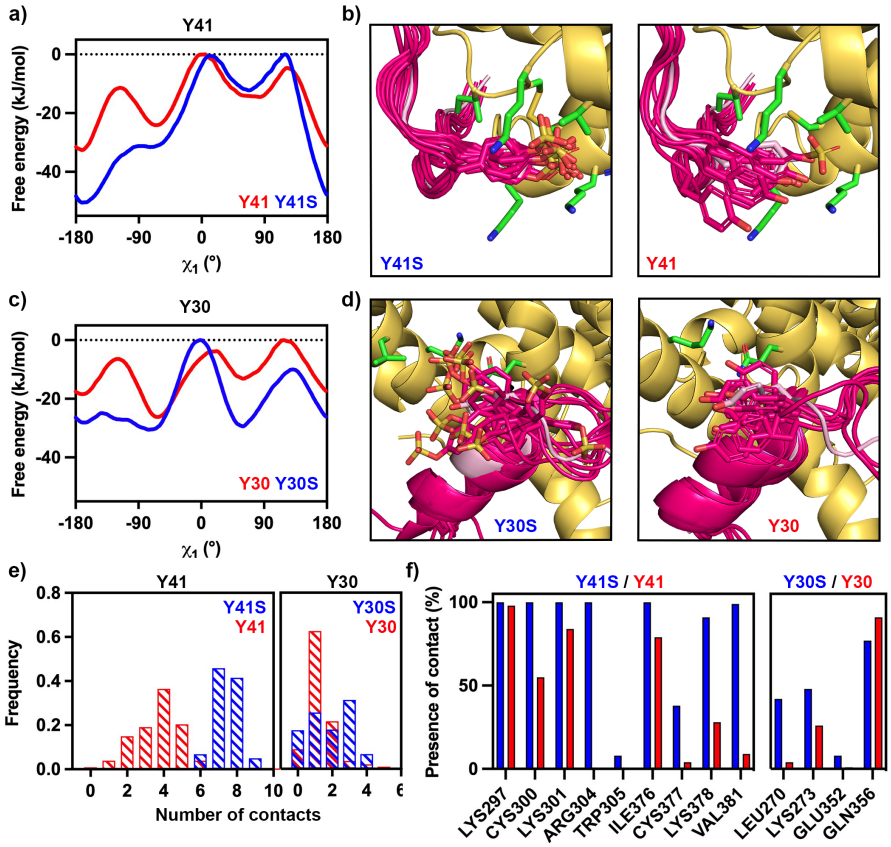


Figure 5.15. Molecular dynamics simulations of Tyr30 and Tyr41 binding with and without sulphation. In all cases, red corresponds to unsulphated and blue corresponds to sulphated forms of Y30 and Y41. (A) Free energy landscapes for residue Tyr41 relative to the χ_1 angle of the tyrosine. (B) Representative images from across the simulation illustrating the degree of motion of Y41 in its sulphated (left) and unsulphated (right) forms. PvDBP shown in yellow cartoon and DARC shown in pink cartoon. Y41 (pink) and nearby relevant side-chains (green) shown as sticks colored by element. (C) Free energy landscapes of for residue Tyr30 relative to the χ_1 angle of the tyrosine. (D) Representative images from across the simulation illustrating the degrees of motion of Tyr30 in its sulphated (left) and unsulphated (right) form. (E) The relative frequency and of the number of contacts formed by PvDBP-RII and Tyr41 (left) and Tyr30 (right) during the simulation. (F) Percentage of frames in which each residue from PvDBP-RII forms interactions with Tyr41 (left) or Tyr30 (right).

5.2.7 Isothermal titration calorimetry of PvDBP-RII binding to DARC ectodomain

In a previous study of DARC sulphation, immunoprecipitation of DARC from cell lysate with PvDBP-RII and PkDBP-RII was almost entirely abrogated by mutation of Tyr41 to Phe(15). Mutation of Tyr30 to Phe, however, had no effect on the ability of PkDBPα-RII to co-immunoprecipitated DARC from cell lysate. While this is supported by both the crystal structure and molecular dynamics simulations of PvDBP-RII with sulphated $DARC_{Ecto}$, our collaborator Tossapol Pholcharee (Higgins group) was able to quantitatively demonstrate the improved binding for sulphated $DARC_{Ecto}$ by isothermal titration calorimetry. Synthetic $DARC_{Ecto}$ peptide in which both Tyr30 and Tyr41 are sulphated bound to PvDBP-RII with an affinity of 58 nM, while a non-sulphated peptide bound at a much lower affinity of 23 μM. A singly sulphated peptide at Tyr30 bound with an affinity of 552 nM, and a singly sulphated peptide at Tyr41 bound with an affinity of 168 nM. Therefore, while both Tyr30 and Tyr41 sulphation individually contributes to $DARC_{Ecto}$ binding to PvDBP-RII, Tyr41 sulphation provides a greater contribution **(Figure 5.16).**

5.2.8 Inhibition of merozoite invasion of erythrocytes by DARC ectodomain

These patterns are also observed in the ability of $DARC_{Ecto}$ peptides to inhibit merozoite invasion of erythrocytes. Our collaborators at the London School of Tropical Medicine and Hygiene (Rob Moon, Franziska Mohring, and Sophia DonVito) we were able to observe the differential inhibition of merozoite invasion in the presence of differentially sulphated synthetic DARC ectodomain peptides. Transgenic *P. knowlesi* parasites

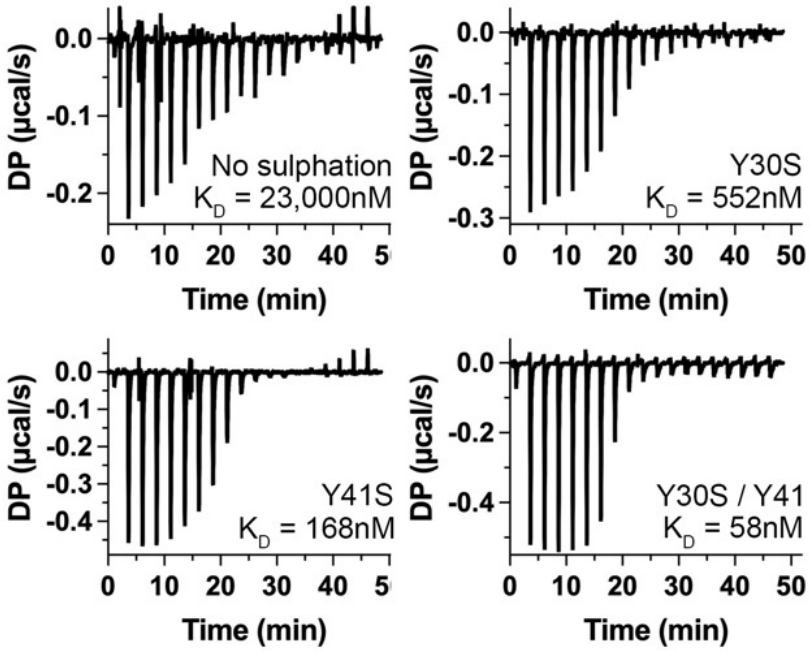


Figure 5.16. Isothermal titration calorimetry measurements of sulphated and unsulphated DARC ectodomain peptides binding to PvDBP-RII. Traces shown are single representative traces for non-sulphated DARC ectodomain peptide, DARC ectodomain peptide sulphated only at Tyr30, only at Tyr41, or both on Tyr30 and Tyr41. The stated Kd values are from n=3 technical replicates.

expressing PvDBP instead of the orthologous PkDBPα have been previously used to demonstrate inhibition of merozoite invasion by PvDBP-RII targeting antibodies(26). Synthetic $DARC_{Ecto}$ binding to PvDBP during invasion competes with DARC ectodomain on erythrocyte surface, thereby preventing transgenic *P. knowlesi* parasite attachment and invasion. While $DARC_{Ecto}$ sulphated at both Tyr30 and Tyr41 inhibited invasion at IC_{50} of 0.72 µM and $DARC_{Ecto}$ singly sulphated at Tyr41 inhibited invasion with IC_{50} of 2.99 µM, both singly sulphated Tyr30 peptide and non-sulphated peptide failed to produce any inhibition. Additionally, synthetic DARC ectodomain peptide sulphated in positions Tyr30 and Tyr41 was able to inhibit erythrocyte invasion of wild-

type *P. knowlesi* at IC_{50} of 0.79 µM, and DARC ectodomain peptide singly sulphated in position Tyr41 inhibited invasion at an IC_{50} of 3.92 µM. Peptide sulphated at Tyr30 or unsulphated peptide did not inhibit *P. knowlesi* invasion. These results echo all previous experimental observations, demonstrating the superior role of Tyr41 sulphation in mediating $DARC_{Ecto}$ binding to PvDBP.

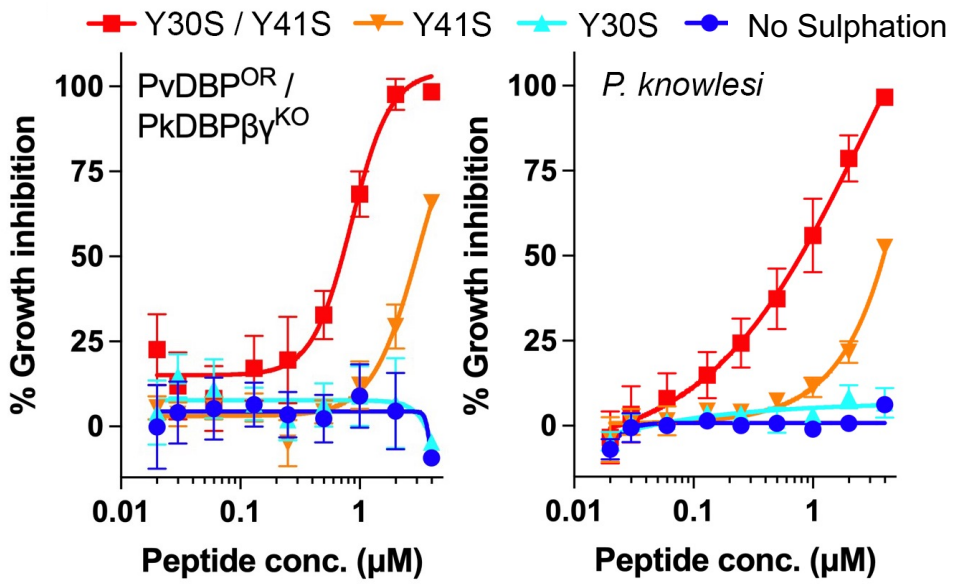


Figure 5.17. Inhibition of transgenic P. knowlesi parasites expressing PvDBP by synthetic DARC ectodomain peptides. Growth inhibitory activity of the same four synthetic peptides in a parasite growth assay using transgenic (PvDBPOP/ $PkDBP\beta\gamma^{KO}$, left) or wild-type (right) *P. knowlesi*. Values shown are averages of n=2 technical replicates, showing the mean and standard error of the mean of four separate biological replicates (n=2 in FyA donor blood and n=2 in FyB donor blood). IC_{50} values were identified using a variable slope four-parameter logistic curve.

5.2.9 Small-angle X-ray scattering of PvDBP-RII in complex with DARC ectodomain

PvDBP-RII purified from bacterial sources has been seen to dimerize in multiple crystal structures, as well as by small-angle X-ray scattering (SAXS) at high concentration in solution(16,30). Therefore, the binding epitope of DB1 at the putative dimerization interface offers a potential mechanism for DB1 inhibition of merozoite invasion. To determine whether PvDBP-RII purified from mammalian cell expression dimerizes in solution, our collaborator Tossapol Pholcharee (Higgins lab) used size-exclusion chromatography coupled to small-angle X-ray scattering (SEC-SAXS) to assess the solution mass PvDBP-RII in complex with DB1 Fab and separately in complex with $DARC_{Ecto}$ and DB9 Fab. Inhibitory mAb DB9 binds away from the dimerization interface and was included to stabilize the PvDBP-RII-$DARC_{Ecto}$ complex to prevent aggregation at high concentrations. The PvDBP-RII-DB1 complex showed the expected mass and maximum dimensions as expected for a monomeric complex **(Figure 5.18A)**. At high concentrations of up to 6mg/ml, no dimerization was observed for the PvDBP-RII-$DARC_{Ecto}$-DB9 complex **(Figure 5.18B)**, which puts into question whether the dimerization observed in PvDBP-RII purified from bacterial sources in both crystal structures and SAXS experiments is physiologically relevant to the *in vivo* invasion process.

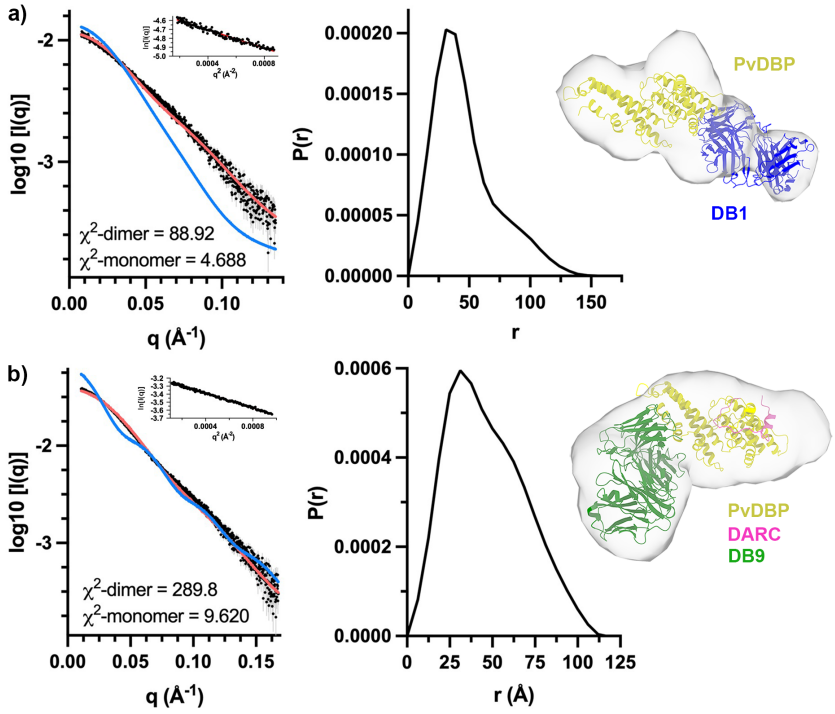


Figure 5.18. Small angle X-ray scattering of PvDBP-RII complexes. Small angle X-ray scattering data (SEC SAXS) for (A) PvDBP-RII in complex with DB1 Fab and (B) PvDBPRII in complex with DB9 Fab and $DARC_{Ecto}$. In each case, the refined scattering data is shown on the left (black circles) fitted with the predicted scattering for monomeric (red) or dimeric (blue) complex. The inset is the Guinier plot. The central panel shows the pair distance distribution function while the right panel shows the calculated envelope into which the monomeric model has been docked.

5.2.10 Purification of PvDBP ectodomain from mammalian cell culture

In the absence of PvDBP-RII dimerization, the mechanism of inhibition of invasion by DB1 binding may be instead due to the disruption of another yet uncharacterized interaction in the functional invasion complex formed by PvDBP and DARC. In the previously described mammalian cell culture expression trial, full-length PvDBP ectodomain ($PvDBP_{Ecto}$) showed expression. To characterize the expression and functionality of the full-length PvDBP ectodomain, and therefore its suitability to probe the broader PvDBP-DARC interaction, a large-scale expression was set up in HEK293F

cells. Following dialysis of the cell culture supernatant, PvDBP ectodomain was purified by NiNTA affinity and size exclusion chromatography **(Figure 5.19A)**. A single peak can be seen in the SEC chromatogram of the NiNTA elution fraction **(Figure 5.19B)**, producing a high molecular weight band by SDS-PAGE **(Figure 5.19C)**. Overnight deglycosylation by PNGase F slightly decreases the observed molecular weight of the purification product, but this does not account for the large difference between expected and observed molecular weight. To assess the secondary structure of the PvDBP ectodomain, circular dichroism measurements were taken between 190-260 nm **(Figure 5.19D)**. The average spectrum shows two peaks around 208 nm and 222 nm, as expected from an α-helical protein, in-line with the known PvDBP-RII structure and RaptorX prediction.

Deconvolution of the CD spectrum using CAPITO(31) predicts the protein to be 18% α-helical, 12% β-strand, and 59% irregular, leaving 11% of the structure unaccounted for. Region II of PvDBP contains 184 residues in α-helices (18.7% of PvDBP ectodomain), in line with the prediction of CAPITO. The prediction of an additional 12% β-strand content further suggests that PvDBP ectodomain contains secondary structure beyond Region II, which does not contain β-strands. However, the 11% of the model that was not accounted for by the prediction suggests the model that was used to calculate the secondary structure composition does not provide a good fit for the CD data. This prediction also contrasts with structural prediction server RaptorX, which predicted RI and RVI to contain α-helical secondary structure, but no β-strands (See section 2.2.5 and **Figure 5.5**).

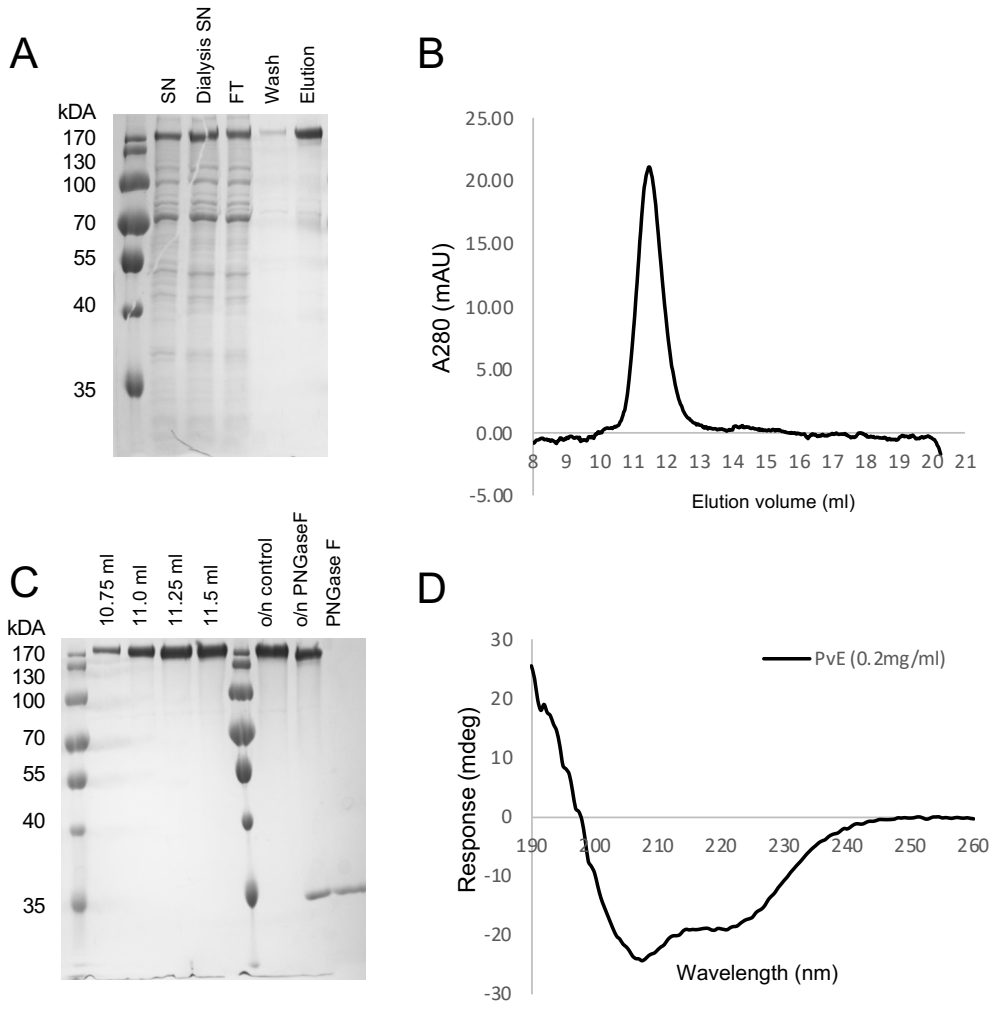


Figure 5.19. Purification of PvDBP ectodomain from HEK293F expression. (A) Reducing SDS-PAGE of NiNTA affinity chromatography purification stages. A high molecular band in the elution fraction corresponds to PvDBP ectodomain with an expected molecular weight of 110 kDa. (B) SEC chromatogram of purified PvDBP ectodomain produces a monomeric band at elution volume of 11.5ml on a Superdex200 10/300 GL column. (C) Reducing SDS-PAGE of PvDBP ectodomain elution fractions produces a single major band at 170 kDa which slightly decreases in moleculaw weight with deglycosylation by PNGase F. (D) CD spectrum of PvDBP ectodomain at 0.2 mg/ml was taken between 190 nm and 260 nm, producing peaks at 208 nm and 222 nm typical of an α-helical protein.

5.2.11 Limited proteolysis of PvDBP ectodomain

As a preliminary means of assessing regions of $PvDBP_{Ecto}$ that are protected from proteolysis, and so may form secondary structural elements beyond RII as suggested by both RaptorX structural prediction and the CD spectrum deconvolution by CAPITO, $PvDBP_{Ecto}$ was subjected to partial digestion by a panel of proteases **(Figure 5.20)**. Due to the high proportion of disorder predicted for PvDBP, it is suspected to be highly susceptible to proteolytic digestion. While small degradation fragments can be produced through the lack of an appropriate cleavage sequence for a specific protease, large stable degradation fragments likely correspond to regions of secondary structure.

Enzymatic digestion of $PvDBP_{Ecto}$ by trypsin, AspN, and GluC produce a stable degradation fragment at the range of 35-50 kDa (labelled Fragment 1, F1), of the expected molecular weight of PvDBP-RII. Enzymatic digestion with chymotrypsin and carboxypeptidase produces a stable digestion fragment at 70 kDa (labelled Fragment 2, F2). Carboxypeptidase hydrolyses the C-terminal amino acid of polypeptides, and a 70 kDa fragment is consistent with the expected molecular weight of an N-terminal RI-RII fragment, at 60 kDa. In addition to producing a fragment of a similar size to PvDBP-RII, trypsin and AspN digestion produces a small fragment which migrates at 25 kDa on SDS-PAGE (labelled Fragment 3, F3). After AspN digestion for 24 hours, the fragment corresponding to the size of RII is not digested, while the smaller 25 kDa band is entirely degraded and can't be seen in the coomasie-stained SDS-PAGE gel. Fragment 3 could be a subpopulation of the Fragment 1 more susceptible to degradation, or a domain of

$PvDBP_{Ecto}$, which may correspond to either RI or RVI. Together, these results support the structural prediction of secondary structure elements beyond RII.

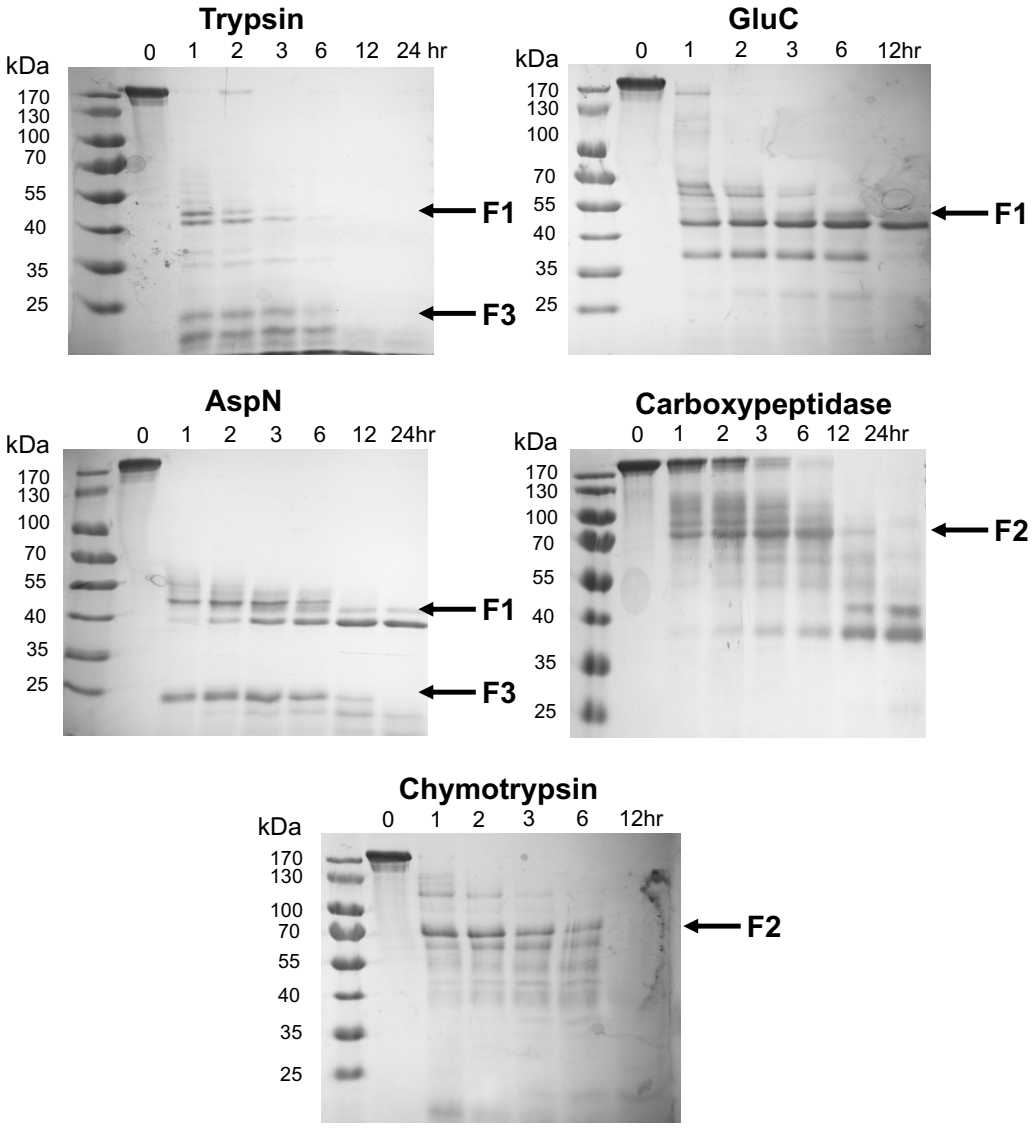


Figure 5.20. Limited proteolysis of PvDBP ectodomain. Reducing SDS-PAGE of PvDBP ectodomain proteolysis by a panel of proteases over a course of 12-24 hours. Trypsin, GluC, and AspN produce a stable degradation fragment (F1) between 50-35 kDa, in-line with the expected mass of PvDBP-RII of 39 kDa. Chymotrypsin and carboxypeptidase produce a stable degradation fragment (F2) with mass of 70 kDa, in-line with the expected size of an RI-RII fragment. Trypsin and AspN digestion also produce a low molecular weight fragment (F3) at 25 kDa.

5.2.12 $PvDBP_{Ecto}$ Binds $DARC_{Ecto}$ and Inhibitory Antibody DB10 in Solution

The observation of a stable degradation fragment of similar size to RII by limited proteolysis suggests RII of $PvDBP_{Ecto}$ might be correctly folded. To confirm whether $PvDBP_{Ecto}$ bound $DARC_{Ecto}$ peptide in solution, $PvDBP_{Ecto}$ was mixed with an excess of $DARC_{Ecto}$ ectodomain peptide to allow for complex formation at RTM. The $PvDBP_{Ecto}$-$DARC_{Ecto}$ complex mixture and controls were purified by size exclusion chromatography, and elution fractions of the relevant peaks inspected by SDS-PAGE **(Figure 5.21)**.

Single component control of $PvDBP_{Ecto}$ produced an elution peak at volumes 11.5ml and an SDS-PAGE band at a molecular weight of over 170 kDa, and single control for $DARC_{Ecto}$ produced a peak at elution volume of 17ml and an SDS-PAGE band at molecular weight of 20 kDa **(Figure 5.21A)**. For each control, there is no visible SDS-PAGE gel band at the molecular weight of the other component **(Figure 5.21B).** In the size-exclusion trace of the complex mixture, two peaks can be seen at the previously observed elution volumes **(Figure 5.21A)**. The high elution volume peak produces a single low molecular weight band by SDS-PAGE corresponding to $DARC_{Ecto}$, whereas the low elution volume peak produces bands corresponding to both proteins, indicating co-migration of $PvDBP_{Ecto}$ and $DARC_{Ecto}$ **(Figure 5.21B)**. The weak staining of the low MW band can be attributed to the large mass ratio of the two proteins (10kDa and 110kDa). It may also indicate that while some $PvDBP_{Ecto}$ can bind $DARC_{Ecto}$, some $PvDBP_{Ecto}$ may be misfolded or at a conformation which doesn't bind $DARC_{Ecto}$. The elution volume of the complex peak is identical to that of $PvDBP_{Ecto}$ alone, which would suggest that $PvDBP_{Ecto}$ does not dimerize upon DARC binding in solution, unlike

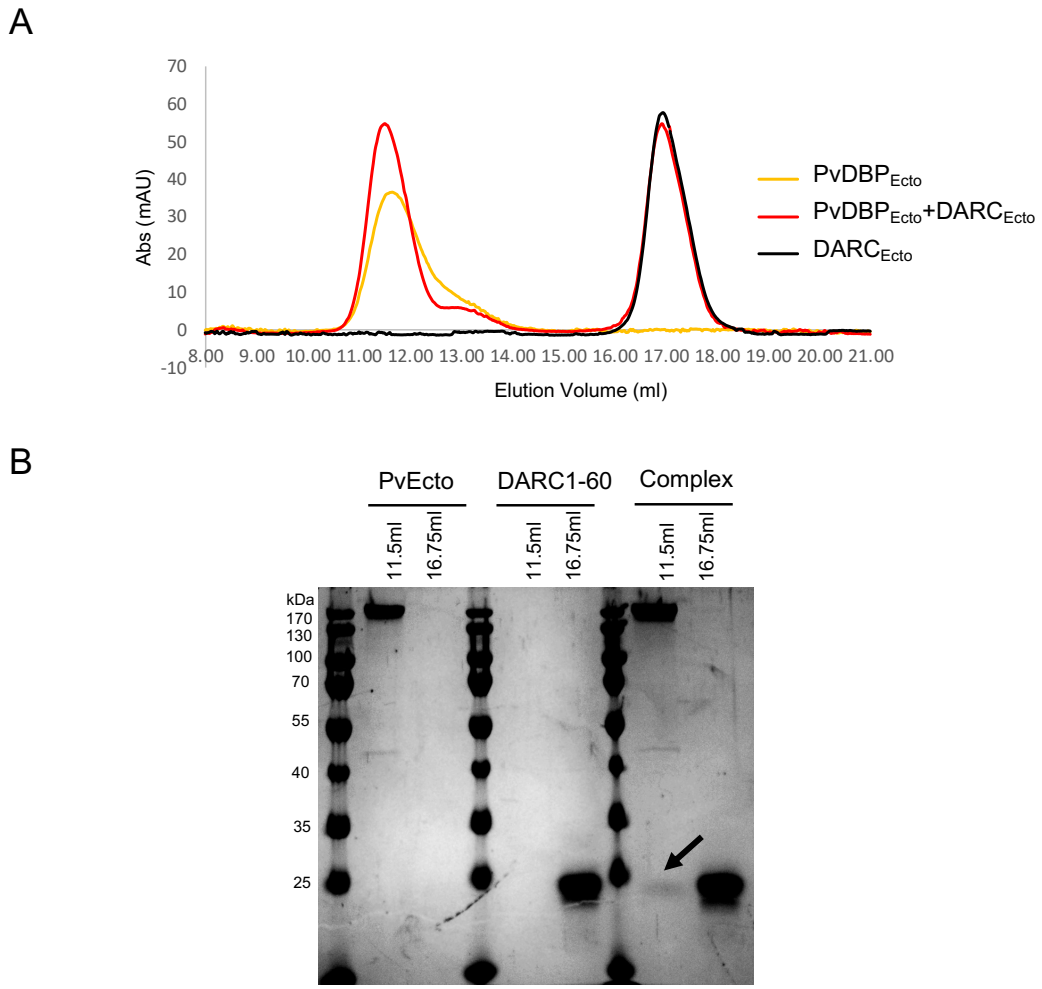


Figure 5.21. PvDBP ectodomain forms a complex with DARC ectodomain. (A) SEC chromatogram of DARC ectodomain (black), PvDBP ectodomain (orange), and complex mixture (red) on an Superdex200 10/300 column. PvDBP ectodomain elutes at a volume of 11.5ml, and DARC ectodomain elutes at a volume of 17ml. (B) SDS-PAGE visualization of elution fraction corresponding to SEC chromatogram peaks. A band at the molecular weight of DARC ectodomain can be seen to co-migrate with the low elution volume peak (11.5ml) in the complex mixture, indicating complex formation.

suggested by previous SAXS characterization of PvDBP-RII from bacterial sources (16), but in agreement with the SAXS measurements of PvDBP-RII from mammalian cell culture performed by our collaborator Tossapol Pholcharee (section 5.2.9).

To evaluate the ability of $PvDBP_{Ecto}$ to bind an inhibitory monoclonal antibody $PvDBP_{Ecto}$ was mixed with DB10 Fab (26) fragment and allowed to form a complex at room temperature. Elution fractions from size-exclusion chromatography of the complex mixture were visualized by SDS-PAGE. Whereas control DB10 Fab produces a peak at an elution volume of 14ml and $PvDBP_{Ecto}$ control produces a peak at elution volume of 11.5ml, the complex elutes at 9.5ml **(Figure 5.22A)**. SDS-PAGE gel of these elution fractions confirms the presence of both DB10 F(ab) and $PvDBP_{Ecto}$ **(Figure 5.22B)**. These results confirm that $PvDBP_{Ecto}$ contains the PvDBP-RII epitope targeted by DB10 and that DB10 can bind $PvDBP_{Ecto}$ in solution.

5.2.13 Purification of full-length DARC from mammalian cell culture

Following the rationale whereby the complete PvDBP-DARC interaction may involve regions of PvDBP outside of Region II, it may also involve regions of DARC beyond the N-terminal DARC extracellular domain. Full characterization of the PvDBP-DARC interaction should therefore aim to characterize the interaction of full-length PvDBP ectodomain and full-length DARC.

To assist in visualization of DARC protein during purification steps, full-length DARC was subcloned into pLEXm vector with a C-terminal TEV-GFP-6xHis, a kind gift from Simon Newstead (University of Oxford). In addition to assisting in visualization, the C-terminal placement of the GFP-6xHis tag allows for purification of full-length protein, as protein which is truncated, or a product of abortive translation will not contain the purification tag. Full-length DARC was expressed in HEK293F cells for 48 hours, cell

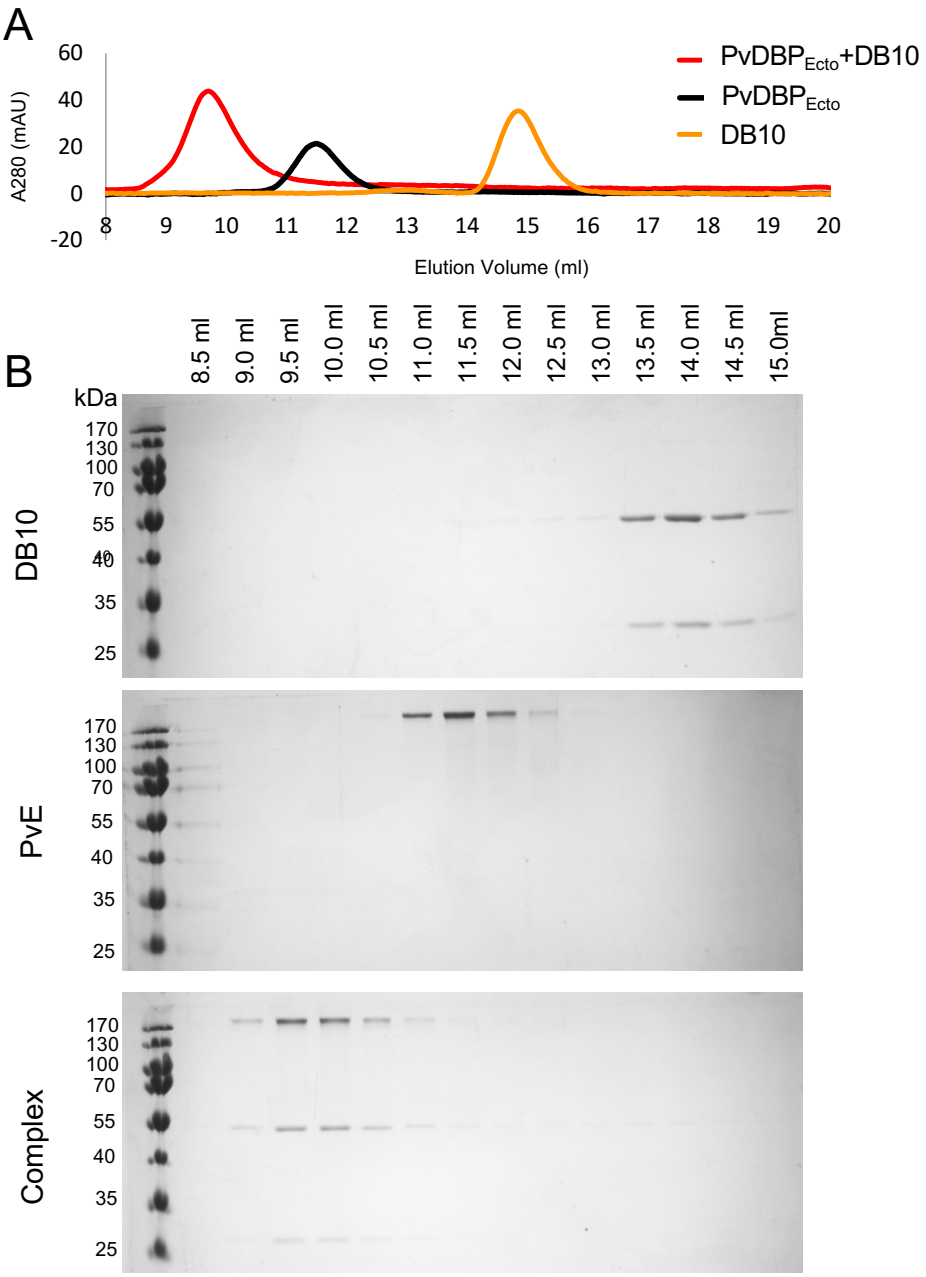


Figure 5.22. PvDBP ectodomain binds monoclonal antibody DB10. (A) SEC chromatogram of DB1, PvDBP ectodomain, and complex mixture on an Superdex200 10/300 column. DB1 elutes at a volume of 15ml, PvDBP ectodomain elutes at a volume of 11.5ml, and the PvDBP ectodomain-DB1 complex elutes at a volume of 9.9ml. (B) SDS-PAGE visualization of elution fraction corresponding to SEC chromatogram peaks. The fast-eluting complex peak produces bands corresponding to both PvDBP ectodomain and DB10, indicating complex formation.

fraction collected by centrifugation, and membranes further isolated by homogenization and ultracentrifugation. To extract DARC-GFP from the cell membrane fraction, it was solubilized in n-Dodecyl-B-D-Maltoside/cholesteryl hemisuccinate (DDM/CHS). Solubilized DARC-GFP was purified by NiNTA affinity chromatography through the C-terminal 6xHis tag, and the GFP-6xHis tag was removed together by cleavage with TEV protease. To visualize DARC-GFP through the purification steps, SDS-PAGE gel of the purification fractions was visualized by western blot with α-DARC antibody **(Figure 5.23A)** and in-gel fluorescence **(Figure 5.23B).** Throughout the solubilization and NiNTA purification, a double band can be seen migrating at the expected 70 kDa for the GFP-DARC fusion protein. In the elution fraction, the band can also be seen by in-gel fluorescence. Following TEV cleavage, a single major band can be seen at 35 kDa by both western blot and in-gel fluorescence. In the western blot, this band corresponds to full-length DARC, while by in-gel fluorescence this band corresponds to GFP, which both have the same expected molecular mass of 35kDa.

Due to both DARC and GFP producing a band at 35 kDa, DARC was further purified by NiNTA to remove GFP-6xHis (known as reverse NiNTA). In the α-DARC western blot, a 35kDa band can be seen in both the flow-through and elution fraction, suggesting that some DARC bound the NiNTA resin. By in-gel fluorescence, a band can only be seen for GFP in the reverse NiNTA elution fraction, suggesting the flow-through fraction contains DARC while the elution fraction contains a mixture of DARC and GFP-6xHis.

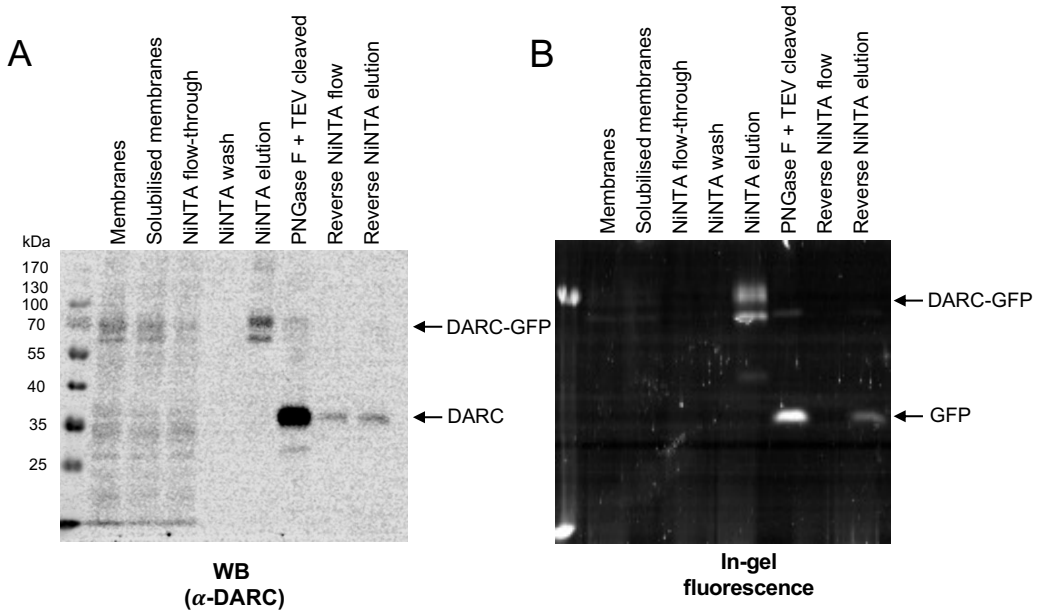


Figure 5.23. Purification of DARC from mammalian cell culture. (A) Western blot probed with goat α-DARC antibody and (B) in-gel fluorescence of recombinant full-length DARC NiNTA affinity purification. A double band at 70 kDa corresponds to the DARC-GFP fusion protein, which disappears after TEV cleavage to produce a fluorescent band at 35 kDa of GFP and 35 kDa of DARC.

5.2.14 PvDBP Ectodomain Binds Full-Length DARC

The ability of full-length DARC to bind $PvDBP_{Ecto}$ was assessed by pull-down of DARC with $PvDBP_{Ecto}$ bound to NiNTA beads or control NiNTA beads, and visualized by SDS-PAGE with Coomassie stain and by western blot probed with α-DARC **(Figure 5.23)**. DARC can be seen by western blot at the expected molecular weight of 35 kDa in the flow-through of the control beads, but not in the wash or elution fractions **(Figure 5.23A)**, indicating that DARC does not bind NiNTA beads on its own. When NiNTA beads were pre-bound to $PvDBP_{Ecto}$, a strong band can be seen in the elution fraction at the expected molecular weights of DARC and $PvDBP_{Ecto}$ by western blot and SDS-PAGE, respectively. PvDBPEcto can also be seen in the elution fraction by Coomassie stain

(Figure 5.23B). The elution of full-length DARC with $PvDBP_{Ecto,}$ but not control NiNTA beads, indicates DARC specifically bound the PvDBP ectodomain.

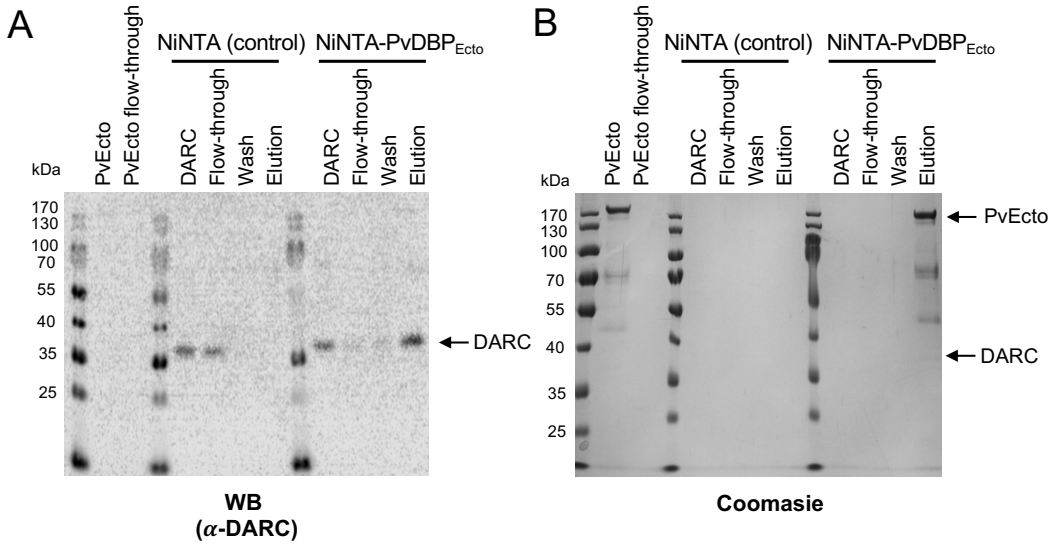


Figure 5.24. Pull-down of full length DARC with PvDBP ectodomain. (A) Western blot probed with goat α-DARC and (B) SDS-PAGE stained with coomassie of recombinant DARC pull-down with PvDBP ectodomain bound to NiNTA beads. A strong band at the expected molecular weight for DARC (35 kDa) appears in the elution fraction with PvDBP ectodomain-bound beads, but not control beads, indicating DARC binds PvDBP ectodomain.

5.3 Discussion and future Work

The *Plasmodium vivax* Duffy Binding Protein has long been known to interact with the extracellular domain of the Duffy Antigen Receptor for Chemokines (DARC) through its minimal binding Region II. The X-ray crystal structure of PvDBP-RII in complex with DARC19-30 is the first X-ray crystal structure of a *Plasmodium* EBL domain in complex with its ligand (32), shedding crucial detail on the minimal interaction required for parasite recognition of reticulocytes. This structure does not reveal a molecular basis for observed effects of DARC ectodomain sulphation of Tyr30 and Tyr41(15), and polymorphism at position 42 producing the FY*A/FY*B alleles(12), observed to impact the binding of PvDBP-RII to DARC.

Previous studies produced both PvDBP-RII and DARC from bacterial sources, unable to produce the post-translational tyrosine sulphation implicated in DARC binding. The X-ray crystal structure of PvDBP-RII in triple complex with the DARC ectodomain (amino acids 1-60) and inhibitory human antibody DB1, all from mammalian sources, finally reveals the molecular basis for the long-hypothesized interaction of the sulphated Tyr41. Providing new detail of DARC31-47 on top of previously observed DARC19-30, the structure shows Tyr41 bound in pocket of positively charged residues on subdomain 2. The horse-shoe shaped DARC ectodomain binding across subdomain 2 is only seen in the presence of Tyr41 sulphation, and further stabilized by a series of electrostatic interaction with positively charged PvDBP-RII residues. The salt-bridge formation of the polymorphic Asp42 of the FY*B allele with a nearby lysine also provides a plausible

mechanism for the increased susceptibility of FY*B erythrocytes to *P. vivax* merozoite invasion.

Through the invaluable collaboration of Tossapol Pholcharee and Bora Guloglu (Higgins group), and Sophia DonVito, Franszieska Mohring, and Rob Moon (London School of Hygeine and Tropical Medicine) we further revealed the relative importance of Tyr41 sulphation over Tyr30 sulphation (33). Molecular dynamics simulation show that the sulphation of Tyr41 over doubles the average number of interactions made by Tyr41, allowing for interactions not possible in the unsulphated Tyr41, and produces a preferred conformation in the compact binding pocket on PvDBP-RII. In contract, sulphation of Tyr30 only slightly increases the number of interactions formed on average across the simulations, while increasing the conformational landscape sampled by Tyr30. Removal of the sulphate on Tyr41 decreases the binding affinity of DARC ectodomain peptide to PvDBP-RII ~9-fold, whereas removal of the sulphate on Tyr30 decreases binding affinity ~3-fold. The relative importance of this post-translational modification is recapitulated by transgenic merozoite invasion inhibition assay, in which only DARC ectodomain peptides with sulphated Tyr41 were able to complete with native DARC on erythrocytes for parasite binding and inhibit invasion by *P. vivax* merozoites.

The crystal structure of the triple complex also reveals the binding epitope of DB1, an inhibitory monoclonal antibody isolated from Phase I trials (20,26). The binding of DB1 on Subdomain 2 directly engages the polymorphic DEK epitope in a prolific network of salt-bridges, explaining why DB1 does not offer strain-transcending immunity. Distinct

from the conserved epitope targeted by human antibodies isolated from natural infection (28), DB1 represents the first structurally characterized vaccine-elicited human antibody binding subdomain 2. It possible that by maintaining a polymorphic epitope of highly reactive residues, *P. vivax* merozoites divert the humoral response away from the nearby DARC binding site. Saturating the nearby epitope with strain-specific antibodies may interfere with B-cell recognition of nearby conserved epitopes and facilitate immune escape of the parasite. The removal of the polymorphic DEK motif has been the subject second-generation vaccine design (23–25). While heterologous prime boost immunization with the DEK-null vaccine design was able to generate a higher strain-transcending immune response, it failed to achieve the same level of lymphoproliferative stimulating capacity and failed to increase the overall inhibition of PvDBP-RII to DARC in the COS7-erythrocyte binding assay. The binding of DB1 to the DEK motif highlights the need for continued improvement of such immuno-focusing approached for future vaccine design.

Binding of DB1 to PvDBP-RII does not preclude DARC binding, but directly clashes with DARC dimerization, which has been proposed by the previous X-ray crystal structures of the PvDBP-RII-DARC complex (16,32). SAXS measurements performed by Tossapol Pholcharee contradict this observation, as no dimerization is observed in solution at concentrations up to 6 mg/ml, raising the possibility that DB1 provides protection by inhibiting a yet undiscovered essential interaction in the complete PvDBP-DARC invasion-competent complex. The DARC extracellular domain has been proposed to undergo remodelling through erythrocyte maturation resulting in *P. vivax* tropism(34).

A single mutation in region VI of the orthologous PyEBL protein alters its intracellular localization and increased parasite virulence by decreasing its preference for young erythrocytes (10). Therefore, regions of PvDBP outside of PvDBP-RII as well as regions of DARC outside of the extracellular domain may both participate in the complete PvDBP-DARC invasion-conducive complex and even impact *P. vivax* tropism. Structural prediction of the PvDBP ectodomain using RaptorX identifies two regions of potential secondary structure beyond Region II. PvDBP ectodomain expressed in mammalian culture produces circular dichroism spectrum which corresponds to 18% α-helical content, in line with the α-helical content of PvDBP-RII out of the entire PvDBP ectodomain (18.7%), and 12% β-strand composition, corresponding to yet uncharacterized regions of the protein which may be involved in the complete interaction of PvDBP with DARC. Limited proteolysis identifying two degradation fragments that suggest secondary structural elements beyond Region II. PvDBP ectodomain is binds DARC ectodomain and inhibitory antibody DB10 in solution, as well as full-length DARC by pulldown. The full-length PvDBP ectodomain is a new functional tool for the continued investigation of the interaction with DARC.

5.4 Materials and methods

5.4.1 Expression and purification of PvDBP-RII from *E. coli* inclusion bodies

PvDBP-RII was expressed in *E. coli* using a construct containing amino acids 194-508 of PvDBP in the pET15con vector backbone, with an N-terminal 6xHis tag and TEV protease cleavage site. This expression construct was transformed into BL21(DE3) cells which were grown at 37°C to OD 0.6-0.8 and induced with 1mM IPTG for 3 hours at 37°C or overnight at 20°C. Bacterial cell pellets were resuspended in 20 mM Tris-HCl pH 8, 300 mM NaCl, 15 mM imidazole, 0.5% TRITON X-100 (lysis buffer) and lysed using a Sonicator S-400 (Misonix, USA) at a power of 70W, 3s on; 7s off, for 6 minutes total. Lysate was spun down at 50,000g for 20 minutes, and an inclusion body purification carried out.

Inclusion bodies were purified by rounds of homogenization, sonication, and centrifugation in high detergent buffer (20mM Tris-HCl pH8, 300 mM NaCl, 15 mM imidazole, 1% TRITON X-100), high salt buffer (20 mM Tris-HCl pH8, 1 M NaCl, 15mM imidazole, 0.5% TRITON X-100), and low Triton-X buffer (20mM Tris-HCl pH8, 300mM NaCl, 15mM imidazole, 0.05% TRITON X-100), before being resuspended in 6M guanidine-hydrochloride, 2mM β-mercaptoethanol, 20mM Tris pH 7.5 overnight to solubilize the inclusion bodies. Solubilised inclusion bodies were clarified by centrifugation at 50,000g for 30 minutes and flash-diluted into 1L cold refolding buffer (400 mM L-arginine, 10 mM EDTA, 0.1 mM phenylmethanesulfonylfluoride, 3 mM reduced glutathione, 0.3 mM oxidized glutathione, pH 8.0).

After >36h at 4°C stirring, sample was clarified by centrifugation at 15,000g and buffer exchanged by 3-4 dialyses against 15L of 150mM NaCl 20 mM Tris pH 7.5 using 10kDA cut-off snakeskin tubing (Thermo Fisher Scientific). Precipitate was removed by spinning at 15,000g for 30 minutes and supernatant filtered through 0.2 μm membrane (Whatman). 5ml NiNTA beads were added for an hour, washed on column with NiNTA wash buffer (300 mM NaCl, 20mM Tris pH 8, and 20 mM imidazole), and bound protein was eluted with NiNTA elution buffer (150mM NaCl, 20mM Hepes pH 7.5, 300mM imidazole). Eluted protein was further purified by size exclusion gel chromatography Superdex 200 10/300, GE Healthcare) into 20mM HEPES pH7.5, 150mM NaCl.

5.4.2 PvDBP Construct Design and Structure Prediction

PvDBP sequence used is that of the SalI strain (UniProt entry P22290). TMHMM v2.0 transmembrane α-helix prediction server (http://www.cbs.dtu.dk/services/TMHMM/) and RaptorX protein structure prediction (http://raptorx.uchicago.edu/) were used to predict domain boundaries. Different N- and C-terminal boundaries for PvDBP-RII were used from previous publications(16,22,27).

5.4.3 Transfection of HEK293F cells

Freestyle 293F cells (Gibco) were grown to a density of 1.5 million cells/ml in Freestyle F17 expression media (Gibco) supplemented with 2 mM glutamine, 50 U/ml penicillin, 50 μg/ml streptomycin, and MEM non-essential amino acids (Gibco). The cells were centrifuged for 10 minutes at 300 g, the supernatant discarded, and the pellet resuspended in fresh media. 1ug/ml of construct DNA at a concentration of 0.5 μg/μl was then added

with 2 ug/ml of PEI-MAX 40 kDa (Polysciences) to 1 ml of Reduced Serum Media (Gibco), and incubated at RTM for 15 minutes before adding to cells.

5.4.4 Small-scale expression trials in HEK293F cells

PvDBP ectodomain constructs were purchased as gene strings from GeneArt (Thermo Fisher Scientific) and cloned into pHLSec vector containing a C-terminal 6xHis tag. Day 5 HEK293F supernatant was clarified by centrifugation at 4000 g for 20 minutes and the supernatant collected. Supernatant pH was adjusted to pH 8 and 1 ml NiNTA resin added for 1 hour. Resin was collected by centrifugation at 500 g for 5 minutes, washed twice with 10 ml of wash buffer (300 mM NaCl, 20 mM Tris pH 8, 20 mM imidazole) and eluted 20 mM Hepes pH 7.5, 150mM NaCl, 300 mM imidazole and analysed by SDS-PAGE.

5.4.5 Purification of full-length DARC from HEK293F cell expression

Gene string of full-length DARC was purchased from GeneArt (Thermo Fisher Scientific) contained the DARC amino acids 1-336 (FyB allele with D42). This gene string was inserted into the pLEXm vector backbone which contained a C-terminal TEV cleavage site, followed by GFP and 6xHis tag, a kind gift from Prof. Simon Newstead. Full-length DARC was expressed in HEK293F cells and harvested by centrifugation on day 2. All purification steps were performed on ice or at 4°C. Cell pellet was resuspended in 20 mM HEPES pH 7.5, 150 mM NaCl, 5% glycerol and membranes were disrupted by gentle homogenization with a dounce homogenizer. Membrane fraction was collected by ultracentrifugation at 41,000 rpm for 1 hour at 4°C, and membranes were solubilized in

buffer concentration of 20mM HEPES pH 7.5, 20mM Imidazole, 150mM NaCl, 5% glycerol and 1% n-Dodecyl-β-D-Maltoside (DDM) /0.2% cholesteryl hemisuccinate (CHS), rotating at 4C for 1 hour. Solubilized membranes were clarified by ultracentrifugation at 41,000 rpm 1 hour, and DARC purified by NiNTA affinity chromatography as mentioned above, with the addition of 3 cmc DDM/CHS to all buffers. Elution fraction was dialyzed against 20mM HEPES pH 7.5, 150mM NaCl overnight at 4°C with TEV protease to enzymatically cleave the GFP-6xHis tag. Samples were inspected by SDS-PAGE and in-gel fluorescence.

5.4.6 Transfection in Expi293F cells

Expi293F cells (Gibco) were grown to a density of 4 million cells/ml in Expi293 Expression Media (Gibco). 1 ug/ml final volume DNA and 2.67 ul/ml final volume ExpiFectamine were separately diluted in Opti-MEM. After a 5-minute incubation, the DNA and ExpiFectamine were mixed and incubated at room temperature for 20 minutes before being added dropwise to the cells. After an overnight incubation at 37°C, transfection enhancers were added as specified in the manufacturer protocol.

5.4.7 Purification of Fab from Expi293F cell expression

DB1-10 antibody constructs were provided by Simon Draper (Jenner Institute, University of Oxford). Transfection was performed as detailed above using a 1:1 mass ratio of heavy and light chain DNA. For transfection, a 1:1 mass ratio of heavy and

Day 5 transfection supernatants were clarified by centrifugation, adjusted to pH 8 with NaOH, and added to 1 ml Pierce protein A-agarose beads (Thermo) for 1 hour. Beads

were washed with NiNTA wash buffer and antibody eluted with 100mM glycine pH 3 and immediately neutralized with 10% volume 1M Tris pH 8.5. After buffer exchange into papain cleavage buffer (20 mM Tris pH 7, 10 mM EDTA, 20 mM L-Cysteine) 1ml of immobilized papain-agarose beads (Thermo) was added and incubated overnight at 37°C. Fc fragments were removed by protein A purification as above, with the protein A bead flow-through containing F(ab) fragment and uncleaved mAb. Protein A flowthrough containing Fab were then purified by size exclusion chromatography on a Superdex75 10/300 column (GE Healthcare).

5.4.8 Purification of DARC ectodomain peptide from Expi293F cell expression

DARC ectodomain peptide was expressed from a construct containing an N-terminal 6xHis tag followed by a TEV cleavage site. The construct contains DARC amino acids 1-60 with cysteines at positions 4, 51, and 54 mutated to alanine to avoid peptide aggregation in solution. DARC ectodomain was purified from day 4 or 5 clarified Expi293F supernatant by NiNTA affinity chromatography. Supernatant was adjusted to pH 8 with NaOH and NiNTA beads were added for 1 hour stirring at room temperature. Beads were washes with NiNTA wash buffer (150 mM NaCl, 20mM Tris pH 8, 20 mM Imidazole) and bound protein was eluted with NiNTA elution buffer (150 mM NaCl, 20mM Tris pH 8, 300 mM Imidazole). Eluted DARC ectodomain peptide was deglycosylated overnight with PNGaseF and 6xHis tag cleaved with TEV protease at 4°C. The following day, the sample was concentrated to 0.5ml with a Vivaspin 3 kDa spin concentrator and protein was purified by size exclusion chromatography on a Superdex75 10/300 GL column (GE Healthcare).

5.4.9 Purification of the PvDBP-RII-DARCEcto-DB1 triple complex from Expi293F cell expression

For crystallization of the PvDBP-RII-DARC-DB1 triple complex, DB1 and DARC ectodomain were purified as described above and added to the clarified cell culture supernatant of PvDBP-RII expression. The triple complex was then purified by NiNTA affinity chromatography following the same protocol as the DARC ectodomain peptide. After elution, the complex mixture was further supplemented with DARC ectodomain peptide. Following overnight inculation at 4°C with PNGaseF and TEV protease, complex mixture was purified by size exclusion chromatography on a Superdex200 10/300 GL column. Relevant elution fractions were concentrated to 10mg/ml for crystallization.

5.4.10 Large-scale expression and purification of PvDBP ectodomain from HEK293F cell expression

PvDBP Ectodomain was purified from day 5 Expi293F supernatant, clarified by centrifugation at 4000 xg for 30 minutes. NiNTA beads would often bleach when incubating in large volumes of cell culture media, and so for volumes larger than 500 ml supernatants were dialysed against 15 L of 150mM NaCl 20 mM Tris pH 7.5 for 4 hours before NiNTA affinity chromatography purification as described above. After elution, PvDBP ectodomain was further purified by size-exclusion chromatography on a Superdex200 GL column (GE Healthcare).

5.4.11 Structural determination of the PvDBP-RII-DB1-DARCEcto triple complex structure

Crystallization screens of the PvDBP-RII-DARC$_{Ecto}$-DB1 complex were set up using the pre-made Morpheus, JCSG Plus, ProPlex, and MIDAS (Molecular Dimensions) by vapour diffusion in sitting drops in MRC 2-well crystallization plates (Swissci, Hampton Research USA). In each screen, 50 ul reservoir solution is places in each well and 100 nl is dispensed in each drop, as well as 100 nl of protein complex mixture by a mosquito (TPP Labtech, UK). Out of the multiple conditions which produced crystals, the best diffracting crystal grew in 15% w/v jeffamine D2003 and 10% v/v ethanol. A single crystal appeared in the drop when inspected on day 12. The crystal was cryoprotected with well solution supplemented with 25% glycerol and cryocooled in liquid nitrogen. The full dataset was collected at the I24 beamline at Diamond by capturing the diffraction pattern produced by 0.2° of crystal rotation exposed to X-ray at wavelength of 0.9999Å for a full 360° crystal rotation, producing 1800 reflections.

This dataset was processed by autoPROC, which utilizes XDS(35) and AIMLESS (v.0.73)(36). As the structure of PvDBP-RII is already known, the phase problem was solved by molecular replacement using PHASER(37) with a search model produced from previously available PvDBP-RII structure, with flexible loops removed (PDB:6R2S). Following the identification of a solution containing the search model for PvDBP-RII, the solution was fixed, and an additional search model was used, this time of the variable domain of a Fab with the CDRs removed, and in the next cycle with the constant domain of the Fab. After identification of a correct solution containing a correctly assembled Fab

facing a molecule of PvDBP-RII which did not fit any more search models of PvDBP-RII or Fab, the molecular replacement solution was refined with BUSTER(38) and missing loops were built and refined using cycles of Coot(39), and BUSTER. Visualizations of the structure were prepared using PyMol.

5.4.12 Circular Dichroism

CD experiments used a Jasco J815 CD Spectrophotometer (Jasco). The protein was first desalted into 10 mM Sodium Phosphate pH 7.5, 150 mM NaF using PD-10 columns (GE Healthcare), and diluted to a concentration of 0.2 (PvE) or 0.1 mg/ml (PvDBP-RII). Spectra were then obtained through averaging 10 measurements taken between 260 nm and 195 nm at 20°C, subtracting a baseline measurement of buffer alone. Spectrum deconvolution was performed using CAPITO (31).

5.4.13 Limited Proteolysis

Limited proteolysis experiments used a 1:100 mass ratio of protease to protein. 0.7ul protease at 1 mg/ml was added to 70ug $PvDBP_{Ecto}$ at room temperature and aliquots added to SDS-PAGE buffer with b-mercaptoethanol and heated to 95°C for 5 minutes to quench the reaction at the specified times and analysed by SDS-PAGE.

5.4.14 Pull-down of full-length DARC with PvDBP ectodomain

For pull-down of DARCfl with $PvDBP_{Ecto}$, NiNTA beads were pre-bound to PvDBPEcto (or buffer) and washed with 20mM HEPES pH 7.5, 150mM NaCl. Purification fraction from full-length DARC NiNTA containing DARC was added to beads for 1 hour 4°C

and washed with 20mM HEPES pH 7.5, 150mM NaCl, 3 CMC (critical micelle concentration) DDM/CHS and 5% glycerol. Samples were eluted with wash buffer supplemented with 250mM Imidazole and samples inspected by western blot.

5.4.15 Western Blot

For western blot, SDS-PAGE gel was briefly soaked in Towbin buffer and Bio-Rad's Immun-Blot PVDF membrane activated by soaking in methanol. SDS-PAGE gel was layered on top of the membrane and between 3 layers of Whatman cellulose filter papers that has been soaked in Towbin buffer supplemented with 20% methanol. Transfer was performed using a semi-dry western blotting system (BioRad) for 1 hour at 50 mA. Following transfer, membrane was blocked in 5% milk powder in PBS-Tween 20 (0.1%) overnight, probed with Goat α-DARC (1:1000) (Thermo Fischer Scientific, PA5-18424), and detected with anti-Goat HRP (1:2000), washing three times between steps. The blot was developed using. ECL Prime Western Blotting Detection Kit (Amersham) and visualized using an Odyssey Fc Dual Mode Imaging System (LI-COR).

5.5 Declaration

Tom Rawlinson (Draper Group, University of Oxford) provided plasmids containing the coding sequence of DB1, isolated from Phase I trials. Original purification protocol and expression construct of PvDBP-RII for *E. coli* was produced by Samuel Gerrard (Higgins Group). The PvDBP-RII-DB1-$DARC_{Ecto}$ structure determination was assisted by Matthew Higgins and Edward Lowe (5.2.3-5.2.6). Isothermal titration calorimetry (5.2.7) and SAXS (5.2.9) were performed by Tossapol Pholcharee (Higgins Group), molecular

dynamics simulations (5.2.6) were performed by Bora Guloglu (Higgins Group), and parasite inhibition assay (5.2.8) was performed by Sophia M. DonVito, Franziska Mohring, and Robert W. Moon (London School of Hygeine and Tropical Medicine) and are included for context and discussion. The relevant methods for all assays performed by our collaborators are written by them and included in Appendix 1.

5.6 Acknowledgement

I would like to thank Simon Draper and Tom Rawlinson for their collaboration and providing us with the sequences of DB1-10. I would like to thank Ed Lowe for his pristine maintenance of the crystallization suite, data collection, and crystallography help. I thank David Staunton for his help with circular dichroism. I'm grateful for the help of Joanne Parker and to Simon Newstead for the pLEXm-GFP vector.

Table 5.1. Crystallographic data collection and refinement

Data collection	**PvDBP-RII-DARC$_{Ecto}$-DB1**
Beamline	Diamond I24
Wavelength	0.9999 Å
Space group	P 2_1 2_1 2_1
Cell dimensions	
a, *b*, *c* (Å)	52.20, 97.95, 287.99
a, b, g (°)	90, 90, 90
Resolution (Å)	92.73 – 2.49 (2.57 – 2.49)
R_{pim}	0.070 (0.735)
Total Reflections	99952 (8634)
Unique Reflections	52982 (4488)
$CC_{1/2}$	0.993 (0.463)
I / sI	5.7 (0.7)
Completeness (%)	100 (100)
Redundancy	1.9 (1.9)
Refinement	
No. reflections	52884
R_{work} / R_{free}	0.198 / 0.225
No. Atoms	
Protein	6011
Ligand/ion	n/a
Water	250
B-values (Å^2)	
Average B-factors	67.0
Protein	68.0
Ligand	n/a
Water	59.2
Wilson B-value	56.4
R.m.s. deviations	
Bond lengths (Å)	0.008
Bond angles (°)	0.985
Ramachandran Plots(%)	
Favoured	96.3
Allowed	3.7
Outliers	0

Numbers in parentheses refer to the highest resolution shell.

$R_{merge} = \Sigma_{hkl} \Sigma_i | I_{hkl,i} - \langle I_{hkl} \rangle | / \Sigma_{hkl} \Sigma_i I_{hkl,i}$ and $R_{meas} = \Sigma_{hkl} (n/(n-1))^{1/2} \Sigma_i | I_{hkl,i} - \langle I_{hkl} \rangle | / \Sigma_{hkl} \Sigma_i I_{hkl,I}$ and $R_{pim} = \Sigma_{hkl} (1/(n-1))^{1/2} \Sigma_i | I_{hkl,i} - \langle I_{hkl} \rangle | / \Sigma_{hkl} \Sigma_i I_{hkl,i}$, where $I_{hkl,i}$ is the scaled intensity of the ith measurement of reflection h, k, l, $\langle I_{hkl} \rangle$ is the average intensity for that reflection, and n is the redundancy.

$CC_{1/2}$ = Pearson correlation coefficient between two random half datasets.

$R_{work} = \Sigma_{hkl} | F_o - F_c | / \Sigma_{hkl} | F_o |$ x 100, where F_o and F_c are the observed and calculated structure factors, respectively.

R_{free} was calculated as for R_{work}, but on a test set comprising 5% of the data excluded from refinement.

5.6 References

1. Battle, K. E. *et al.* Mapping the global endemicity and clinical burden of *Plasmodium vivax*, 2000–17: a spatial and temporal modelling study. *The Lancet* **394**, 332–343 (2019).
2. Kumar, R., Agarwal, D. & Kumar, P. Severe *Plasmodium vivax* Malaria in Children: An emerging threat. *J Pediat Sci* **6**, (2014).
3. Naha, K., Dasari, S. & Prabhu, M. Spectrum of complications associated with *Plasmodium vivax* infection in a tertiary hospital in South–Western India. *Asian Pac J Trop Med* **5**, 79–82 (2012).
4. Hulden, L. & Hulden, L. Activation of the hypnozoite: A part of *Plasmodium vivax* life cycle and survival. *Malar J* **10**, 90 (2011).
5. Wells, T. N. C., Burrows, J. N. & Baird, J. K. Targeting the hypnozoite reservoir of *Plasmodium vivax*: the hidden obstacle to malaria elimination. *Trends Parasitol* **26**, 145–151 (2010).
6. Robinson, L. J. *et al.* Strategies for Understanding and Reducing the *Plasmodium vivax* and *Plasmodium ovale* Hypnozoite Reservoir in Papua New Guinean Children: A Randomised Placebo-Controlled Trial and Mathematical Model. *PLoS Med* **12**, e1001891 (2015).
7. Nascimento, J. R. *et al.* Prevalence of glucose 6-phosphate dehydrogenase deficiency in highly malaria-endemic municipalities in the Brazilian Amazon: A region-wide screening study. *The Lancet Regional Health - Americas* **12**, 100273 (2022).
8. Adams, J. H. *et al.* A family of erythrocyte binding proteins of malaria parasites. *Proc Natl Acad Sci* **89**, 7085–7089 (1992).
9. Singh, S. K., Hora, R., Belrhali, H., Chitnis, C. E. & Sharma, A. Structural basis for Duffy recognition by the malaria parasite Duffy-binding-like domain. *Nature* **439**, 741–744 (2005).
10. Otsuki, H. *et al.* Single amino acid substitution in *Plasmodium yoelii* erythrocyte ligand determines its localization and controls parasite virulence. *Proc Natl Acad Sci U S A* **106**, 7167–7172 (2009).
11. Tournamille, C. *et al.* Structure–function analysis of the extracellular domains of the Duffy antigen/receptor for chemokines: characterization of antibody and chemokine binding sites. *Br J Haematol* **122**, 1014–1023 (2003).
12. King, C. L. *et al.* Fya/Fyb antigen polymorphism in human erythrocyte duffy antigen affects susceptibility to *Plasmodium vivax* malaria. *Proc Natl Acad Sci* **108**, 20113–20118 (2011).
13. Cavasini, C. E. *et al.* Duffy blood group gene polymorphisms among malaria vivax patients in four areas of the Brazilian Amazon region. *Malar J* **6**, a167 (2007).
14. Langhi, D. M. & Bordin, J. O. Duffy blood group and malaria. *https://doi.org/10.1080/10245330500469841* **11**, 389–398 (2013).
15. Choe, H. *et al.* Sulphated tyrosines mediate association of chemokines and *Plasmodium vivax* Duffy binding protein with the Duffy antigen/receptor for chemokines (DARC). *Mol Microbiol* **55**, 1413–1422 (2005).

16. Batchelor, J. D., Zahm, J. A. & Tolia, N. H. Dimerization of *Plasmodium vivax* DBP is induced upon receptor binding and drives recognition of DARC. *Nat Struct Mol Biol* **18**, 908–914 (2011).
17. Michon, P., Fraser, T. & Adams, J. H. Naturally acquired and vaccine-elicited antibodies block erythrocyte cytoadherence of the *Plasmodium vivax* Duffy binding protein. *Infect Immun* **68**, 3164–3171 (2000).
18. Grimberg, B. T. *et al. Plasmodium vivax* Invasion of Human Erythrocytes Inhibited by Antibodies Directed against the Duffy Binding Protein. *PLoS Med* **4**, e337 (2007).
19. Moreno, A. *et al.* Preclinical assessment of the receptor-binding domain of *Plasmodium vivax* Duffy-binding protein as a vaccine candidate in rhesus macaques. *Vaccine* **26**, 4338–4344 (2008).
20. Payne, R. O. *et al.* Human vaccination against *Plasmodium vivax* Duffy-binding protein induces strain-transcending antibodies. *JCI Insight* **2**, e93683 (2017).
21. Singh, K. *et al.* Malaria vaccine candidate based on Duffy-binding protein elicits strain transcending functional antibodies in a Phase I trial. *NPJ Vaccines* **3**, 48 (2018).
22. Sampath, S. *et al.* Glycan Masking of *Plasmodium vivax* Duffy Binding Protein for Probing Protein Binding Function and Vaccine Development. *PLoS Pathog* **9**, e1003420 (2013).
23. Ntumngia, F. B. & Adams, J. H. Design and immunogenicity of a novel synthetic antigen based on the ligand domain of the *Plasmodium vivax* Duffy binding protein. *Clinical and Vaccine Immunology* **19**, 30–36 (2012).
24. Chen, E., Salinas, N. D., Ntumngia, F. B., Adams, J. H. & Tolia, N. H. Structural Analysis of the Synthetic Duffy Binding Protein (DBP) Antigen DEKnull Relevant for *Plasmodium vivax* Malaria Vaccine Design. *PLoS Negl Trop Dis* **9**, e0003644 (2015).
25. Ntumngia, F. B. *et al.* Immunogenicity of a synthetic vaccine based on *Plasmodium vivax* Duffy binding protein region II. *Clinical and Vaccine Immunology* **21**, 1215–1223 (2014).
26. Rawlinson, T. A. *et al.* Structural basis for inhibition of *Plasmodium vivax* invasion by a broadly neutralizing vaccine-induced human antibody. *Nat Microbiol* **4**, 1497–1507 (2019).
27. Chen, E. *et al.* Broadly neutralizing epitopes in the *Plasmodium vivax* vaccine candidate Duffy Binding Protein. *Proc Natl Acad Sci* **113**, 6277–6282 (2016).
28. Urusova, D. *et al.* Structural basis for neutralization of *Plasmodium vivax* by naturally acquired human antibodies that target DBP. *Nat Microbiol* **4**, 1486–1496 (2019).
29. Withers-Martinez, C. *et al.* Malarial EBA-175 Region VI Crystallographic Structure Reveals a KIX-Like Binding Interface. *J Mol Biol* **375**, 773–781 (2008).
30. Batchelor, J. D. *et al.* Red Blood Cell Invasion by *Plasmodium vivax*: Structural Basis for DBP Engagement of DARC. *PLoS Pathog* **10**, e1003869 (2014).
31. Wiedemann, C., Bellstedt, P. & Görlach, M. CAPITO—a web server-based analysis and plotting tool for circular dichroism data. *Bioinformatics* **29**, 1750–1757 (2013).

32. Batchelor, J. D. *et al.* Red Blood Cell Invasion by *Plasmodium vivax*: Structural Basis for DBP Engagement of DARC. *PLoS Pathog* **10**, (2014).
33. Moskovitz, R. & Pholcharee, T., *et al*. Structural basis for DARC binding in reticulocyte invasion by Plasmodium vivax. *Nat Comms **14***, 3637 (2023).
34. Ovchynnikova, E. *et al.* DARC extracellular domain remodeling in maturating reticulocytes explains *Plasmodium vivax* tropism. *Blood* **130**, 1441–1444 (2017).
35. Kabsch, W. XDS. *Acta Cryst* **66**, 132 (2010).
36. Evans, P. Scaling and assessment of data quality. *Acta Cryst* **D62**, 72–82 (2005).
37. McCoy, A. J. *et al.* Phaser crystallographic software. *J Appl Crystallogr* **40**, 674 (2007).
38. Bricogne G., B. E. , B. M. , F. C. , K. P. , P. W. and R. P. S. A. , S. O. S. , V. C. 'BUSTER version 2.10.4'''. *Cambridge, United Kingdom: Global Phasing Ltd.* (2017).
39. Emsley, P. & Cowtan, K. Coot: model-building tools for molecular graphics. *Acta crystallogr* **D60**, 2126–2132 (2004).

CHAPTER 6:
Concluding Remarks

6.1 Concluding remarks

In 1984, the nucleotide sequence of the gene encoding the *Plasmodium falciparum* circumsporozoite protein was isolated from a bacterial gene display library through its detection by a monoclonal antibody, opening the door for recombinant protein vaccine development targeting the malaria liver stage(1). The ensuing rush to characterize the immunogenic potential of the major B cell epitopes of the circumsporozoite protein has produced the only currently approved malaria vaccine, RTS,S, which began its development in the late 1980s, only gaining WHO approval in 2021(2). Long before its approval, it was known that RTS,S vaccination possessed an integral problem: antibody titres and protective efficacy wane rapidly following vaccination(3). Therefore, even before the approval of RTS,S, the race for an improved second-generation vaccine was afoot.

It was not until 2017 that the first X-ray crystal structures of human monoclonal antibodies in complex with peptides derived from the CSP major repeat region were published from the Wilson lab(4), followed very shortly thereafter from the Julien lab (5), revealing conserved characteristics in binding the NANP major repeat epitope(6). Since then, multiple publications concerning homotypic interactions between the Fabs of repeat-targeting mAbs in complex with rsCSP or NANP repeat peptides (7–10) have revealed them to be a source of increased antibody avidity, producing sterile protection in mouse models. However, the limited B-cell receptor repertoire stimulated by NANP repeats(9), together with their compositional simplicity, have raised concerns that they act as a decoy, preventing or diminishing an immune response to other protective epitopes

on CSP (11). Indeed, the continued isolation of monoclonal antibodies from sporozoite immunization have revealed the junctional epitope (12,13) and the minor repeat epitope (14,15) as targets of highly protective antibodies both in animal models and clinical settings.

The same enthusiasm did not extend towards the N-terminal domain and C-terminal domain of CSP, and only a few monoclonal antibodies that bind the N-terminal(16,17) and C-terminal (18,19) domains have been structurally characterized. Through our structural characterization mAbs targeting the N-terminal domain of CSP, we revealed they provide protection by mouse liver burden and bind to two novel epitopes as well as a previous epitope. Through our structural characterization of MAL071 mAbs, we revealed the breadth of antibody lineages encoding mAbs targeting the C-terminal domain of CSP: the previously described α-epitope and well as the conserved β-epitope, as well as a new epitope targeted by mAb 1504. Despite the promise of the β-epitope to produce strain-transcending antibody response, mAbs targeting the αTSR domain do not to date provide comparable protection to mAbs targeting the major repeats, minor repeats, or junctional epitope.

Accordingly, most second-generation CSP vaccine designs now focus on improving antibody titres and avidity towards highly protective major repeat and junctional epitope (20–24). Through characterization of novel epitopes on both the N- and C-terminus of CSP, we have shown that other CSP epitopes may provide protection, and their incorporation in future immunogen design should be investigated. Until then, we cannot

rule out the potential protective benefits of including these epitopes alone, or alongside more protective epitopes, in second generation-vaccine design. In the absence of evidence to suggest these novel epitopes diminish the immune response to more protective epitopes, second-generation vaccine designs stand only to profit by including multiple epitopes to capture a broader immunological response.

The ability to fully contextualize the determinants of a successful immune response against *Plasmodium* vaccine antigens demands an understanding of their native conformations and mechanisms of physiological action. Using a panel of N-terminal CSP haplotypes, we revealed that antibodies targeting conserved N-terminal epitopes are susceptible to polymorphisms distant from their binding site, suggesting potential secondary structural elements in the CSP N-terminal domain. The suggestion of secondary structural elements in CSP and epitope masking joins the existing body of work that suggests that the CSP protein undergoes conformational transitions during parasite development in the mosquito and in the human host(25,26). N-terminal domain cleavage is integral to the switch from a migratory to an invasive phenotype, and transgenic parasites expressing a cleaved N-terminal domain are sensitized to inhibition by C-terminal targeting antibodies. Recently, binding of major and minor repeat-targeting mAbs has been shown unmask the C-terminal domain of CSP and increased the binding of C-terminal mAbs(27). However, this did not result in increased protection in the mouse liver burden assay. Transgenic parasites expressing CSP with a cleaved N-terminal domain fail to leave the intradermal injection site, while they successfully establish an infection if injected intravenously. CSP-binding mAbs have been shown to act in the skin

(28,29), and therefore assessing the inhibitory effects of N-terminal and C-terminal mAbs by IV injection, as routinely performed in the livery burden assay, could provide different results to intradermal injection.

The discrepancy between the ability of the mouse liver burden model to account for observed correlates of protection from the MAL071 trial might suggest antibodies targeting different epitopes on CSP could provide protection through different mechanisms that do not translate to the mouse model. Antibodies targeting the CSP N-terminal and C-terminal domains have been shown to fix complement C1q, a correlate of protection in both RTS,S vaccinees and PNG children(30–33). Other Fc related effector functions have also been suggested to mediate protection (34–36). The sequence conservation of some CSP epitopes and not others suggests that they participate in interactions that are beneficial to parasite survival, as their sequence conservation comes as the cost of vulnerability to strain-transcending immune responses. The conserved N-terminal epitope targeted by mAbs 3A3 and mNCSP9 and mNCSP10 described in this thesis has recently been shown to bind the negative complement regulator C4b-binding protein (37), and CSP has been shown to suppress the protective respiratory burst of Kupffer cells(38). It is therefore not unreasonable to assume that other epitopes of CSP may be involved in other immunomodulatory activities. While mAbs which target epitopes with immunomodulatory activities may not provide protection on their own, they could act synergistically by sensitizing parasites to more inhibitory mAbs.

In addition to our choice of protection model, the characterization of antibody responses and binding interactions that contribute to invasion can also be confounded by our choices of *in vitro* expression systems. Through the characterization of a panel of mAbs targeting the CSP C-terminus from the MAL071 trial, we revealed a new epitope targeted by mAb 1504 that is the target of O-fucosylation(39–42). Our structure lacks O-fucosylation as our αTSR protein is expressed in bacterial cells. However, it is unclear whether RTS,S contains this post-translational modification, whether αTSR O-fucosylation is a target of protective immunity, or whether O-fucosylation alters the conformation of CSP on the sporozoite surface. The importance of post-translational modifications in host-pathogen interactions is clear from the importance of tyrosine sulphation of the CCR5 receptor for its binding to the HIV envelope trimer(43), sialic acid on receptors of influenza haemagglutinin(44), and now also from the binding of PvDBP-RII to the sulphated DARC ectodomain(45). In addition to post-translational modifications, the expression systems used to produce antigens can affect our ability to discern the mechanisms of host-pathogen interactions. Using PvDBP-RII from mammalian cell expression, our colleague Tossapol Pholcharee (Higgins lab) showed that the dimerization proposed using PvDBP-RII from bacterial sources does not occur with protein purified from mammalian culture. While many groups use CSP expressed in bacterial sources, RTS,S is produced by batch fermentation in yeast, and it may be the case that CSP produced in bacteria, yeast, and on the sporozoite surface display different conformations and differently present inhibitory epitopes. Uncovering the potential confounding effects of using different expression systems on our characterization of host-pathogen interaction is therefore crucial to our

understanding of the physiological role of different epitopes in invasion processes and their potential as vaccine components.

Although the gene encoding PvDBP was discovered in 1992(46), the difficulties in maintaining *in vitro P. vivax* cultures have hampered the investigation of *P. vivax* biology and by extension inhibitory antibodies targeting PvDBP. Therefore, compared to PfCSP, far fewer monoclonal antibodies have been characterized to bind PvDBP-RII(47–50), and the field is in its relative infancy. The continued structural characterization of the fine epitopes of both inhibitory and non-inhibitory antibodies is required to build up our understanding of the immunological landscape provided by PvDBP-RII vaccination. Second generation vaccine design has already focused on targeting the polymorphic DEK motif(51), and our crystal structure of DB1 in complex with this polymorphic epitope reasserts the need for an improved second-generation vaccine design that can produce a strain-transcending antibody response.

Much like the case for PfCSP, conserved epitopes on PvDBP-RII also imply participation in interactions valuable enough to the invasion process to risk a strain-transcending antibody response. One such example is subdomain 3 of PvDBP-RII, which is not currently known to be involved in PvDBP-RII-DARC interaction and is the target of protective antibodies(50). Subdomain 3 of PvDBP-RII may participate in yet uncharacterized parts of the PvDBP-DARC invasion-competent complex or bind a new interaction partner altogether. Structural prediction software RaptorX predicts secondary structural elements in PvDBP beyond RII, in agreement with our preliminary

characterization of the full-length PvDBP ectodomain. In the orthologous *P. yoleii* PyEBL Region VI, a single amino acid mutation altered the erythrocyte binding preferences of the parasite(52). Considering the restrictive erythrocyte preference of *P. vivax*(53), and it may also be the case that other domains in the full length PvDBP impart such invasion selectivity by recruiting novel binding partners or participating in the complete PvDBP-DARC interaction.

Previously, the lack of antibodies characterized to bind different epitopes on the N- and C-termini of CSP, as well as PvDBP-RII, limited our ability to pinpoint epitope-specific mechanisms of protection on either *Plasmodium* vaccine antigen. The antibody structures, receptor engagement mechanisms, and recombinant proteins described herein comprise a molecular toolkit that can be used to assess the importance of specific epitopes in processes of invasion, migration, and immunomodulatory activities, and therefore their protective potential in order to inform second-generation vaccine design.

6.2 References

1. Enea, V. *et al.* DNA Cloning of *Plasmodium falciparum* Circumsporozoite Gene: Amino Acid Sequence of Repetitive Epitope. *Science (1979)* **225**, 628–630 (1984).
2. Nadeem, A. Y., Shehzad, A., Islam, S. U., Al-Suhaimi, E. A. & Lee, Y. S. Mosquirix™ RTS, S/AS01 Vaccine Development, Immunogenicity, and Efficacy. *Vaccines (Basel)* **10**, 1033–1039 (2022).
3. White, M. T. *et al.* Immunogenicity of the RTS,S/AS01 malaria vaccine and implications for duration of vaccine efficacy: secondary analysis of data from a phase 3 randomised controlled trial. *Lancet Infect Dis* **15**, 1450–1458 (2015).
4. Oyen, D. *et al.* Structural basis for antibody recognition of the NANP repeats in *Plasmodium falciparum* circumsporozoite protein. *Proc Natl Acad Sci* **114**, E10438–E10445 (2017).
5. Triller, G. *et al.* Natural Parasite Exposure Induces Protective Human Anti-Malarial Antibodies. *Immunity* **47**, 1197-1209.e10 (2017).
6. Pholcharee, T. *et al.* Structural and biophysical correlation of anti-NANP antibodies with in vivo protection against *P. falciparum*. *Nat Commun* **12**, 1063 (2021).
7. Oyen, D. *et al.* Cryo-EM structure of *P. falciparum* circumsporozoite protein with a vaccine-elicited antibody is stabilized by somatically mutated inter-Fab contacts. *Sci Adv* **4**, 8529 (2018).
8. Kucharska, I. *et al.* High-density binding to *Plasmodium falciparum* circumsporozoite protein repeats by inhibitory antibody elicited in mouse with human immunoglobulin repertoire. *PLoS Pathog* **18**, e1010999 (2022).
9. Fisher, C. R. *et al.* T-dependent B cell responses to *Plasmodium* induce antibodies that form a high-avidity multivalent complex with the circumsporozoite protein. *PLoS Pathog* **13**, e1006469 (2017).
10. Martin, G. M. *et al.* Affinity-matured homotypic interactions induce spectrum of PfCSP-antibody structures that influence protection from malaria infection. *bioRxiv* 2022.09.20.508747 (2022) doi:10.1101/2022.09.20.508747.
11. Chatterjee, D. *et al.* Avid binding by B cells to the *Plasmodium* circumsporozoite protein repeat suppresses responses to protective subdominant epitopes. *Cell Rep* **35**, 108996 (2021).
12. Oyen, D. *et al.* Structure and mechanism of monoclonal antibody binding to the junctional epitope of *Plasmodium falciparum* circumsporozoite protein. *PLoS Pathog* **16**, (2020).
13. Kisalu, N. K. *et al.* A human monoclonal antibody prevents malaria infection and defines a new site of vulnerability on *Plasmodium falciparum* circumsporozoite protein. *Nat Med* **24**, 408 (2018).
14. Wang, L. T. *et al.* A potent anti-malarial human monoclonal antibody targets circumsporozoite protein minor repeats and neutralizes sporozoites in the liver. *Immunity* **53**, 733 (2020).
15. Martin, G. M. *et al.* Structural basis of epitope selectivity and potent protection from malaria by PfCSP antibody L9. *bioRxiv* (2022) doi:10.1101/2022.10.07.511358.

16. Thai, E. *et al.* A high-affinity antibody against the CSP N-terminal domain lacks *Plasmodium falciparum* inhibitory activity. *J Exp Med* **217**, e20200061 (2020).
17. Tan, J. *et al.* Functional human IgA targets a conserved site on malaria sporozoites. *Sci Transl Med* **13**, eabg2344 (2021).
18. Beutler, N. *et al.* A novel CSP C-terminal epitope targeted by an antibody with protective activity against *Plasmodium falciparum*. *PLoS Pathog* **18**, e1010409 (2022).
19. Scally, S. W. *et al.* Rare PfCSP C-terminal antibodies induced by live sporozoite vaccination are ineffective against malaria infection. *J Exp Med* **215**, 63 (2018).
20. Langowski, M. D. *et al.* Optimization of a *Plasmodium falciparum* circumsporozoite protein repeat vaccine using the tobacco mosaic virus platform. *Proc Nat Acad Sci* **117**, 3114–3122 (2020).
21. Jelínková, L. *et al.* An epitope-based malaria vaccine targeting the junctional region of circumsporozoite protein. *NPJ Vaccines* **6**, (2021).
22. Langowski, M. D. *et al.* Restricted valency (NPNA)n repeats and junctional epitope-based circumsporozoite protein vaccines against *Plasmodium falciparum*. *NPJ Vaccines* **7**, 13 (2022).
23. Atcheson, E., Hill, A. V. S. & Reyes-Sandoval, A. A VLP for validation of the *Plasmodium falciparum* circumsporozoite protein junctional epitope for vaccine development. *npj Vaccines 2021 6:1* **6**, 1–9 (2021).
24. Francica, J. R. *et al.* Design of Alphavirus Virus-Like Particles Presenting Circumsporozoite Junctional Epitopes That Elicit Protection against Malaria. *Vaccines (Basel)* **9**, 287 (2021).
25. Herrera, R. *et al.* Reversible Conformational Change in the *Plasmodium falciparum* Circumsporozoite Protein Masks Its Adhesion Domains. *Infect Immun* **83**, 3771 (2015).
26. Coppi, A. *et al.* The malaria circumsporozoite protein has two functional domains, each with distinct roles as sporozoites journey from mosquito to mammalian host. *J Exp Med* **208**, 341–356 (2011).
27. Wang, L. T. *et al.* Protective effects of combining monoclonal antibodies and vaccines against the *Plasmodium falciparum* circumsporozoite protein. *PLoS Pathog* **17**, e1010133 (2021).
28. Aliprandini, E. *et al.* Cytotoxic anti-circumsporozoite antibodies target malaria sporozoites in the host skin. *Nature Microbiology 2018 3:11* **3**, 1224–1233 (2018).
29. Flores-Garcia, Y. *et al.* Antibody-Mediated Protection against *Plasmodium* Sporozoites Begins at the Dermal Inoculation Site. *mBio* **9**, e02194-18 (2018).
30. Kurtovic, L. *et al.* Human antibodies activate complement against *Plasmodium falciparum* sporozoites, and are associated with protection against malaria in children. *BMC Med* **16**, 1–17 (2018).
31. Kurtovic, L. *et al.* Induction and decay of functional complement-fixing antibodies by the RTS,S malaria vaccine in children, and a negative impact of malaria exposure. *BMC Med* **17**, 1–14 (2019).
32. Kurtovic, L. *et al.* Complement in malaria immunity and vaccines. *Immunol Rev* **293**, 38–56 (2020).

33. Kurtovic, L., Drew, D. R., Dent, A. E., Kazura, J. W. & Beeson, J. G. Antibody Targets and Properties for Complement-Fixation Against the Circumsporozoite Protein in Malaria Immunity. *Front Immunol* **12**, 775659 (2021).
34. Das, J. *et al.* Delayed fractional dosing with RTS,S/AS01 improves humoral immunity to malaria via a balance of polyfunctional NANP6- and Pf16-specific antibodies. *Med* **2**, 1269-1286.e9 (2021).
35. Feng, G. *et al.* Mechanisms and targets of Fcγ-receptor mediated immunity to malaria sporozoites. *Nat Commun* **12**, 1–16 (2021).
36. Kurtovic, L. *et al.* Multifunctional Antibodies Are Induced by the RTS,S Malaria Vaccine and Associated With Protection in a Phase 1/2a Trial. *J Infect Dis* **224**, 1138 (2021).
37. Khattab, A. *et al.* Hijacking the human complement inhibitor C4b-binding protein by the sporozoite stage of the *Plasmodium falciparum* parasite. *Front Immunol* **13**, (2022).
38. Usynin, I., Klotz, C. & Frevert, U. Malaria circumsporozoite protein inhibits the respiratory burst in Kupffer cells. *Cell Microbiol* **9**, 2610–2628 (2007).
39. Payne, R. O. *et al.* Human vaccination against *Plasmodium* vivax Duffy-binding protein induces strain-transcending antibodies. *JCI Insight* **2**, e93683 (2017).
40. Singh, K. *et al.* Malaria vaccine candidate based on Duffy-binding protein elicits strain transcending functional antibodies in a Phase I trial. *NPJ Vaccines* **3**, 48 (2018).
41. Swearingen, K. E. *et al.* Interrogating the *Plasmodium* Sporozoite Surface: Identification of Surface-Exposed Proteins and Demonstration of Glycosylation on CSP and TRAP by Mass Spectrometry-Based Proteomics. *PLoS Pathog* **12**, e1005606 (2016).
42. Lopaticki, S. *et al.* Protein O-fucosylation in *Plasmodium falciparum* ensures efficient infection of mosquito and vertebrate hosts. *Nature Communications 2017 8:1* **8**, 1–10 (2017).
43. Farzan, M. *et al.* Tyrosine sulfation of the amino terminus of CCR5 facilitates HIV-1 entry. *Cell* **96**, 667–676 (1999).
44. Weis, W. *et al.* Structure of the influenza virus haemagglutinin complexed with its receptor, sialic acid. *Nature* **333**, 426–431 (1988).
45. Moskovitz, R. & Pholcharee, T., *et al*. Structural basis for DARC binding in reticulocyte invasion by Plasmodium vivax. *Nat Comms **14***, 3637 (2023).
46. Adams, J. H. *et al.* A family of erythrocyte binding proteins of malaria parasites. *Proc Natl Acad Sci* **89**, 7085–7089 (1992).
47. Valizadeh, V., Zakeri, S., Mehrizi, A. A., Mirkazemi, S. & Djadid, N. D. Natural acquired inhibitory antibodies to *Plasmodium vivax* Duffy binding protein (PvDBP-II) equally block erythrocyte binding of homologous and heterologous expressed PvDBP-II on the surface of COS-7 cells. *Med Microbiol Immunol* **205**, 85–95 (2016).
48. Ntumngia, F. B. *et al.* Conserved and variant epitopes of *Plasmodium vivax* duffy binding protein as targets of inhibitory monoclonal antibodies. *Infect Immun* **80**, 1203–1208 (2012).

49. Carias, L. L. *et al.* Identification and Characterization of Functional Human Monoclonal Antibodies to *Plasmodium vivax* Duffy-Binding Protein. *The Journal of Immunology* **202**, 2648–2660 (2019).
50. Rawlinson, T. A. *et al.* Structural basis for inhibition of *Plasmodium vivax* invasion by a broadly neutralizing vaccine-induced human antibody. *Nat Microbiol* **4**, 1497–1507 (2019).
51. Chen, E., Salinas, N. D., Ntumngia, F. B., Adams, J. H. & Tolia, N. H. Structural Analysis of the Synthetic Duffy Binding Protein (DBP) Antigen DEKnull Relevant for *Plasmodium vivax* Malaria Vaccine Design. *PLoS Negl Trop Dis* **9**, e0003644 (2015).
52. Otsuki, H. *et al.* Single amino acid substitution in *Plasmodium yoelii* erythrocyte ligand determines its localization and controls parasite virulence. *Proc Natl Acad Sci U S A* **106**, 7167–7172 (2009).
53. Thomson-Luque, R. & Bautista, J. M. Home Sweet Home: *Plasmodium vivax*-Infected Reticulocytes—The Younger the Better? *Front Cell Infect Microbiol* **11**, e675156 (2021).

APPENDIX 1:

C.V.

Re'em Moskovitz

Department of Integrative Structural and Computational Biology
The Scripps Research Institute
10550 North Torrey Pines Road, La Jolla, CA 92037
Email: rmoskovitz@scripps.edu Email: reem.moskovitz@gmail.com

Education

The Scripps Research Institure, La Jolla, CA 2021-2023
PhD in Biochemistry
Thesis: Structural Investigation of Receptor Engagement and Monoclonal Antibodies Targeting *Plasmodium* Vaccine Antigens
Advisor: Prof. Ian A. Wilson

University of Oxford, Oxford, UK 2018-2021
DPhil in Biochemistry
Thesis: Structural Investigation of Receptor Engagement and Monoclonal Antibodies Targeting *Plasmodium* Vaccine Antigens
Advisor: Prof. Matthew K. Higgins

University of Oxford, Oxford, UK 2013-2017
MBiochem
Thesis: Bispecific antibodies targeting metastatic breast cancer
Supervisor: Max Crispin

Employment and research

The Scripps Research Institute, La Jolla, CA 2021-2023
Graduate student, Laboratory of Ian A. Wilson

- Structural characterization of antibodies targeting the *P. falciparum* circumsporozoite protein.

University of Oxford, Oxford, UK 2018-2021
Graduate student, Laboratory of Matthew K. Higgins

- Structural characterization of *P. vivax* duffy binding protein in complex with inhibitory antibodies and its receptor DARC.

University of Oxford, Oxford, UK 2017-2018
Graduate student, Laboratory of Nicole Zitzmann

- Characterization of iminosugar impact on flavivirus NS1 secretion

University of Oxford, Oxford, UK 2016-2017
Masters student, Laboratory of Max Crispin

- Design and characterization of bispecific antibodies targeting metastatic breast cancer cell lines using aberrant glycosylation

Publications

Moskovitz, R., Pholcharee, T., DonVito, S. M., Guloglu, B., Lowe, E., Mohring, F., Moon, R. W., & Higgins, M. K. Structural basis for DARC binding in reticulocyte invasion by Plasmodium vivax. *Nat Comms **14***, 3637 (2023).

Awards

Skaggs-Oxford Scholarship 2017-2023
Undergraduate scholarship, Christ Church, Oxford 2017

APPENDIX 2:

Publications

nature communications

Article

https://doi.org/10.1038/s41467-023-39357-w

Structural basis for DARC binding in reticulocyte invasion by *Plasmodium vivax*

Received: 28 February 2023

Accepted: 6 June 2023

Published online: 19 June 2023

Check for updates

Re'em Moskovitz[1,3], Tossapol Pholcharee[1,3], Sophia M. DonVito[2], Bora Guloglu[1], Edward Lowe[1], Franziska Mohring[2], Robert W. Moon[2] & Matthew K. Higgins[1]

The symptoms of malaria occur during the blood stage of infection, when the parasite replicates within human red blood cells. The human malaria parasite, *Plasmodium vivax*, selectively invades reticulocytes in a process which requires an interaction between the ectodomain of the human DARC receptor and the *Plasmodium vivax* Duffy-binding protein, PvDBP. Previous studies have revealed that a small helical peptide from DARC binds to region II of PvDBP (PvDBP-RII). However, it is also known that sulphation of tyrosine residues on DARC affects its binding to PvDBP and these residues were not observed in previous structures. We therefore present the structure of PvDBP-RII bound to sulphated DARC peptide, showing that a sulphate on tyrosine 41 binds to a charged pocket on PvDBP-RII. We use molecular dynamics simulations, affinity measurements and growth-inhibition experiments in parasites to confirm the importance of this interaction. We also reveal the epitope for vaccine-elicited growth-inhibitory antibody DB1. This provides a complete understanding of the binding of PvDBP-RII to DARC and will guide the design of vaccines and therapeutics to target this essential interaction.

In many regions of the world, *Plasmodium vivax* is the predominant parasite that causes human malaria. Leading to around 14.5 million diagnosed cases each year, it accounted for an estimated 61% of malaria in the Americas and 48% in South East Asia in 2017[1]. With studies suggesting that the impact of this parasite is underestimated[2,3], morbidity caused by *P. vivax* is a major global health problem and an effective vaccine is urgently required to contribute to the malaria eradication effort.

The symptoms of malaria occur when parasites replicate within the blood. In the case of *P. vivax*, invasion of red blood cells is highly dependent on the reticulocyte Duffy antigen/receptor for chemokines (DARC). The importance of DARC as an invasion receptor[4] was first shown over 45 years ago, with the demonstration that the related parasite, *Plasmodium knowlesi*, is unable to invade blood cells taken from individuals with the Duffy-negative phenotype[5]. These people have a mutation in their DARC gene which makes the receptor undetectable on circulating reticulocytes. Duffy negativity was also found to prevent African-Americans from being infected with *P. vivax* through mosquito bite[6]. The widespread prevalence of *P. vivax* across the world, together with its much-reduced occurrence in regions of Africa where Duffy-negativity is widespread, highlight the importance of DARC as a determinant of *P. vivax* susceptibility[7]. Indeed, while *P. vivax* is occasionally capable of infecting Duffy-negative individuals, this is linked to lower parasite load and more than 15-fold reduced likelihood of causing clinical disease[8–10]. Preventing DARC-mediated invasion remains a primary approach to prevent clinical vivax malaria.

The parasite binding partner for DARC is the Duffy binding protein, PvDBP[11] and multiple lines of evidence highlight the important nature of their interaction. In the closely related, genetically tractable parasite, *P. knowlesi*, knockout of PkDBPα prevents invasion of Duffy-positive erythrocytes in vitro[12–14]. While PvDBP knockout in *P. vivax* has not been technically possible, due to challenges with maintaining this parasite in culture conditions, immunisation of mice, rabbits and non-human primates with the RII region of PvDBP (PvDBP-RII) induces

[1]Department of Biochemistry, University of Oxford, South Parks Road, Oxford OX1 3QU, UK. [2]London School of Hygiene and Tropical Medicine, Keppel Street, London WC1E 7HT, UK. [3]These authors contributed equally: Re'em Moskovitz, Tossapol Pholcharee. e-mail: matthew.higgins@bioch.ox.ac.uk

inhibitory antibodies that block binding of PvDBP to DARC[15,16]. In humans, high titres of naturally acquired antibodies that target PvDBP-RII and prevent DARC binding in vitro, are associated with reduced risk of *P. vivax* infection[17], lower parasite densities following invasion and decreased risk of clinical malaria[18,19]. Immunisation of human volunteers with recombinant viral vectors expressing PvDBP-RII induces strain-transcending antibodies which prevent recombinant PvDBP-RII from binding to DARC while human antibodies, derived from either vaccination or natural infection, are inhibitory of invasion[13,20]. PvDBP is therefore the primary blood stage vaccine candidate to prevent vivax malaria.

With both intact PvDBP and DARC proving challenging to produce, molecular studies have used smaller fragments to narrow down functionally important regions[21], with a ~ 350 amino acid residue Duffy-binding-like (DBL) domain known as PvDBP-RII, shown to bind DARC[22]. PvDBP-RII binds to the sixty-residue N-terminal ectodomain of DARC[23]. The first structural study related to PvDBP was a crystal structure of PkDBP-RII, from *P. knowlesi*[24]. This was followed by structures of *Plasmodium vivax* DBP-RII bound to a 30 residue-long peptide ($DARC_{14-43}$), of which 11 residues ($DARC_{19-30}$) were ordered and were observed in the structure as a helical peptide[25].

However, DARC is post-translationally modified by sulfation of two tyrosine residues, Y30 and Y41 and mutation of Y41 to phenylalanine reduced PvDBP binding[26]. These residues are not observed in existing structures, most likely because the DARC ectodomain used was bacterially expressed and therefore lacked tyrosine sulfation[26,27]. Studies of *P. knowlesi* DBP-RII also proposed the locations for binding sites of the sulfated tyrosines, with positively charged patches on PkDBP-RII suggested to form the binding sites for Y41[24] and Y30[28]. Indeed, a later refinement of the PkDBP-RII structure showed a sulfate ion bound in the proposed binding site for Y41[28]. Mutations have also been described in regions of PvDBP which do not contact $DARC_{19-30}$ but which are known to contribute to full-length DARC binding[29,30] and a polymorphism in residue 42 of DARC is the sole change in the Fy^a blood group, which reduces the likelihood and severity of *P. vivax* infection[31]. Indeed, NMR experiments indicate that residues from 14-43 of DARC show chemical shifts on binding to PvDBP-RII[25]. The full interaction between PvDBP and DARC therefore remains to be defined.

Structural approaches have also started to reveal how the PvDBP-DARC interaction can be blocked by mouse and human monoclonal antibodies. Two human monoclonals bind the region of PvDBP involved in $DARC_{19-30}$ binding and dimerisation[20]. In contrast, a broadly inhibitory human monoclonal, from a vaccinated human volunteer, binds away from this site[13], as do inhibitory mouse antibodies[32]. The molecular mechanisms by which these antibodies work are uncertain.

In this study, we determine the structural basis for the interaction of PvDBP with the DARC ectodomain and the human invasion blocking antibody, DB1. By using DARC proteins expressed in human cells, we define the binding site for sulfated tyrosine 41. This reveals the molecular basis for the role of tyrosine sulfation in the essential interaction between PvDBP and DARC in reticulocyte invasion by *P. vivax*.

Results

Structural characterisation of the PvDBP-DARC interaction

To determine the structure of PvDBP-RII bound to sulfated DARC ectodomain we started by expressing the N-terminal 60 residues of DARC ($DARC_{ecto}$) in HEK293 cells. This was purified and assessed by mass spectrometry, with the predominant peak having the mass expected for the peptide with the addition of two sulfates (Supplementary Fig. 1). We also expressed PvDBP-RII in HEK293 cells and this was mixed with $DARC_{ecto}$ for crystallisation. As no crystals formed, we attempted to use Fab fragments from monoclonal antibodies which bind to PvDBP-RII, but do not prevent it from binding to $DARC_{ecto}$, as crystallisation chaperones[13]. A complex of PvDBP-RII, $DARC_{ecto}$ and the Fab fragment of the DB1 monoclonal antibody[13] formed crystals which diffracted to 2.49 Å resolution. Molecular replacement using the PvDBP-RII[13] structure as a search model provided phase information and the resultant electron density map revealed density for residues 19-47 of $DARC_{ecto}$ (Fig. 1 and Supplementary Table 1).

A comparison with the previously determined structure[25] of PvDBP-RII bound to $DARC_{ecto}$ expressed in bacteria shows DARC residues 19-30 to adopt the same binding mode in both cases, forming an α-helix which packs against subdomain 2 of PvDBP-RII, with a root mean square deviation of 0.22 Å over the helical residues 22-29 of DARC (Fig. 1b). While this is the only region of DARC observed in the previous study, we now also observe clear density for residues 31-47. These form an elongated peptide which wraps, in a horse-shoe-shaped trajectory, around a protrusion on the surface of PvDBP-RII subdomain 2. Clear density was observed for each residue, including a binding pocket for Y41 and the sulfate on Y41 (Fig. 1c), which closely matched a binding site previously proposed[28]. Also visible is the side chain of residue D42, which is polymorphic (D42G) in the Fy^a/Fy^b blood group variant (Fig. 1c), but which does not make clear interactions with PvDBP-RII. Residues 48-60 are not visible in the crystal structure, suggesting a disordered linker between the PvDBP-RII-binding region of the ectodomain and the DARC transmembrane region, which starts at residue 61.

Sulfated Y41 binds to a stable binding pocket on PvDBP while Y30 is dynamic

The structure allows us to assess the role of sulfation of Y30 and Y41 of DARC on the interaction with PvDBP. A previous study has shown that mutation of Y30 to F, which removes the hydroxyl group, as well as the potential for sulfation, did not affect PvDBP-RII binding[26]. Indeed, in our structure, the Y30 side chain was clearly visible in the electron density, but no evidence was seen for sulfation, suggesting either that the sulfate was not present, or that it was disordered in the electron density (Fig. 1d). The side chain did not contact PvDBP-RII, but instead interacts with a neighbouring DB1 Fab fragment through crystal contacts.

In contrast, the side chain of Y41, together with clear density for a sulfate group, was observed. This docks into a positively charged pocket on the PvDBP-RII surface, where the sulfate makes direct salt-bridges with K301 and R304 (Fig. 1c). This is consistent with sulfated Y41 (Y41-S) forming an important part of the binding interface. Indeed, the more substantial Y41F mutation, which removes both sulfate and hydroxyl group, reduces PvDBP binding[26] and this interaction is likely to be important for residues 31-47 to adopt their correct binding conformation.

We next assessed the stability of the binding modes of Y30 and Y41 using metadynamics simulations allowing us to generate the relative free energy landscapes of the side chains of sulfated and non-sulfated versions of Y30 and Y41[33,34]. These simulations were run for three different molecular models, generated from our crystal structure. These were sulfated on both Y30 and Y41, sulfated on just Y30 and sulfated on just Y41. In each case, we analysed the ensemble of structures generated during the simulation, the free energy surfaces and the number and duration of contacts formed between each tyrosine residue and PvDBP-RII (Fig. 2).

In the case of Y41, sulfation leads to an average free energy decrease of 7.63 kJ/mol with the decrease in free energy concentrated in the existing global minimum, at approximately $\chi_1 = -161°$, where we observed a local decrease of 17.87 kJ/mol, compared with $\chi_1 = -144.3°$ in the crystal structure (Fig. 2a). This corresponds with Y41 adopting a more preferred location when sulfated (Fig. 2b). In contrast, while sulfation of Y30 leads to an average free energy decrease of 8.75 kJ/mol, this changes the shape of the free energy surface, with the free energy barrier at approximately $\chi_1 = -120°$ disappearing (Fig. 2c) and Y30 being able to explore a

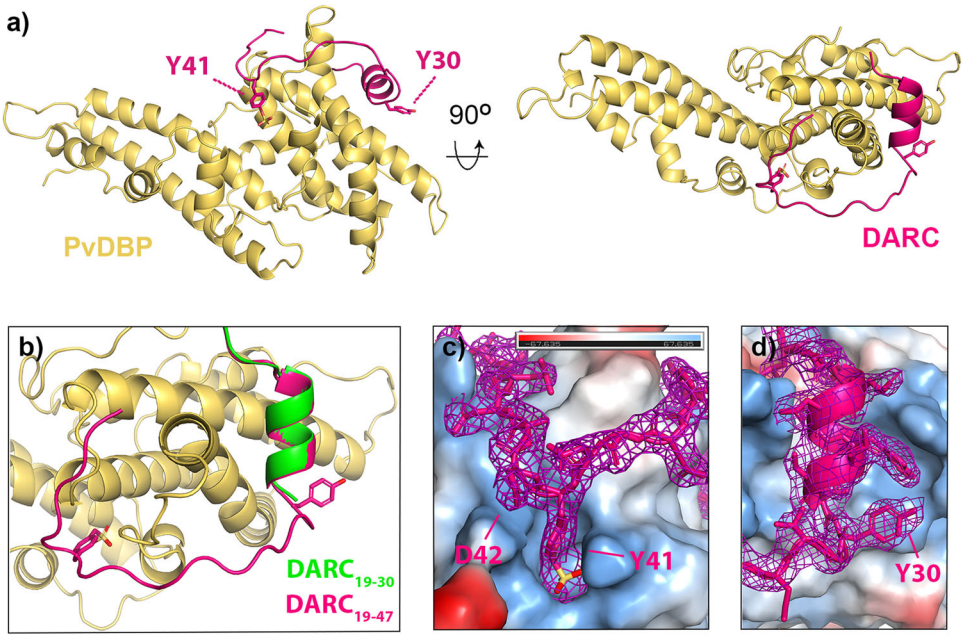


Fig. 1 | The structure of PvDBP-RII bound to sulfated DARC ectodomain. a The structure of PvDBP-RII (yellow) bound to the DARC ectodomain (pink). Residues Y30 and Y41 from DARC are highlighted as sticks, with sulfur in yellow and oxygen in red. **b** A close up of the DARC ectodomain, showing residues 19-47 of the sulfated ectodomain coloured as **a**), overlayed with residues 19-30 of the non-sulfated ectodomain in green (from PDB: 4NUV)[25]. **c** A close up of residue 41 of DARC, with DARC and the electron density surrounding DARC in pink and PvDBP-RII as a surface coloured by electrostatics (blue as positive charge and red as negative, estimated in pymol). **d** A close up of residue 30 of DARC, with DARC and the electron density surrounding DARC in pink and PvDBP-RII as a surface coloured by electrostatics (blue as positive charge and red as negative, estimated in pymol). In both **c**, **d**, the region of the $2F_O$-F_C map within 2 Å of DARC is shown at a contour level of 1.1.

wider set of χ_1 configurations when sulfated (Fig. 2d). The location of Y30 in the crystal structure has $\chi_1 = 71.6°$, which lies close to the local energy minima at $\chi_1 = \sim 65°$ in the free energy landscape. Therefore, while the sulfate on Y30 is not observed in the crystal structure, and Y30 does not contact PvDBP-RII, simulations suggest that a flexible Y30S can interact with PvDBP-RII through a dynamic electrostatic interaction.

We next assessed the number of contacts which each residue from DARC forms with PvDBP and determined the fraction of the simulation during which each contact occurs. Using a heavy atom distance cut-off of 4.5 Å to define contacts, we observe that both Y30 and Y41 make more contacts with PvDBP when sulfated. This is much more pronounced for Y41 where the average number of contacts increases from 3.64 to 7.46, whereas in Y30 we observe a shift from 1.30 to 1.87 (Fig. 2e). We observe a similar pattern when considering the durability of specific interactions, with Y41 making more interactions with PvDBP than Y30 and with sulfation increasing both the number and durability of interactions (Fig. 2f). In particular, Y41 interacts continuously with R304 during the simulation, which it can only reach when sulfated. We therefore find that sulfation of Y41 stabilises a specific location for the side chain in which it makes strong electrostatic interactions, while sulfation of Y30 does not lead to the formation of such a favourable contact, but instead increases the strength and durability of a smaller number of transient interactions.

Y41-S contributes more to binding affinity and erythrocyte invasion than Y30-S

The nature of the compact binding pocket for the sulfate on Y41, and the lack of a similar binding pocket for that on Y30, lead to the prediction that the sulfate on Y41 contributes more to the binding affinity than that on Y30. To test this, we generated a set of peptides containing the ordered region of DARC ectodomain (residues 19-47) and analysed their binding to PvDBP-RII by isothermal titration calorimetry (ITC) (Fig. 3a and Supplementary Fig. 2). A peptide in which both Y30 and Y41 are sulfated bound to PvDBP-RII with an affinity of 58 nM, while a peptide in which neither sulfate is present, bound with much lower affinity of 23 µM, quantifying the importance of sulfation for this interaction. We next tested peptides in which either Y30 or Y41 is sulfated. A peptide in which Y30 is sulfated, but Y41 is not, bound with an affinity of 552 nM, showing that the loss of Y41 sulfation leads to a ~9-fold reduction in affinity. In contrast, a peptide in which Y41 is sulfated but Y30 is not, bound with an affinity of 168 nM, with a ~3.5-fold reduction in binding affinity from the fully sulfated peptide. Therefore, both sulfates impact binding affinity, with Y41 providing a greater contribution to affinity.

We next assessed whether the differential effects of Y30 and Y41 sulfation on the affinity of DARC for PvDBP are mirrored during red blood cell invasion in vitro. To test this, we used a transgenic *P. knowlesi* line which has been modified to express PvDBP instead of the native, orthologous DARC binding protein, PkDBPα[13,14]. This transgenic parasite invades Duffy-positive erythrocytes in culture and is similarly affected by PvDBP-RII-targeting antibodies as *P. vivax* clinical isolates[13]. As it is currently technically impossible to generate transgenic erythrocyte lines in which DARC sulfation is specifically modulated, we instead assessed the ability of our four DARC ectodomain peptides to inhibit the growth of this transgenic PvDBP-expressing line, by measuring the effect of different concentrations of each peptide in a growth inhibition assay (Fig. 3b). We found that the Y30-S/Y41-S double sulfated peptide was most effective at blocking parasite growth (IC_{50} = 0.72 µM), followed by the Y41-S peptide (IC_{50} = 2.99 µM), with no growth inhibition observed for the Y30-S and non-sulfated peptides. Therefore, the effect of the peptides on parasite growth inhibition and the affinity that the peptides have for PvDBP-RII show the same pattern, with sulfation of Y41 having the greatest effect on peptide efficacy and sulfation of Y30 making a significant, but smaller difference.

We also conducted the equivalent experiment using unmodified (wild-type) *P. knowlesi* and observed a similar outcome, with

https://doi.org/10.1038/s41467-023-39357-w

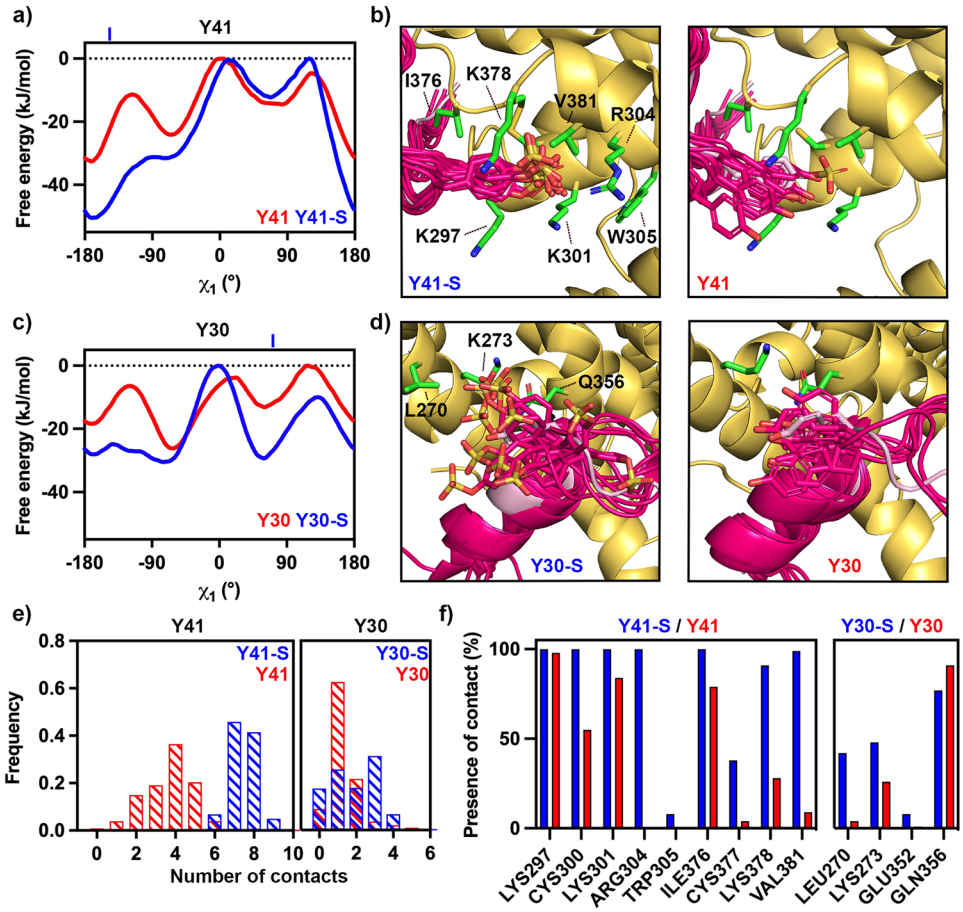


Fig. 2 | Molecular dynamics simulations indicate ordered binding of Y41 but not Y30. a Free energy landscapes for residue Y41 sulfated (blue) and non-sulfated (red) relative to the χ_1 angle of the tyrosine, showing that sulfation favours a single binding position. In the crystal structure, $\chi_1 = -144.3°$, indicated by a blue line above the graph. **b** Representative images from across the simulation, showing the degree of motion of Y41 in its sulfated (left) and non-sulfated (right) forms. In each case, PvDBP is yellow and DARC is bright pink. The crystal structure is shown for comparison in light pink. In each case, sulfate atoms are yellow, oxygen atoms red and nitrogen atoms blue. **c** Free energy landscapes for residue Y30 sulfated (blue) and non-sulfated (red) relative to the χ_1 angle of the tyrosine, showing that sulfation disfavours a single binding position. In the crystal structure, $\chi_1 = 71.6°$, indicated by a blue line above the graph. **d** Representative images from across the simulation, showing the degree of motion of Y30 in its sulfated (left) and non-sulfated (right) forms, coloured as in **b**). **e** The frequency of the number of contacts formed between PvDBP-RII and Y41 (left) and Y30 (right) in the sulfated (blue) and non-sulfated (red) forms during the simulations. **f** The percentage of frames from across the simulation in which each residue from PvDBP forms interactions with Y41 (left) and Y30 (right) in the sulfated (blue) and non-sulfated (red) forms. Source data are provided as a Source data file.

IC_{50} = 0.79 μM for the double sulfated peptide, IC_{50} = 3.92 μM for Y41-S and no inhibition observed for non-sulfated and Y30-S peptides, highlighting the parallel in DARC binding between PvDBP and PkDBPα. Therefore, while a panel of PvDBP RII-targeting antibodies which blocked invasion of *P. vivax* clinical isolates and PvDBP-expressing *P. knowlesi* (including DB1 and DB9) were not cross-reactive against wild-type *P. knowlesi*[13], the similar effect of DARC-based peptides on these two parasite lines indicates that PvDBP and PkDBPα engage DARC in a similar way.

Mapping the epitope for growth-neutralising antibody DB1

We next analysed the location of the epitope for DB1 (Fig. 4). This antibody inhibits growth of transgenic *P. knowlesi* parasites expressing PvDBP and of a subset of patient isolates of *P. vivax* which express different PvDBP variants[13]. Notably, DB1 binds to a site on PvDBP-RII which contains the polymorphic ^{339}DEK^{341} motif[35], making direct contact with these residues (Supplementary Fig. 3), explaining in part why it is not a strain-transcendent neutralising antibody[13]. DB1 also binds to a site which does not overlap the DARC binding surface, explaining why it does not directly block $DARC_{ecto}$ binding[13] (Fig. 4a).

Previous structural studies of PvDBP-RII have observed dimers to form within crystals and have also shown DARC-dependent dimerisation at high concentrations in solution in the presence of a non-sulfated DARC peptide[25,27]. DB1 would block this proposed dimerisation interface, with the Fab fragment overlapping with the second PvDBP copy and associated DARC peptide from the dimer (Fig. 4b). To determine whether the mechanism of action of DB1 is inhibition of PvDBP-RII dimerisation, we used small-angle X-ray scattering to assess the solution mass of a complex consisting of PvDBP-RII bound to Fab fragment of DB1. As predicted, the PvDBP-RII:DB1 complex showed the mass and maximum dimensions expected for a monomeric complex (Supplementary Fig. 4). We also conducted SAXS experiment for PvDBP-RII bound to Y30-S Y41-S $DARC_{19-47}$, but found that aggregation confounded collection of interpretable data. We therefore collected SAXS data for PvDBP-RII bound to Y30-S Y41-S $DARC_{19-47}$ and to the Fab fragment of antibody DB9. As DB9 binds distant from the dimerisation interface it would not prevent dimer formation. Both in SEC-SAXS experiments, in which the complex was passed through a size-exclusion column immediately before SAXS data collection (Supplementary Fig. 4), or when studied at high concentrations of up to 6 mg/ml in solution

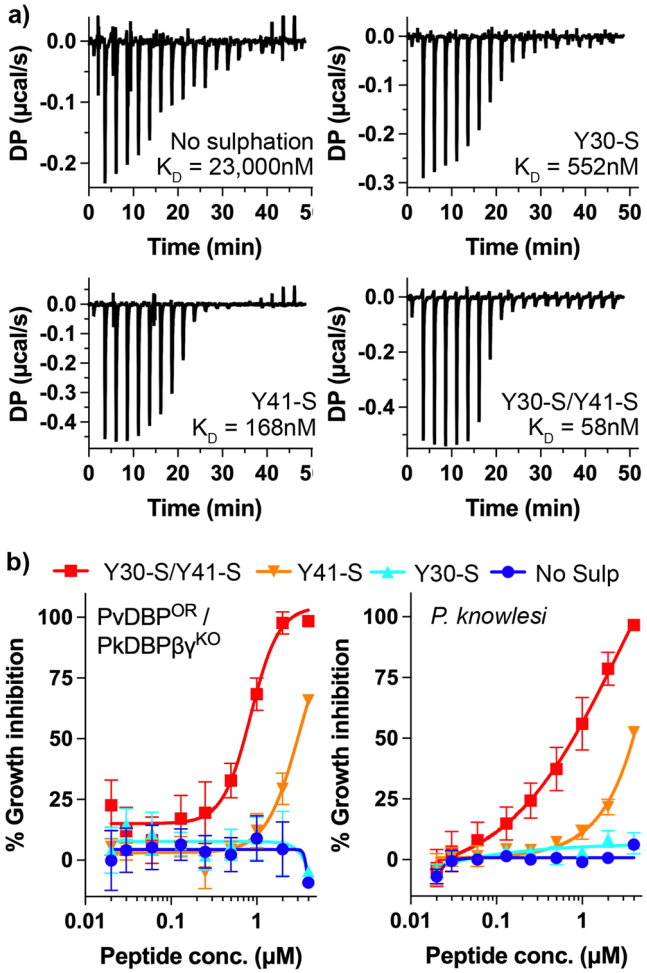


Fig. 3 | The effect of tyrosine sulfation of DARC on PvDBP-RII affinity and parasite invasion. a Isothermal titration calorimetry measurements of the binding of synthetic DARC peptides to PvDBP-RII. Shown are single representative traces for non-sulfated peptide and peptides sulfated on Y30, on Y41 or on both 30 and 41. Each stated K_D value is the mean from n = 3 technical replicates. **b** Growth-inhibitory activity for the same four peptides in an assay which assess the growth of a *Plasmodium knowlesi* line in which PkDBPs have been replaced by PvDBP ($PvDBP^{OR}$/$PkDBP\beta\gamma^{KO}$, left) or wild-type *Plasmodium knowlesi* (right). The Y30-S/Y41-S peptide inhibited with an IC_{50} of 0.72 µM for $PvDBP^{OR}$/$PkDBP\beta\gamma^{KO}$ and 0.79 µM for *P. knowlesi*. The Y41-S peptide inhibited with an IC_{50} of 2.99 µM for $PvDBP^{OR}$/$PkDBP\beta\gamma^{KO}$ and 3.92 µM for *P. knowlesi*. Technical replicates ($n = 2$) from each assay were averaged, and data presented represents the mean ± standard error of the mean of four separate biological replicates ($n = 2$ in Fy^a donor blood, and $n = 2$ in Fy^b, to account for variation between DARC alleles). IC_{50} values were identified using a variable slope four-parameter logistic curve. Source data are provided as a Source data file.

(Supplementary Fig. 5) we did not observe dimerisation of the PvDBP-RII:DB9:$DARC_{19-47}$ complex. As PvDBP-RII bound to sulfated $DARC_{19-47}$ does not dimerise in our hands, we cannot therefore conclude that DB1 acts by blocking dimerisation.

Discussion

Sulfation of DARC has been known for decades to play an important role in its binding to both cytokines and to PvDBP. However, previous structural studies used bacterially expressed DARC ectodomains, which lack tyrosine sulfation. To test whether these sulfates impact PvDBP binding, we therefore determined a structure of PvDBP-RII in complex with a sulfated DARC ectodomain. In the presence of tyrosine sulfation, we see an additional 17 residues of DARC, binding in an extended conformation around a protrusion on the PvDBP surface. We found that the sulfate on Y41 docks into a compact pocket on PvDBP, making direct interactions which are likely to be required for residues 31-47 of DARC to become ordered. Indeed, specific removal of the sulfate on Y41 leads to a ~9-fold reduction in affinity and negates growth-inhibitory activity at the concentrations tested. In contrast, Y30 plays a less significant role in the interaction, not binding to PvDBP in the structure, dynamic in molecular dynamics simulations and with specific removal of the sulfate leading to ~3.5- and ~4-fold reductions in affinity and growth inhibitory activity.

Our study also reveals the epitope for the growth-neutralising antibody DB1 and shows that it binds to a polymorphic site distant from the DARC binding site, as predicted based on previous studies which show that DB1 does not block DARC binding[13]. Instead, DB1 binds in a location which would overlap with a putative dimerisation interface on PvDBP-RII[27]. The growth-neutralising antibodies which target PvDBP-RII, and have known structures, bind to a variety of locations, suggesting a range of possible molecular mechanisms for neutralisation (Fig. 4c). DB9[13] and 2D10[32] lie on subdomain 3, distant from both DARC binding site and the putative dimerisation interface, 092096[20] blocks both DARC binding and occludes the putative dimerisation interface and DB1 blocks only the putative dimerisation interface. However, our SAXS data revealed monomers of PvDBP-RII complexes in solution, even at high concentrations, leading us to question whether PvDBP-RII dimerisation is physiological and whether blocking of dimerisation is a mechanism of inhibition (Supplementary Figs. 4 and 5). Studies in which full-length PvDBP is assessed in the context of parasite invasion will be required to resolve whether dimerisation occurs in vivo.

Our study, therefore presents a complete view of the interaction between DARC and PvDBP-RII and reveals the role of DARC sulfation on PvDBP binding. However, our view of the complete PvDBP protein remains incomplete. Studies of PvDBP have long focused on the RII domain, through ease of production and due to the demonstration that this domain contains the DARC binding site. However, questions remain, which will only be answered when we understand the structure of full-length PvDBP and how it binds to full-length DARC. For example, it is also possible that the putative dimerisation interface observed in PvDBP-RII has other roles in full-length PvDBP, which are affected by antibody binding. Further study is also required to understand the role of the DARC Fy^a/Fy^b polymorphism on PvDBP binding as the role of the polymorphic residue 42 is not certain from this study. Nevertheless, we now reveal, for the first time, the full interaction between the ectodomain of DARC and PvDBP-RII, showing the details of this interaction critical for red blood cell invasion in *P. vivax*. This identifies new surfaces of PvDBP which could be targeted by small molecules or antibodies that block the interaction with DARC, or that can be included in vaccine immunogens. These findings will guide future design of therapeutic agents to target the scourge of malaria.

Methods

Protein expression and purification

For crystallisation, the coding sequence for PvDBP-RII (D194-S508) was cloned into the pHLsec vector, which included a C-terminal 6xHis tag. DARC ectodomain (M1-S60, numbered as for the mature polypeptide) was cloned into the pENTR4 vector containing a C-terminal TEV protease cleavage site and 6xHis tag. Residues C4, C51 and C54 were changed to A to avoid disulfide formation and were not part of the PvDBP-RII binding site. DB1 heavy and light chains were supplied in the AbVec-hIgG1 and AbVec-hIgKappa vectors respectively. The constructs were transfected into Expi293 cells (Thermo Fisher Scientific) using the ExpiFectamin 293 Transfection Kit (Gibco). The transfected cells were collected after 4 days and the supernatant clarified by centrifugation at 10,000 × *g* and supplemented with 150 mM NaCl and 20 mM imidazole (final concentration).

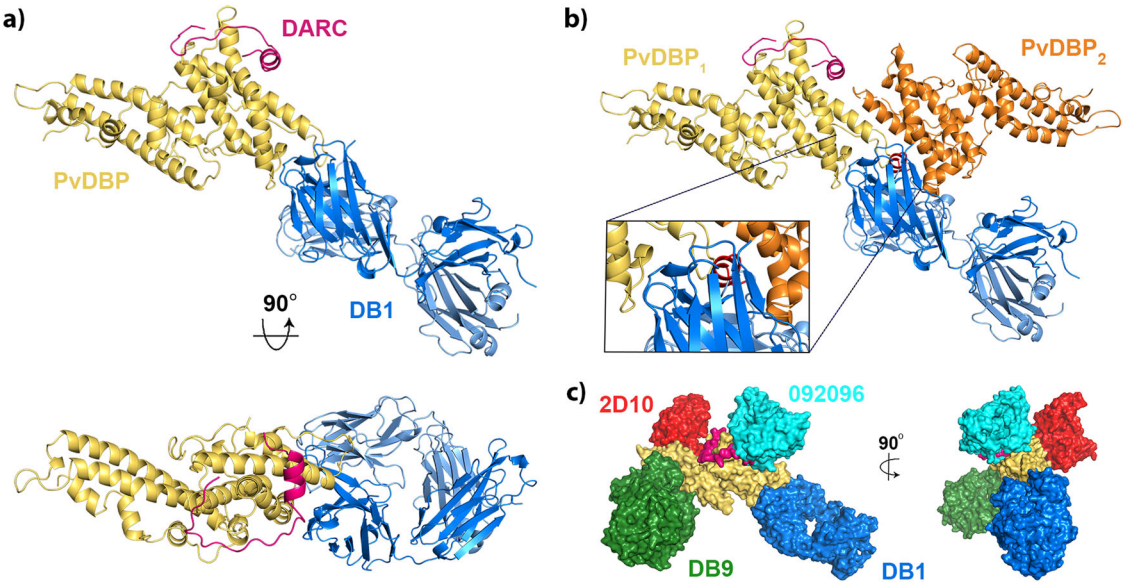


Fig. 4 | Structural basis for neutralising antibody binding to PvDBP. a Structure of PvDBP-RII (yellow) bound to DARC (pink) and antibody DB1. **b** A model of the putative PvDBP dimer (yellow and orange) bound to DARC and DB1, derived from PDB: 4NUV, showing that DB1 clashes with the putative dimerisation interface. **c** A composite structure in which four different neutralising antibodies, DB1 (blue), DB9 (green)[13], 2D10 (red)[32] and 092096 (cyan)[20] are docked on to the structure of PvDBP-RII (yellow) and DARC (pink).

For isothermal titration calorimetry, PvDBP-RII (D194-T521) was expressed with an N-terminal monomeric Fc domain (mono-Fc). Three alanine substitution mutations, T257A, S353A and T422A, were introduced to the PvDBP-RII sequence to remove potential N-linked glycosylation sites. The construct was transfected into Expi293 cells as above and harvested after 5 days. The mono-Fc tagged PvDBP-RII was purified using HiTrap Protein A HP column (Cytiva).

DB1 antibody was purified by binding clarified cell supernatant to Protein A Agarose beads (Thermo Fisher Scientific), with elution into 100 mM glycine pH 3.0 and was quickly neutralised with 1 M Tris-HCl pH 8.0. To generate DB1 Fab fragments, purified DB1 was buffer exchanged into 150 mM NaCl, 20 mM HEPES pH 7.5, 20 mM L-cysteine for overnight cleavage at 37 °C with immobilised papain, followed by protein-A agarose purification to remove Fc and uncleaved DB1 antibody.

PvDBP-RII and DARC ectodomain used for crystallisation was purified by immobilised-metal-affinity chromatography by batch binding clarified cell supernatant to Ni-NTA resin, with elution into 300 mM imidazole, 150 mM NaCl, 20 mM HEPES pH 8.0 and was buffer exchanged into 150 mM NaCl, 20 mM HEPES pH 7.5 using a Vivaspin 3 kDa column. TEV protease and PNGase F were added to DARC ectodomain overnight at 4 °C to remove the TEV-6xHis tag and glycans, respectively.

Crystallisation, data collection, and structure determination

Crystallisation trials were carried out using vapour diffusion in sitting drops, mixing 100 nl protein complex solution and 100 nl well solution. Crystals were visible from day 12 with a well solution of 15% w/v jeffamine D-2003 and 10% v/v ethanol. The crystals were cryoprotected by transfer into drops of well solution supplemented with 25% glycerol and were cryo-cooled in liquid nitrogen for data collection.

Data was collected at the I24 beamline at Diamond at a wavelength of 0.9999 Å. After processing by autoPROC, the dataset was scaled using AIMLESS (v.0.73)[36], producing a complete dataset at a resolution of 2.5 Å. The structure was solved by molecular replacement with Phaser MR (v.2.8.3)[37] using a search model for PvDBP-RII (PDB: 6R2S). The model was built and refined using cycles of COOT (v.0.8.9.2)[38] and BUSTER (v.2.10)[39].

Molecular dynamics simulations

All simulations performed using OpenMM v7.7[40]. Models of PvDBP (residues 217-509) and DARC (residues 19-47) were capped at C- and N-termini using N-methyl and acetyl groups, respectively, protonated at pH of 7.5 using H++[41] and were soaked in truncated octahedral water boxes with a padding distance of 1 nm. NaCl was added to 150 mM while neutralising charges as described in[42]. Systems were parameterised using the Amber14-SB force field[43] and water modelled using TIP3P-FB[44] and tleap[45]. For sulfotyrosine residues, we used parameters from[46]. Three systems were prepared from our crystal structure, with both Y30 and Y41 sulfated, with only Y30 sulfated and with only Y41 sulfated.

Non-bonded interactions were calculated using the particle mesh Ewald method[47] with a real-space cut-off of 0.9 nm and error tolerance of 0.0005. Water molecules and heavy atom-hydrogen bonds were rigidified using SETTLE[48] and SHAKE[49] algorithms, respectively. Hydrogen mass repartitioning[50] was used to allow 4 fs time steps. Simulations were run using the mixed-precision CUDA platform in OpenMM using the Middle Langevin Integrator with a friction coefficient of 1 ps^{-1} and the Monte-Carlo Barostat at a pressure of 1 atm. We equilibrated systems using a multi-step protocol: (i) energy minimisation over 10,000 steps, (ii) heating of the NVT ensembles from 100 K to 300 K over 200 ps, (iii) 200 ps simulation of the NPT ensembles at 300 K, (iii) cooling of the NVT ensembles from 300 K to 100 K over 200 ps, (iv) energy minimisation over 10,000 steps, (v) heating of the NVT ensembles from 100 K to 300 K over 200 ps, and (vi) 5 ns simulation of the NPT ensembles at 300 K.

We initialised well-tempered metadynamics using Plumed[51]. The first pair of simulations was biased on the χ_1 and χ_2 angles of DARC position 30. These were initialised with structures with both Y30 and Y41 sulfated and with just Y41 sulfated, using an initial hill height of 1.2 kJ/mol, a bias factor of 10, and bias widths of 0.07 rad, with biases being deposited every 500 steps. The second pair of simulations was biased on the χ_1 and χ_2 angles of DARC position 41. These were initialised with structures with both Y30 and Y41 sulfated and with just Y30 sulfated, using an initial hill height of 3.0 kJ/mol, a bias factor of 10, and bias widths of 0.07 rad, with biases being deposited every 500 steps. We found that a lower hill height of 1.2 kJ/mol was

insufficient to overcome free energy barriers in the system. For the second pair of simulations, we applied harmonic restraints on the backbone positions of the DARC peptide using the crystal structure as the reference and a force constant of 1500 kJ/(mol nm^2). Production simulations were performed for 500 ns and convergence was assessed using block error analysis on the computed free energy surfaces with respect to χ_1 and χ_2 angles of the biased positions. To recover unbiased ensembles from our simulations, we calculated weights (w) for each configuration (s) using the time-independent reweighting scheme (Eq. (1))[52]:

$$w(s) \propto \exp\left(\frac{V(s)}{k_B T}\right) \quad (1)$$

where $V(s)$ is the configuration-dependent bias at the end of the simulation and $k_B T$ is the product of the Boltzmann constant and temperature. We used MDTraj (v. 1.9.6)[53] to analyse trajectories.

Isothermal titration calorimetry

Isothermal titration calorimetry (ITC) experiments were performed on a MicroCal PEAQ-ITC (Malvern). PvDBP-RII used in the ITC experiments was tagged N-terminally with a monomeric Fc domain (mono-Fc) and contained T257A, S353A and T422A substitutions to remove N-linked glycosylation sites; modifications are not in close proximity to the DARC binding site and hence should not interfere with binding. All synthetic peptides used in the ITC experiments were purchased from Cambridge Research Biochemicals (Billingham, UK) with the purity level of 95%. Prior to the measurement, mono-Fc tagged PvDBP-RII was extensively dialysed against 1x phosphate-buffered saline (PBS), and the peptides were dissolved in the same dialysis buffer to prevent buffer mismatch. The peptides were placed in the syringe at a concentration of ~130 μM for Ac-QLDFEDVWNSS-[Y(SO3H)]-GVNDSFPDG D-[Y(SO3H)]-DANLEL-NH_2, ~300 μM for Ac-QLDFEDVWNSSYGVNDSFP DGDYDANLEL-NH2, ~200 μM for Ac-QLDFEDVWNSS-[Y(SO3H)]-GVND SFPDGDYDANLEL-NH_2, and ~260 μM for Ac-QLDFEDVWNSSYGVNDS FPDGD-[Y(SO3H)]-DANLEL-NH_2, whereas the concentration of mono-Fc tagged PvDBP-RII in the cell was ~20 μM for all experiments. The peptide concentrations were determined by BCA assay using the Pierce Rapid Gold BCA Protein Assay Kit (ThermoFisher Scientific), and the protein concentration was determined by UV absorbance at 280 nm. The titrations were all performed with peptides in the syringe and mono-Fc tagged PvDBP-RII in the cell and consisted of a single 0.4 μl injection followed by 18 injections of 2 μl with injection duration of 4 s, injection spacing of 150 s, stir speed of 750 rpm, and reference power of 10 μcal/s. Experiments were conducted at 25°C in triplicate ($n = 3$), and the data are reported as the arithmetic mean ± SD. Fitting of the integrated titration peaks was performed with MicroCal PEAQ-ITC Analysis Software (Malvern) provided with the instrument, then all data were exported to and plotted in Prism 9 (Dotmatics).

Small angle X-ray scattering

Mono-Fc tagged PvDBP-RII used for SAXS experiments was expressed in Expi293 cells (Thermo Scientific) as described above and purified using the CaptureSelect C-tagXL Affinity Matrix (Thermo Scientific). The elution was concentrated and buffer-exchanged into 20 mM HEPES, 150 mM NaCl pH 7.5 using a PD-10 Desalting Column (Cytiva) before TEV cleavage (1:100 TEV to protein ratio) overnight at 4 °C. After cleavage, mono-Fc was removed using Pierce Protein A agarose beads (Thermo Scientific). The flow-through containing PvDBP-RII was then mixed with DB1 or DB9 Fab (1.5:1 Fab to protein ratio) for 1 h before concentration and size-exclusion chromatography on a Superdex 200 Increase 10/300 GL column (Cytiva). The fractions containing PvDBP-RII with Fabs were concentrated or were mixed with $DARC_{19\text{-}47}$ Y30-S/Y41-S double sulfated peptides in case of the PvDBP-RII-DB9 Fab complex for 1 h prior to concentration.

Small-angle X-ray scattering (SAXS) data were collected at beamline B21 at the Diamond Light Source (Didcot, UK). Scattering was detected using X-rays at a wavelength of 0.99 Å and an Eiger 4 M detector with a detector-sample distance of 4.014 m. For the PvDBP-RII:DB9 Fab complexes with or without Y30-S/Y41-S double sulfated peptides, experiments were performed via two methods: (1) batch mode where 35 μl of samples at 6, 3, 1 mg/ml concentrations with corresponding matching buffers were injected directly into the capillary, using the EMBL Arinax sample handling robot, for data collection, and (2) SEC-SAXS where 50 μl of 6 mg/ml samples were gel filtered on the Shodex PROTEIN KW403-4F column (Shodex Denko Europe) equilibrated with 20 mM HEPES, 150 mM NaCl, pH 7.5 prior to data collection. The data for PvDBP-RII:DB1 complex were only collected using the SEC-SAXS method at the starting concentration of 6 mg/ml.

The data were processed using ScÅtter[54] with the ATSAS software suites[55]. For SEC-SAXS, buffer frames were averaged and subtracted from averaged frames of the complex peak fractions. The radius of gyration (Rg), distance distribution function P(r) and the maximum particle diameter (Dmax) were determined using ScÅtter. Twenty-nine ab initio initial bead models were generated with DAMMIF[55] from the ATSAS software suites in ScÅtter and averaged with DAMAVER[56] followed by refinement against the original data using DAMMIN[57]. The 20 Å envelope of the refined bead model was generated in Chimera[58]. Crystal structures of PvDBP-RII in complex with DB9 Fab[13] (PDB: 6R2S) overlayed with the Y41-S DARC peptide structure obtained in this study and the crystal structure of PvDBP-RII with DB1 Fab from the current study were fitted into the envelopes using Chimera. CRYSOL[55] was used to derive theoretical scattering data from monomeric and dimeric version of PvDBP-RII:DB9 or PvDBP-RII:DB1 complexes and to compare these data with the experimental results.

Growth inhibition assays with transgenic *P. knowlesi*

To investigate DBP-DARC interactions in vitro, the variably sulfated DARC ectodomain peptides described above were used to competitively inhibit the host-parasite interaction between erythrocytic DARC and parasite-expressed DBP, which is essential for invasion and subsequent replication. Growth inhibition assays were run as previously described in refs. 13,14 with parasite growth measured via lactate dehydrogenase (LDH) assay after one intraerythrocytic cycle (approx. 27 h) in the presence of various peptides, prepared in twofold dilution curves. Each 96-well plate included internal controls (infected, untreated erythrocytes and uninfected erythrocytes) which were used to calculate the percentage growth inhibition in each treatment well using the following formula (Eq. (2))[13,14]:

$$\%\ \mathrm{GIA} = 100 - \left(\left(\frac{\mathrm{OD}_{\mathrm{sample}} - \mathrm{OD}_{\mathrm{uninfected\ RBCs}}}{\mathrm{OD}_{\mathrm{infected\ RBCs}} - \mathrm{OD}_{\mathrm{uninfected\ RBCs}}}\right) \times 100\right) \quad (2)$$

Assays were conducted with a minimum of 2 technical replicates, and data presented represents averages from four separate experiments ($n = 2$ each using Fy^a and Fy^b donor red blood cells). Assays were performed using both *P. knowlesi* wild-type A1-H.1 (expressing PkDBPα), as well as transgenic *P. knowlesi* $PvDBP^{OR}$/$PkDBP\beta\gamma^{KO}$, which expresses the *P. vivax* DBP as an orthologue replacement of the homologous PkDBPα. IC_{50} values were identified using a variable slope four-parameter logistic curve, calculated using GraphPad Prism v9.4.1.

Reporting summary

Further information on research design is available in the Nature Portfolio Reporting Summary linked to this article.

Data availability

Coordinates and structure factors generated in this study have been deposited in the Protein Data Bank with accession code 8A44. Source data are provided with this paper.

References

1. Battle, K. E. et al. Mapping the global endemicity and clinical burden of *Plasmodium vivax*, 2000-17: a spatial and temporal modelling study. *Lancet* **394**, 332–343 (2019).
2. Howes, R. E. et al. *Plasmodium vivax* transmission in Africa. *PLoS Negl. Trop. Dis.* **9**, e0004222 (2015).
3. Price, R. N., Douglas, N. M. & Anstey, N. M. New developments in *Plasmodium vivax* malaria: severe disease and the rise of chloroquine resistance. *Curr. Opin. Infect. Dis.* **22**, 430–435 (2009).
4. Horuk, R. et al. A receptor for the malarial parasite *Plasmodium vivax*: the erythrocyte chemokine receptor. *Science* **261**, 1182–1184 (1993).
5. Miller, L. H., Mason, S. J., Dvorak, J. A., McGinniss, M. H. & Rothman, I. K. Erythrocyte receptors for (*Plasmodium knowlesi*) malaria: Duffy blood group determinants. *Science* **189**, 561–563 (1975).
6. Miller, L. H., Mason, S. J., Clyde, D. F. & McGinniss, M. H. The resistance factor to *Plasmodium vivax* in blacks. The Duffy-blood-group genotype, FyFy. *N. Engl. J. Med.* **295**, 302–304 (1976).
7. World Health Organisation. *World Malaria Report 2019* (WHO, 2019).
8. Popovici, J., Roesch, C. & Rougeron, V. The enigmatic mechanisms by which *Plasmodium vivax* infects Duffy-negative individuals. *PLoS Pathog.* **16**, e1008258 (2020).
9. Menard, D. et al. *Plasmodium vivax* clinical malaria is commonly observed in Duffy-negative Malagasy people. *Proc. Natl Acad. Sci. USA* **107**, 5967–5971 (2010).
10. Twohig, K. A. et al. Growing evidence of *Plasmodium vivax* across malaria-endemic Africa. *PLoS Negl. Trop. Dis.* **13**, e0007140 (2019).
11. Adams, J. H. et al. The Duffy receptor family of *Plasmodium knowlesi* is located within the micronemes of invasive malaria merozoites. *Cell* **63**, 141–153 (1990).
12. Singh, A. P. et al. Targeted deletion of *Plasmodium knowlesi* Duffy binding protein confirms its role in junction formation during invasion. *Mol. Microbiol.* **55**, 1925–1934 (2005).
13. Rawlinson, T. A. et al. Structural basis for inhibition of *Plasmodium vivax* invasion by a broadly neutralizing vaccine-induced human antibody. *Nat. Microbiol.* **4**, 1497–1507 (2019).
14. Mohring, F. et al. Rapid and iterative genome editing in the malaria parasite *Plasmodium knowlesi* provides new tools for *P. vivax* research. *Elife* **8**, e45829 (2019).
15. de Cassan, S. C. et al. Preclinical assessment of viral vectored and protein vaccines targeting the Duffy-binding protein region II of *Plasmodium vivax*. *Front. Immunol.* **6**, 348 (2015).
16. Moreno, A. et al. Preclinical assessment of the receptor-binding domain of *Plasmodium vivax* Duffy-binding protein as a vaccine candidate in rhesus macaques. *Vaccine* **26**, 4338–4344 (2008).
17. Cole-Tobian, J. L. et al. Strain-specific duffy binding protein antibodies correlate with protection against infection with homologous compared to heterologous *Plasmodium vivax* strains in Papua New Guinean children. *Infect. Immun.* **77**, 4009–4017 (2009).
18. King, C. L. et al. Naturally acquired Duffy-binding protein-specific binding inhibitory antibodies confer protection from blood-stage *Plasmodium vivax* infection. *Proc. Natl Acad. Sci. USA* **105**, 8363–8368 (2008).
19. Nicolete, V. C., Frischmann, S., Barbosa, S., King, C. L. & Ferreira, M. U. Naturally acquired binding-inhibitory antibodies to *Plasmodium vivax* Duffy binding protein and clinical immunity to malaria in rural Amazonians. *J. Infect. Dis.* **214**, 1539–1546 (2016).
20. Urusova, D. et al. Structural basis for neutralization of *Plasmodium vivax* by naturally acquired human antibodies that target DBP. *Nat. Microbiol.* **4**, 1486–1496 (2019).
21. Chitnis, C. E. & Miller, L. H. Identification of the erythrocyte binding domains of *Plasmodium vivax* and *Plasmodium knowlesi* proteins involved in erythrocyte invasion. *J. Exp. Med.* **180**, 497–506 (1994).
22. Chitnis, C. E. & Sharma, A. Targeting the *Plasmodium vivax* Duffy-binding protein. *Trends Parasitol.* **24**, 29–34 (2008).
23. Chitnis, C. E., Chaudhuri, A., Horuk, R., Pogo, A. O. & Miller, L. H. The domain on the Duffy blood group antigen for binding *Plasmodium vivax* and *P. knowlesi* malarial parasites to erythrocytes. *J. Exp. Med.* **184**, 1531–1536 (1996).
24. Singh, S. K., Hora, R., Belrhali, H., Chitnis, C. E. & Sharma, A. Structural basis for Duffy recognition by the malaria parasite Duffy-binding-like domain. *Nature* **439**, 741–744 (2006).
25. Batchelor, J. D. et al. Red blood cell invasion by *Plasmodium vivax*: structural basis for DBP engagement of DARC. *PLoS Pathog.* **10**, e1003869 (2014).
26. Choe, H. et al. Sulphated tyrosines mediate association of chemokines and *Plasmodium vivax* Duffy binding protein with the Duffy antigen/receptor for chemokines (DARC). *Mol. Microbiol.* **55**, 1413–1422 (2005).
27. Batchelor, J. D., Zahm, J. A. & Tolia, N. H. Dimerization of *Plasmodium vivax* DBP is induced upon receptor binding and drives recognition of DARC. *Nat. Struct. Mol. Biol.* **18**, 908–914 (2011).
28. Yogavel, M., Chhibber-Goel, J., Jamwal, A., Gupta, S. & Sharma, A. Engagement rules that underpin DBL-DARC interactions for ingress of *Plasmodium knowlesi* and *Plasmodium vivax* into human erythrocytes. *Front. Mol. Biosci.* **5**, 78 (2018).
29. Hans, D. et al. Mapping binding residues in the *Plasmodium vivax* domain that binds Duffy antigen during red cell invasion. *Mol. Microbiol.* **55**, 1423–1434 (2005).
30. VanBuskirk, K. M., Sevova, E. & Adams, J. H. Conserved residues in the *Plasmodium vivax* Duffy-binding protein ligand domain are critical for erythrocyte receptor recognition. *Proc. Natl Acad. Sci. USA* **101**, 15754–15759 (2004).
31. King, C. L. et al. Fy(a)/Fy(b) antigen polymorphism in human erythrocyte Duffy antigen affects susceptibility to *Plasmodium vivax* malaria. *Proc. Natl Acad. Sci. USA* **108**, 20113–20118 (2011).
32. Chen, E. et al. Broadly neutralizing epitopes in the *Plasmodium vivax* vaccine candidate Duffy Binding Protein. *Proc. Natl Acad. Sci. USA* **113**, 6277–6282 (2016).
33. Barducci, A., Bussi, G. & Parrinello, M. Well-tempered metadynamics: a smoothly converging and tunable free-energy method. *Phys. Rev. Lett.* **100**, 020603 (2008).
34. Laio, A. & Parrinello, M. Escaping free-energy minima. *Proc. Natl Acad. Sci. USA* **99**, 12562–12566 (2002).
35. Chen, E., Salinas, N. D., Ntumngia, F. B., Adams, J. H. & Tolia, N. H. Structural analysis of the synthetic Duffy Binding Protein (DBP) antigen DEKnull relevant for *Plasmodium vivax* malaria vaccine design. *PLoS Negl. Trop. Dis.* **9**, e0003644 (2015).
36. Winn, M. D. et al. Overview of the CCP4 suite and current developments. *Acta Crystallogr. D Biol. Crystallogr.* **67**, 235–242 (2011).
37. McCoy, A. J. et al. Phaser crystallographic software. *J. Appl. Crystallogr.* **40**, 658–674 (2007).
38. Emsley, P., Lohkamp, B., Scott, W. G. & Cowtan, K. Features and development of Coot. *Acta Crystallogr. D Biol. Crystallogr.* **66**, 486–501 (2010).
39. Bricogne, G. et al. 'BUSTER version 2.10.4' (Global Phasing Ltd., 2017).
40. Eastman, P. et al. OpenMM 7: rapid development of high performance algorithms for molecular dynamics. *PLoS Comput. Biol.* **13**, e1005659 (2017).
41. Anandakrishnan, R., Aguilar, B. & Onufriev, A. V. H++ 3.0: automating pK prediction and the preparation of biomolecular structures for atomistic molecular modeling and simulations. *Nucleic Acids Res.* **40**, W537–W541 (2012).

42. Machado, M. R. & Pantano, S. Split the charge difference in two! a rule of thumb for adding proper amounts of ions in MD simulations. *J. Chem. Theory Comput.* **16**, 1367–1372 (2020).
43. Maier, J. A. et al. ff14SB: improving the accuracy of protein side chain and backbone parameters from ff99SB. *J. Chem. Theory Comput.* **11**, 3696–3713 (2015).
44. Eyal, N. F. S. & Karpus, M. Simulation of activation free energies in molecular systems. *J. Chem. Phys.* **105**, 1902–1921 (1996).
45. Case, D. A. et al. Amber 2022 (University of California, 2022).
46. Takefumi, Y., Okajima, R., Miyanabe, K. & Tsumoto, K. Modified AMBER force-field (FUJI) parameters for sulfated and phosphorylated tyrosine residues: development and application to CCR5-derived peptide systems. *AIP Conf. Proc.* **2186**, 030013 (2019).
47. Darden, T., York, D. & Pedersen, L. Particle mesh Ewald: an N·log(N) method for Ewald sums in large systems. *J. Chem. Phys.* **98**, 10089–10092 (1993).
48. Miyamoto, S. K. & Kollman, P. A. Settle: an analytical version of the SHAKE and RATTLE algorithm for rigid water models. *J. Comput. Chem.* **13**, 952–962 (1992).
49. Ryckaert, J., Ciccotti, G. & Berendsen, H. J. C. Numerical integration of the cartesian equations of motion of a system with constraints: molecular dynamics of n-alkanes. *J. Comput. Phys.* **23**, 327–341 (1977).
50. Hopkins, C. W., Le Grand, S., Walker, R. C. & Roitberg, A. E. Long-time-step molecular dynamics through hydrogen mass repartitioning. *J. Chem. Theory Comput.* **11**, 1864–1874 (2015).
51. consortium, P. Promoting transparency and reproducibility in enhanced molecular simulations. *Nat. Methods* **16**, 670–673 (2019).
52. Branduardi, D., Bussi, G. & Parrinello, M. Metadynamics with adaptive Gaussians. *J. Chem. Theory Comput.* **8**, 2247–2254 (2012).
53. McGibbon, R. T. et al. MDTraj: a modern open library for the analysis of molecular dynamics trajectories. *Biophys. J.* **109**, 1528–1532 (2015).
54. Rambo, R. P. & Tainer, J. A. Accurate assessment of mass, models and resolution by small-angle scattering. *Nature* **496**, 477–481 (2013).
55. Franke, D. et al. ATSAS 2.8: a comprehensive data analysis suite for small-angle scattering from macromolecular solutions. *J. Appl. Crystallogr.* **50**, 1212–1225 (2017).
56. Volkov, V. V. & Svergun, D. I. Uniqueness of ab initio shape determination in small-angle scattering. *J. Appl. Crystallogr.* **36**, 860–864 (2003).
57. Svergun, D. I. Restoring low resolution structure of biological macromolecules from solution scattering using simulated annealing. *Biophys. J.* **76**, 2879–2886 (1999).
58. Pettersen, E. F. et al. UCSF Chimera–a visualization system for exploratory research and analysis. *J. Comput. Chem.* **25**, 1605–1612 (2004).

Acknowledgements

M.K.H. is a Wellcome Trust Investigator (220797/Z/20/Z). R.M. and T.P. are funded by the Skaggs-Oxford graduate scholarship. B.G. is funded by the Wellcome PhD programme in Cellular Structural Biology. S.M.D. is supported by a UK Medical Research Council LID PhD studentship. R.W.M. was supported by the UK Medical Research Council (MRC Career Development Award MR/M021157/1). The authors thank Simon Draper for the coding sequence for antibody DB1 and the plasmid construct for monoFc-tagged PvDBP-RII. We thank the staff at Diamond beamline I04 for help with crystallographic data collection and staff at Diamond beamline B21 for help with SAXS data collection.

Author contributions

R.M. produced proteins and R.M., E.L. and M.K.H. determined the crystal structure. T.P. conducted ITC and SAXS experiments. B.G. performed molecular dynamics analysis. S.M.D., F.M. and R.W.M. conducted parasite growth-inhibition experiments. R.W.M. and M.K.H. devised the study. M.K.H. drafted the manuscript and all authors discussed the results and commented on the manuscript.

Competing interests

The authors declare no competing interests.

Additional information

Supplementary information The online version contains supplementary material available at https://doi.org/10.1038/s41467-023-39357-w.

Correspondence and requests for materials should be addressed to Matthew K. Higgins.

Peer review information *Nature Communications* thanks Ram Kothandan, Wai-Hong Tham and the other, anonymous, reviewer(s) for their contribution to the peer review of this work. A peer review file is available.

Reprints and permissions information is available at http://www.nature.com/reprints

Publisher's note Springer Nature remains neutral with regard to jurisdictional claims in published maps and institutional affiliations.

Open Access This article is licensed under a Creative Commons Attribution 4.0 International License, which permits use, sharing, adaptation, distribution and reproduction in any medium or format, as long as you give appropriate credit to the original author(s) and the source, provide a link to the Creative Commons license, and indicate if changes were made. The images or other third party material in this article are included in the article's Creative Commons license, unless indicated otherwise in a credit line to the material. If material is not included in the article's Creative Commons license and your intended use is not permitted by statutory regulation or exceeds the permitted use, you will need to obtain permission directly from the copyright holder. To view a copy of this license, visit http://creativecommons.org/licenses/by/4.0/.

© The Author(s) 2023